Sequential Vapor Phase Deposition Processes for Perovskite Thin Film Photovoltaics

Zur Erlangung des akademischen Grades eines

DOKTORS DER INGENIEURWISSENSCHAFTEN
(Dr.-Ing.)

von der KIT-Fakultät für
Elektrotechnik und Informationstechnik
des Karlsruher Instituts für Technologie (KIT)

angenommene

DISSERTATION

von

M.Sc. Alexander Sebastian Diercks
geb. in Mannheim, Deutschland

Tag der mündlichen Prüfung:	15.12.2025
Hauptreferent:	Prof. Dr. Ulrich W. Paetzold
Korreferent:	Prof. Dr. Hendrik J. Bolink

Kurzfassung

Photovoltaik steht im Zentrum des globalen Bestrebens nach erneuerbaren Energielösungen zur Reduzierung der Kohlenstoffdioxid-Emissionen und zur Deckung des weltweit steigenden Energiebedarfs. Unter den neuartigen Photovoltaik-Technologien haben Perowskite aufgrund ihrer rasanten Steigerung der Solarzelleneffizienz (*engl.: power conversion efficiency*, PCE), die mittlerweile mit der konventioneller Siliziumsolarzellen vergleichbar ist, große Aufmerksamkeit erlangt. Perowskit-Solarzellen bieten mehrere Vorteile die typisch für Dünnschichttechnologien sind, darunter ein geringer Materialverbrauch und kostengünstige Herstellungsmethoden. Ihre herausragenden optoelektronischen Eigenschaften, wie anpassbare Bandlücken und hohe Absorptionskoeffizienten, machen sie zu vielversprechenden Kandidaten für die nächste Generation der Photovoltaik. Besonders vielversprechend sind Tandem-Solarzellen, die Perowskitsolarzellen mit Siliziumsolarzellen kombinieren und eine effizientere Nutzung des Sonnenspektrums ermöglichen. Perowskit/Silizium-Tandemsolarzellen erreichen PCEs nahe 35% und übertreffen damit bereits das theoretische Limit von Einzel-Solarzellen.

Für die Skalierung von Perowskit-Photovoltaik von der Laborfertigung zur industriellen Produktion ist die Entwicklung von hochdurchsatzfähigen, industriekompatiblen Abscheidemethoden erforderlich. Vakuumbasierte Abscheidungsmethoden bieten gegenüber lösungsbasierten Ansätzen entscheidende Vorteile, wie eine verbesserte Homogenität über große Flächen und die konforme Beschichtung strukturierter Oberflächen. In den letzten Jahren hat die sequentielle Gasphasenabscheidung zunehmend an Bedeutung gewonnen, da sie mit einem deutlichen Anstieg der berichteten PCEs verbunden ist und die Ergebnisse der bislang intensiver untersuchten Co-Sublimationsverfahren übertrifft. Durch die Auftrennung der simultanen Abscheidung aller Ausgangsmaterialien in aufeinanderfolgende Prozessschritte ermöglicht die sequentielle Gasphasenabscheidung eine verbesserte Prozesskontrolle und höhere Flexibilität, während die allgemeinen Vorteile der vakuumbasierten Abscheidungsmethoden erhalten bleiben. Trotz dieser Vorteile sind vakuumbasierte Abscheidungsmethoden in der Literatur zur Perowskit-Photovoltaik weiterhin deutlich unterrepräsentiert und stehen vor zentralen Herausforderungen, die für eine erfolgreiche Kommerzialisierung überwunden werden müssen. Eine wesentliche Einschränkung stellt die schlechte Reproduzierbarkeit dar, die vor allem auf das komplexe Sublimationsverhalten der häufig verwendeten organischen Materialien Methylammoniumiodid und Formamidiniumiodid (FAI) zurückzuführen ist und die Entwicklung vakuum-prozessierter Perowskit-Solarzellen erheblich erschwert. Darüber hinaus ist das Perowskit-Wachstum in Co-Sublimationsverfahren stark substratabhängig, was eine individuelle Anpassung der Prozessparameter für jedes Substrat erforderlich macht. Diese Substratabhängigkeit erhöht die Komplexität und schränkt die allgemeine Anwendbarkeit von Co-Sublimationsverfahren ein. Zusätzlich stellen die von Natur aus langsamen Abscheideraten der genutzten organischen Ausgangsmaterialien einen kritischen Engpass für eine kosteneffiziente industrielle Aufskalierung dar.

Diese Arbeit untersucht die sequentielle Gasphasenabscheidung als vielversprechenden Ansatz zur Überwindung der Limitierungen vakuumbasierter Abscheidungsmethoden in der Perowskit-Photovoltaik. Die Analyse des Sublimationsverhaltens von FAI zeigt, wie die Partikelgröße und Tiegelgeometrie die Reproduzierbarkeit auf Laborebene beeinflussen. In sequentiellen Gasphasenabscheidungsprozessen beginnt die Umwandlungsreaktion zur Perowskitphase während eines kontrollierten Tempervorgangs an der Grenzfläche der nacheinander separat abgeschiedenen Schichten. Dies stellt einen großen Unterschied zu Co-Sublimationsverfahren dar, bei denen die Kristallisation direkt auf dem Substrat während dem Abscheidungsprozess erfolgt. Das Perowskitwachstum bei der Co-Sublimationsverfahren ist stark substratabhängig, was in der Literatur bereits

umfassend untersucht wurde, wohingegen vergleichbare Studien zur sequentiellen Gasphasenabscheidung unterrepräsentiert sind. In diesem Zusammenhang zeigt die Bildung von Formamidinium-Blei-Triiodid eine ausgeprägte Substratabhängigkeit, was die Bedeutung der Substratauswahl und der Anpassung der Prozessparameter hervorhebt. Zur Einstellung der gewünschten Bandlücke für eine effiziente Integration sequentiell abgeschiedener Perowskite in Perowskit/Silizium-Tandemsolarzellen (TSCs) werden in dieser Arbeit verschiedene Ansätze zur kompositionellen Modifikation innerhalb der sequentiellen Gasphasenabscheidung vorgestellt, die in einem Proof-of-Concept für eine monolithische Perowskit/Silizium-Tandemsolarzelle münden. Um die langsamen Abscheideraten der organischen Materialien zu überwinden, wird eine alternative vakuumbasierte Abscheidungsmethode untersucht, Close-Space Sublimation (CSS). Dieses Verfahren ermöglicht deutlich schnellere Abscheidungen von vollständigen Schichten innerhalb von 10 Minuten, und zeigt signifikante Unterschiede in der kompositionellen Kontrolle im Vergleich zu konventionellen vakuum-basierten Gasphasenabscheidung. Abschließend wird die Integration dieser CSS-prozessierten WBG-Perowskite in monolithische Perowskit/Silizium-Tandemsolarzellen untersucht, wobei Siliziumsolarzellen mit unterschiedlichen Oberflächenstrukturen zum Einsatz kommen.

Abstract

Photovoltaics is in the spotlight of the global push for renewable energy solutions to mitigate carbon dioxide emissions and meet rising global energy demands. Among emerging photovoltaics technologies, perovskites have gained significant attention due to their rapid power conversion efficiency (PCE) improvements, now approaching those of conventional silicon-based solar cells. Perovskite solar cells (PSCs) offer several advantages typical for thin-film technologies, including low material consumption and inexpensive fabrication methods. Their outstanding optoelectronic properties, such as tunable bandgaps and high absorption coefficients, make them a promising candidate for next-generation photovoltaics. Particularly promising are tandem solar cells that combine perovskites with silicon, enabling more efficient utilization of the solar spectrum. Perovskite/silicon tandem solar cells (TSCs) reach PCEs close to 35%, already exceeding the theoretical limit of single-junction solar cells.

Scaling perovskite photovoltaics from laboratory to industrial manufacturing requires the development of high-throughput, industry-compatible deposition techniques. Vapor phase deposition methods offer distinct advantages over solution-based approaches, such as improved uniformity over large areas and conformal coating on textured surfaces. In recent years, sequential layer deposition has gained increasing attention due to a notable rise in reported PCEs, surpassing those achieved with the more extensively studied co-deposition approach. By decoupling the simultaneous deposition of all precursor materials into subsequent deposition steps, sequential layer deposition promises improved process control and process versatility while retaining the general advantages of vapor-phase deposition. Despite these advantages, vapor phase deposition methods remain significantly underrepresented in the perovskite photovoltaics literature and face key challenges that must be addressed for successful commercialization. A major limitation is the poor reproducibility and repeatability, largely attributed to the complex sublimation behavior of the commonly employed organic precursor materials methylammonium iodide and formamidinium iodide (FAI), hampering the development of vapor-phase-deposited PSCs. Furthermore, perovskite growth in co-deposition processes is highly substrate-dependent, necessitating individual adjustment of process parameters for each substrate type. This substrate dependency adds complexity and limits the general applicability of co-deposition. Additionally, the inherently slow deposition rates of the commonly used organic precursors represent a critical bottleneck for cost-effective industrial upscaling.

This thesis explores sequential layer deposition as a promising approach to overcome the limitations of vapor-phase processing in perovskite photovoltaics. By examining the sublimation behavior of FAI, precursor particle size and sublimation crucible geometry influence reproducibility and repeatability in laboratory-scale fabrication. In sequential layer deposition processes, the conversion reaction to the perovskite phase starts during a controlled annealing step at the interface of the subsequently deposited layers, unlike to co-deposition processes, where crystallization occurs directly on the substrate. Perovskite growth from co-deposition suffers from a strong substrate-dependency, which is well studied in literature, while similar studies for sequential layer deposition processes are scarce. In this thesis, it is found that the formation of formamidinium lead tri-iodide shows a pronounced dependence on substrate properties, highlighting the importance of substrate selection and the adjustment of process parameters. To achieve the required bandgap tuning for efficient integration of sequentially deposited perovskites into perovskite/silicon TSCs, this thesis presents several compositional engineering strategies within sequential deposition, culminating in a proof-of-concept two-terminal tandem device. Addressing the challenge of slow organic precursor deposition, close-space sublimation (CSS) is introduced as an alternative vapor phase deposition technique. This method enables significantly faster deposition rates,

achieving complete layers within 10 minutes, and reveals distinct differences in compositional control compared to conventional vapor phase deposition methods. Finally, the integration of these CSS-processed WBG perovskites into two-terminal perovskite/silicon TSCs is explored using silicon bottom cells with different surface textures.

Contents

List of Abbreviations

PV	Photovoltaics
PCE	Power conversion efficiency
PSC	Perovskite solar cell
CIGS	CuIn(Ga)Se_2
TSC	Tandem solar cell
MAI	Methylammonium iodide
FAI	Formamidinium iodide
CTL	Charge transport layer
ETL	Electron transport layer
HTL	Hole transport layer
MPP	Maximum power point
FF	Fill factor
TCO	Transparent conductive oxide
2T	Two-terminal
4T	Four-terminal
QCM	Quartz-crystal microbalance
XRD	X-ray diffraction
GIWAXS	Grazing-incident wide-angle X-ray scattering
SEM	Scanning electron microscopy
WLI	White-light interferometry
PL	Photoluminescence
AFM	Atomic force microscopy
J-V	Current-voltage characteristics
EQE	External quantum efficiency
LBIC	Laser-beam induced current mapping
NBG	Narrow-bandgap
WBG	Wide-bandgap

r.H.	relative humidity
MeO	MeO-2PACz
FAPI	Formamidinium lead triiodide
ARC	Anti-reflective coating
FWHM	Full-width at halt maximum

1 Introduction

1.1 Motivation

Climate change stands as one of the most pressing and complex challenges of the 21st century.[1] Among the many contributing factors, the rapid growth of the global population and the ever-increasing demand for energy have placed immense pressure on natural resources and intensified greenhouse gas emissions. In response to this escalating crisis, the transition to renewable energy sources has become not only desirable but essential for reducing carbon dioxide emissions and mitigating environmental impact.[2] Among the various renewable technologies, solar energy represents a particularly compelling solution. The sun delivers an extraordinary amount of energy to the Earth's surface, far exceeding global consumption needs, making it one of the most abundant and accessible sources of clean power.[3] Consequently, photovoltaics (PV) has emerged as a cornerstone of sustainable energy strategies.[4] Currently, the solar energy market is dominated by silicon-based technologies, accounting for approximately 95% of the global market share. Over the past few decades, these technologies have demonstrated consistent improvements in performance. In 2025, LONGi reported a new record power conversion efficiency (PCE) of 27.3% achieved on a large-area module.[5–8] These values are already close to the practical efficiency limit of silicon single-junction solar cells, leaving only little room for further improvement.[9] As a result, PV has become the most cost-effective technology for generating electricity from renewable sources.[4] Despite these advancements, the production of silicon remains highly energy intensive.[10] The purification of raw silicon material is a complex and energy demanding process, negatively impacting the overall environmental footprint of PV manufacturing. Nevertheless, technological progress has led to notable reductions in material usage.[4]

In recent years, organic-inorganic metal halide perovskites have emerged as a promising class of materials within the field of thin-film PV, drawing significant attention from academic and industrial communities.[11, 12] Reported PCEs of single-junction perovskite solar cells (PSCs) have increased dramatically to almost 27% in 2025, highlighting their great potential and competitiveness compared to conventional established thin-film technologies like copper indium gallium selenide or cadmium telluride solar cells.[7, 8] One of the key advantages of perovskites lies in their compatibility with low-temperature and cost-effective fabrication processes.[13, 14] In addition to their economic appeal, perovskites exhibit outstanding optoelectronic properties, including high absorption coefficients, long charge carrier lifetimes, and excellent charge transport characteristics.[15–18] The ability to tune the bandgap of perovskite materials through compositional engineering makes perovskites suitable not only for high-efficiency single-junction solar cells but also for their integration into tandem solar cell (TSC) architectures.[17–19] In TSCs, absorbers with different bandgaps are stacked to capture a broader range of the solar spectrum. This design enables a more efficient utilization of high-energy photons while also absorbing lower-energy photons that would otherwise pass through a single-junction device. By extending the spectral response, TSCs can surpass the theoretical efficiency limit of conventional single-junction solar cells.[20, 21] In perovskite/silicon TSCs, perovskites are integrated as the wide-bandgap (WBG) top cell ($E_g \approx 1.68$ eV) on top of a silicon bottom cell ($E_g = 1.1$ eV).[22, 23] Reported PCEs of perovskite/silicon TSCs have recently reached 34.85%, already surpassing the theoretical limit of single-junction solar cells, demonstrating the immense potential of perovskite-based PV to meet growing global energy demands.[7, 8, 24]

Fabrication methods of perovskite absorbers can be broadly grouped into two main categories: (i) solution-based and (ii) vapor phase deposition methods. Solution-based techniques, such as spin-coating,[25–27] inkjet-printing,[28–30] blade coating,[31–33] spray-coating[34–36] and slot-die coating[37–39], currently dominate research. In contrast, vapor phase deposition techniques, including co-deposition and sequential layer deposition, remain comparatively underexplored, with less than 2% of publications focusing on these techniques.[11, 12] This predominant focus on solution-based deposition methods results from lower equipment costs, as well as their simplicity and much faster optimization cycling.[11, 40]

In co-deposition, all precursor materials are deposited simultaneously in a single process step. Conversely, sequential layer deposition describes the decoupled, subsequent deposition of all precursor materials in two or more process steps. First reports of vapor phase deposition for the fabrication of PSCs reach back to Liu *et al.* in 2013, achieving PCEs of 15.4% using a co-deposition process.[41] To date, highest reported PCEs of co-deposited PSCs have reached 23.1%, lagging behind those of their solution-processed counterparts.[42] Recently, sequential layer deposition processes have gained a lot of attention due to reported PCEs of over 26% in 2024, demonstrating the potential and competitiveness of vapor phase deposition for efficient fabrication of PSCs.[43] A summary of the reported champion PCEs for solution-based and vapor-phase-deposited PSCs is displayed in Figure 1.1.

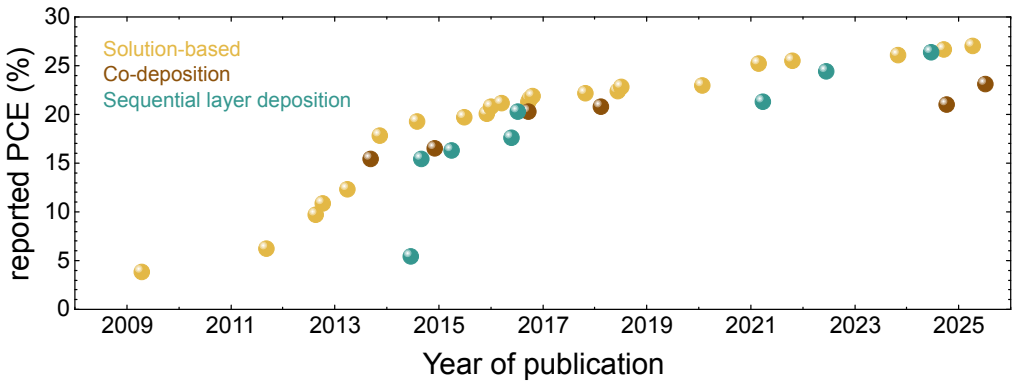

Figure 1.1: Evolution of reported champion power conversion efficiencies (PCEs) for solution-based and vapor-phase-deposited perovskite solar cells (PSCs) over the years (updated until 17.10.2025).

For a successful transition from laboratory-scale fabrication to industry-scale manufacturing, the development of scalable and industry-compatible deposition methods is essential. In that regard, vapor phase deposition methods offer significant advantages over solution-based fabrication methods and are already well-established for other industrial thin-film manufacturing.[11, 44, 45] The ability to achieve uniform film deposition over large areas is especially important for efficient upscaling.[46–48] In 2023, Ritzer *et al.* presented the first fully vapor-phase-deposited perovskite solar module (51 cm^2) using a co-deposited perovskite absorber with low upscaling losses, reaching a PCE of 16.6%.[48] Vapor phase deposition methods are particularly interesting for the fabrication of perovskite/silicon TSCs due to their conformal deposition over textured or rough surfaces, setting them apart from solution-based methods.[49–51] Roß *et al.* showed the first fabrication of fully textured perovskite/silicon TSCs with a co-deposited perovskite top cell. The achieved PCE of 24.5% is still the highest for perovskite/silicon TSCs with a vapor-phase-deposited perovskite top cell.[50] Furthermore, vapor phase deposition processes are compatible with continuous in-line processing, making them a promising candidate for high-throughput manufacturing.[40]

However, vapor phase deposition still faces multiple challenges. The most commonly used organic precursor materials, methylammonium iodide (MAI) and formamidinium iodide (FAI), are known to exhibit complex

sublimation characteristics which significantly hampers process control.[52–54] As a consequence, these materials exhibit rather slow deposition rates compared to the employed inorganic precursor materials, limiting throughput and process effectiveness.[40] In addition, the inherent variability of these organic precursor materials contributes to persistent reproducibility challenges across fabrication processes.[55–57] Overcoming these limitations is critical to unlocking the full potential of vapor phase deposition for a successful transition to industry-scale manufacturing of high-efficiency perovskite-based solar cells.[11, 40, 47]

Among the two most common vapor phase deposition methods in the field of perovskite PV, co-deposition and sequential layer deposition, the majority of research focuses on co-deposition processes.[11, 12] Co-deposition processes exhibit a pronounced dependence on the substrate. Numerous studies have already investigated the influence of the substrate on perovskite growth and the resulting film properties.[58–60] In contrast, during sequential layer deposition, perovskite formation initiates at the interface between the deposited precursor layers rather than at the interface with the underlying substrate, representing a fundamental difference between the two approaches. Compared to co-deposition processes, studies on the impact of the underlying substrate on the perovskite formation in sequential layer deposition processes are scarce.[61]. Furthermore, sequential layer deposition offers two processing advantages over co-deposition: (i) due to the sequential deposition of the precursor materials, a better process control of each individual material is provided, potentially improving reproducibility and repeatability,[43] and (ii) the overall speed of co-deposition processes is governed by the slowest deposition rate, which is typically dictated by the employed organic precursors. The decoupling of the co-deposition process therefore allows for an improved overall process effectiveness.[40]

In order to increase the deposition rates of the organic precursor materials, alternative vapor phase deposition methods, such as close-space sublimation (CSS), can be considered. In CSS, the distance between the source and the substrate is reduced to a few millimeters, allowing not only for higher deposition rates, but also an improved material utilization. Additionally, CSS operates at significantly higher working pressures (1-100 mbar) compared to conventional vapor phase deposition methods, which generally require high-vacuum conditions (10^{-6} mbar). This feature facilitates simpler system design and reduced operational costs, making CSS a promising candidate for scalable and economically viable industrial manufacturing.[62–64]

1.2 Research Questions

Scalable and consistent fabrication of perovskite absorber layers with industry-compatible deposition methods remains one of the main challenges for the successful commercialization of PSCs. Vapor phase deposition combines several key advantages for industrial fabrication, such as homogeneous large-area coating and conformal coating over textured substrates. Reproducible and repeatable processing is of utmost importance for advancing vapor-phase-deposited perovskites but remains challenging due to difficult process control of multi-source co-sublimation processes, as well as strong substrate-dependent growth of co-deposited perovskite thin films. Furthermore, the comparably low deposition rates of the organic precursors present a hurdle for efficient high-throughput fabrication of perovskite-based single-junction and tandem PV.

This thesis addresses these challenges of vapor phase deposition processes for the fabrication of perovskite thin films in PV with the following research questions:

I Analysis of sublimation behavior of FAI for improved reproducibility and repeatability of FAI-based vapor phase deposition processes
How do precursor particle size and sublimation crucible geometry impact the effusion behavior of FAI during sublimation?

II Understanding substrate-dependent growth of sequentially deposited perovskite thin films
How do different hole transport layers affect the perovskite film formation and final layer quality of sequentially deposited perovskite thin films?

III Compositional engineering for sequentially deposited wide-bandgap perovskite absorber layers
What strategies can be employed to tailor the perovskite composition in sequential layer deposition processes, and what are the various methodological approaches available?

IV Increasing deposition rates of organic precursor materials
Can CSS overcome the slow deposition rates of organic precursor materials from conventional sublimation crucibles for the fabrication of vapor-phase-deposited WBG PSCs?

V Integration of fully vacuum-processed perovskite top cells into two-terminal perovskite/silicon tandem architectures
How does the morphology of the silicon bottom cell influence the growth of CSS-processed perovskite absorber layers and resulting PCE of 2T perovskite/silicon TSCs?

The stated research questions are addressed in the introduction and summary sections of the respective chapters. Chapter 7 summarizes and relates the key findings of this thesis to the respective research question. Furthermore, a final outlook with future research question based on these key findings is presented.

1.3 Outline

Chapter 1 provides a concise overview of perovskite PV in relation to the evolving landscape of renewable energy solutions. In addition, the chapter outlines the motivation behind this thesis and presents the research questions addressed in this work.

Chapter 2 outlines the theoretical background required for this work, addressing the crystallographic and optoelectronic behavior of organic-inorganic metal halide perovskites and discussing the fundamental principles of PSCs. Furthermore, the principles of vapor phase deposition, including key process characteristics and thin-film growth models, are introduced. Finally, an overview of sequential physical vapor deposition, the main fabrication method used in this thesis, is presented.

The experimental methods of this work are introduced in Chapter 3, describing the experimental fabrication processes and characterization methods of perovskite thin films and solar cells used in this work.

Chapter 4 focuses on the investigation of sublimation behavior of FAI from effusion sources by analyzing the effect of different precursor particle sizes and sublimation crucible geometries on the directionality of the emitted vapor flux (research question **I**).

Chapter 5 presents the first systematic investigation into substrate-dependent growth behavior of perovskite thin films fabricated *via* conventional sequential layer deposition (research question **II**). In addition, various strategies for tuning the chemical composition of the perovskite absorber to engineer its bandgap are discussed. Finally, this chapter demonstrates the first integration of WBG PSCs, fabricated *via* sequential deposition, into perovskite/silicon tandem architectures, serving as a proof-of-concept device (research question **III**).

Chapter 6 in-detail studies a two-step vapor phase deposition technique that enables high-rate deposition of organic precursor materials using CSS (research question **IV**). The successful integration of high-performance single-junction PSCs into 2T perovskite/silicon TSCs, employing various silicon bottom cell morphologies, demonstrates the industrial relevance of CSS as a scalable deposition method (research question **V**).

Chapter 7 offers a comprehensive summary of this thesis, contextualizing the key findings with respect to the initial research questions. Finally, an outlook is provided that discusses how the findings of this thesis can inform subsequent advancements in vapor phase deposition, facilitating the transition of perovskite PV toward industrial applicability.

2 Fundamentals

This chapter provides the theoretical framework necessary to understand and assess the results of this thesis. It introduces hybrid metal halide perovskites, focusing on their crystal structure and optoelectronic properties. The working principle of perovskite solar cells is explained, along with key photovoltaic performance metrics. Device architectures for single-junction and tandem solar cells are discussed. Additionally, the fundamentals of vapor phase deposition are introduced, including general principles and film growth models. The chapter concludes with an overview on sequential layer deposition processes, which represent the primary fabrication method employed in this work.

2.1 Organic-Inorganic Metal Halide Perovskite Semiconductors

Perovskite describes a material class with the general crystal structure ABX_3 that originates from the mineral calcium titanate ($CaTiO_3$), named after the Russian mineralogist Lev Aleksevich Perovski. In recent years, organic-inorganic metal halide perovskites have gained significant attention in the field of photovoltaics due to their exceptional optoelectronic properties.

2.1.1 Crystallographic Properties

Figure 2.1 shows the cubic unit cell of the general perovskite crystal structure ABX_3. It consists of an A-site cation in the center surrounded by BX_6 octahedrons with B-site cations and X-site anions in the corners. In organic-inorganic metal halide perovskites, the A-site cation is typically an organic molecules like methylammonium ($CH_3NH_3^+$, MA^+) or formamidinium ($CH_3(NH_3)_2^+$, FA^+), or the inorganic cations cesium (Cs^+). The B-site cation is usually lead (Pb^{2+}) or tin (Sn^{2+}), and the X-site anion can be iodide (I^-), bromide (Br^-) and chloride (Cl^-). By changing the specific ratios of multiple anions and cations at each site, the perovskite composition can be adjusted, leading to a change in the optoelectronic properties of the final perovskite.

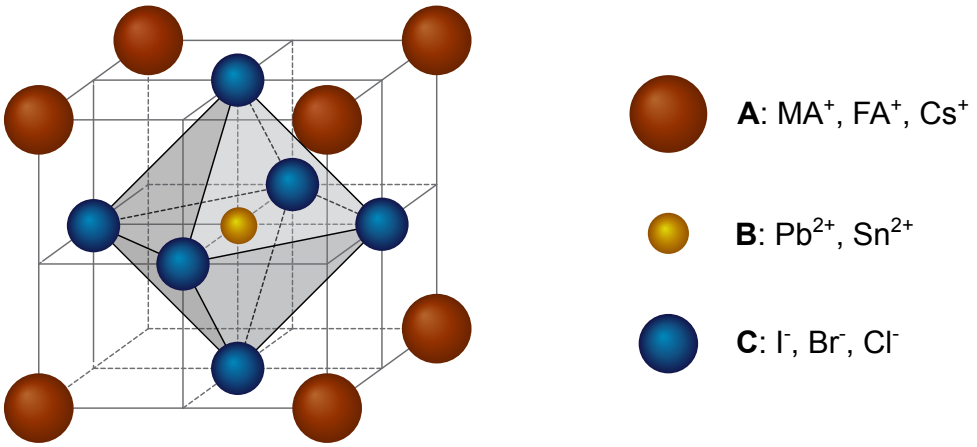

Figure 2.1: Schematic of the cubic unit cell of the perovskite crystal structure ABX_3. In case of organic-inorganic metal halide perovskites **A** is a monovalent cation (MA^+, FA^+ or Cs^+), **B** is a divalent metal cation (Pb^{2+}, Sn^{2+}) and **C** is a halide anion (I^-, Br^-, Cl^-). The cube corners of the unit cell are occupied by **A**-cations, the **B**-cation is located in the center and **X**-anions lie in the center of the sides.

A decisive factor in whether a perovskite material adopts a (pseudo-)cubic perovskite crystal structure are the ionic radii of the A-, B- and X-ions involved in forming the crystal lattice. The degree of distortion in a perovskite crystal structure can be estimated using the Goldschmidt tolerance factor t:[65]

$$t = \frac{r_A + r_X}{\sqrt{2} \cdot (r_B + r_X)} \tag{2.1}$$

with r_A, r_B and r_X being the ionic radii of the corresponding A-, B- and X-ions.

For an ideal cubic crystal structure, the Goldschmidt tolerance factor lies between $0.9 < t < 1.0$. Smaller tolerance factors ($0.8 < t < 0.9$) result in tetragonal, orthorhombic or rhombohedral crystal structures. When $t < 0.8$ or $t > 1.0$, non-perovskite crystal structures are formed.[66–68] It should be noted, that these values represent theoretical approximations. Besides the cubic α-phase, depending on their exact chemical composition, perovskite materials can exhibit other photoactive structural phases, namely β (tetragonal) or γ

(orthorhombic). Non-perovskite phases are referred to as δ-phases (e.g., trigonal or hexagonal). The formation of these phases are dependent on the employed fabrication method and temperature during fabrication.[67, 69]

2.1.2 Optoelectronic Properties

Perovskite thin films generally exhibit a polycrystalline structure due to the commonly employed fabrication methods and the associated crystallization mechanisms, which favor the formation of multiple crystalline grains rather than a single crystal. During both solution-based and vapor-based deposition processes, crystallization occurs during film formation, throughout solvent evaporation during annealing and at the substrate interface, leading to the simultaneous nucleation and growth of numerous crystallites that merge into a continuous polycrystalline film without epitaxial alignment. Due to their exceptional optoelectronic properties, organic-inorganic metal halide perovskites are a promising candidate for next-generation photovoltaics, even in polycristalline thin films.

High absorption coefficients

Organic-inorganic metal halide perovskites exhibit exceptionally high absorption coefficients $\geq 10^4$ cm^{-1}, exceeding those of crystalline silicon and conventional thin-film photovoltaic materials like cadmium telluride and gallium arsenide.[16, 70] This outstanding absorption capability enables efficient light harvesting even with comparably thin absorber layers of typically a few hundred nanometers, resulting in minimal material consumption. The direct bandgap nature of perovskites allows for strong optical transitions and nearly complete absorption of incident photons with energies above the bandgap ($E_\gamma \geq E_g$) even in thin films.

Long charge carrier diffusion lengths and high defect tolerance

Perovskite semiconductors exhibit a remarkably high tolerance to intrinsic defects.[71, 72] This enables comparably long charge carrier lifetimes, often exceeding 1 μs, even in polycrystalline films. Combined with high charge carrier mobilities (typically >10 $cm^2V^{-1}s^{-1}$), charge carrier diffusion lengths can exceed several micrometers.[73–75] These properties, coupled with the requirement for only thin absorber layers resulting from their high optical absorption coefficients, significantly increase the probability of charge carrier extraction, making perovskite materials highly effective for PV applications.

Bandgap tunability through compositional engineering

Perovskite materials are particularly attractive for optoelectronic applications due to their tunable bandgap, which can be precisely adjusted through compositional engineering. The bandgap of Pb-based perovskites can be varied from approximately 1.5 - 3.1 eV. This tunability is achieved by modifying the components of the ABX_3 crystal structure. Substitution of the halide ion I^- with Br^- or Cl^- leads to an increase of the bandgap, whereas replacing the B-cation Pb^{2+} partially or entirely with Sn^{2+} results in a decrease of the bandgap. On the other hand, exchanging the predominantly used organic cations (MA^+ or FA^+) with inorganic cations like cesium (Cs^+) increases the bandgap.[76, 77] This wide range of accessible bandgaps makes perovskites an ideal candidate for PV applications, including single-junction solar cells, as well as their application in tandem photovoltaics in combination with established thin-film solar cells (e.g. perovskite/silicon or perovskite/$CuIn(Ga)Se_2$).

2.2 Perovskite-based Solar Cells

2.2.1 Working Principle of Perovskite Solar Cells

Solar cells are optoelectronic devices that convert the energy of incident light into electrical energy through the photovoltaic effect. The basic principle of perovskite solar cells is described in the following and can be summarized in four steps: (1) absorption of incident photons in the photoactive absorber layer, (2) creation of free charge carriers, (3) charge carrier separation through charge transport layers (CTLs) and (4) extraction of charge carriers at the respective electrode contacts.

Figure 2.2a displays a schematic of a perovskite solar cell to illustrate the four steps. The intrinsic perovskite absorber layer is sandwiched between two CTLs, an electron transport layer (ETL) and a hole transport layer (HTL) and contacting electrodes.

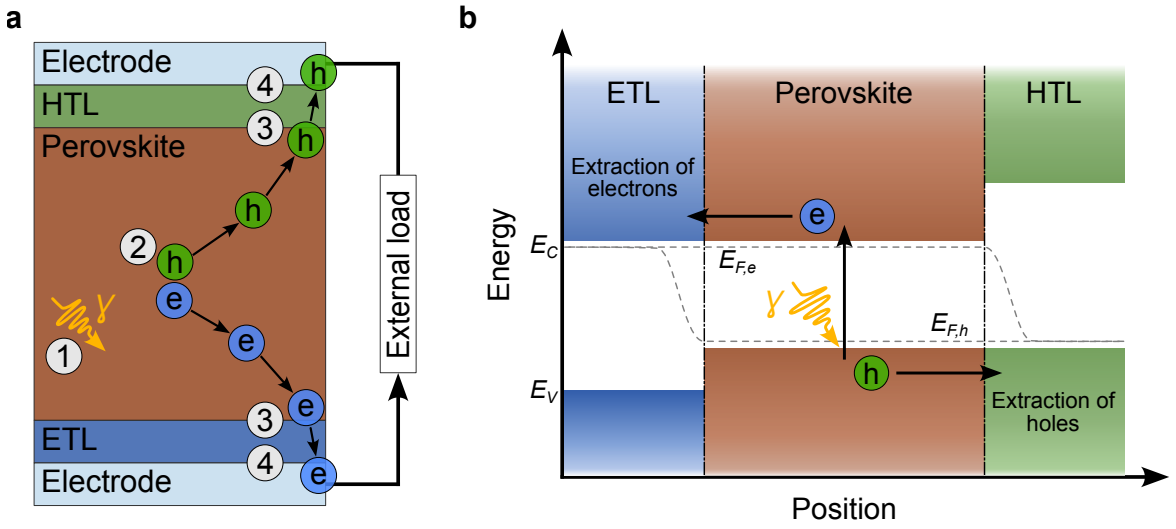

Figure 2.2: Working principle of a perovskite solar cell. **a** Illustration of the four fundamental steps for charge carrier generation and extraction in a perovskite solar cell, where the perovskite absorber layer is sandwiched between two charge transport layers (ETL = electron transport layer, and HTL = hole transport layer) connected to respective electrodes: (1) absorption of incident photons in the photoactive absorber layer, (2) creation of free charge carriers (e = electrons, h = holes), (3) charge carrier separation through adjacent charge transport layers (ETL and HTL), and (4) extraction of the generated charge carriers at the electrodes. **b** Idealistic energy band diagram of a perovskite solar cell under illumination and open-circuit conditions. Absorbed incident photon energy leads to quasi-Fermi level splitting into the two quasi-Fermi levels of electrons ($E_{F,e}$) and holes ($E_{F,h}$) and excitation (e) of an electron from the valence band (E_V) into the conduction band (E_C).

Absorption of incident photons

To excite an electron from the valence band to the conduction band, the energy of the incident photon ($E_\gamma = h\nu$) needs to be equal or exceed the bandgap of the material ($E_\gamma \geq E_g$). Photons with lower energy than the bandgap ($E_\gamma < E_g$) are transmitted through the material, while the additional energy ($E_\gamma > E_g$) results in thermalization losses.

Generation of free charge carriers

The excitement of an electron from the valence band (E_V) to the conduction band (E_C) leads to the generation of an electron-hole pair, which dissociates into free negative (electrons, e) and positive (holes, h) charge carriers. These charge carriers move inside the (E_C) and (E_V), respectively, and are driven through two principle driving forces: (i) Diffusion, arising from gradient in the chemical potential, reflecting spatial differences in charge

carrier concentration, and (ii) drift, caused by a gradient in the electrical potential (electric field). Together, both forces (chemical potential and electrical potential) define the electrochemical potential within the material.

Separation of electron-hole pairs

In the following, the charge carrier separation is described according to Würfel *et al.*[78, 79] To derive the total charge carrier current of electrons (e) and holes (h) considerint both driving forces within the material, first their individual contribution is presented. In case of a pure electrical force (drift) due to an electrical field (E) inside the absorber, the charge carrier current ($J_{drift,i}$) is:

$$J_{drift,e,h} = e \cdot n_{e,h} \cdot \mu_{e,h} \cdot E = \sigma_{e,h} \cdot E = -\frac{\sigma_{e,h}}{e \cdot z_{e,h}} \cdot \mathrm{grad}(e \cdot z_{e,h} \cdot \Phi) \tag{2.2}$$

with e being the elementary charge (with $z_e = -1$ and $z_h = 1$, for electrons and holes), $n_{e,h}$ the concentration of charge carriers, $\mu_{e,h}$ the charge carrier mobility and $\sigma_{e,h}$ the electrical mobility of charge carriers. Φ is the electric potential, causing a diffusive driving force described by $-grad(e \cdot z_{e,h} \cdot \Phi)$ on the charge carriers.

In case of a pure chemical force (diffusion) due to a gradient in charge carrier concentration inside the absorber, the charge carrier current ($J_{diff,e,h}$) is given by Fick's law:

$$J_{diff,e,h} = e \cdot z_{e,h} \cdot (-\frac{\mu_{e,h} \cdot k_B \cdot T}{e}) \cdot \mathrm{grad}(n_{e,h}) = e \cdot z_{e,h} \cdot (-D_{e,h}) \cdot \mathrm{grad}(n_{e,h}) = -\frac{\sigma_{e,h}}{e \cdot z_{e,h}} \cdot \mathrm{grad}(\Phi_{chem,e,h}) \tag{2.3}$$

with $D_{e,h} = (\frac{\mu_{e,h} \cdot k_B \cdot T}{e})$ describing the diffusion coefficient, k_B being the Boltzmann constant and T the temperature. $\Phi_{chem,e,h}$ is the chemical potential, causing the electric force gradient ($-grad(\Phi_{chem,e,h})$) on the charge carriers.

Since both driving forces (drift and diffusion) contribute simultaneously to the total charge carrier current J_{total}, both $J_{drift,e,h}$ and $J_{diff,e,h}$ need to be added:

$$J_{total,e,h} = -\frac{\sigma_{e,h}}{e \cdot z_{e,h}} \mathrm{grad}(e \cdot z_{e,h} \cdot \Phi + \Phi_{chem,e,h}) = -\frac{\sigma_{e,h}}{e \cdot z_{e,h}} \cdot \mathrm{grad}(\eta_{e,h}) \tag{2.4}$$

with $\eta_{e,h}$ being the electrochemical potential of the charge carriers.

For semiconductors at thermodynamic equilibrium, the electrochemical potential of electrons is equivalent to the Fermi level (E_F). The Fermi-level describes the energy at which the probability of occupancy for electronic states is 50%, according to the Fermi-Dirac distribution. For temperatures above absolute zero ($T > 0\ K$), electron states below E_F are statistically more likely to be occupied, whereas electron states above E_F are less likely to be occupied. Illumination of a solar cell and subsequent generation of charge carriers alters with the electron and hole densities in the conduction and valence band, respectively. The increase in electron density tends to shift the Fermi level upward, closer to the conduction band minimum, while the increase in hole density simultaneously pushes it downward, toward the valence band maximum. Since a single Fermi level cannot simultaneously reflect both states, this apparent contradiction is resolved by introducing two separate so-called quasi-Fermi levels - one for electrons ($E_{F,e}$) and one for holes ($E_{F,h}$). This phenomenon, known as quasi-Fermi level splitting, is illustrated in Figure 2.2b.[80, 81]

$E_{F,e}$ lies closer to the conduction band due to the increased electron density, while $E_{F,h}$ is closer to the valence band due to the higher hole density. The energy difference between both quasi-Fermi levels can be expressed

as an energy eV, with V representing the difference between the solar cell's electrodes. In this context, the electrochemical potential of electrons in the conduction band is directly represented by their quasi-Fermi level, ($\eta_e = E_{F,e}$), indicating the degree of occupancy of conduction band states. Similarly, the electrochemical potential of holes corresponds to their quasi-Fermi level, ($\eta_h = E_{F,h}$), which describes the occupation of states in the valence band.

Therefore, the resulting charge-carrier currents depend on the gradients of the quasi-Fermi levels and electrical conductivities of electrons and holes:

$$J_{total,e,h} = -\frac{\sigma_{e,h}}{e \cdot z_{e,h}} \cdot \mathrm{grad}(E_{F,e,h}) \tag{2.5}$$

Selective extraction of charge carriers

Solar cells rely on the selective extraction of charge carriers at the interfaces with the CTLs. In PSCs, charge carrier separation is realized using a *p-i-n* heterostructure, in which the intrinsic absorber layer is sandwiched between an hole-selective (HTL) and electron-selective (ETL) CTL. "*P-i-n*" hereby refers to the HTL (*p*), the intrinsic perovskite absorber layer (*i*) and the ETL (*n*), and does not refer to doping as in the case for silicon *pn*-heterojunctions. In such a *p-i-n* heterostructure, the direction of the desired charge carrier current is opposite to the maximum gradient of the quasi-Fermi levels (Figure 2.2b).

Efficient operation of perovskite solar cells relies heavily on the selective extraction of charge carriers through the CTLs. ETLs must exhibit a large energy-level offset in the valence band edge (E_V) relative to the absorber and exhibit high electron conductivity, together with low hole conductivity in order to selectively extract electrons. Similarly, HTLs must exhibit low electron and high hole conductivities in order to selectively extract holes, and a significant offset in the conduction-band edge E_C compared to the absorber. Due to these properties, CTLs behave like membranes, only allowing the individually desired charge carrier species to pass while blocking the other. The charge carriers are extracted *via* the respective electrodes, resulting in the flow of an electric current through the external load.[78]

For open-circuit conditions, when the solar cell is illuminated but not connected to a load, no photocurrent flows and the generated charge carriers accumulate at the respective electrodes until reaching an equilibrium state. In this case, the difference in quasi-Fermi levels at the electrodes defines the open-circuit voltage (V_{OC}). For short-circuit conditions, when the solar cell is illuminated and connected to a load without any potential barrier, the generated carriers are extracted efficiently without accumulating at the interfaces, and the photocurrent reaches its maximum value, known as the short-circuit current density (J_{SC}). When illuminated and connected to an external load, the solar cell functions between these two limiting conditions, generating both a photovoltage and photocurrent, generating electrical power output. At intermediate points, the external load provides a finite resistance, simultaneously enabling partial current flow while maintaining a voltage.

In case of an ideal solar cell, the current-voltage relationship can be derived from Equation 2.6, considering all generated and extracted charge carriers within the absorber:

$$J = \int_0^d e \cdot (G(x) - R(x)) \cdot dx \tag{2.6}$$

with J being the current density, d the absorber thickness, R the recombination rate and G the generation rate.

The generation rate G is divided into the generation rate in the dark (G_{dark}) and the generation rate caused by illumination (G_{illu}) (Equation 2.7)

$$G(x) = G_{dark} + G_{illu}(x) \tag{2.7}$$

while the recombination rate R is described in Equation 2.8:

$$R(x) = R_{dark} \cdot exp\left(\frac{E_{F,e}(x) - E_{F,h}(x)}{k_B \cdot T}\right) = R_{dark} \cdot exp\left(\frac{eV}{k_B \cdot T}\right) \tag{2.8}$$

with R_{dark} describing the recombination rate in the dark and $E_{F,e}(x) - E_{F,h}(x)$ the difference in quasi Fermi levels, which can be expressed in energy eV.

In an equilibrium state, the generation rate and recombination rate ($G_{dark} = R_{dark}$) and the current density J is given by:

$$J = e \cdot \int_0^d \left(G_{dark} \cdot (\left(xp\left(\frac{eV}{k_B \cdot T}\right) - 1\right) - G_{illu} \cdot x\cdot\right) dx \tag{2.9}$$

$$J = e \cdot exp\left(\frac{eV}{k_B \cdot T} - 1\right) \cdot \int_0^d G_{dark} \cdot dx - e \cdot \int_0^d G_{illu}(x) \cdot dx \tag{2.10}$$

When considering two limiting cases of the equation, the terms depending on the generation rate can be more precisely identified. Under short-circuit conditions (where the voltage $V = 0$), the first term in the equation vanishes entirely and $\int_0^d G_{illu}(x) \cdot dx$ now represents the short-circuit current density J_{SC}.

In the second case, the current density is examined in the dark ($G_{illu} = 0$) and under high negative voltage bias $exp\left(\frac{eV}{k_B \cdot T}\right) \ll 1$. This term is referred to as the dark saturation current density J_0. From these considerations, the current density-voltage characteristics of an ideal solar cell can be derived:

$$J = J_0 \cdot \left(exp\left(\frac{eV}{k_B \cdot T}\right) - 1\right) - J_{SC} \tag{2.11}$$

2.2.2 Electrical Characteristics and Photovoltaic Metrics

Comparing the current-voltage characteristics of an ideal solar cell to the Shockley equation for the electrical description of a diode shows that an ideal solar cell can be described by an equivalent circuit of a diode and a current source (Equation 2.12).

$$I = I_{ph} - I_d - I_{sh} \tag{2.12}$$

with I_{ph} being the photocurrent, I_d the radiative recombination losses and I_{sh} the shunt resistance current.

Apart from radiative recombination losses, a real solar cell suffers from resistive losses. Therefore, a series resistance (R_{Series}) and a shunt resistance (R_{Shunt}) are added to the equivalent circuit resulting in the one-diode model to describe a real solar cell (Figure 2.3a).

By using the diode equation, the resulting output current I_V can be described as:

$$I(V) = I_{ph} - J_0 \cdot \left(epx\left(\frac{e \cdot V - I \cdot R_{Series}}{n \cdot k_B \cdot T}\right) - 1\right) - \left(\frac{V + I \cdot R_{Series}}{R_{Shunt}}\right) \tag{2.13}$$

with I_0 describing the dark saturation current, n representing the ideality factor and V the voltage of the solar cell.

For an ideal solar cell with $R_{\text{Series}} = 0$ and $R_{\text{Shunt}} = \infty$ can be assumed:

$$I(V) = I_{ph} - I_0 \cdot \left(epx \left(\frac{e \cdot V}{n \cdot k_B \cdot T} \right) - 1 \right) \tag{2.14}$$

In order to compare the quality and performance of solar cells, there are fundamental parameters that can be extracted and calculated from the corresponding current-voltage curve of the solar cell (Figure 2.3b).

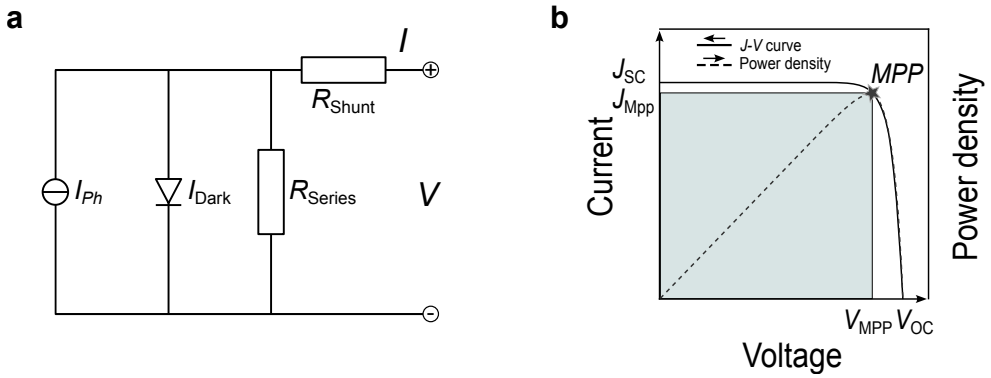

Figure 2.3: Electrical and photovoltaic characteristics of a perovskite solar cell. **a** Equivalent circuit of a perovskite solar cell based on the one-diode model to describe the electrical behavior, with a photocurrent source (I_{Ph}), radiative recombination losses (I_{D}) and resistive elements (R_{Series} and R_{Shunt}). **b** Exemplary current-voltage (*J-V*) curve under illumination to show the general photovoltaic performance metrics short-circuit current density (J_{SC}) and open-circuit voltage (V_{OC}), as well as maximum power point (MPP) with corresponding current density (J_{MPP}) and voltage (V_{MPP}). These values are used to calculate the fill factor (FF) and power conversion efficiency (PCE) of the solar cell.

The short-circuit current (I_{SC}) describes the maximum current of the solar cell and is measured under short-circuit conditions ($V = 0$):

$$I_{SC} = I(V = 0) \approx I_{ph} \tag{2.15}$$

For better comparability between solar cells with different active area sizes, the current is converted into a current density by dividing I_{SC} through the active area (A):

$$J_{SC} = \frac{I_{SC}}{A} \tag{2.16}$$

The V_{OC} describes the maximum achievable voltage of the solar cell at open-circuit conditions ($I(V = 0)$) and is expressed as:

$$V_{OC} = \frac{n \cdot k_B \cdot T}{e} \cdot \ln \left(\frac{I_{ph}}{I_0} + 1 \right) \tag{2.17}$$

The maximum power output of a solar cell is defined as the power output at operation at the maximum power point (MPP):

$$P_{MPP} = J_{MPP} \cdot V_{MPP} \tag{2.18}$$

The fill factor (FF) defines the difference between the maximum reachable power output ($P_{max} = J_{SC} \cdot V_{OC}$) and the power at the MPP:

$$FF = \frac{J_{MPP} \cdot V_{MPP}}{J_{SC} \cdot V_{OC}} \tag{2.19}$$

The power conversion efficiency (PCE) describes the output power density of a solar cell at the MPP, and represents the most important metric of a solar cell:

$$PCE = \frac{P_{MPP}}{P_{incident}} = \frac{FF \cdot J_{SC} \cdot V_{OC}}{1000 \cdot Wm^{-2}} \tag{2.20}$$

with $P_{incident} = 1000 \cdot Wm^{-2}$, representing standard illumination using the AM1.5G spectrum.

The individual impact of R_{Shunt} (parallel resistance) and R_{Series} (series resistance) on the current-voltage (*J-V*) curve and solar cell performance are illustrated in Figure 2.4. An estimation of R_{Shunt} and R_{Series} can be calculated from the slope of the *J-V* curve at V_{OC} and J_{SC} , corresponding to Equation 2.13:

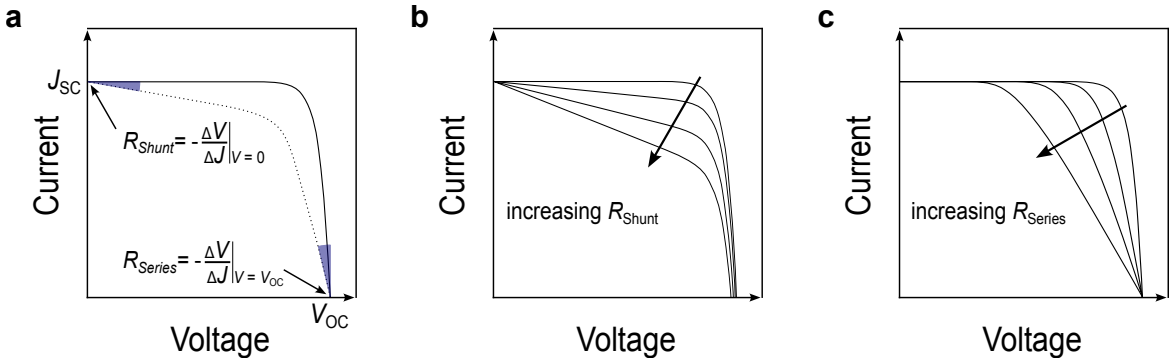

Figure 2.4: Influence of series (R_{Series}) and shunt (R_{Shunt}) resistances on the current-voltage (*J-V*) characteristics of solar cell. **a** Estimation of R_{Series} and R_{Shunt} from the slope of the *J-V* curve at open-circuit ($V = V_{\text{OC}}$) and short-circuit ($V = 0$) conditions. **b/c** Illustration of decreasing R_{Shunt} and increasing R_{Series} on the *J-V* characteristics of a solar cell, respectively. Both result in a decrease in fill factor (FF) and consequently a decrease in power conversion efficiency (PCE).

R_{Shunt} can result from grain boundaries and defects in the absorber layer (leading to short circuits). Decreased R_{Shunt} negatively impacts the V_{OC} of the device, leading to a reduced FF (Figure 2.4b). Poor conductivity in the adjacent layers (ETLs/HTLs, electrodes) of the perovskite can lead to an increase in R_{Series}. Higher R_{Series} mainly reduces the FF, while J_{SC} and V_{OC} remain constant (Figure 2.4c).

2.2.3 Theoretical Efficiency Limits of Single-Junction Solar Cells

The fundamental efficiency limit of single-junction solar cells is related to the band structure of semiconductors. In semiconductors, only photons with equal or higher energy than the bandgap ($E_\gamma \geq E_g$) can generate electron-hole pairs (Figure 2.5a). When $E_\gamma < E_g$, the photons pass through the absorber without generating electron-hole pairs. Excess energy for high-energy photons with $E_\gamma > E_g$ is dissipated as thermalization. Figure 2.5b illustrates the thermalization losses of a silicon solar cell with a bandgap of 1.12 V under the AM1.5G solar spectrum.

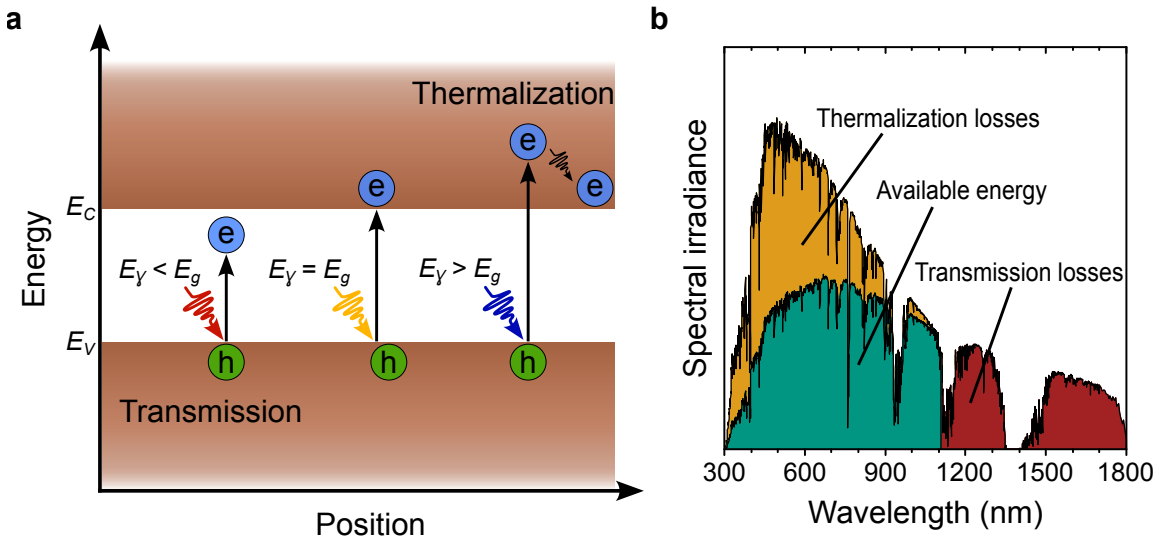

Figure 2.5: a Schematic energy band diagram of a semiconductor with a conduction band (E_C), valence band (E_V) and the resulting bandgap energy (E_g). Incoming photons with their respective energy (E_γ) can either result in transmission losses ($E_\gamma < E_g$) or excitation of excitons ($E_\gamma \geq E_g$) which results in the generation of an electron-hole pair (e and h). Excess energy ($E_\gamma > E_g$) results in thermalization losses as photons. **b** Exemplary representation of the utilization of the solar spectrum for a single-junction solar cell with a bandgap of 1.12 eV, to illustrate the available energy (green), as well as thermalization (yellow) and transmission (red) losses.

In 1961, William Shockley and Hans Queisser introduced the detailed balance limit to quantify the maximum theoretical efficiency of a single-junction solar cell under standard solar illumination, considering the following assumptions:[82]

1. complete absorption of photons with $E_\gamma \geq E_g$
2. zero absorption of photons with $E_\gamma < E_g$
3. each absorbed photon generates exactly one electron-hole pair ($t_s = 1$)
4. perfect selectivity of contact layers with negligible series resistance
5. absence of non-radiative recombination losses

Since the presented model does not consider non-radiative recombination losses as well as other optical and resistive recombination losses, the practical efficiency limit of a single-junction solar cell is lower than the theoretically estimated values.[82, 83] For a silicon solar cell with a bandgap of 1.12 V, the theoretical efficiency limit is 32.6%, while reported record efficiencies of silicon solar cells reach 27%.[6, 84]

A potential solution to overcome the theoretical efficiency limits of single-junction solar cells are multi-junction solar cells. In this technology, several solar cells (with different bandgaps) are stacked on top of each other and electrically connected, leading to reduced thermalization losses due more efficient utilization of the solar spectrum.

2.2.4 Device Architectures of Single-Junction Perovskite Solar Cells

In a typical perovskite solar cell, the photoactive perovskite absorber layer is embedded between two charge transport layers (CTLs) and adjacent electrodes. The substrate is usually made of rigid glass.

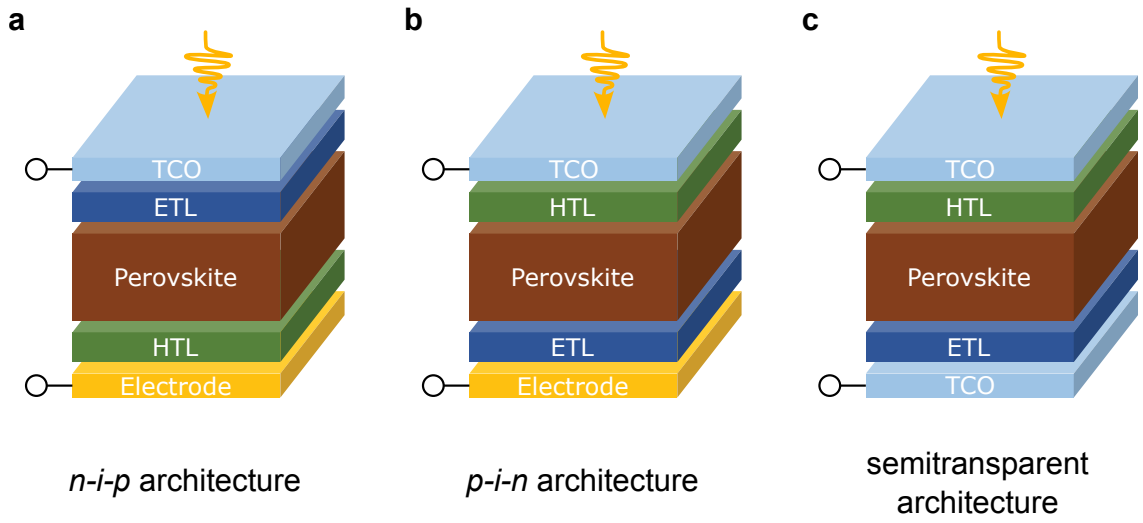

Figure 2.6: Illustration of established device architectures for planar perovskite solar cells (PSCs) consisting of the perovskite absorber layer sandwiched by two charge transport layers (ETL = electron transport layer, and HTL = hole transport layer). The generated and separated charges are extracted through the adjacent electrode and/or transparent conductive oxides (TCO). **a** Layer stack of the *n-i-p* architecture. Incident light first passes through the ETL before reaching the perovskite absorber layer. **b** Layer stack of the *p-i-n* (or inverted) architecture. Here, incoming light enters through the HTL-side of the layer stack. c Semitransparent solar cell layer stack, in which the rear electrode is replaced with a transparent electrode or TCO, allowing non-absorbed light to pass through the entire layer stack.

Depending on the direction of incident light, two main device architectures are commonly employed: (i) the standard architecture (*n-i-p*), and (ii) the inverted architecture (*p-i-n*), as shown in Figure 2.6b/c, respectively. To ensure light absorption, the electrode facing the incoming light must be transparent, typically comprising of a transparent conductive oxide (TCO) such as indium tin oxide (ITO) or indium zinc oxide (IZO). In opaque devices, the rear electrode is usually a metal layer of gold (Au), silver (Ag) or copper (Cu). By replacing the opaque metal electrode with a second TCO, a semitransparent solar cell architecture is obtained (Figure 2.6d). Semitransparent architectures play a crucial role in multi-junction solar cells where light must pass through multiple absorber layers, enabling enhanced light harvesting and higher overall efficiencies of multi-junction devices.

2.2.5 Perovskite/Silicon Tandem Solar Cells

Multi-junction solar cells are designed to surpass the theoretical limit of single-junction solar cells by incorporating multiple absorber layers with distinct bandgaps to more efficiently utilize the solar spectrum.[20, 85, 86] Tandem solar cells (TSCs) describe a multi-junction solar cell with two solar cells (top and bottom subcell) stacked on top of each other. High-energy photons are absorbed by the wide-bandgap top cell, while lower-energy photons pass through and are absorbed by the narrow-bandgap bottom cell. This spectral division reduces both transmission and thermalization losses, enhancing overall energy conversion.

Two main architectures dominate tandem PV design: (i) monolithically interconnected two-terminal (2T) and (ii) mechanically stacked four-terminal (4T) configurations. Figure 2.7 displays corresponding schematics of the two tandem solar cell configurations for perovskite/silicon tandem solar cells.

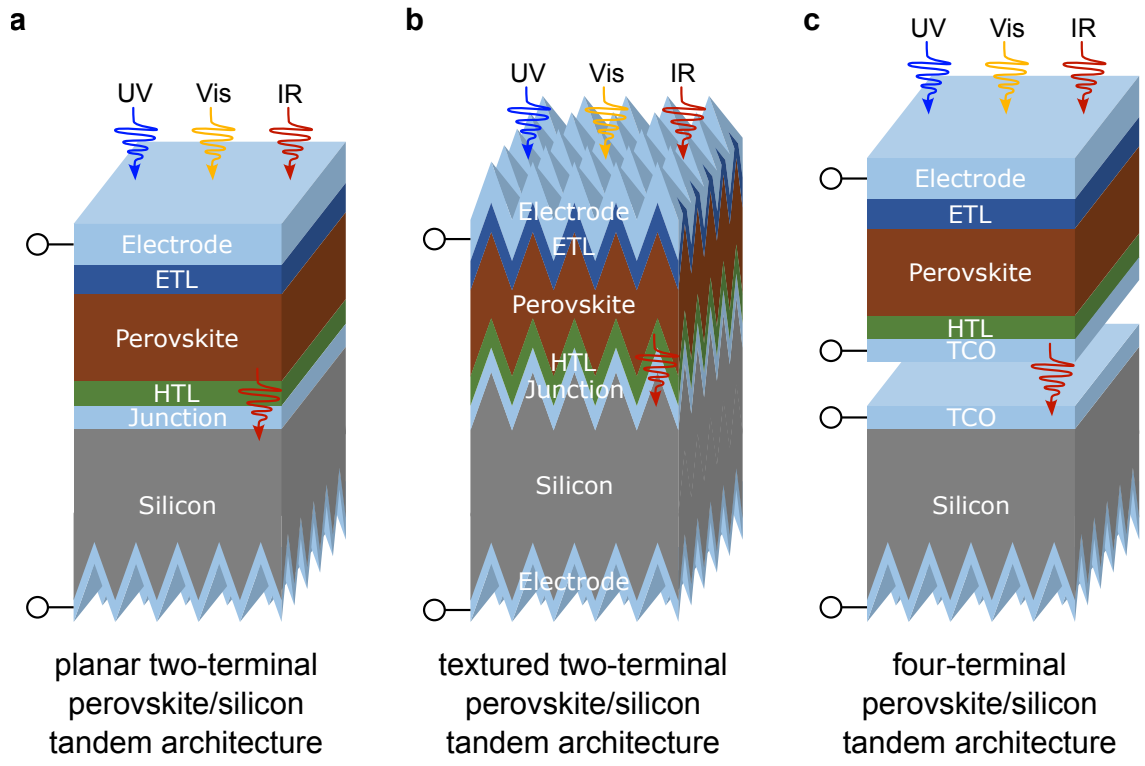

Figure 2.7: Schematic of typical perovskite/silicon tandem solar cell architectures. **a/b** Two-terminal (2T) or monolithic perovskite/silicon tandem architectures, in which two sub-cells are optically and electrically connected in series *via* a recombination junction layer, on planar and textured silicon bottom cells, respectively. **c** Four-terminal (4T) perovskite/silicon tandem architecture, with two sub-cells optically stacked on top of each other, while being operated individually. As for the top cell, a semitransparent device architecture is needed so the not-absorbed light can pass through and enter the bottom cell.

In 2T perovskite/silicon TSCs, both sub-cells are optically and electrically coupled in series, with the top cell fabricated directly on the bottom cell (Figure 2.7a). This integration introduces fabrication challenges such as processing compatibility, especially in case of textured silicon bottom cells, and minimizing recombination losses at the junction, typically formed by a thin TCO or tunnel diode.[87, 88] The device voltage is the sum of all sub-cell voltages, while the current is limited by the lowest current-supplying sub-cell, making current matching between both sub-cells critical. In contrast, 4T tandems feature optically connected, but independently fabricated and operated sub-cells (Figure 2.5b). This architecture is more resilient to spectral and temperature variations, but suffers from increased optical losses due to additional TCO layers and reflection at interfaces.[87]

Due to their easily tunable bandgap perovskite semiconductors offer great prospects for use in tandem applications, enabling integration with different narrow-bandgap solar cell technologies like crystalline silicon. For optimal performance of perovskite/silicon TSCs, the perovskite bandgap lies around 1.7 eV.[89] Reported certified record PCEs have achieved values of 34.85% and 30.24% for 2T and 4T perovskite/silicon tandem architectures, respectively[7, 24, 90] - surpassing the records of both single-junction silicon (27.3%) and PSCs (26.95%).[6–8]

2.3 Vapor Phase Deposition

In this section, the fundamental process characteristics and growth models of vapor phase deposition for the fabrication of perovskites are discussed. Furthermore, the basics of the sequential layer deposition method, the

primary perovskite deposition method used in this work, as well as the perovskite film formation process from this deposition method are introduced.

2.3.1 Process Characteristics of Vapor Phase Deposition

Phase Transition from Liquid/Solid into Gas Phase

Vapor phase deposition is one of the most fundamental and well-characterized techniques for fabricating thin films on solid substrates. In case of perovskites, the main vapor phase deposition processes, co-deposition and sequential layer deposition, rely on thermal sublimation from a point source (in literature mostly referred to as thermal evaporation) of the precursor materials under high-vacuum conditions. In thermal sublimation, a precursor material is converted into the vapor phase through thermal energy input and subsequently condenses onto the substrate surface. The phase transition may occur *via* either evaporation from the molten state or sublimation directly from the solid phase. The specific behavior of a material during vaporization is described by its vapor pressure curve, which defines the equilibrium relationship between temperature and pressure at which the vapor phase coexists with the liquid or solid phase. To calculate the saturation vapor pressure, the Clausius Clapeyron equation is used, assuming ideal gas behavior for the vapor phase:

$$\frac{dp}{dT} = \frac{\Delta S_m}{\Delta V_m} \tag{2.21}$$

with ΔS_m describing the change in molar entropy during phase transition and ΔV_m describing the change in molar volume during phase transition.

When assuming an isobaric reversible phase transition $\Delta S_m = \frac{\Delta H_m}{T}$, and $\Delta V \approx V_{gas}$ (since the molar volume of a species in gas form is much larger than that of the respective solid/liquid form), Equation 2.21 can be written as:

$$\frac{dp}{dT} = \frac{1}{T} \cdot \frac{\Delta H_m}{V_{gas}} \tag{2.22}$$

with ΔH_m describing the change in molar enthalpy during phase transition.

By applying the ideal gas law $p \cdot V = R \cdot T$:

$$\frac{dp}{dT} = \frac{1}{T} \cdot \frac{\Delta H_m \cdot p}{R \cdot T} \tag{2.23}$$

$$\frac{dp}{p} = \frac{\Delta H_m}{R} \cdot \frac{dT}{T^2} \tag{2.24}$$

$$ln\,(p) = \frac{\Delta H_m}{R} \cdot \frac{1}{T_1} - \frac{1}{T_2} + C \tag{2.25}$$

$$p = C \cdot exp\left(\frac{-\Delta H_m}{R \cdot \Delta T}\right) \tag{2.26}$$

where p is the pressure, V the volume and R the ideal gas constant.

In order to calculate the number of molecules leaving undergoing a phase transition into gas phase from a defined surface A, assuming a system in equilibrium, is given by:

$$\frac{1}{A} \cdot \frac{dN}{dT} = \sqrt{\frac{N_A}{2\pi \cdot k_B}} \cdot \frac{P}{\sqrt{M \cdot T}} \tag{2.27}$$

with dN being the number of molecules undergoing phase transition into the gas phase, N_A the Avogadro's number, P the saturation vapor pressure and M the molar mass of species transitioning into gas phase.

However, in a non-ideal real scenario two additional terms must be considered to account for backscattering molecules (described by the evaporation constant α_υ) and hydrostatic pressure (p). This leads to the Hertz-Knudsen equation, which describes the general evaporation/sublimation rate of a liquid/solid material from a source with the area A:

$$\frac{1}{A} \cdot \frac{dN}{dT} = \alpha_\nu \cdot \sqrt{\frac{N_A}{2\pi \cdot k_B}} \cdot \frac{P - p}{\sqrt{M \cdot T}} \tag{2.28}$$

Mean Free Path in the Gas Phase

Vapor transport under vacuum conditions can be impacted by chemical and/or mechanical interactions of molecules in the gas phase. Mechanical interactions in the vapor phase can be described in a first approximation as an elastic collision process between molecules regarded as rigid spheres. The mean free path λ (average pathlength between two collisions) of a molecule in the gas phase can be calculated based on kinetic gas theory:[91]

$$\lambda = \frac{k_B \cdot T}{\sqrt{2}\pi \cdot p \cdot d^2} \tag{2.29}$$

where p is the background pressure in the system and d is the diameter of the molecule.

In case of transport of molecules *A* (M_A, p_A, d_A) through a medium of a different species *B* (M_B, p_B, d_B), the average mean free path of the molecules in the system can be calculated by:

$$\lambda = \frac{4 \cdot k_B \cdot T}{\sqrt{1 + \frac{M_A}{M_B}} \cdot (d_A + d_B)^2 \cdot \pi \cdot p_B} \tag{2.30}$$

with p_B being the background pressure in the system.

It becomes obvious, that the mean free path decreases due to an increased number of potential collision partners resulting from higher background pressure. Conversely, it increases with rising temperature, as the kinetic energy of the molecules becomes greater. From Equation 2.28, it follows directly that low process pressures are essential to reduce the probability of collisions and maximize the mean free path of the molecules. This means, that the distance between the source and the substrate should be considerably smaller than the mean free path to ensure that a significant portion of molecules emitted from the source can travel through the vapor phase and reach the substrate. Most vapor phase deposition processes therefore require and operate under high-vacuum conditions.

Effusion Characteristics from a Point Source

The effusion characteristics of conventional point or effusion sources are discussed in the following section. Under conditions where the mean free path (λ) of the emitted molecules significantly exceeds the distance to the substrate, intermolecular collisions within the vapor phase can be considered negligible. In such cases, and assuming no localized vapor pressure buildup at the source, Knudsen's cosine law (Equation 2.29) for evaporation from a parallel plane provides a valid theoretical framework for describing the angular distribution of the emitted vapor flux.[91]

$$I(\theta) \propto cos^n(\theta) \tag{2.31}$$

A schematic display of the geometrical source-to-substrate layout is provided in Figure 2.8a.

With a horizontal substrate, the angle θ is related to the distance x along the horizontal substrate as well as the height of the holder x_h:

$$\theta(x) = arctan\left(\frac{x}{x_h}\right) \tag{2.32}$$

Therefore, Equation 2.29 can be expressed as:

$$I(x) \propto cos^n\left(\theta(x)\right) = cos^n\left(arctan\left(\frac{x}{x_h}\right)\right) \tag{2.33}$$

This means, that the intensity I decreases with increasing distance from the source by the inverse square law. The distance R from the source to a point x on the substrate is given by:

$$R = \sqrt{x^2 + x_h^2} \tag{2.34}$$

Usually, the distance x_h is a constant value predetermined by the vacuum chamber dimensions. Therefore, the intensity $I(x)$ at a given point x on the horizontal substrate becomes:

$$I(x) = \frac{cos^n\left(arctan\left(\frac{x}{x_h}\right)\right)}{R^2} = \frac{cos^n\left(arctan\left(\frac{x}{x_h}\right)\right)}{x^2 + x_h^2} \tag{2.35}$$

Assuming that the thickness $t(x)$ is proportional to the corrected intensity $I(x)$, a proportionality factor A is introduced, and $t(x)$ can be calculated by:

$$t(x) = A \cdot \frac{cos^n\left(arctan\left(\frac{x}{x_h}\right)\right)}{x^2 + x_h^2} \tag{2.36}$$

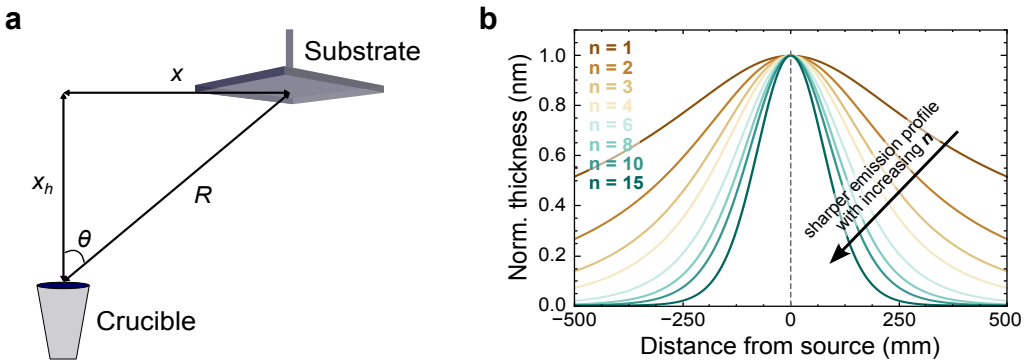

Figure 2.8: Theoretical analysis of effusion behavior from a point source. **a** Geometrical source-to-substrate layout in a vacuum chamber with the height of the holder (x_h), horizontal distance of the substrate to the source (x) and resulting direct distance R. **b** Idealized evaporation cones and the effect of different values for the exponent n calculated using the derived formula, assuming a proportionality factor $A = 1$ (Equation 2.34). Increasing n-values lead to sharper emission profiles, lower n-values result in a broader emission profile.

A graphical representation of differences in the resulting evaporation cone, mainly influenced by variation of the exponent n, over the distance of the substrate to the emitting source is presented in Figure 2.8b. Depending on the used effusion source geometry and sublimed material, the directionality of the emitted vapor flux can change drastically. It should be noted, that these are idealized evaporation cones, which serve to allow for a reasonable approximation of the spatial directionality of the emitted vapor flux and therefore resulting homogeneity on the substrate.

Initial Growth Models of Vapor Phase Deposition Processes

Thin-film formation during vapor phase deposition begins as molecules adsorb onto the substrate surface and coalesce into clusters, eventually forming a continuous film. This process is governed by complex interactions between the adsorbed molecules and the substrate, influenced by factors such as the molecular flux onto the substrate, the ambient pressure, temperature of the substrate, surface structure, diffusion of the molecules on the surface, and the surface energy.

Initial molecular adhesion is determined by physisorption and chemisorption processes. Molecules that are not reflected or desorbed migrate across the surface due to their kinetic energy and surface interactions, aggregating into multi-molecule clusters. These clusters facilitate crystallization, as they can act as nucleation sites from which the subsequent film growth proceeds (Figure 2.9a). Generally, thin-film growth from vapor phase deposition typically follows one of the three classical modes (Figure 2.9b/c/d):

1. Frank-van der Merwe (layer-by-layer growth),[92–95]
2. Volmer-Weber (island growth),[96]
3. Stranski-Krastanow (layer plus island growth).[97]

These modes reflect the balance between adsorption dynamics, surface mobility, and interfacial energies, and are particularly sensitive in perovskite materials due to their reactive nature and complex crystallization pathways.

In sequential layer deposition processes, the main method for the fabrication of perovskite thin films used in this work, the precursor materials are deposited in subsequent deposition steps. At the interfaces formed between the respective materials, chemical reactions may already occur during the deposition process. These

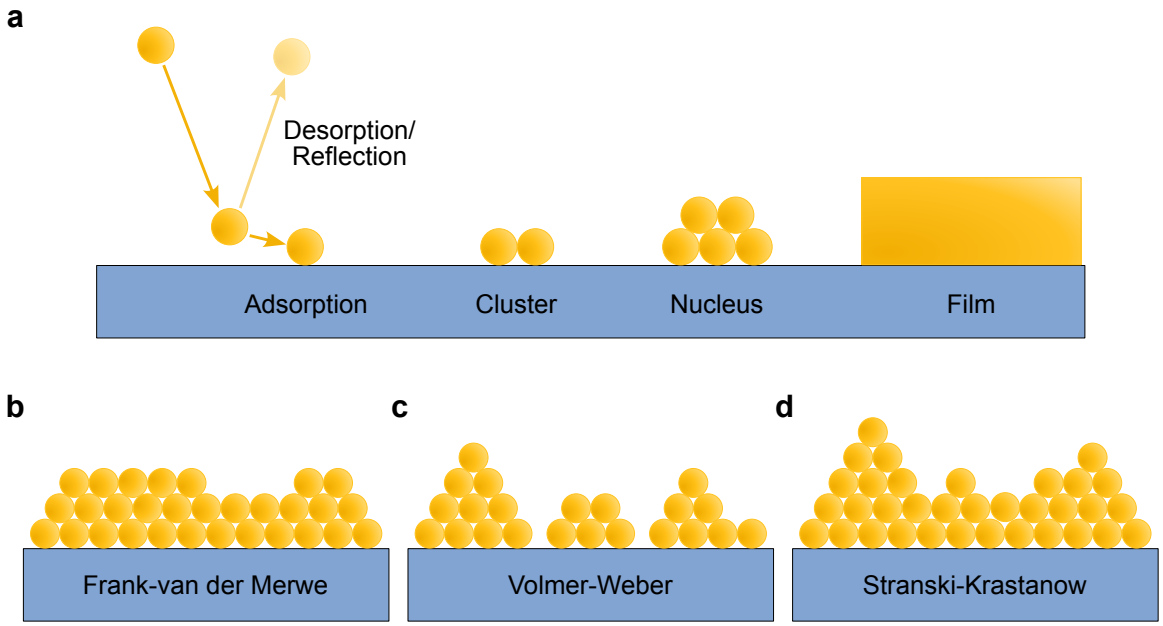

Figure 2.9: General overview of established growth models for vapor phase deposition processes. **a** Illustration of initial interaction between impinging molecule and substrate surface. **b** Schematic of the three main growth models for thin-film formation from vapor phase deposition: (i) Frank-van der Merwe (layer-by-layer growth), (ii) Volmer-Weber (island growth) and (iii) Stanski-Krastanow (layer & island growth).

reactions can inhibit the applicability of the presented initial growth models based on non-reactive conditions. A comprehensive understanding of these processes remains challenging and has not yet been described.

2.3.2 Sequential Layer Deposition

Among the various vapor phase deposition techniques explored for the fabrication of perovskite absorber layers, co-deposition and sequential layer deposition are the most commonly used methods.[11, 12] Co-deposition involves the simultaneous deposition of all precursor materials in a single process step, enabling their concurrent arrival and crystallization on the substrate surface (Figure 2.10a). As a result, the perovskite phase forms directly during deposition. The resulting absorber layers can be immediately integrated into complete perovskite solar cells without requiring intermediate processing steps. To further enhance the morphological and optoelectronic quality of the perovskite film, a post-deposition annealing step at elevated temperatures is often employed. The stoichiometry of the final perovskite film is controlled by adjusting the individual deposition rates of each precursor source. Compositional tuning within the co-deposition process is typically achieved by introducing additional precursor materials during evaporation.[98, 99]

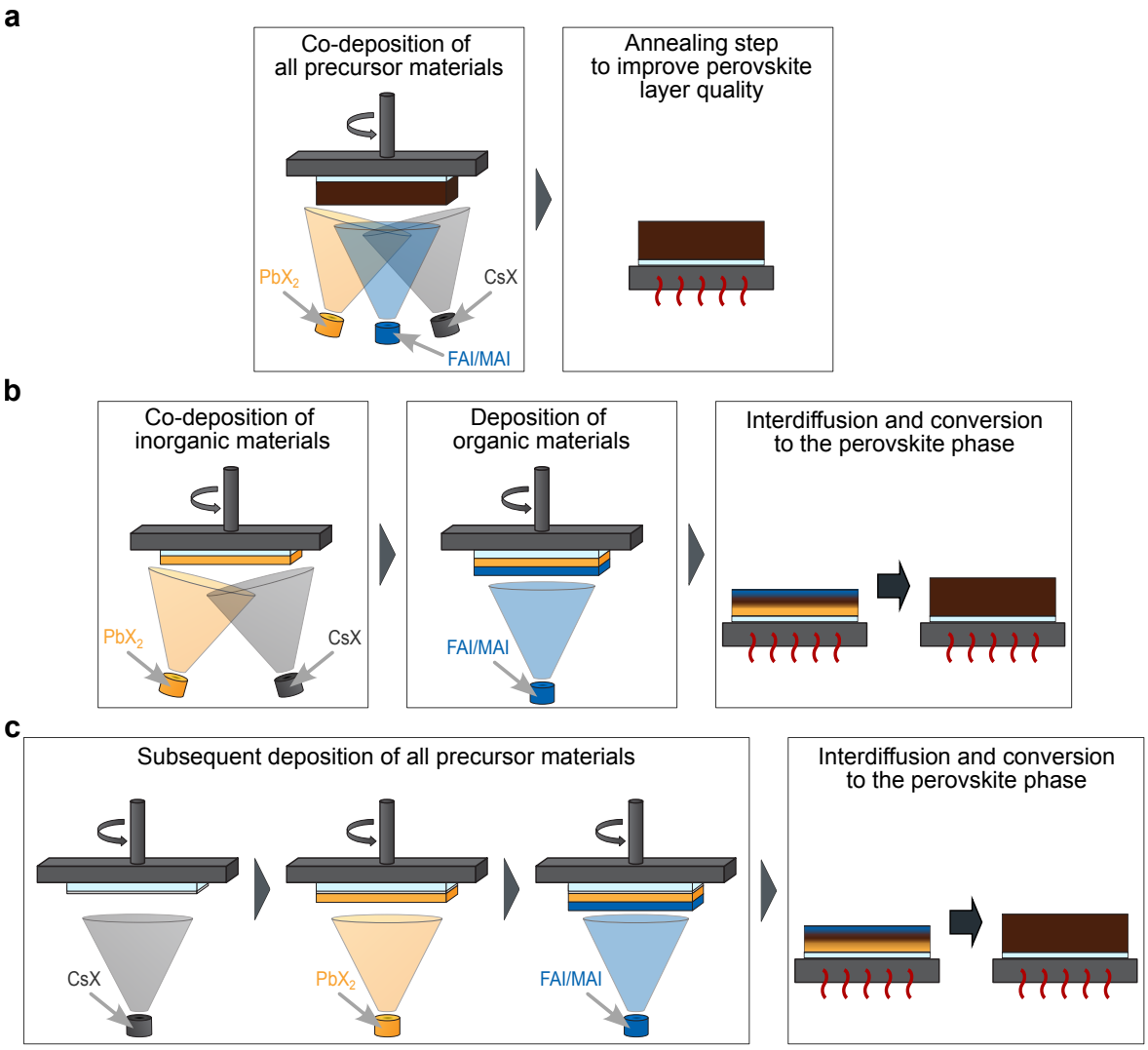

Figure 2.10: Difference of co-deposition and sequential layer deposition processes. **a** Exemplary schematic of co-deposition process with a subsequent annealing step to improve the layer quality of the deposited perovskite thin film. **b** Illustration of two-step sublimation process with a co-deposition step of the inorganic precursor materials, followed by the deposition of the organic materials. **c** Schematic of a layer-by-layer (or multi-step) deposition approach with each precursor material being deposited individually in subsequent deposition steps. In contrast to the co-deposition process (**a**), in sequential layer deposition processes cases (**b** and **c**) a thermal post-treatment step is necessary to facilitate the interdiffusion and mixing of both deposited layers and initiate the conversion reaction to the perovskite phase.

Sequential layer deposition represents an alternative approach to vapor-phase fabrication, wherein the deposition of all precursor materials does not take place simultaneously in a single, but rather in two or more subsequent deposition steps (Figure 2.10b/c).[100–102] Different approaches have been reported in literature. From two-step processes with a separate deposition of all inorganic precursors in a co-deposition step, followed by the deposition of the organic precursors, to multi-step approaches with separate deposition steps of all precursor materials individually in different orders.[43, 100, 101, 103] In contrast to the co-deposition method, the final stoichiometry of the perovskite film is controlled by the deposited layer thicknesses of each deposition step. This means, that the individual precursors could be deposited at their maximum deposition rates, enabling a faster overall deposition rate in industrial applications regardless of the increased numer of deposition steps. Additional precursor materials for compositional engineering of the perovskite can further be introduced in additional deposition steps or in an existing deposition step *via* co-deposition. A key difference to the co-deposition method lies in the crystallization behavior of the perovskite material (Figure 2.11). In sequential

deposition, the precursors do not crystallize directly into the perovskite phase upon reaching the substrate. Instead, the deposited materials form a layered stack of individual precursor films (Figure 2.11a). Although reactions between the individual materials may occur at the interfaces, the layers remain practically unmixed. Consequently, a thermal treatment step following the deposition of all layers is essential to induce interdiffusion and mixing of the stacked layers. During this process, the conversion reaction between the deposited precursors takes place, leading to the formation of the final perovskite crystal structure (Figure 2.5b/c).

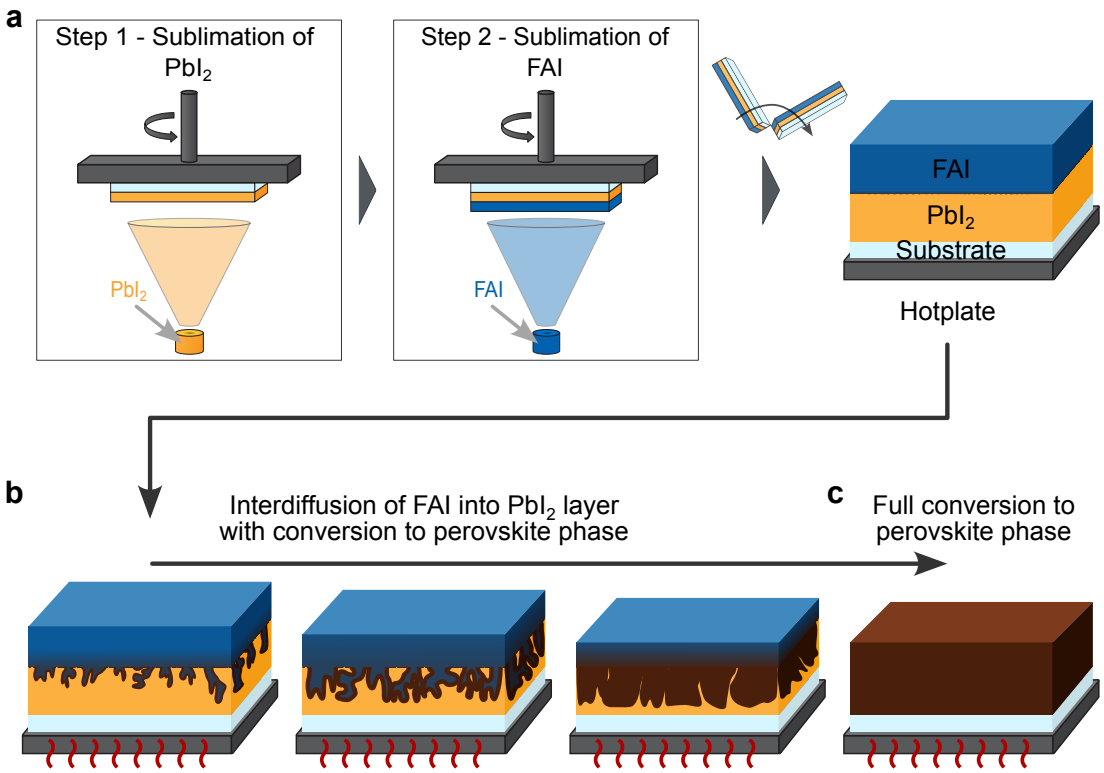

Figure 2.11: Schematic representation of the conversion reaction of sequential vapor-phase-deposited perovskite absorbers. **a** 2-Step deposition scheme of employed fabrication process used in this work. **b** Initial and ongoing interdiffusion of the secondly deposited organic layer (FAI) into the firstly deposited inorganic scaffold (PbI_2), occurring concurrently with the conversion reaction, during annealing. **c** Final perovskite layer after full conversion of the two deposited layer (FAI and PbI_2).

Annealing Step in Vapor Phase Deposition Processes

In the context of perovskite solar cells fabricated by vapor phase deposition, annealing is a widely used thermal treatment process to improve the crystallinity, morphology, and optoelectronic properties of the deposited perovskite layer. The term “annealing” refers to the heating of a material to a specific temperature for a set time, to promote rearrangement of atoms or molecules within the material into a more stable and ordered structure. During the annealing, crystallinity of amorphous or poorly crystalline phases can be improved, and defects in the crystal structure can be corrected. Additionally, pinholes in the perovskite layer can be eliminated, and perovskite grains can grow, leading to better charge transport and reduced recombination losses. Furthermore, an annealing step is applied to convert non-desirable perovskite phases into the photoactive phases of the material, e.g. a phase transition of the photo-inactive β-$FAPbI_3$ (yellow-phase) into the photoactive α-$FAPbI_3$ (black-phase).[104]

As mentioned above, a thermal treatment step in sequential layer deposition processes is essential to promote interdiffusion and chemical interaction of the subsequently deposited precursor materials. This process facilitates the formation of a uniform and crystalline perovskite phase by enabling the conversion of initially stacked

unreacted layers into the final active material. Therefore, this thermal treatment step does not represent a pure annealing step, since it does serve primarily to form the perovskite phase. In literature, this step is mostly referred to as an annealing step and therefore will be named as such in this thesis.

Close-Space Sublimation

One of the main challenges in vapor phase deposition processes, both co-deposition and sequential layer deposition, is the inherently slow deposition rate of organic precursor materials (mostly MAI and FAI).[40, 105] Close-space sublimation (CSS) offers a promising alternative to conventional vapor phase deposition techniques. The key distinction lies in the significantly reduced gap between the substrate and the precursor source in the millimeter-range.[62, 64, 105] This close gap enables much higher deposition rates without requiring high vacuum conditions in the process chamber, with operating pressures typically ranging from 1-100 mbar. Another difference compared to conventional vapor phase deposition methods is the source design in CSS processes. Instead of using point sources for the sublimation of the precursors, CSS can employ large-area sources. The precursor material is ground into fine powder and distributed homogeneously inside the source. In combination with the reduced gap between substrate and source, this allows for a much higher material usage and deposition over large areas. As a result, CSS is particularly well-suited for scalable deposition of organic precursors at high deposition rates.[62, 64]

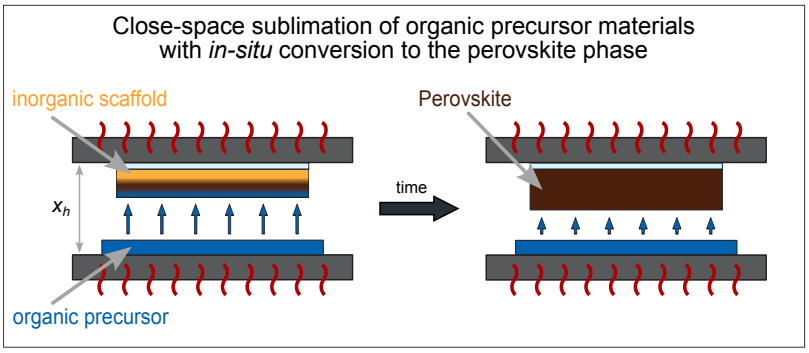

Figure 2.12: Schematic of a close-space sublimation (CSS) process of organic precursor materials onto a prior deposited inorganic scaffold. Both the organic source and the substrate are kept at elevated temperatures, which results in an *in-situ* conversion to the perovskite phase during deposition. The reduced space between the organic source and the substrate (x_h) furthermore allows for much shorter deposition times compared to the previously described sequential sublimation processes from a point source.

In sequential deposition processes, CSS can be employed as the second deposition step of the organic precursors onto a previously deposited inorganic scaffold. A general process scheme of such a CSS process is displayed in Figure 2.11. This two-step approach using CSS for organic deposition offers an additional advantage compared to the previously reported two-step processes. Due to the reduced gap between the source and the substrate, the substrate is typically maintained at elevated temperatures, often matching the sublimation temperature of the source material. This results in an *in-situ* conversion of the inorganic scaffold with the CSS-deposited organic precursors to the perovskite phase without relying on a post-deposition annealing step.[64, 105]

3 Experimental Methods

This chapter outlines the experimental methodologies employed for the fabrication and characterization of perovskite thin films and solar cells. The fabrication section details the employed deposition processes of all relevant layers and materials used in this thesis. In addition, the used solar cell architectures of each chapter are summarized. The characterization section describes the techniques applied to analyze the properties of the fabricated thin films. Furthermore, the methods used to analyze the device performance of the fabricated perovskite-based solar cells are described.

3.1 Fabrication processes

3.1.1 Materials

Perovskite Absorber Layers

Chapter 4/5:
FAI (Formamidinium iodide) was purchased from *Greatcell Solar Materials*. PbI_2 (lead iodide), $PbBr_2$ (lead iodide), CsI (cesium iodide), CsBr (cesium bromide) and CsCl (cesium chloride) were purchased from *TCI Chemicals*.

Chapter 6:
PbI_2 (lead iodide), $PbBr_2$ (lead iodide) and MAI (methylammonium iodide) were purchased from *Luminescence Technology*. MABr (methylammonium bromide) and FAI (formamidinium iodide) were purchased from *Greatcell Solar Materials*. $EDAI_2$ (ethylene-diammonium di-iodide) was purchased from *Sigma-Aldrich*.

Charge-Transport Layers

Chapter 4/5:
MeO-2PACz, 2PACz and TaTm (N4,N4,N4”,N4”-tetra([1,1’-biphenyl]-4-yl)-[1,1’:4’,1”-terphenyl]-4,4”-diamine) were purchased from *TCI Chemicals*. PTAA was purchased from *Xi’an Yuri Solar Co*. C_{60} (fullerene-C_{60}) was purchased from *Sigma–Aldrich*.

Chapter 6:
TaTm (N4,N4,N4”,N4”-tetra([1,1’-biphenyl]-4-yl)-[1,1’:4’,1”-terphenyl]-4,4”-diamine) was purchased from *TCI Chemicals*. CS90112 (2,2’,2"-(cyclopropane-1,2,3-triylidene)tris(2-(p-cyanotetrafluorophenyl)acetonitrile)) and BCP (bathocuproine) were purchased from *Luminescence Technology*. C_{60} (fullerene-C_{60}) was purchased from *MBraun (Creaphys)*.

Solvents and other Materials

Isopropanol, acetone and toluene were purchased from *VWR Chemicals*

3.1.2 Deposition Methods

Substrate cleaning

Planar *p-i-n* PSCs were fabricated using ITO-covered rigid glass substrates. Two different types of glass substrates were used in this thesis.

Chapter 5:
Pre-patterned ITO substrates (15 Ohm/sq, Luminescence Technology) were cut to sizes of 16 mm × 16 mm and cleaned with acetone and isopropanol in an ultrasonic bath for 15 minutes each. Substrates were treated with oxygen plasma for 5 minutes immediately prior to the deposition of the HTL.

Chapter 6:
Pre-patterned ITO substrates with a size of 30 mm x 30 mm (Kintec Company) were used. The substrates were subsequently cleaned with soap (2% Mucasol™ in water), water and isopropanol in an ultrasonic bath, followed

by 20 minutes UV-ozone treatment prior to the deposition of the HTL. Prior to tandem cell fabrication, silicon bottom cells were cleaned by sonicating for 5 minutes in acetone, then 5 minutes in IPA followed by a 15 minutes UV-ozone treatment.

Hole Transport Layers (HTLs)

nPACz (MeO-2PACz and 2PACz) and TaTm thin films were fabricated *via* physical vapor deposition from a crucible in a thermal evaporation system (Creaphys, OPTIvap). All films were deposited at pressures of approximately 5×10^{-6} mbar, with rates of 0.15-0.25 $Å s^{-1}$ measured using a quartz crystal microbalance (QCM). nPACz-HTLs had a final (measured) thickness of 4 nm, TaTm had a final (measured) thickness of 3 nm. nPACz-HTL films were washed using a 1-step spin-coating program (3000 rpm for 30 s) with 150 μL of ethanol, dynamically added after 10 s. Washed films were dried at 100 °C for a further 10 min. NiO_x layers were sputtered from a NiO_x target using 100 W power with pure Ar at 1 mTorr. PTAA precursor solution was prepared by dissolving PTAA in Toluene. PTTA films were fabricated *via* spincoating by applying 100 μL solution (1 mmol/ml) per substrate followed at 3000 rpm for 30 sec with a subsequent drying step on a hotplate (100 °C, 10 min).

For the p-doped HTL layer used in **Chapter 6**, TaTm and CS90112 (as p-dopant) were co-sublimed at a rate of 0.8 and 0.12 $Å s^{-1}$ by heating them at temperatures of around 300 °C and 130 °C respectively. For the fabrication of TSCs, the additional NiO_x HTL layer (15 nm for planar, and 25 nm for textured silicon bottom cells) was sputtered from a NiO_x target using 100 W power with pure Ar at 1 mTorr on the silicon bottom cell with ITO layer. To account for the increased surface area of the textured devices (nano- and micro-textured) the deposited thickness of all other HTL materials was increased by a factor of 1.7.

Electron Transport Layers (ETLs)

Chapter 5:
The ETL comprised of 20 nm C_{60} and 35 nm SnO_x. C_{60} was vacuum-deposited at 0.1 - 0.2 $Å s^{-1}$ at a pressure of approximately $1x10^{-6}$ mbar in a vacuum evaporation system (Optivap from CreaPhys, now MBraun Dresden). SnO_x was deposited *via* atomic layer deposition (ALD). SnO_2 is deposited *via* ALD using an Arradiance's GEMStar XT Thermal ALD system integrated into an N_2-filled glovebox. N_2 was used as a carrier and purge gas, with TDMASn and H_2O (in-house) as precursor and oxidizer respectively. Due to its low vapour pressure, the TDMASn source was heated to 70 °C and allowed to equilibrate for 60 min before deposition. To prevent condensation, the carrier line for TDMASn was kept at 130 °C during deposition. Prior to deposition, the chamber with loaded samples was pumped to ~50 mbar and allowed to remain at the desired temperature for 10 minutes to equilibrate samples. SnO_x was deposited over 200 cycles using the following parameters: 0.5 s TDMASn pulse with 12 s purge at 50 sccm, then a 1.0 s H_2O pulse with 12 s purge at 50 sccm. For all samples the chamber temperature was 80 °C.

Chapter 6:
The ETL comprised of 18 nm C_{60} and 8 nm BCP. The deposition rate for C_{60} was 0.5 $Å s^{-1}$ while the thinner BCP was deposited at 0.2 $Å s^{-1}$. For the fabricated semitransparent single-junction PSCs and perovskite/silicon TSCs, BCP was replaced with a 35 mm SnO_2 layer. SnO_2 is deposited *via* ALD using an Arradiance's GEMStar XT Thermal ALD system integrated into an N_2-filled glovebox. For SnO_2 deposition, the ALD chamber is heated to 60 °C, the bottle containing the Sn precursor tetrakis(dimethylamino)tin (TDAT) was heated to 60 °C, and the bottle of water (oxidizer) was not heated. The precursor manifolds were heated to 115 and 140 °C respectively. The SnO_2 deposition process consists of a series of purges of TDAT for 550 ms and water vapor

for 200 ms, each of them followed by N_2 purges to clear off the precursors from the ALD chamber. To account for the increased surface area of the textured devices (nano- and micro-textured) the deposited thickness of all other ETL materials was increased by a factor of 1.7.

Passivation Layers

$EDAI_2$ surface passivation layer was deposited in a high vacuum chamber at 10^{-6} mbar at a rate of about 0.1-0.15 $Ås^{-1}$.

Electrodes

All samples were finished with a metallic rear electrode of either 75 nm Au, 100 nm Ag or 300 nm Ag (for tandem devices) using a bell jar evaporation system, with evaporation rates of 0.5 – 2.0 $Ås^{-1}$ and chamber pressures of ~$1x10^{-6}$ mbar. Cell active area was defined by a shadow mask. For samples in **Chapter 5** this resulted in a 10.5 mm^2 active area, for samples in **Chapter 6** in 5 mm^2 and for tandem devices the active area was 50 mm^2. ST and tandem devices did not evaporate the metallic electrode on the active area, expect for metallic fingers of 100 μm width, used to improve the effective TCO sheet resistance.

Perovskite Layers

Chapter 4/5:
For perovskite deposition, two nitrogen glovebox integrated PEROvap (CreaPhys, now MBraun Dresden) evaporators were employed to separate the deposition of inorganic and organic materials (Figure 3.1). Quartz-crystal microbalances (QCMs) were used to measure the rate of each material. A cooling inner surface, surrounding all evaporation sources, was set to -20 °C. Prior to the heating process, the system was evacuated for 60 min, with a standard base pressure at start of heating of $3x10^{-6}$ mbar. For every process, the evaporation rate of each material was kept constant by manual or automatic adjustment of the source temperature. Substrate temperature (20 °C) and substrate rotation speed (10 rpm) were held constant for all experiments. For the first step, the PbI_2 rates during evaporation were 0.1 – 2.0 $Ås^{-1}$ (standard: 1 $Ås^{-1}$). When adding CsI to the PbI_2 deposition step, the inorganic materials were co-deposited with rates of 1 $Ås^{-1}$ and 0.1 $Ås^{-1}$ resulting in a layer thickness of 300 nm and 30 nm for PbI_2 and CsI, respectively. CsX seed layers were deposited at deposition rates of 0.3 $Ås^{-1}$ with a final layer thickness of 30 nm in every case. For WBG PSCs using a co-deposition step of PbI_2 and $PbBr_2$ after the CsX seedlayer, PbI_2 was deposited at 1 $Ås^{-1}$, while the deposition rate of $PbBr_2$ was adjusted depending on the desired ratio. The final layer thicknesses were 300 nm in total.

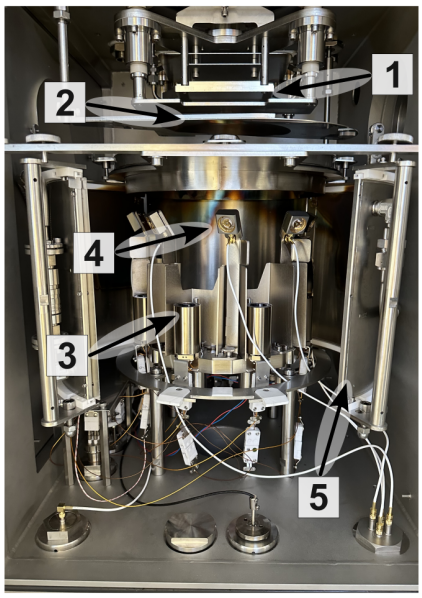

Figure 3.1: Image of the used perovskite deposition chamber (PEROvap, MBraun) used for the deposition processes of perovskite precursors in this thesis. 1) Substrate station with substrate heating, 2) Closed substrate shutter, 3) Sublimation crucible source, 4) Quartz-crystal microbalance (QCM) holder, 5) Cooling shield (kept at -20 °C).

After the deposition of the inorganic layer the samples were transferred to a second PEROvap evaporator for the deposition of FAI. The vertical source-to-substrate distance is 300 mm, with the point source positioned off-axis (~150 mm apart) to the substrate center without tilt. The lateral distance from source to QCM was 75 mm, enabling scaling from thickness distribution to deposition rate profile in Chapter 4. For each experiment, fresh precursor material (FAI: 1 g) was placed into the used crucibles. The system was evacuated, reaching a base pressure of <1.0 x 10^{-5} mbar at the start of heating. A cooling inner surface surrounding all sublimation sources was maintained at -20 °C, and the substrate temperature was kept constant at 18 °C. The FAI deposition rate was automatically controlled and kept at 0.2 $Å s^{-1}$ in all cases, with a standard FAI layer thickness of 200 nm and 280 nm in Chapter 4 and Chapter 5, respectively. After deposition, in case of perovskite fabrication, all samples were annealed at 170 °C for 15 min in ambient atmosphere with a controlled relative humidity (r.H. ~30%).

Chapter 6:
For the different inorganic precursor compositions (PbI_2, $Pb(I_{0.67}Br_{0.33})_2$, $Pb(I_{0.33}Br_{0.67})_2$, $PbBr_2$), PbI_2 and $PbBr_2$ were mixed in the desired molar ratios and melted at 360 °C in N_2 at atmospheric pressures prior to sublimation. Pure All inorganic scaffolds were deposited at a rate of 1 $Å s^{-1}$ attained at a temperature of 250 °C. The rate and final thickness of 250 nm were controlled in an individual QCM placed above the sublimation source.

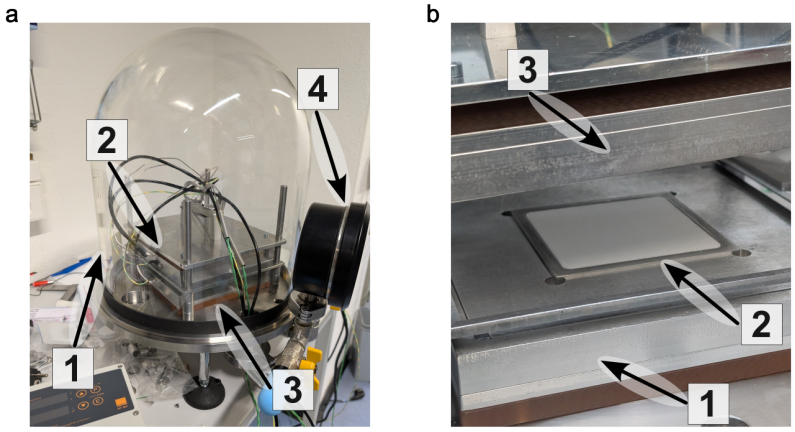

Figure 3.2: a Image of custom built Close-space sublimation (CSS) setup for deposition of organic precursors with 1) Glass housing, 2) Hotplate for substrate heating, 3) Hotplate for source heating and 4) Pressure gauge to control pressure during process. **b** Close-up of 1) Hotplate with large-area inlet for organic precursor powder source. The substrates are placed right above the source, 2) Dry organic powder source and 3) Hotplate for substrate heating.

After deposition of the inorganic scaffolds, the samples were transferred to the CSS setup. The different organic source compositions for the CSS deposition step were obtained by mixing MAI and MABr in the corresponding relative mass ratios (1 mg_{MAI} : 0 mg_{MABr}, 3 mg_{MAI} : 1 mg_{MABr}, 1 mg_{MAI} : 1 mg_{MABr}, 0 mg_{MAI} : 1 mg_{MABr}.) The mixture was then ground with a mortar to obtain a homogeneous mixture of fine powder. This ground organic precursor powder was then evenly distributed in a metal tray, which serves as the source for the CSS process. The samples were placed above the source with a gap of 3 mm before heating the source to 100 °C for MA-based and 130 °C for FAI sources (Figure 3.2). To initiate the deposition process, the chamber was pumped down to 1 mbar and kept at this pressure during deposition. After that, the chamber is vented with N_2 and brought back to atmospheric pressure. The additional annealing step (10 minutes at 100 °C) is carried out in a humidity-controlled setup with a relative humidity of ~35%.

3.1.3 Device architectures

This section provides an overview of the device architectures of the fabricated perovskite-based solar cells in this thesis with the previously described deposition methods. All single-junction solar cells are fabricated in the *p-i-n* architecture. For the fabricated two-terminal (2T) perovskite/silicon tandem solar cells (TSCs) in Chapter 5, planar silicon bottom cells were used.

Table 3.1: Material selection and architectures of sequentially deposited perovskite solar cells in Chapter 5.

	Section 5.3.3 / & Section 5.4.3	Section 5.5.1 & Section 5.5.2	Section 5.6
Architecture	opaque	opaque	2T perovskite/silicon TSC
Substrate	glass	glass	planar silicon
Front electrode	Ag	Ag	IZO with Ag-grid
HTL	MeO, 2PACz, TaTm, NiO_x, PTAA	MeO	NiO_x + MeO
Absorber layer	$FAPbI_3$	$FA_xCs_{1-x}Pb(I_aBr_bCl_c)_3$	$FA_xCs_{1-x}Pb(I_aBr_bCl_c)_3$
ETL	C_{60} + ALD-SnO_x	C_{60} + ALD-SnO_x	C_{60} + ALD-SnO_x
Rear electrode	ITO	ITO	ITO

Table 3.2: Material selection and architectures of CSS-processed perovskite solar cells in Chapter 6.

	Section 6.3	Section 6.4.1	Section 6.4.1	Section 6.4.2
Architecture	opaque	opaque	opaque	semitransparent
Substrate	glass	glass	glass	glass
Front electrode	Ag	Ag	Ag	Ag
HTL	p-doped TaTm	p-doped TaTm	p-doped TaTm	p-doped TaTm
Absorber layer	$MAPb(I_xBr_{1-x})_3$	$MAPb(I_xBr_{1-x})_3$	$MAPb(I_xBr_{1-x})_3$	$MAPb(I_xBr_{1-x})_3$
Passivation	-	$EDAI_2$	$EDAI_2$	-
ETL	C_{60} + BCP	C_{60} + BCP	C_{60} + BCP	C_{60} + ALD-SnO_x
Anti-reflective coating	-	-	LiF	-
Rear electrode	ITO	ITO	ITO	ITO

CSS-processed 2T perovskite/silicon TSCs were fabricated on differently textured silicon bottom cells (planar, nano-textured and micro-textured). In the table, the silicon bottom cell morphology for each case is not further specified.

Table 3.3: Material selection and architectures of CSS-processed two-terminal perovskite/silicon tandem solar cells in Chapter 6.

	Section 6.5	Section 6.5	Section 6.5.1
Architecture	2T perovskite/silicon TSC	2T perovskite/silicon TSC	2T perovskite/silicon TSC
Substrate	silicon	silicon	silicon
Front electrode	IZO with Ag-grid	IZO with Ag-grid	IZO with Ag-grid
HTL	p-doped TaTm	NiO_x + p-doped TaTm	NiO_x + p-doped TaTm
Absorber layer	$MAPb(I_xBr_{1-x})_3$	$MAPb(I_xBr_{1-x})_3$	$MAPb(I_xBr_{1-x})_3$
Passivation	-	$EDAI_2$	$EDAI_2$
ETL	C_{60} + ALD-SnO_x	C_{60} + ALD-SnO_x	C_{60} + ALD-SnO_x
Junction	ITO	ITO	ITO

3.2 Characterization Methods

3.2.1 Characterization of Perovskite Thin Films

X-Ray Diffraction Analysis

X-ray diffraction (XRD) was used to conduct crystal structure analysis of perovskite layers. In substances possessing a periodic lattice structure, constructive interference and, consequently, detectable diffraction, occurs when the Bragg condition is satisfied, expressed as:

$$n\lambda = 2d\ sin(\theta) \tag{3.1}$$

where n denotes the diffraction order, λ is the wavelength of the incident X-rays, d represents the interplanar spacing, and θ is the angle of incidence (Figure 3.3a). In this study, XRD measurements were performed using a Bruker D2 Phaser diffractometer in the Bragg-Brentano configuration. The instrument utilizes a Cu-Kα radiation source with a wavelength of 1.5405 Å. The X-rays are directed onto the sample surface, and diffraction

intensities are recorded by a position-sensitive detector with an angular resolution of 0.01°, across a specified 2θ range.

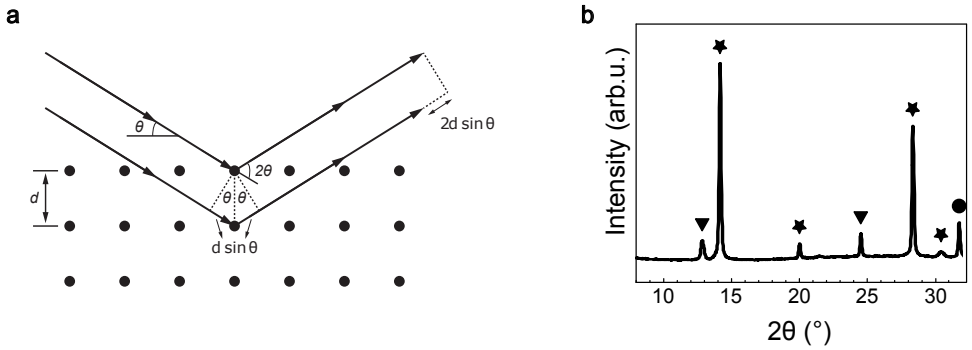

Figure 3.3: a Working principle of X-ray diffraction (XRD) analysis, with n = diffraction order, λ = wavelength of the incident X-rays, d = interplanar spacing, and θ = incidence angle. **b** Exemplary XRD pattern of a perovskite thin film on ITO. Triangles, stars and circles denote PbI_2, perovskite and ITO phases.

XRD spectra were measured for perovskite layers deposited on substrates with unpatterned ITO and the stated HTL (Chapter 5) as well as of full devices (Chapter 6). Figure 3.3b shows an examplary XRD pattern of a perovskite thin film over a 2θ range from 8-32°. The corresponding structural phases of the detected perovskite, PbI_2 and ITO phases are denoted with stars, triangles and circles, respectively.

Grazing-Incident Wide-Angle X-Ray Scattering

Grazing-incidence wide-angle X-ray scattering (GIWAXS) is a surface-sensitive structural characterization technique used to probe the crystalline properties of thin films. By directing X-rays at a shallow incidence angle, GIWAXS provides information on phase composition, crystallinity, and crystal orientation near the film surface (schematic in Figure 3.4a.

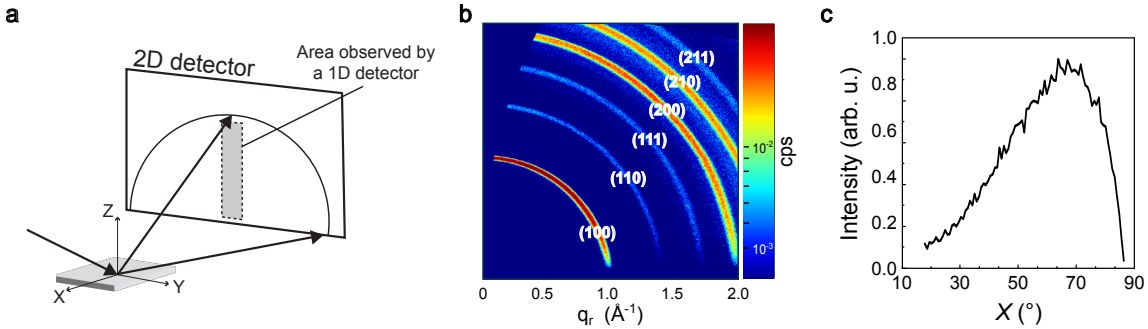

Figure 3.4: a Schematic of grazing-incident wide-angle X-ray scattering (GIWAXS) analysis. **b** Exemplary GIWAXS pattern of a perovskite thin film with denoted perovskite crystal phases. **c** Extracted pole-figure corresponding to the (100)-perovskite phase from the GIWAXS pattern.

The GIWAXS measurements were carried out on a Bruker D8 Advance equipped with a copper X-ray source (40 kV, 40 mA), Goebel mirror, a 0.5 mm micro mask and a 0.3 mm snout on the primary track and an Eiger2 R 500K 2D detector on the secondary track. For each measurement the incidence angle is 0.16° and the integration time for each frame is 90 min. We first projected all acquired images onto a virtual detector directly behind

the real goniometer circle using home-developed program in MATLAB.2 For reshaping the experimentally acquired data into 2D diffractograms in reciprocal space, we used the open-access software GIXSGUI.

An exemplary GIWAXS pattern is displayed in Figure 3.4b. The different circles represent corresponding crystal phases and their preferred orientation depending on the position of the intensity maximum. By integrating the measured intensity of each circle over the incident angle, so-called pole figures can be derived to compare crystal orientations of the different crystal phases (Figure 3.4c).

Scanning Electron Microscopy

Scanning electron microscopy (SEM) is an imaging technique that provides high-resolution information on the surface morphology and microstructure of materials. The sample surface is scanned with a focused electron beam, resulting in interactions between the electrons and atoms. These interactions produce secondary and backscattered electrons that are detected to form detailed images.

SEM images were taken with a LEO Gemini 1530 SEM from Zeiss, with aperture sizes of 20-30 μm and a gun accelerating voltage of 5-10 kV. For surface analysis, perovskite films were deposited on glass substrates with unpatterned ITO and the used HTL (Figure 3.5a). To reduce charging effects at the surface of the sample, the perovskite surface and sample station were connected with a silver tape. For cross-section images, the samples were cut and broken in half in a N_2-filled GB to reduce degradation of the exposed perovskite layer at the break edge. Prior to the SEM measurement, a thin platinum layer (3 nm) was deposited on the break edge to enhance conductivity and reduce charging effects (Figure 3.5b).

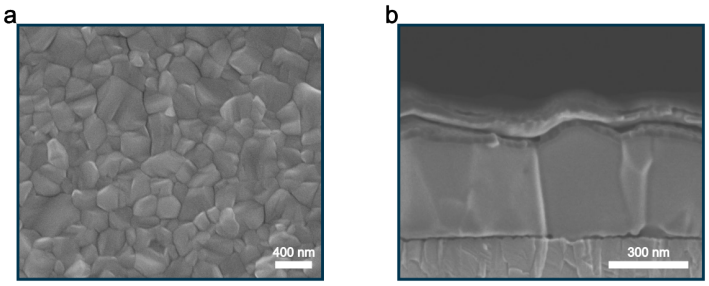

Figure 3.5: a/b Exemplary surface and cross-section image of a perovskite absorber layer and perovskite solar cell, respectively.

White-Light Interferomety

White-light interferometry (WLI) is a non-contact optical profilometry technique that measures film thickness and surface topography with nanometer precision. It works by shining white light onto the sample and comparing the light reflected from the film surface and a reference mirror. The difference in how these reflections overlap creates an interference pattern that shows the film's thickness and surface shape.

The deposited FAI layer thicknesses in Chapter 4 were determined using a WLI from Bruker (Bruker Contour GT-X500) (Figure 3.6). Step height of the coated edges was detected using a combined mode of white light interferometry and phase shift imaging called UXI. A 5x magnification lens with an additional field of view lens of 0.55x were used to depict the edges. The working distance of the 5x objective is 6.7 mm. Light was set to values between 0.15 and 0.18%. Evaluation was done using the Vision64 Software of Bruker.

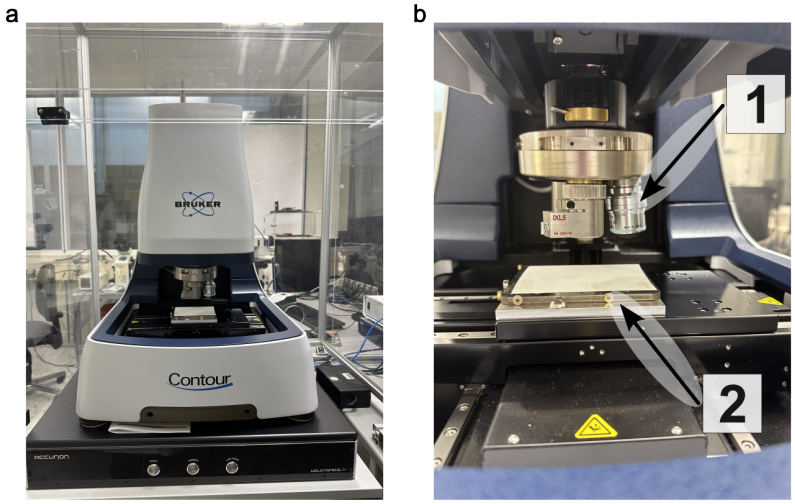

Figure 3.6: a/b Overview image and close-up of the white-light interferometry (WLI) used in this thesis, with 1) Revolving turrent with different lenses and 2) Sample stage .

Photoluminescence and k-mapping

Photoluminescence

Photoluminescence (PL) spectroscopy is a non-destructive optical characterization technique employed to probe the electronic and optical properties of semiconducting materials. Upon photoexcitation, electrons are excited to higher energy levels and subsequently undergo radiative recombination, emitting photons that reflect the material's electronic structure. Analysis of the emission energy and intensity provides information on bandgap energy, defect states, and recombination mechanisms.

The PL spectra in this work were measured with an Avantes Avaspec2048 spectrometer. Perovskite films were illuminated with a diode laser of Integrated Optics, emitting at 515 nm. All the spectra were collected with an integration time of 1 s. Exemplary PL spectra of three different perovskite thin films are displayed in Figure 3.7a.

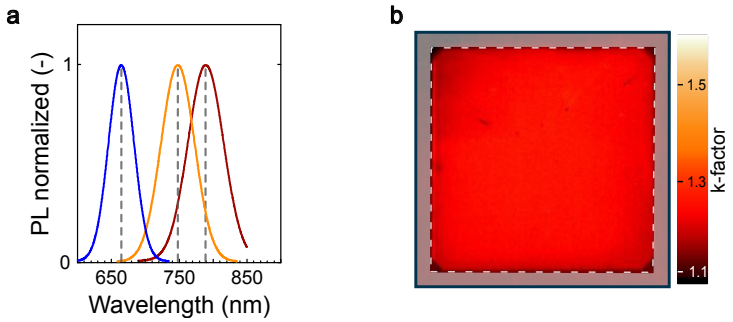

Figure 3.7: a Photoluminescence (PL) spectra of three different perovskite thin films. **b** Exemplary k-factor map obtained from light intensity-dependent PL-imaging (k-imaging) of a perovskite top cell on a nano-textured silicon bottom cell.

k-Imaging

k-Imaging (Light-intensity-dependent PL mapping) is a spatially resolved optical technique used to study how the PL response of a material varies with excitation intensity. By recording PL maps at different illumination intensities, it enables the investigation of carrier recombination mechanisms, trap states, and non-radiative losses

across the film surface. Therefore, k-mapping can be used to identify spatial inhomogeneities in optoelectronic properties and assess defect distributions.

In this thesis, an in-house built k-imaging system was used. Two 467 nm LED bars excite the sample in an 45° symmetrical alignment. The image is recorded by a sCMOS camera equipped with a macro zoom lens and an exposure time of 500 ms. To eliminate the detection of excitation light and other noise, a 695 nm absorptive long-pass filter is attached to the lens and a background correction performed. Images are recorded intensity dependent within an excitation range, equivalent to 0.005-0.2 suns based on photon flux. The k-factor is extracted as the exponent from fitting the intensity dependent PL intensities pixel-wise with a power law model and aggregated as a heat map (Figure 3.7b).

Atomic Force Microscopy

Atomic force microscopy (AFM) is a surface characterization technique that can provide topographical information at nanometer scale. By scanning a sharp probe attached to a cantilever across the sample surface, interactions between the tip and surface atoms are measured through deflections of the cantilever. These deflections are converted into a detailed height map, revealing properties of the surface morphology of the film. AFM is therefore employed to analyze the film surface roughness as well as grain sizes of the material.

AFM-measurements were performed with a Bruker Dimension Icon (USA) with an integrated xy-axis table using the Tapping Mode (Figure 3.8).

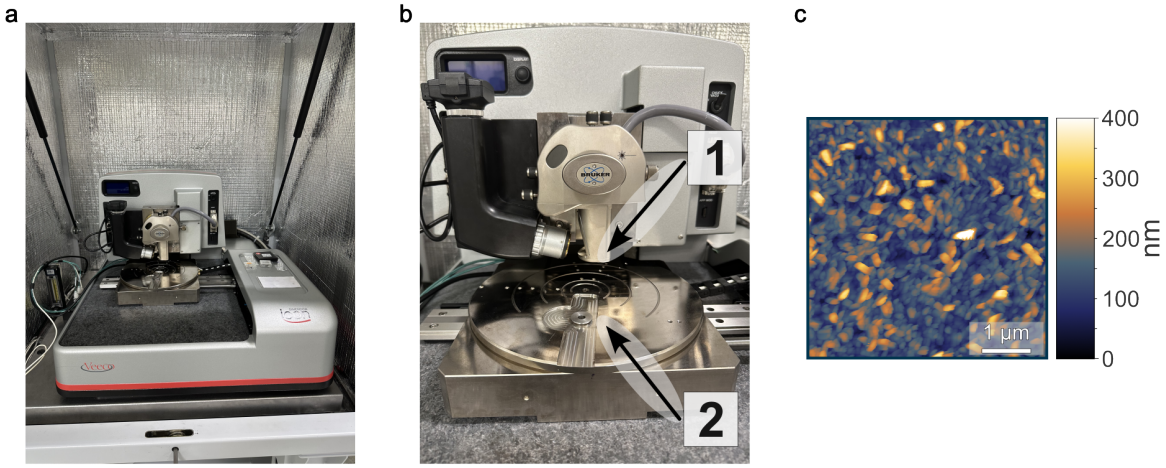

Figure 3.8: a/b Overview image and close-up of the atomic force microscope (AFM) used in this thesis, with 1) Cantilever and 2) Substrate stage. **c** Exemplary AFM measurement of a vapor-phase-deposited lead iodide (PbI_2) layer.

3.2.2 Characterization of Perovskite Solar Cells

Current-Density Voltage Measurements

Single-Junction Solar Cells

Current-voltage (*J-V*) characteristics of single-junction PSCs were measured using a class AAA solar simulator (Newport, Oriel Sol3A) at a power density of 100 mW cm^{-2}, calibrated using a reference silicon solar cell (Newport) equipped with a KG5 bandpass filter to simulate the air-mass 1.5 global (AM1.5G) solar spectrum. Scan rate during measurement was set to 0.6 V s^{-1} using a source meter (Keithley, 2400 A). Hysteresis Index (HI) is calculated as $HI = (PCE_{bw} - PCE_{fw})/PCE_{bw}$. PCE_{bw} refers to the PCE from the reverse scan from V_{OC} to 0 V,

PCE_{fw} refers to the forward scan from 0 V to V_{OC}. Maximum power point (MPP) tracking measurements are carried out using the same experimental setup as the *J-V* characterizations (N_2-atmosphere, room temperature and standard AM1.5G illumination). The solar cell temperature during measurements was actively regulated to 25 °C. During tracking, the applied voltage is periodically adjusted by ±0.01 V for 0.3 s, and the maximum obtained power conversion efficiency (PCE) is continuously recorded at one-second intervals (Figure 3.9b).

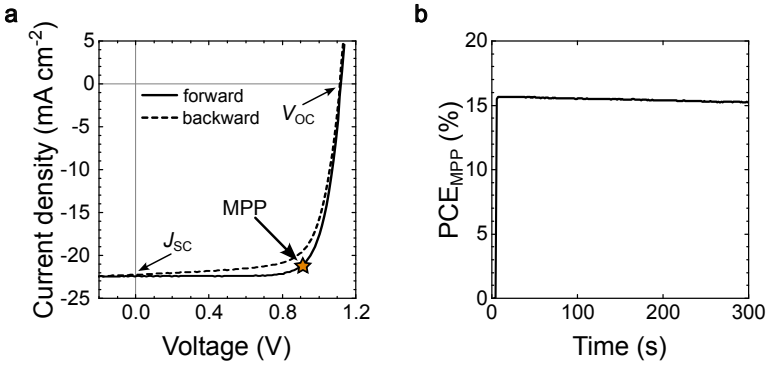

Figure 3.9: a Exemplary current-voltage (*J-V*) characteristics of a single-junction perovskite solar cell. **b** Corresponding maximum power point (MPP)-tracking for 300 seconds.

Tandem Solar Cells

The *J-V* characteristics of the fabricated perovskite/silicon TSCs were measured with a class AAA LED-based solar simulator (Wavelabs, LS-2) with a scan rate set at 0.6 Vs^{-1} using a sourcemeter (Keithley 2400) with an AM1.5G spectra (100 $mWcm^{-2}$). The solar simulator irradiation intensity was calibrated using a certified silicon solar cell (Fraunhofer ISE). *J-V* measurements of TSCs were performed in ambient atmosphere. A shadow mask with an area of 1 × 1 cm^2 was used to define the active area of the device.

External Quantom Efficiency

External quantum efficiency (EQE) is a characterization method used to determine the spectral response of photovoltaic devices. It is defined as the ratio of the number of collected charge carriers to the number of incident photons and is usually expressed as a function of the wavelength λ. By integrating the spectral response over the solar spectrum, the short-circuit current density ($J_{EQE,int}$) of the device can be calculated (Figure 3.10).

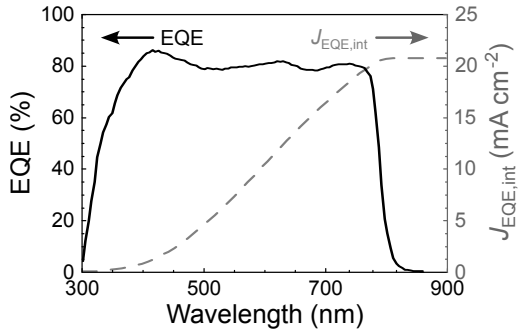

Figure 3.10: Exemplary external quantum efficiency (EQE) measurement of a perovskite solar cell with the integrated current density.

Single-Junction Solar Cells

For the sensitive EQE measurements, the cell was illuminated by a QuartzTungsten-Halogen lamp (Newport

Apex 2-QTH) through a monochromator (Newport CS130-USB-3-MC), a chopper at 279 Hz and a focusing lens. The device current was measured as a function of energy from 2.1 eV to 1.2 eV in 0.02 eV steps using a lock-in amplifier. The system was calibrated, and the solar spectrum mismatch was corrected using a calibrated silicon reference cell.

Tandem Solar Cells

EQE was measured using an Enlitech QE-R Quantum Efficiency System. To measure the spectral response of each sub-cell in the 300 to 1200 nm range we use a beam spot with an area of 1 mm^2. A halogen lamp is used to illuminate the sub-cell for which the EQE is not being analyzed. When the EQE of the perovskite top cell was analyzed an 850 nm long pass filter was applied to the halogen lamp to saturate the current generated by the silicon bottom cell, and when the EQE of the silicon bottom cell was analyzed a 550 nm short pass filter was used to saturate the current generated by the perovskite top cell. The current mismatch generated within the tandem device by this light bias leads to a shift in the operating voltage of the sub-cell being measured. Hence, without a voltage bias the sub-cell under measurement is in reverse bias and therefore a bias voltage is needed to bring it back to short-circuit conditions. The voltage bias applied is in the range of the V_{OC} of the non-analyzed sub-cell, that is around 0.6 V when analyzing the EQE of the perovskite top cell and around 1.0 V when analyzing the EQE of the silicon bottom cell.

Laser-Beam Induced Current Mapping

Laser-beam induced current (LBIC) mapping is a characterization technique used to assess the spatially resolved local photoresponse and uniformity of photovoltaic devices. In this method, a focused laser beam is scanned across the device surface while the resulting photocurrent is measured at each position. The measured data produces a current map that reflects variations in charge collection efficiency, revealing local defects, inhomogeneities, or shunting paths.

In this thesis, LBIC mapping was conducted using a custom-built set-up employing two continuous-wave laser sources, a lock-in amplifier (SR830, Stanford Research Systems) and a chopper operating at 470 Hz for signal enhancement. The samples are placed on a XY-motorized sample stage for scanning. For the analysis of perovskite/silicon TSCs, the perovskite and silicon sub-cells were illuminated and scanned with continuous-wave laser sources of 530 nm and 850 nm, respectively (Figure 3.11).

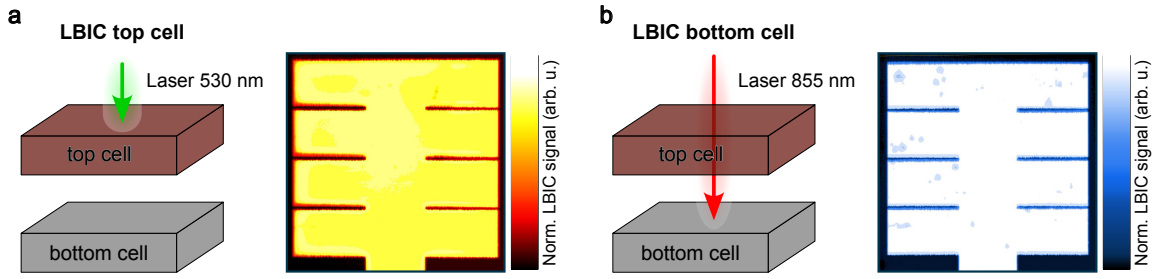

Figure 3.11: Laser-beam induced current (LBIC) mapping of a two-terminal (2T) perovskite/silicon tandem solar cell (TSC). **a** Scanning of the perovskite top cell with a continuous-wave laser source of 530 nm and resulting LBIC map of the perovskite top cell. **b** Scanning of the silicon bottom cell with a continuous-wave laser source of 850 nm and resulting LBIC map of the silicon bottom cell.

4 Impact of Formamidinium Iodide Precursor Material Particle Size and Crucible Geometry on Sublimation Behavior

Abstract

Vapor phase deposition processes for the fabrication of perovskite solar cells hold great potential for successful transition from laboratory- to industrial-scale. The effectiveness of these deposition methods relies heavily on precise process control, as well as consistent reproducibility and repeatability. A key challenge in this regard lies in controlling the sublimation behavior of the commonly employed organic precursor materials FAI and MAI. Analysis of commercial FAI precursor powder reveals great discrepancies of the FAI particle size distribution across different fabrication batches, resulting in inconsistent experimental conditions during sublimation processes. In this chapter the impact of particle size of FAI precursor material and different sublimation crucible geometries on the effusion characteristics is analyzed. The results demonstrates a strong dependency of particle size and crucible geometry on the directionality of the emitted vapor flux. Changes in the emission profile directly influence deposition homogeneity across a substrate, which in addition depends on the actual vacuum chamber design. Analysis of commonly used inorganic precursor materials shows, that the effusion behavior further depends on the sublimed material. These findings reveal potential parameters that influence reproducibility and repeatability of laboratory-scale vapor phase deposition processes and highlight the importance of thoughtful vacuum chamber design.

Acknowledgements and Contributions

Parts of this chapter review the published research article "*Particle Size Matters – Impact of Particle Size and Crucible Geometry on Sublimation Behavior of Formamidinium Iodide*" in *Advanced Materials Technologies*, 2025 (DOI: 10.1002/admt.202501549) by Alexander Diercks, Julian Petry, Thomas Feeney, Richard Thelen, Paul Fassl, and Ulrich W. Paetzold. Some figures in this chapter were adapted with permission from Wiley. The contributions of all authors according to the CRediT system are listed in Table A.2.

4.1 Introduction

Transition from laboratory-scale research to industrial-scale fabrication remains a key challenge for successful commercialization of perovskite solar cells.[11, 46] Most research on perovskite solar cells focuses on solution-based deposition methods, whereas only less than 2% of all publications report on vapor-based fabrication processes.[12] However, vapor phase deposition methods possess several advantages regarding fabrication of high-quality perovskite thin films for industrially relevant applications. Homogeneous deposition over large areas and solvent-free processing facilitate industrial in-line processing and prevent the need of toxic solvents.[11, 40, 46] Furthermore, the ability to conformally cover textured or rough surfaces, essential for the fabrication of industrially relevant perovskite-silicon tandem photovoltaics, sets vapor phase deposition processes apart from solution-based ones.[47–49] For a long time, reported PCEs of vapor-phase-deposited PSCs have been lacking behind those of their solution-processed counterparts. However, recently reported PCEs of sequentially vapor-phase-deposited PSCs reaching PCEs of ~27% close the gap, proving the competitiveness of vapor phase deposition methods in this regard.[7, 43] The combination of these aspects makes vapor phase deposition a promising option for industrial high-throughput fabrication of efficient perovskite-based solar cells, critical for cost-effective upscaling.[11, 40]

Despite their advantages, there are still some challenges for further advancing vapor phase deposition processes for fabrication of PSCs to overcome. Commonly known, laboratory-scale vapor phase deposition processes deposition suffer from poor reproducibility and repeatability, including strong fluctuations in perovskite thin film properties in subsequent depositions and difficulties in transferring recipes from one vacuum-system to another. Film properties of thermally sublimed perovskites and resulting PCEs of PSCs are known to be highly sensitive to different parameters such as the underlying substrate,[58–60, 101, 106] impurities of the employed precursor materials[52, 55, 57] and material stoichiometry of the final perovskite thin film.[53, 54, 60, 106, 107] Additionally, various studies revealed a strong impact of different deposition conditions during the process, such as the chamber pressure, substrate temperature and deposition rates.[52, 59, 107–110] The sublimation behavior of the commonly employed organic precursor materials MAI and FAI has been found to be one of the main contributors to the observed difficulties in process control.[52, 55, 105] While the sublimation behavior of MAI has been studied in much detail,[53–55, 57, 59, 60, 107, 108, 111, 112] there is only a very limited number of corresponding studies on FAI,[52, 101, 109] even though recent record PCEs of solution-processed and vapor-phase-deposited PSCs build on FA-based perovskite compositions.[43]

This chapter focuses on gaining a deeper understanding of the sublimation behavior of FAI to enable better process control and improve the reproducibility and repeatability of FAI-based vapor phase deposition processes (research question **I**). In literature, there are no fundamental studies yet on how changes in precursor material particle size and sublimation crucible geometry can impact the sublimation behavior of FAI sublimation processes. Therefore, a technical analysis of the impact of different FAI particle sizes as well as different sublimation crucible geometries, namely conical and cylindrical, on the effusion characteristics during FAI deposition is presented.

4.2 Particle Size Distribution in Commercial Formamidinium Iodide Precursor Powders

While for solution-based deposition processes different FA halides (iodide, bromide and chloride) are commonly used as precursor materials, vapor phase deposition processes primarily employ FAI as their FA-source. A schematic of the emitted FAI vapor flux from a conical sublimation crucible is illustrated in Figure 4.1a.

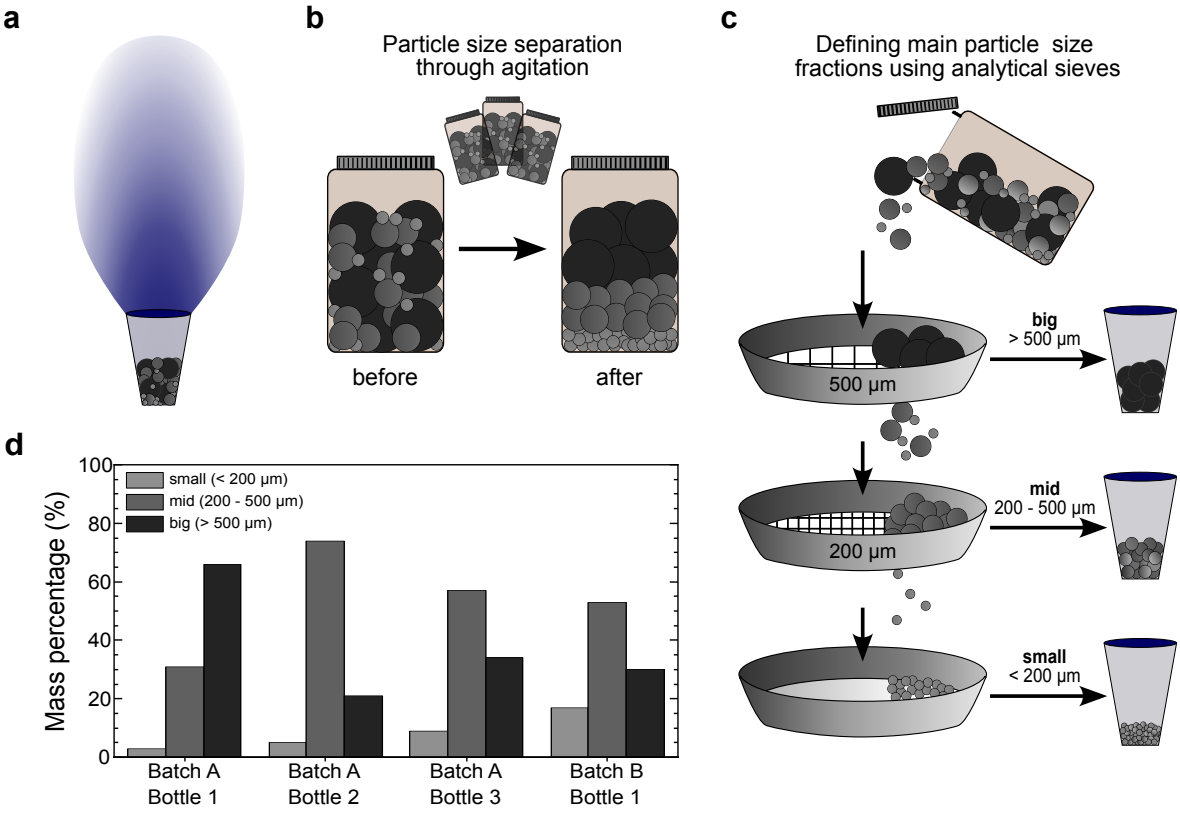

Figure 4.1: a Illustration of the FAI vapor flux emitted from a conical sublimation crucible. **b** Schematic illustration of granular convection process ("Brazil-nut effect") showing de-mixing effects of different particle sizes in dry powders from material agitation inside precursor bottle. **c** Illustration of process to define main particle size fractions (small: x < 200 µm, mid: 200-500 µm and big: x > 500 µm) using analytical sieves of different mesh-sizes**. d** Particle size distribution of FAI from Greatcell Solar Materials in different bottles and fabrication batches (A/B). Adapted with permission from Wiley.

The majority of reports on FA-based sublimation processes use commercially available FAI from Greatcell Solar Materials, which was also used in this work (Table A.5).[43, 52, 59, 98–102, 104, 106, 113–129] Interestingly, the used FAI precursor material from Greatcell Solar Materials exhibits a broad particle size distribution (Figure A.1). Changes in particle size distribution can lead to variations in particle size compositions for different sublimation processes. The particle size distribution of small amounts (usually around 1-2 g per sublimation process) taken from the FAI bottle for different sublimation processes inevitably changes when using bottles from different fabrication batches. These inconsistencies are further increased due to the so-called granular convection process (also known as "Brazil-nut effect"). This granular convection process describes a de-mixing phenomenon of dry powders with various particle sizes due to agitation of the mixture. A schematic illustration of this process is shown in Figure 4.1b. Variations in particle size distribution lead to inconsistent experimental conditions, which may affect the reproducibility of the sublimation process. Using analytical sieves of different mesh sizes, three main particle size fractions were defined: small (< 200 µm), mid (200-500 µm), and big (> 500 µm) (Figure 4.1c and Figure A.1). Furthermore, when analyzing different FAI precursor bottles from

different fabrication batches (**A** and **B**), drastic variations in the obtained particle size distribution are detected (Figure 4.1d). In addition to the numerous factors influencing perovskite film formation, these inconsistencies in the properties of commercial precursor materials introduce further complexity to achieving reproducible processing in laboratory-scale setups.

There are no fundamental studies yet on how changes in precursor material particle size and sublimation crucible geometry can impact the sublimation behavior of FAI sublimation processes. In the following sections, a technical analysis of the impact of different FAI particle sizes as well as different sublimation crucible geometries, namely conical and cylindrical, on the effusion characteristics during FAI deposition is presented.

4.3 Effusion Characteristics of Formamidinium Iodide

In this section, a technological analysis of the sublimation behavior of FAI from effusion sources is conducted. Therefore, the previously defined main particle size fractions are investigated on their impact on the directionality of the emitted FAI vapor flux from conical and cylindrical sublimation crucibles. The applied fit-function to derive the evaporation cones from experimentally determined data points is introduced in Chapter 2 (Equation (2.36)).

4.3.1 Derivation of Evaporation Cone for Conical and Cylindrical Crucibles

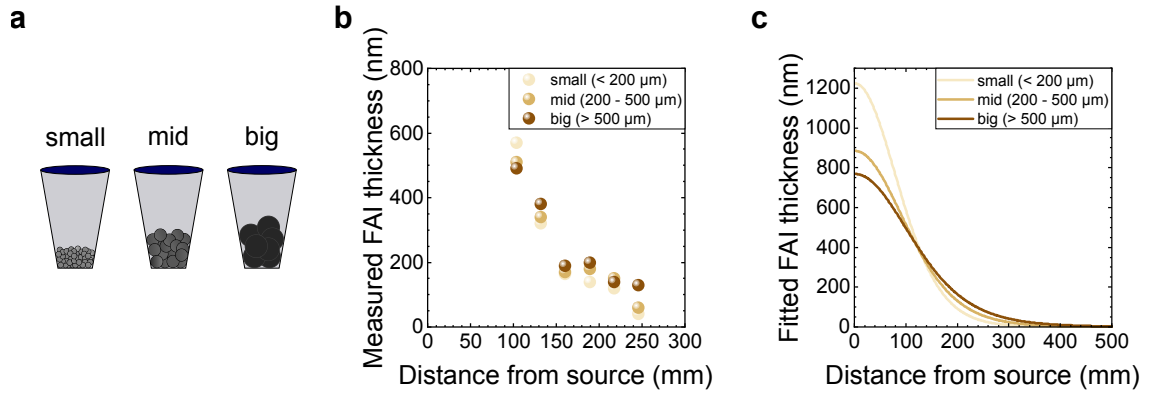

Figure 4.2: a Distribution of defined particle size fractions (small, mid, big) into conical crucibles. **b** Measured formamidinium iodide (FAI) film thickness on substrate after deposition with a constant deposition rate on a non-rotating substrate for individual sublimation processes with FAI powder of the defined particle size fractions (small, mid and big) from conical crucibles. **c** Extrapolated evaporation cone fit for the corresponding measured film thicknesses, calculated by the previously described formula (Equation 2.36).

In order to analyze the effusion characteristics of FAI when deposited from conical crucibles, sublimation processes were carried out with each of the three FAI particle size fractions small, mid and big (Figure 4.2a). The sublimation deposition was carried out at a static deposition rate on glass substrates placed in a non-rotating substrate holder, with resulting lateral distances of the glass substrates to the sublimation source of 75.7, 103.9, 132.2, 160.5, 188.8, 217.1 and 245.4 mm. Figure 4.2b shows the measured FAI layer thickness on the individual glass substrates at their corresponding lateral position for each of the three FAI particle size fractions (Table A.6). When comparing the measured layer thicknesses of the three particle size fractions, strong differences are visible. The measured thickness gradient as a function of the lateral distance from the substrate to the sublimation source is more pronounced for the small particle size fraction than for mid or big. Using the fit-function (Equation 2.36), the measured data points for each particle size fraction (small, mid and

big) can be fitted to obtain an approximation of the shape of the evaporation cone, which provides insights into the directionality of the emitted vapor flux (Table A.7). Figure 4.2c displays the extrapolated fits for the three particle size fractions, revealing great changes depending on the particle size fraction. Small particle size fraction results in a much greater thickness gradient over the lateral distance of the substrate from the source than both mid and big fractions. From these results a correlation between particle size and thickness gradient can be drawn, where smaller particle sizes lead to greater thickness gradients on the substrate.

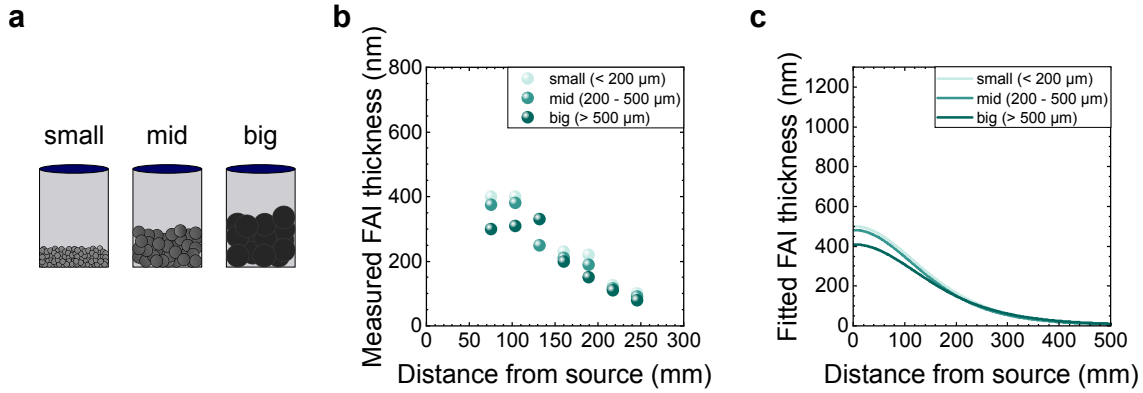

Figure 4.3: a Distribution of defined particle size fractions (small, mid, big) into cylindrical crucibles. **b** Measured formamidinium iodide (FAI) film thickness on substrate after deposition with a constant deposition rate on a non-rotating substrate for individual sublimation processes with FAI powder of the defined particle size fractions (small, mid and big) from cylindrical crucibles. **c** Extrapolated evaporation cone fit for the corresponding measured film thicknesses, calculated by the previously described formula (Equation 2.36).

Conversely, FAI effusion characteristics when deposited from cylindrical crucibles are much less affected by the used particle size fraction (Figure 4.3a). The measured thicknesses for each of the three particle size fractions show much less deviation amongst themselves, with comparable resulting thickness gradients as a function of the lateral distance of the substrate to the sublimation source (Figure 4.3b and Table A.6). Comparing the obtained thickness gradients from cylindrical crucibles to the ones from conical crucibles, cylindrical crucibles lead to much less pronounced gradients for all three particle size fractions (Figure 4.3a). The obtained evaporation cones after fitting the measured data points with Equation 2.36 show very similar shapes for all three particle sizes for cylindrical crucible geometries (Figure 4.3c and Table A.7). These results show that particle size as well as crucible geometry can impact the directionality of the emitted vapor flux.

4.3.2 Impact of Particle Size and Crucible Geometry on Directionality of Vapor Flux

To further analyze how different particle size fractions and crucible geometries affect the directionality of the sublimation behavior of FAI, the resulting effusion characteristics depending on both parameters are examined in more detail. The derived evaporation cones for the three defined particle size fractions (small, mid and big) and both crucible geometries (conical and cylindrical) allow for a more in-depth analysis of the spatial directionality of the emitted vapor flux. Figure 4.4a/d displays a schematic illustration of the differences of FAI deposition from both crucible geometries, conical and cylindrical, respectively. The previously described results showed a more focused vapor flux for conical crucibles, resulting in a more pronounced material thickness gradient, while cylindrical crucibles lead to a more de-focused vapor flux and less pronounced material thickness gradient.

Since all sublimation processes were carried out in the same vacuum chamber at a constant static deposition rate of 1 $Å s^{-1}$ measured by a quartz-crystal microbalance (QCM) at a lateral position of 75 mm to the source,

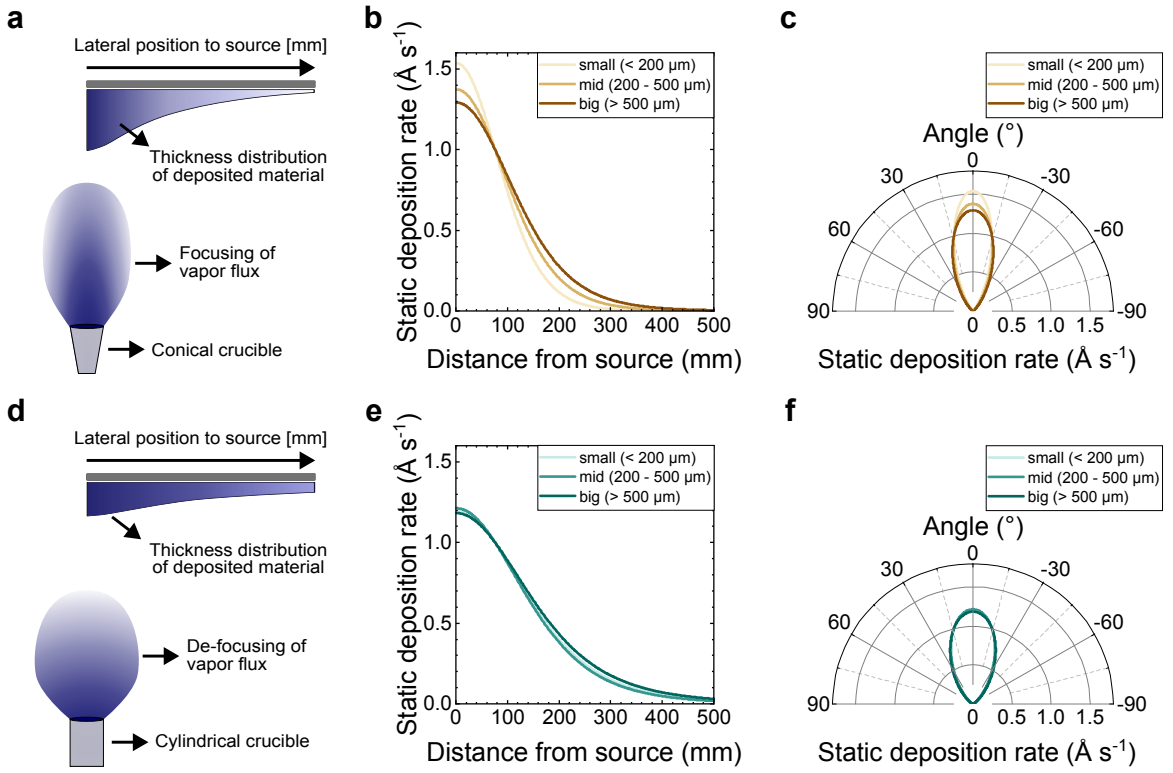

Figure 4.4: **a/d** Schematic representation of the emitted formamidinium iodide (FAI) vapor flux and deposition on the substrate originating from conical and cylindrical crucible geometries, respectively. **b/d** Comparison of static deposition rate profiles as a function of lateral distance of the substrate from the source with a normalized deposition rate of 1 $Å s^{-1}$ at the corresponding position of the quartz crystal microbalance (QCM) for conical and cylindrical crucibles, respectively. **e/f** Comparison of angular emission profiles as a function of particle size for conical and cylindrical crucibles, respectively. Adapted with permission from Wiley.

the evaporation cones can be normalized and adjusted to this point. Figure 4.4b/e shows the resulting static deposition rate profiles for the three different particle size fractions and deposition from conical and cylindrical sublimation crucibles, respectively. Static deposition rate profiles from conical crucibles are highly impacted by the used particle size fraction (Figure 4.4b). This underscores the importance of homogenizing FAI precursor particle size before processing to maintain similar effusion characteristics when using conical sublimation crucibles. Especially considering the significant deviations in particle size distribution of commercial FAI powders (Figure 4.1c), strong variations in the spatial effective deposition rate are inevitable without homogenizing the used precursor material. Conversely, cylindrical crucibles exhibit almost identical static rate deposition profiles for all three particle size fractions, with a generally much broader, less directional emitted vapor flux (Figure 4.4e). To summarize, conical crucibles lead to strong beam-focusing of the vapor flux and an overall more directional emission profile which is highly particle size dependent (Figure 4.4c). Cylindrical crucibles show a less directional vapor flux, with similar emission profiles independent of the particle size fraction, making them the preferred choice against inconsistent precursor particle size distribution (Figure 4.4f).

These findings reveal that both particle size and sublimation crucible geometry impact the sublimation behavior and directionality of the emitted vapor flux of FAI in vapor phase deposition processes, a never before reported phenomenon regarding vapor-based fabrication of perovskite solar cells. Combination of conical crucibles and inconsistent FAI particle size distribution can negatively impact process repeatability and reproducibility, while cylindrical crucibles are less vulnerable towards inconsistent particle size distributions, potentially improving repeatable processing.

4.4 Analysis of Deposition Homogeneity

Changes in the effective deposition rate depending on the lateral distance from the substrate to the sublimation source can lead to variations in the deposited layer thickness over the substrate holder. Usually, substrate holders in vacuum-chambers used for sublimation processes make use of rotating substrate holder stations in order to improve the homogeneity of the deposited film over the whole substrate holder area. In multi-material systems, due to the arrangement of the used sublimation sources, a rotating substrate station is necessary to obtain similar material compositions over the whole area. Variations in vapor flux directionality caused by changes in crucible geometry and precursor particle size can lead to differences in effective deposition rates across the substrate depending on its lateral position to the source. Therefore, it is crucial to understand how a change in effective deposition rate affects the homogeneity of the deposition across the substrate.

In this section, the effect of both sublimation crucible geometries, conical and cylindrical, on the deposition homogeneity is examined for different lateral source to substrate distances. Furthermore, different particle size fractions are analyzed and compared. Finally, the optimal source to substrate distances for each individual combination (crucible geometry and particle size fraction) is presented, by calculating the point with the lowest grade of inhomogeneity in material thickness.

4.4.1 Comparison of Conical and Cylindrical Sublimation Crucibles

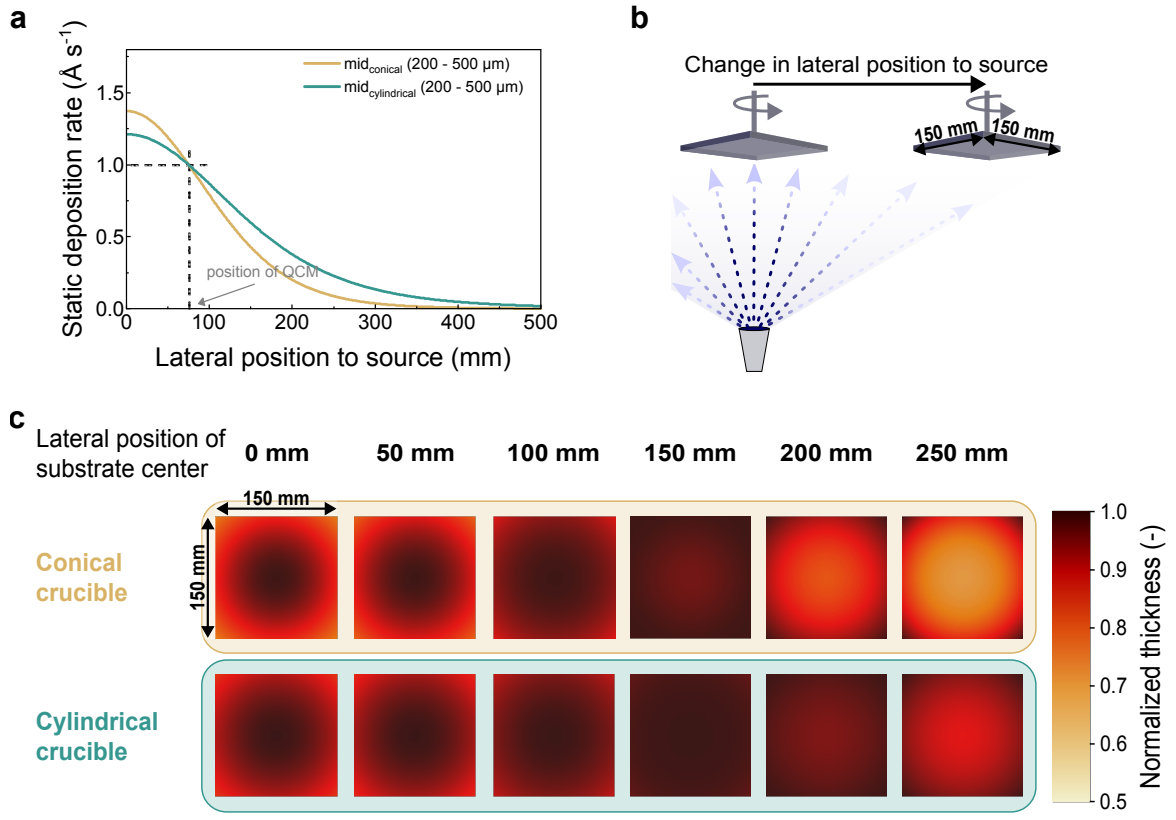

Figure 4.5: a Comparison of static deposition rates for the mid particle size fraction, extracted from Figure 4.2e, for conical and cylindrical sublimation crucibles. **b** Schematic illustration of the simulated lateral movement of the substrate holder relative to the sublimation source. **c** Normalized heatmaps representing simulated film thickness distributions from deposition using conical and cylindrical crucibles across a rotating substrate holder. The substrate holder is positioned at different lateral distances from the sublimation source (0 mm, 50 mm, 100 mm, 150 mm, 200 mm, and 250 mm). Adapted with permission from Wiley.

To analyze the impact of different sublimation crucible geometries as well as source arrangement in the vacuum chamber, the FAI deposition homogeneity from conical and cylindrical crucibles at different lateral source to substrate distances is compared. For these experiments, the static deposition rate profiles of the defined mid particle size fraction (200 - 500 µm) from both crucible geometries are used (Figure 4.5a) to simulate the deposited material thicknesses on a substrate with dimensions of 150 mm x 150 mm. The center of the substrate is then positioned at different lateral positions from the source, to extract the material thickness profile regarding the lateral source to substrate distance, while keeping the vertical distance from substrate to the source constant. To simulate a rotating substrate holder, the extracted thickness profile is then rotated 360° over the center of the substrate to determine the spatial thickness distribution of deposited material over the whole substrate. Figure 4.5b illustrates the simulated movement of the rotating substrate in lateral direction from the sublimation source. The extracted normalized material thickness profiles at defined positions (0 mm, 50 mm, 100 mm, 150 mm, 200 mm and 250 mm) for deposition from both sublimation crucible geometries are displayed in Figure 4.5c. In case of deposition from conical crucibles, strong variations in thickness distribution over the whole substrate are visible when comparing the heatmaps at different lateral positions. At the extreme cases, gradients in material thickness from center to the edges of the substrate of -25%$_{rel}$ at a lateral position of 0 mm and inverted gradients from edges to center of ~45% at 250 mm are detected, also quantified by the corresponding diagonal thickness profiles (Figure A.2a). Conversely, cylindrical crucibles show maximum deviations in material thickness of -20%$_{rel}$ and ~12%$_{rel}$, respectively (Figure A.2b). Overall, heatmaps extracted from the static rate deposition profile from cylindrical crucible show much more homogeneous material thickness distributions at all defined lateral positions. These results show, that the previously found broader emission profile of cylindrical crucibles leads to a better deposition homogeneity on the substrate with respect to lateral distance from the substrate to the sublimation source compared to conical crucibles.

4.4.2 Dependence on Formamidinium Iodide Precursor Particle Size

The impact of different particle size fractions on the deposition homogeneity of FAI sublimation processes follows the previously shown results. Figure 4.6a/b shows the comparison of the static rate deposition profiles from conical and cylindrical crucibles using small and big particle size fractions, respectively. A simulation of the material thickness profiles at different lateral positions from the substrate to the source are extracted and extrapolated over a simulated full rotation of the substrate. The resulting normalized heatmaps at lateral positions of 0 mm, 100 mm and 200 mm for all four cases are displayed in Figure 4.6c. Comparing the material thickness homogeneity for depositions with the small particle size fraction from conical crucibles reveals the strongest deviations of up to ~57%$_{rel}$ from the center of the substrate to the edges (at 300 mm). The most homogeneous deposition over all depicted lateral positions of the substrate is achieved for depositions using big particle size fraction and a cylindrical sublimation crucible. These results visually highlight the impact of crucible geometry and particle size on the spatial deposition homogeneity of FAI depositions, which are in line with the previously revealed findings from Section 4.3. The corresponding diagonal thickness profiles for all shown constellations can be found in the appendix (Figure A.3 and Figure A.4). From these diagonal thickness profiles, the normalized thickness inhomogeneity (IH) can be calculated:

$$Normalized\ inhomogeneity\ [-] = \frac{(thickness_{max} - thickness_{min})}{thickness_{mean}}$$

This value allows a quantitative comparison of the deposition homogeneity for different configurations. Furthermore, by plotting the IH as a function of lateral distance from substrate to sublimation source, the optimal distance for the most homogeneous deposition over the substrate can be identified.

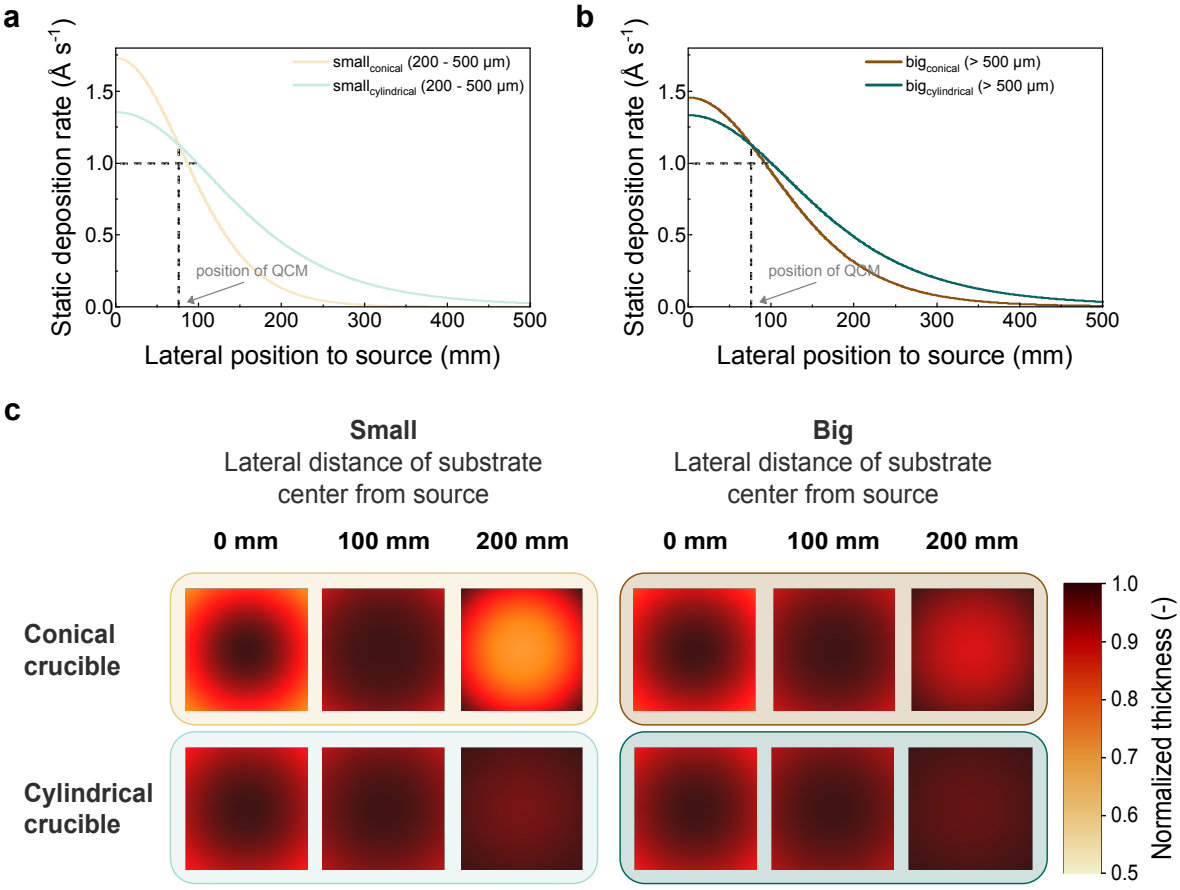

Figure 4.6: a/b Comparison of static deposition rates for the small and big particle size fractions, extracted from Figure 4.2b and e, for conical and cylindrical sublimation crucibles. **c** Normalized heatmaps representing simulated film thickness distributions from deposition from conical and cylindrical crucibles across a rotating substrate holder. The substrate holder is positioned at different lateral distances from the sublimation source (0 mm, 100 mm, 200 mm) for both particle size fractions small and big.

Figure 4.7 shows the correlation of IH with respect to the lateral source to substrate distance for all three defined particle size fractions (small, mid and big) when deposited from conical (Figure 4.7a) and cylindrical (Figure 4.7b) crucibles. In the case of deposition from conical crucibles, the resulting point of most homogeneous deposition varies significantly for all three particle size fractions, with optimal distances of 122 mm, 137 mm and 149 mm for small, mid and big, respectively. In contrast, deposition from cylindrical crucibles is much less dependent on the FAI particle size, showing only slight differences in the corresponding points of most homogeneous deposition (small = 171 mm, mid = 168 mm, and big = 177 mm), clearly positioning cylindrical crucibles as the preferred crucible of choice.

These results clearly demonstrate the impact of particle size in combination with sublimation crucible geometry on the effusion characteristics of FAI and the resulting effect on deposition homogeneity. Furthermore, it becomes obvious, that depending on the experimental conditions (particle size fraction and sublimation crucible geometry) and source arrangement in the employed vacuum chamber, deposition homogeneity can vary substantially, potentially explaining the difficulty of recipe transfer from one system to another.

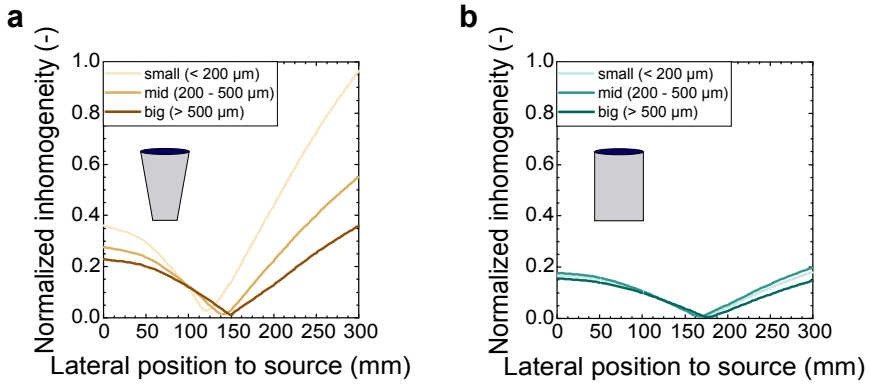

Figure 4.7: a/b Comparison of normalized thickness inhomogeneity derived from simulated deposition profiles over a rotating substrate holder for the three defined FAI particle size fractions for deposition from conical crucibles (**a**) and cylindrical crucibles (**b**). Adapted with permission from Wiley.

4.5 Sublimation Behavior of Inorganic Precursor Material

In order to determine whether the previously observed changes in effusion characteristics are material-dependent, the vapor flux directionality of the most common inorganic precursor materials for sublimed perovskite solar cells, lead iodide (PbI_2) and cesium iodide (CsI), are analyzed.

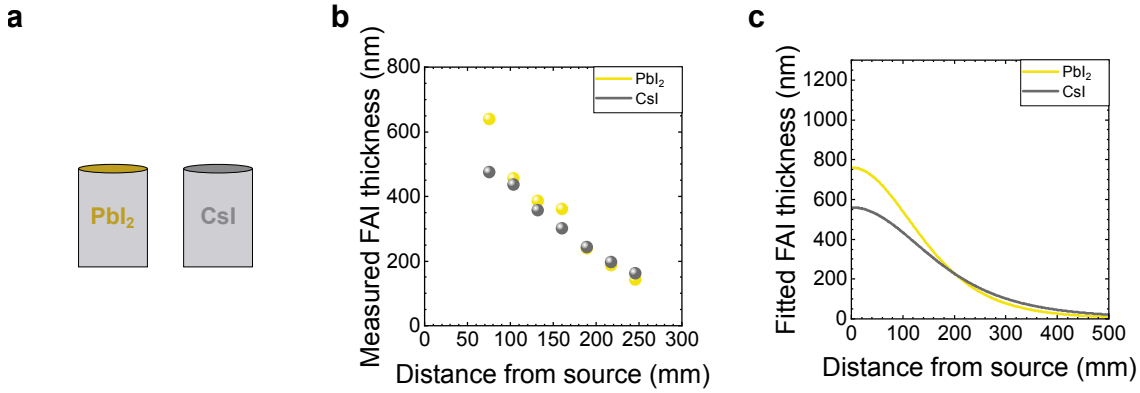

Figure 4.8: a Schematic of inorganic materials CsI and PbI_2 in cylindrical crucibles. **b** Measured film thickness of PbI_2 and CsI on substrate after deposition with a constant deposition rate on a non-rotating substrate for individual sublimation processes from cylindrical crucibles. **c** Extrapolated evaporation cone fit for the corresponding materials, calculated by the previously described formula (Equation 2.36).

Since cylindrical crucibles lead to much broader vapor flux and deposition homogeneity, only effusion characteristics from cylindrical crucibles are analyzed (Figure 4.8a). Similar to the experimental procedure from Section 4.3, static deposition of both materials on glass substrates with defined distances to the sublimation source was performed. Figure 4.8b shows the measured layer thicknesses for PbI_2 and CsI after deposition (Table A.6). Slight differences are detectable for substrates located closer to the emitting source. When fitting the measured thickness data with Equation 2.36, the thickness gradient of PbI_2 shows a more pronounced course than that of CsI (Table A.7).

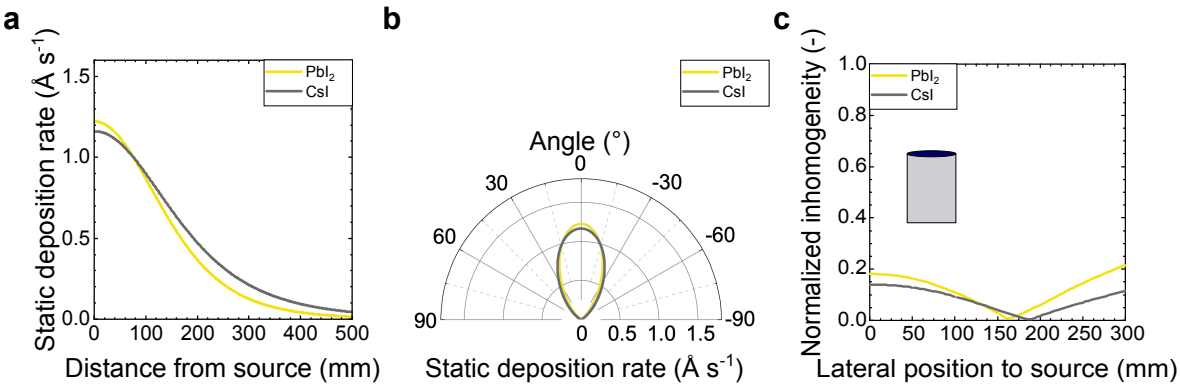

Figure 4.9: a Comparison of static deposition rate profiles of PbI_2 and CsI as a function of lateral distance of the substrate from the source with a normalized deposition rate of 1 Å/s at the corresponding position of the quartz crystal microbalance (QCM). **b** Comparison of angular emission profiles of PbI_2 and CsI from cylindrical crucibles, respectively. **c** Comparison of normalized thickness inhomogeneity derived from simulated deposition profiles over a rotating substrate holder for PbI_2 and CsI from deposition from cylindrical crucibles.

The resulting static rate deposition profiles are displayed in Figure 4.9a. Both materials show a broad, less directional vapor flux, comparable to the static rate deposition profiles for all three FAI particle size fractions when deposited from cylindrical crucibles (Figure 4.9b). However, PbI_2 exhibits a slightly more directional vapor flux than CsI, demonstrating, that effusion characteristics are not only depending on the geometry of the sublimation crucible, but are also material dependent. A corresponding analysis of the point of most homogeneous deposition reveals a difference of 20 mm in the optimal distance from substrate to source between the two materials, with 165 mm for PbI_2 and 185 mm for CsI (Figure 4.9c and Figure A.5).

4.6 Impact of Vacuum Chamber Design on Process Homogeneity

The previously shown results reveal a strong influence of particle size, crucible geometry and precursor material on the sublimation characteristics and directionality of the emitted vapor flux, leading to differences in optimal source-to-substrate distance for maximum deposition homogeneity. Consequently, for optimized process control of multi-material deposition processes, the influence of source-to-substrate distance variations on material homogeneity must be carefully evaluated. Conventional, commercial vacuum-chambers are designed in a way, that all sublimation sources are placed equidistantly around the substrate. Reproducible fabrication of uniform and high-quality perovskite thin films *via* vapor phase deposition (both sequential layer deposition and co-deposition) critically depends on precise control of the material ratios. In this section, the deposition homogeneity of a simulated multi-source deposition process of FAI (mid particle size fraction), PbI_2 and CsI with two different source to substrate configurations is analyzed (Figure 4.10).

Case **A** represents an equidistant source to substrate configuration with all three sources placed at 150 mm from the center of the substrate, similar to the experimental setup used in this thesis. Case **B** shows an optimized scenario, in which each sublimation crucible is positioned at the material-depending optimal source to substrate distance for most homogeneous deposition over the substrate (PbI_2 = 165 mm, FAI = 168 mm, and CsI = 185 mm). In both cases, cylindrical crucible geometries are used for all materials.

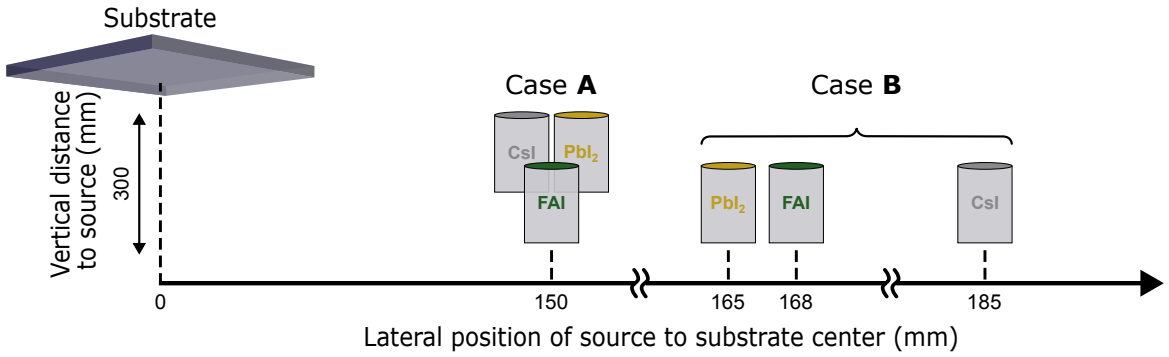

Figure 4.10: Schematic illustration of two different source to substrate configurations inside a vacuum chamber. Case **A** represents an equidistant arrangement with source to substrate distances of 150 mm of each material, comparable to the used vacuum chamber in this work. Case **B** represents an optimized arrangement with individually optimized source to substrate distances for most homogeneous deposition for each precursor material (FAI mid = 168 mm, PbI_2 = 165 mm and CsI = 185 mm). Adapted with permission from Wiley.

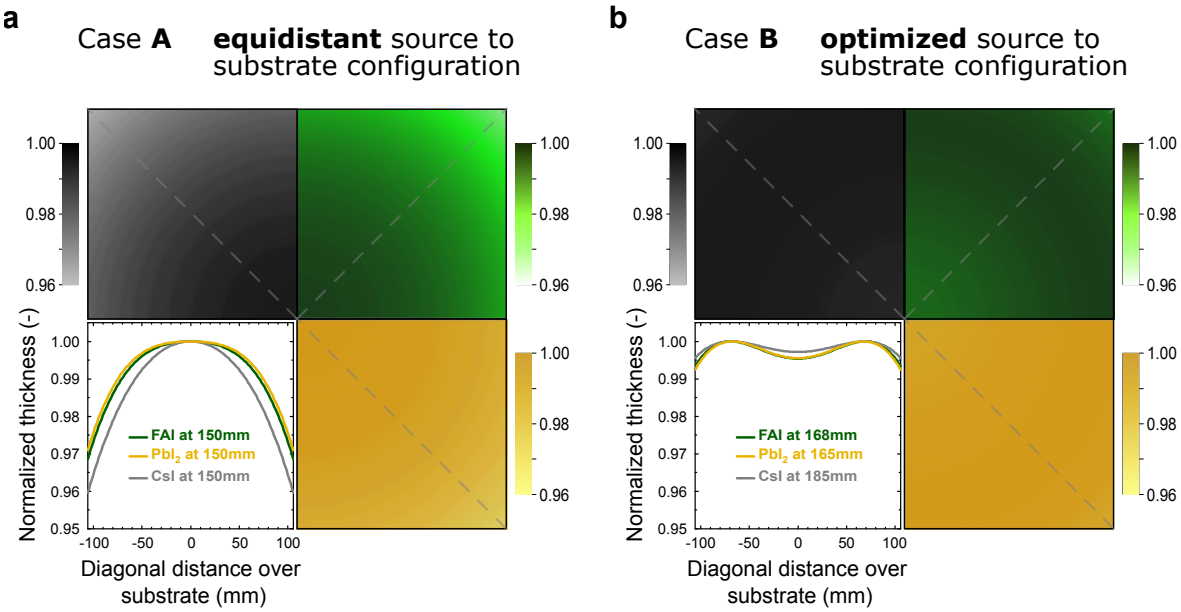

Figure 4.11: a Heatmaps of simulated thickness profiles from cylindrical crucibles over a rotating substrate holder for CsI, FAI (mid particle size fraction) and PbI_2 at an equidistant lateral source to substrate distance of 150 mm (Case **A**). **b** Heatmaps of simulated thickness profile over a rotating substrate holder for CsI, FAI and PbI_2 with an individually optimized lateral source-to-substrate distance of 185 mm, 165 mm and 168 mm (Case **B**) respectively. Adapted with permission from Wiley.

In case of equidistant source to substrate configuration (Case **A**, see Figure 4.11a), the diagonal profiles of the deposited material thickness for all three materials show a gradient from the center to the edge of each substrate, resulting in deviations of up to ~4% in case of CsI and ~3% for FAI and PbI_2. The observed discrepancies in deposited material thicknesses inevitably lead to changes in material ratios over the whole substrate. Optimized source to substrate distances for each material (Case **B**, see Figure 4.11b) result in individually minimized thickness deviations, with maximum deviations from center to corner of the substrate of ~0.07% for PbI_2, ~0.06% for FAI and ~0.05% for CsI. The much more homogeneous diagonal profiles of each individual material subsequently result in an increased material ratio homogeneity over the whole substrate. These results demonstrate the importance of careful vacuum chamber design for improved compositional uniformity of the deposited perovskite layer over the whole substrate area.

Unequally designed vacuum chambers with different lateral source to substrate distances as well as vertical heights of the substrate inevitably lead to changes in deposition homogeneity, impeding the transfer of process

recipes from one vacuum system to another. A potential solution to the resulting discrepancies between vacuum systems, demonstrated by the presented findings, could be the implementation of individually movable sources. In this way, each source can be adjusted for the individual material-dependent optimal position of the corresponding sublimation source. This would improve the homogeneity of each deposited material over the whole substrate area, and result in higher compositional uniformity of the resulting perovskite layer, facilitating the transfer of process recipes and reproducibility amongst vacuum chambers.

4.7 Summary

Reproducibility and repeatability of organic sublimation processes have been identified as major challenges of vapor-based fabrication processes of perovskite thin films, yet they remain critical for advancing the understanding and optimization of vapor-phase-deposited perovskite solar cells. In this chapter, a technological analysis of the sublimation behavior of FAI has been conducted to understand the impact of precursor particle size and sublimation crucible geometry on the effusion characteristics and deposition homogeneity (research question **I**).

Particle size distributions of commercial FAI precursor powders exhibit significant discrepancies across different fabrication batches when analyzed with analytical sieves of varying mesh sizes. Changes in the particle size distribution of the precursor material hinder consistent experimental conditions between sublimation processes. To understand the impact of different FAI particle sizes on the sublimation behavior, three main particle size fractions were defined (small, mid and big). Sublimation from conical crucibles on a non-rotating substrate using these defined particle size fractions revealed a strong impact of precursor particle size on the directionality of the emitted FAI vapor flux. Measured material thickness gradients on the substrate showed much more pronounced thickness gradients for small particle sizes. Thickness gradients from sublimation experiments with the mid and big particle size fractions showed decreasing material thickness gradients due to broader and more uniform emission profiles. These findings demonstrate that the particle size of the precursor material exerts a significant influence on the directionality of vapor flux emitted from conical crucibles during sublimation.

Comparison of the effusion characteristics of FAI from different sublimation crucible geometries (conical and cylindrical) further revealed a strong impact of the sublimation crucible geometry on the directionality of the emitted vapor flux. In contrast to conical crucibles, significantly broader emission profiles were observed when cylindrical crucibles were employed. Interestingly, for cylindrical geometries, similar material thickness gradients were recorded across all particle size fractions, indicating that the emission profile is largely independent of precursor particle size. As a result, cylindrical crucibles are the preferred geometry for achieving more reproducible and repeatable sublimation processes.

Additionally, the effusion characteristics of inorganic precursor materials, specifically PbI_2 and CsI, from cylindrical crucibles showed a material-dependent variation in sublimation behavior and deposition homogeneity. These findings indicate that the physical properties of the employed precursors significantly influence the vapor distribution during their sublimation. Material-dependent differences in the directionality of the emitted vapor flux affect the resulting material composition in multi-material deposition processes, where uniformity and stoichiometry are critical. Two simulated cases with differing vacuum chamber layouts underscore these findings and highlight the importance of tailored vacuum chamber design for sublimation processes to improve repeatable and reproducible processing.

5 Sequential Vapor Phase Deposition from Sublimation Crucibles for Perovskite Thin Films

Abstract

The rapid increase in reported PCEs of PSCs fabricated by sequential vapor phase deposition processes to more than 26% has resulted in a vast interest of industry and academia. In contrast to widely studied co-deposition fabrication processes, fundamental studies on sequential layer deposition processes are scarce, especially for the *p-i-n* architecture which is crucial for the integration into industrially relevant tandem architectures. In this chapter, the impact of different HTLs on the morphological and microstructural properties of pure $FAPbI_3$ perovskite thin films is investigated. Characterization of the fabricated perovskite thin films reveals a strong influence of the underlying substrate on the final layer quality. Further analysis indicates that the microstructural properties of the initially deposited inorganic layer are already strongly impacted by the substrate, significantly affecting the conversion reaction to the perovskite phase. Consequently, the possibility to manipulate these properties by adjusting process parameters such as deposition rate and substrate temperature is studied. Furthermore, different approaches of compositional engineering by using several inorganic precursor materials in one or multiple deposition steps are presented. Finally, first 2T perovskite/silicon TSCs are presented, serving as a proof-of-concept for the successful monolithic integration of sequentially deposited perovskite thin films in tandem architectures.

Acknowledgements and Contributions

Parts of this chapter review the published research article "*Sequential Evaporation of Inverted $FAPbI_3$ Perovskite Solar Cells – Impact of Substrate on Crystallization and Film Formation*" in *ACS Energy Letters*, 2025 (DOI: 10.1021/acsenergylett.4c03315) by Alexander Diercks, Julian Petry, Thomas Feeney, Roja Singh, Thongan Zhao, Hang Hu, Yang Li, Ulrich W. Paetzold, and Paul Fassl. Some figures in this chapter were adapted with permission from *American Chemical Society*. The contributions of all authors according to the CRediT system are listed in Table A.3.

5.1 Introdution

Reported PCEs of vapor-phase-deposited PSCs have been lacking behind those of their solution-processed counterparts (Figure 1.1) for a long time. Recently, sequentially deposited PSCs have shown a rapid increase in reported PCEs in the last few years, reaching over 26% in 2024, not only overtaking those of co-deposited ones, but also closing the gap to solution-processed PSCs.[43] This steep increase represents astonishing progress, considering that less than 2% of all publications on PSCs report on vapor phase deposition.[12] The combination of reported PCEs with the general advantages and properties of vapor phase deposition processes proves the great potential of sequential layer deposition for successful transition to industrial-scale fabrication and commercialization.[11, 46]

Related to all publications on vapor phase deposition, most research in this field focuses on co-deposition processes, with only 21 (*updated until 17.10.2025*) publications reporting on sequential layer deposition methods (Table A.8). Figure 5.1 shows the reported champion PCEs of the corresponding publications. First reports on sequential layer deposition reach back to 2014 by Chen *et al.*, reaching decent PCEs of 15.4%, using $PbCl_2$ and MAI as precursor materials in their process.[130] In 2020, Tavakoli *et al.*, reported the first sequentially deposited PSCs with PCEs of more than 20% for a pure $MAPbI_3$ perovskite composition, on par with PCEs of co-deposited PSCs at that time.[103] A year later, Feng *et al.* showed for the first time PSCs with a MA-free $FACsPbI_3$ perovskite absorber, reaching PCEs of 21% on small areas and 14.6% on 10 cm^2 modules.[100] More recently, Yi *et al.* proved the great potential of sequential layer deposition by reporting PCEs of 24.4% in 2023 and finally PCEs of over 26% in 2024, the highest reported PCE for vapor-phase-deposited PSCs.[43, 131]

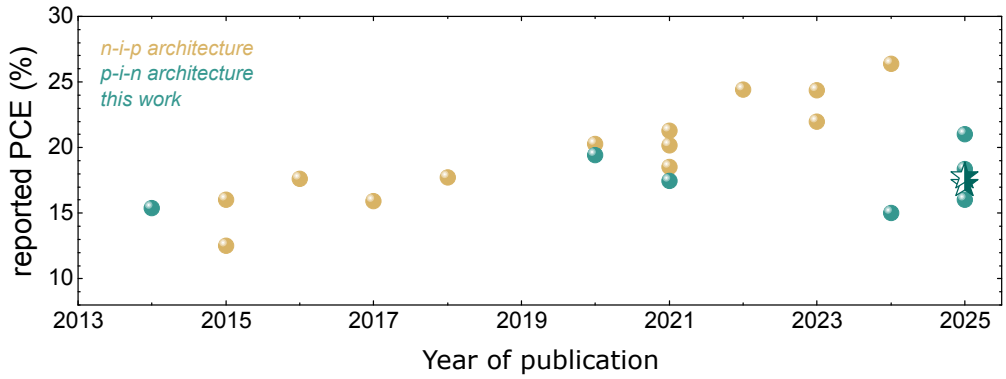

Figure 5.1: Overview of reported champion power conversion efficiencies (PCEs) of all sequential layer deposition processes from literature (*updated until 17.10.2025*). The stars represent the champion PCEs achieved in this work.

The majority of publications on sequential layer deposition processes focus on narrow bandgap (NBG) perovskite compositions, mainly $MAPbI_3$ and $FACsPbI_{3-x}Cl_x$ (Table A.8).[43, 100–103, 111, 113, 115, 116, 122, 126–128, 130–137] Various approaches to sequential layer deposition processes are used, from sequential deposition of single precursors to multilayer approaches with repeating sequences, as well as co-deposition of inorganic materials followed by the subsequent deposition of organic materials (as already described in chapter 2).[100, 103, 113, 132, 134, 135, 138, 139] Most studies on vacuum-based sequential layer deposition processes report on PSCs in the *n-i-p* architecture,[100, 103, 111, 113, 115, 116, 122, 131–133, 136] leaving the *p-i-n* architecture highly underrepresented.[102, 103, 126, 128, 130, 135, 137] This is despite it possesses various advantages regarding future applications, such as facile integration into monolithic tandem architectures and higher operational stability.[140–143] Furthermore, de-coupling of the deposition of all precursor materials into several subsequent deposition steps promises several advantages: (i) the possibility to use different vacuum chambers for each precursor material, potentially leading to a reduction in cross-contamination and

therefore higher reproducibility, and (ii) the potential for industrially relevant in-line processing using linear evaporators.[11, 40]

As mentioned, compared to the more commonly studied co-deposition process, research on sequential layer deposition is scarce. Especially, in-depth understanding of crystallization dynamics, impact of deposition parameters and substrate-dependent growth of the deposited perovskite layer are not yet studied. A key difference between sequential layer deposition and co-deposition processes lies in the conversion and crystallization step of the perovskite phase.[101] The simultaneous deposition of all precursors during co-deposition processes leads to an immediate formation of perovskite nano crystallites at the interface to the substrate during the deposition.[58, 144] Conversely, in sequential layer deposition processes, conversion to the perovskite phase happens at the interface of the sequentially deposited materials in a necessary subsequent annealing step. This annealing step induces intermixing of the deposited components by diffusion and leads to conversion and crystallization to the perovskite phase.

This chapter focuses on understanding the impact of different hole transport layers and deposition parameters on the formation of pure $FAPbI_3$ perovskite thin films fabricated *via* the subsequent deposition of PbI_2 and FAI (research question **II**). In-depth analysis of the morphology and microstructure of the firstly deposited PbI_2 layer and the resulting impact on the conversion to the $FAPbI_3$ perovskite phase is conducted using scanning electron microscopy (SEM), atomic force microscopy (AFM) and grazing-incident wide-angle X-ray scattering (GIWAXS). Significant differences in the growth and crystal orientation of PbI_2 are detected, which consequently impact the conversion and final film quality of the perovskite phase. Coupling these findings with different FAI to PbI_2 ratios and their resulting solar cell performance, an unexpected correlation between X-ray diffraction (XRD) pattern and PCE is found, which can serve as a guideline plot for future process optimizations. Variation in process parameters of the PbI_2 deposition step (deposition rate and substrate temperature during deposition) allow for manipulation of the morphological and microstructural PbI_2 film properties.

Furthermore, the successful incorporation of different cesium halide precursors (CsI, CsBr and CsCl) as well as of lead bromide ($PbBr_2$) into the perovskite crystal structure is shown by adding these components to the inorganic scaffold, proving the ease of compositional engineering *via* sequential layer deposition for the fabrication of WBG PSCs (research question **III**). Finally, for the first time, prototypes of monolithic perovskite/silicon TSCs using a sequentially deposited perovskite top cell are presented.

5.2 Fabrication of Formamidinium Lead Triiodide Perovskite Solar Cells *via* a Two-Step Sublimation Process

The employed 2-step deposition process for the fabrication of $FAPbI_3$ perovskite thin films is displayed in Figure 5.2. The first deposition step comprises the sublimation of the inorganic material (PbI_2), followed by the subsequent deposition of the organic material (FAI). After the deposition of FAI, deposited layers are placed on a hotplate at 170 °C for 15 minutes, similar to reported annealing conditions for sequential vapor phase deposition processes.[116, 122, 126, 131, 138, 139] During this annealing step, the FAI layer diffuses into the PbI_2 scaffold and reacts to the perovskite phase.

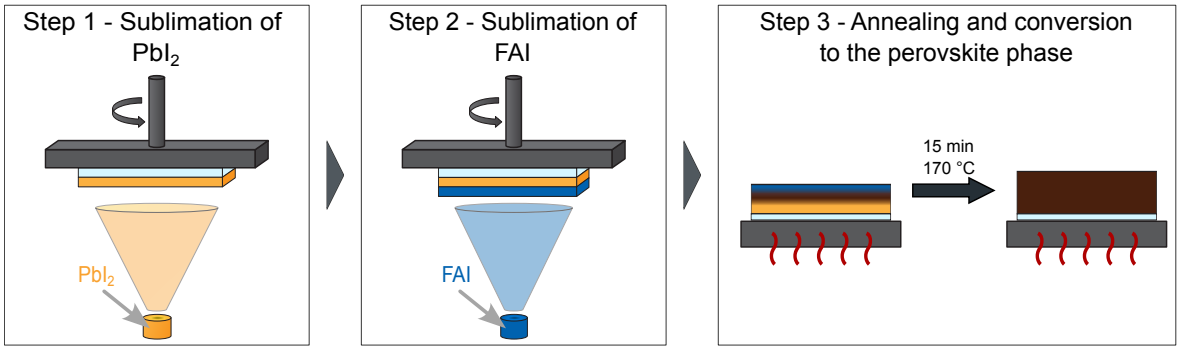

Figure 5.2: Schematic of the employed sequential layer deposition process for the fabrication of formamidinium lead triiodide ($FAPbI_3$) perovskite thin films with an additional annealing step, with Step 1 = sublimation of lead iodide (PbI_2), Step 2 = sublimation of formamidinium iodide (FAI) and Step 3 = annealing and conversion to the perovskite phase.

In two-step fabrication processes, the annealing step is essential for converting the sequentially deposited precursor materials into the perovskite structure. This applies to purely dry-dry processes as well as to hybrid (dry-solution) and fully solution-based two-step fabrication approaches. It was found that the annealing step in two-step processes is preferably carried out in ambient air with a relative humidity (r.H.) around 30% to achieve improved device performance. Numerous studies in the literature on solvent-based or hybrid fabrication processes report a beneficial effect of humidity on the perovskite film quality.[116, 145–149] In the case of sequential vapor-phase deposition, Nambiar *et al.* demonstrated that humidity promotes interdiffusion between the inorganic and organic precursors. Annealing in a humid atmosphere resulted in a perovskite absorber layer with higher crystallinity and larger grain sizes.[127]

A comparison of annealing in N_2 atmosphere *vs.* ambient air with a r.H. of ~30% was conducted to investigate the impact on PSC device performance and perovskite thin film quality. Similar to the findings in literature, annealing in ambient conditions leads to a significant improvement in device performance of the sequentially vapor-phase-deposited $FAPbI_3$ PSCs (Figure 5.3a).

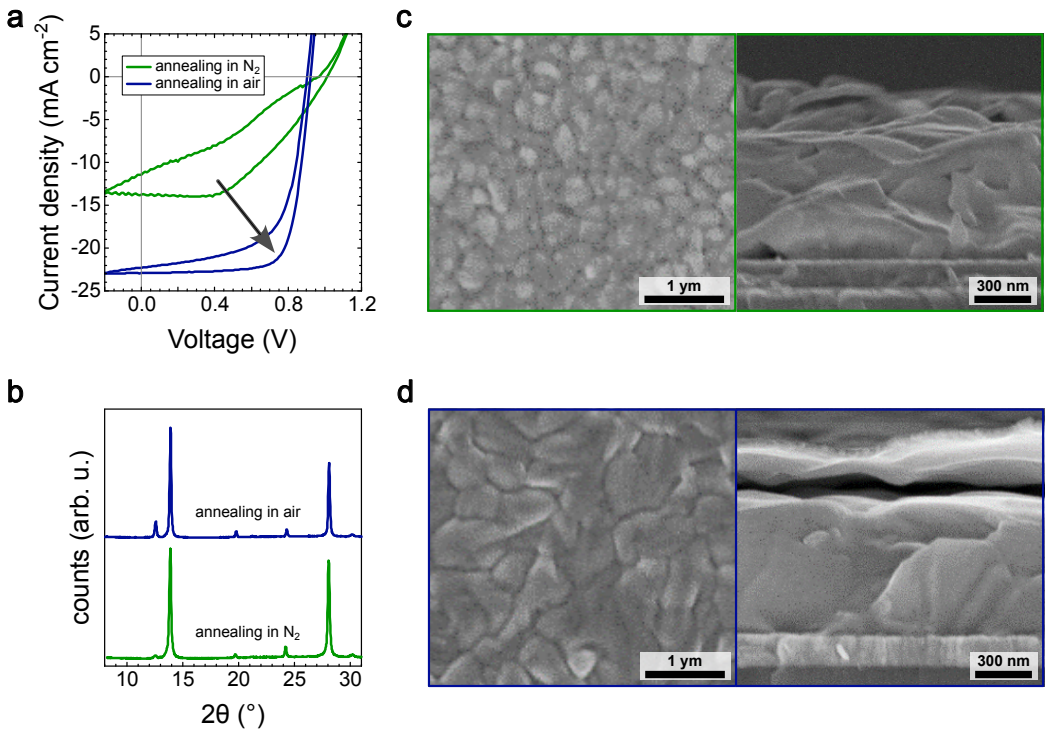

Figure 5.3: Analysis of annealing conditions for sequentially deposited $FAPbI_3$ perovskite solar cells (PSCs). **a** Current-voltage (*J-V*) characteristics of fabricated $FAPbI_3$ PSCs in N_2-atmosphere and in air with a relative humidity (r.H.) ~30%. **b** X-ray diffraction (XRD) analysis of corresponding perovskite thin films. **c/d** Surface and cross-sectional scanning electron microscopy (SEM) images of corresponding perovskite thin films.

XRD measurements reveal that both annealing conditions lead to a conversion to the perovskite phase, with little residual PbI_2 (Figure 5.3b). However, annealing in N_2 atmosphere leads to a broader peak signal, indicating a lower grade of crystallinity. Comparing the perovskite morphology of both films show much larger grain sizes for in-air annealed perovskite thin films, as well as a less disoriented cross-section of the perovskite layers (Figure 5.3c/d). These findings are in line with studies in literature, showing the beneficial effect of in-air annealing for two-step vapor-phase-deposited perovskite thin films.

5.3 Substrate-Dependent Formation of Formamidinium Lead Triiodide Perovskite Thin Films

The focus of this section lies on the understanding of substrate-dependent crystallization and film formation of sequentially deposited $FAPbI_3$ perovskite thin films on different HTLs and the resulting impact on the performance of the final PSCs. First, the effect of different HTLs on the primarily deposited PbI_2 layer is investigated, followed by a detailed analysis of the resulting perovskite layer quality and final PSC performance. For this, five different HTLs are chosen: (i) vacuum-processed MeO-2PACz (from now on referred to as MeO), (ii) vacuum-processed 2PACz, (iii) vacuum-processed TaTm, (iv) sputtered NiO_x and (v) solution-processed PTAA.

5.3.1 Morphological and Microstructural Analysis of Lead Iodide Layer

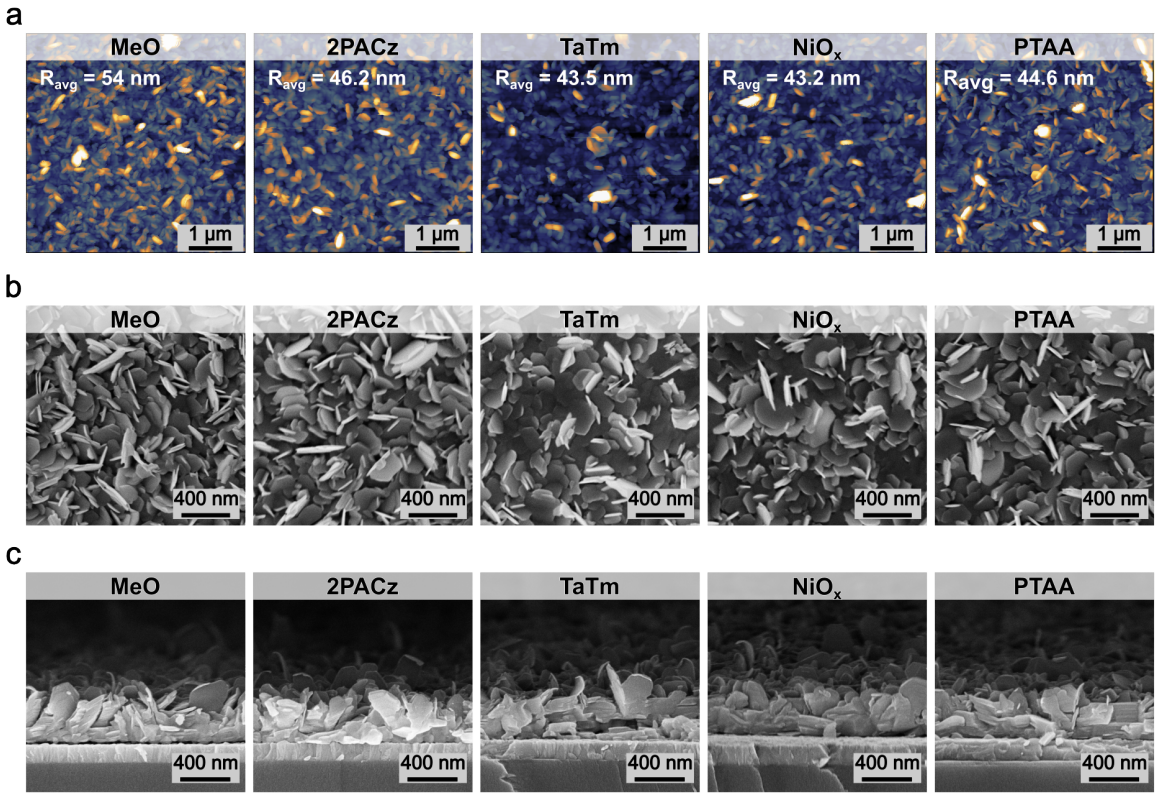

Figure 5.4: **a** Atomic force microscopy analysis of deposited lead iodide (PbI_2) layers on five different hole transport layers (HTLs) with average surface roughness values. **b** Scanning electron microscopy (SEM) surface images of corresponding PbI_2 layers on the five different HTLs. **c** Corresponding SEM cross section images of the PbI_2 layers. Adapted with permission from American Chemical Society.[101]

In order to investigate the effect of different underlying substrates on the vacuum deposited PbI_2 layer, the morphological and microstructural analysis was conducted. Figure 5.4 shows the morphological analysis of the deposited PbI_2 layers using AFM and SEM. On all five HTLs, the typical platelet structure for vacuum-deposited PbI_2 is visible on the images from AFM (Figure 5.4a) as well as surface and cross-sectional images from SEM (Figure 5.4b/c, respectively). AFM measurements reveal slight variations of the average surface roughness (R_{avg}) between all films, with values reaching from R_{avg}= 43.2 nm in case of NiO_x to R_{avg} = 54 nm in case of MeO (Figure 5.4a). Increased surface roughness directly translates to a larger surface area, which is in contact with the subsequently deposited FAI. This increase in contact area can impact the initial conversion reaction to the perovskite phase during annealing, resulting in different perovskite layer properties. Additionally, the higher surface roughness potentially leads to a more porous film, affecting the interdiffusion of the organic cations into the firstly deposited inorganic layer. While this effect has been observed for dry-wet hybrid two-step processes,[148, 150] the impact in dry-dry two-step processes has not yet been understood. SEM images only show slight changes regarding the morphology of the deposited PbI_2 thin film amongst the different HTLs. However, the orientation of the typical PbI_2 platelets seems to change slightly depending on the underlying HTL. PbI_2 platelets on MeO and 2PACz appear to be more vertically orientated, which could explain the slightly higher R_{avg}, while on NiO_x, TaTm and PTAA more horizontally orientated platelets are visible (Figure 5.4b/c). These changes in morphology prove, that morphological properties of vacuum-deposited PbI_2 thin films are impacted by the underlying substrate, which potentially affects the conversion to the final perovskite phase after deposition of FAI in the second deposition step.

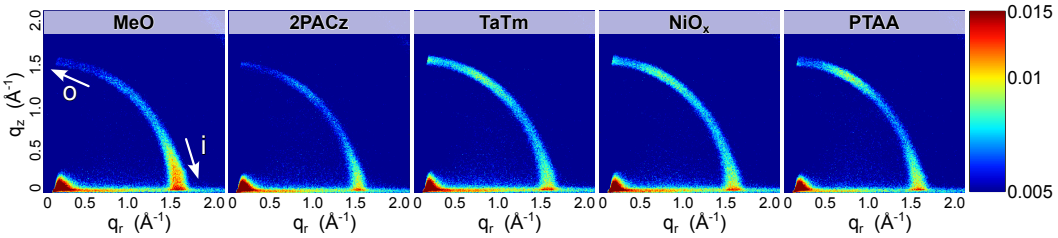

Figure 5.5: Grazing-incident X-ray scattering (GIWAXS) measurements of lead iodide (PbI_2) layers on the five different hole transport layers (HTLs). "**o**" and "**i**" denote out-of-plane and in-plane orientation of the crystallites. Adapted with permission from American Chemical Society.[101]

GIWAXS measurements of the vacuum-deposited PbI_2 thin films additionally confirm a change in microstructural properties depending on the underlying substrate. GIWAXS analysis provides insights on crystal growth orientations and overall degree of crystallinity.[151] Figure 5.5 shows the GIWAXS pattern of the PbI_2 thin films on the different HTLs. On all HTLs, an intensity maximum in an in-plane orientation (denoted as "**i**") is revealed, corresponding to a perpendicular growth of the (001)-plane of the deposited PbI_2 crystallites on the substrate. PbI_2 layers on TaTm, NiO_x and PTAA furthermore show a second preferred orientation in an out-of-plane orientation (denoted as "**o**"), with an angle of 60-70° to the surface of the substrate. This second orientation maximum cannot be found in PbI_2 layers deposited on MeO and 2PACz, also displayed in the corresponding pole figures with integrated intensity plotted over the azimuth angle in Figure A.6. Changes in the crystal orientation of the PbI_2 layer directly impact interdiffusion of organic cations and subsequent conversion reaction to the perovskite phase during annealing. This effect has been shown not only for hybrid dry-wet two-step processes, but also for dry-dry two-step processes.[152–156] Yi *et al.* reported the beneficial effect of a highly out-of-plane orientated vacuum-processed $Pb(I:Cl)_2$ mixture on the quality of their sequentially vacuum-deposited perovskite thin film.[116]

Substrate-dependent growth of vacuum-deposited PbI_2 thin films, and the resulting impact on conversion to the perovskite phase for sequentially deposited perovskite thin films has not been studied yet. The presented results prove that the underlying substrates strongly impact the morphological and microstructural properties of vacuum-deposited PbI_2 layers, showing changes in preferred orientation of PbI_2 crystallites, grain size of the PbI_2 platelets and overall average film surface roughness.

5.3.2 Impact of Underlying Substrate on Conversion to Perovskite Phase

Conversion to the perovskite phase in sequential vapor phase deposition processes starts at the interface of the subsequently deposited layers during annealing. Changes in the morphology and microstructural properties of the firstly deposited PbI_2 layer due to different underlying HTLs can influence the interdiffusion of the secondly deposited FAI into this layer and therefore impact the conversion reaction to the final perovskite phase. To investigate the effect of underlying substrates on the conversion to the perovskite phase, the fabricated perovskite thin films after annealing were analyzed using SEM and XRD.

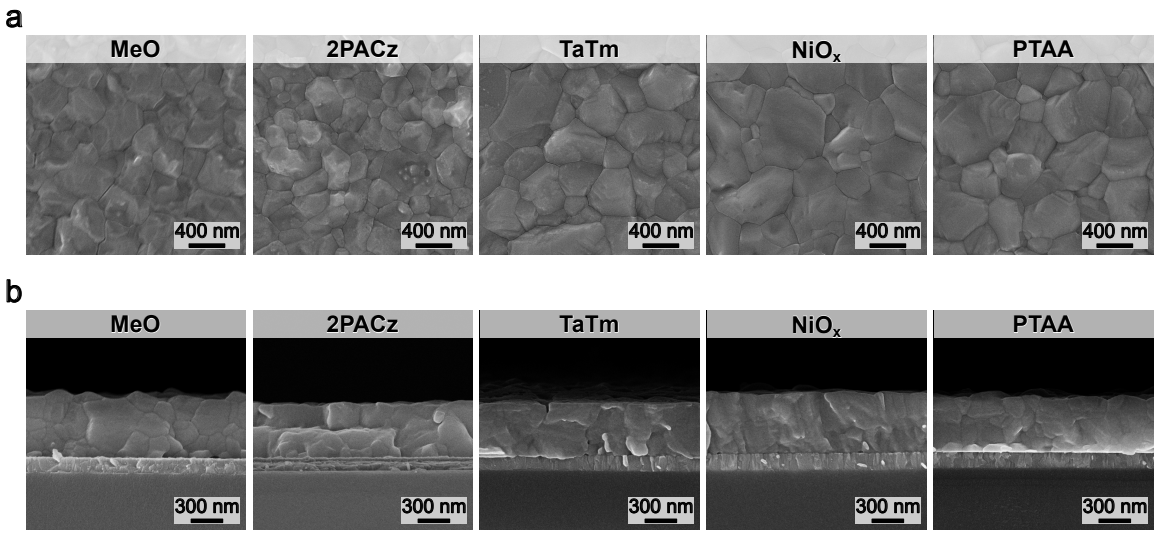

Figure 5.6: Top view (**a**) and cross-sectional (**b**) scanning electron microscopy (SEM) images of perovskite thin films on different hole transport layers (HTLs) (MeO, 2PACz, TaTm, NiOx, PTAA). Adapted with permission from American Chemical Society.[101]

Figure 5.6a/b shows top view and cross-section SEM images of the perovskite thin films on the five different employed HTLs (MeO, 2PACz, TaTm, NiO_x and PTAA). Substantial changes in grain size are detected amongst the different substrates. Films on MeO and 2PACz show comparably smaller grains, compared to films on TaTm, NiO_x and PTAA (Figure 5.6a). Grain size analysis reveals an average grain area of ~0.075 μm^2 for films on MeO, and ~0.13 μm^2 on PTAA (Figure A.7). Furthermore, cross-sectional images reveal a slightly more disoriented growth of the perovskite grains on MeO and 2PACz, while films on TaTm, NiO_x and PTAA show a more oriented, columnar growth. Coupling these findings to the earlier found differences in morphology and microstructure of the corresponding PbI_2 layers, a correlation can be drawn. PbI_2 layers on MeO and 2PACz both showed only one preferred orientation in a more in-plane orientation, while PbI_2 layers on TaTm, NiO_x and PTAA exhibited a second preferred orientation in an out-of-plane orientation. It appears that a mainly in-plane orientation of the PbI_2 layer leads to rather small and disoriented perovskite grains, and a more out-of-plane PbI_2 favors larger perovskite grains.

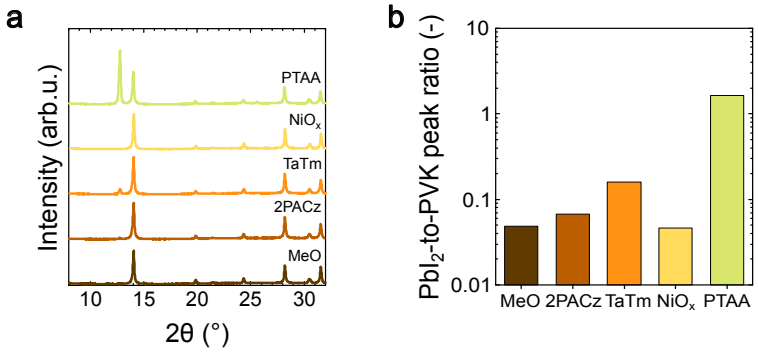

Figure 5.7: a X-ray diffraction (XRD) pattern of fabricated perovskite thin films on different hole transport layers (HTLs). **b** Corresponding (001)-PbI_2-to-(100)-perovskite (PbI_2-to-PVK) peak ratios. Adapted with permission from American Chemical Society.[101]

XRD analysis further shows strong deviations in the obtained reflection pattern (Figure 5.7a). More specifically, the peak intensity ratio of the (001)-PbI_2 to (100)-perovskite (PbI_2-to-PVK peak ratio) amongst the different perovskite thin films changes substantially. While films on MeO, 2PACz, TaTm and NiO_x exhibit low (001)-PbI_2 peak intensities, with PbI_2-to-PVK peak ratios of 0.049, 0.067, 0.16 and 0.046, respectively, the perovskite thin

film on PTAA shows a PbI_2-to-PVK peak ratio of 1.638. A change in XRD pattern indicates different crystallinity of the perovskite phase, most likely due to different conversion reaction. Several reports in the literature observed a beneficial effect of residual lead iodide found by XRD analysis on the performance of the final PSCs.[157, 158]

5.3.3 Performance of Formamidinium Lead Triiodide Perovskite Solar Cells

The growth of perovskite thin films is impacted by the underlying substrate, specifically the used HTL, and results in changes of the perovskite layer quality. Any change in the quality of the perovskite layer directly affects the performance of the corresponding PSCs. To investigate the impact of different HTLs and resulting perovskite thin films on the photovoltaic performance, PSCs in the *p-i-n* architecture were fabricated using the layer stack [glass/ITO/HTL/$FAPbI_3$/C_{60}/ALD-SnO_x/Ag] (Figure 5.8a), employing the earlier introduced HTLs (MeO, 2PACz, TaTm, NiO_x and PTAA).

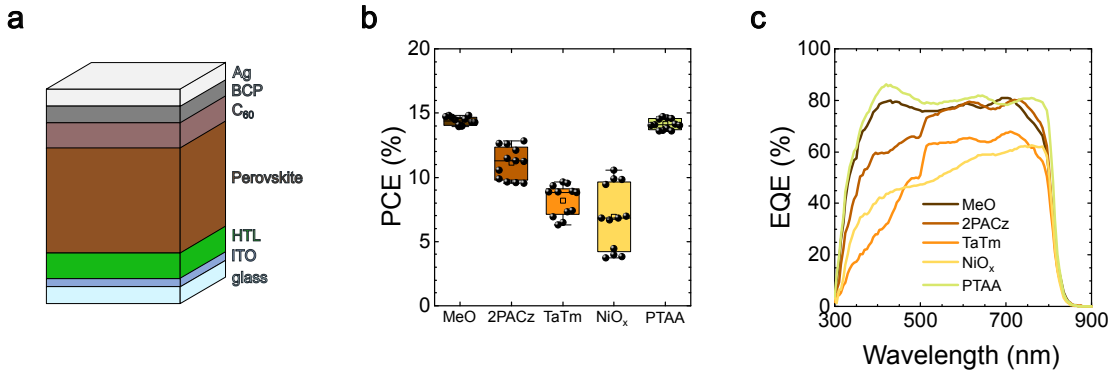

Figure 5.8: a Layerstack of perovskite solar cells (PSCs) in p-i-n architecture using different hole transport layers (HTLs). **b** Power conversion efficiency (PCE) boxplot statistics of fabricated PSCs with different HTLs. **c** External quantum efficiency (EQE) measurements of best-performing PSCs on different HTLs. Adapted with permission from American Chemical Society.[101]

When comparing the resulting PCE statistics of the fabricated PSCs, significant differences are visible (Figure 5.8b and Figure A.8). Interestingly, PSCs on MeO and PTAA yield similar performance, despite showing the greatest differences in the corresponding PbI_2-to-PVK peak ratios (Figure 5.7b). This indicates that the measured 2D XRD pattern do not serve as a reliable indicator for comparable performance of complete PSCs. EQE measurements show great discrepancies between all HTLs. PSCs on MeO and PTAA yield an average EQE of ~80% over the whole wavelength range, in line with the better overall performance of the PSCs (Figure 5.8c). 2PACz, TaTm and NiO_x show poor EQE signals, especially in the shorter wavelength region. All configurations show a similar bandgap, extracted from EQE measurements. A direct comparison of the *J-V* measurements of the best-performing PSCs on each HTL, together with corresponding MPP-tracking are displayed in Figure A.9.

As demonstrated in Section 5.3, the underlying substrate plays a critical role in growth of the firstly deposited PbI_2 layer, and conversion to the final perovskite phase, impacting the morphological and crystallographic properties of the final perovskite thin film. To analyze how the degree of conversion and final PSC performance are correlated on each HTL, deposited FAI-to-PbI_2 layer thickness ratios were systematically varied.

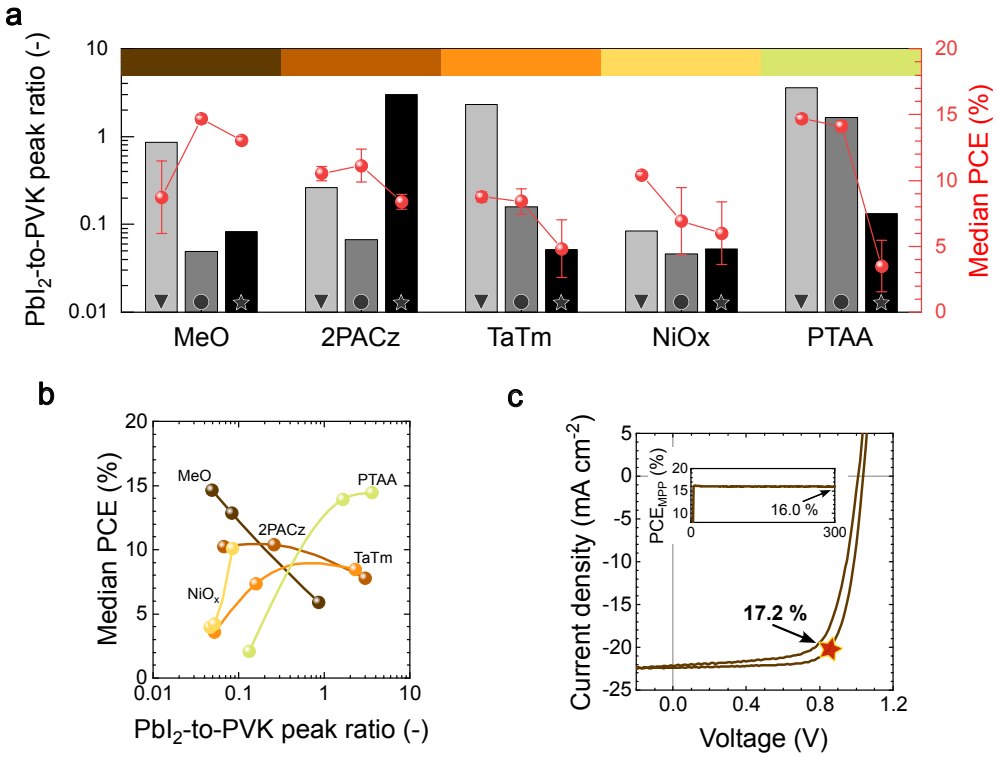

Figure 5.9: **a** (001)-PbI_2-to-(100)-perovskite peak ratio evolution from X-ray diffraction (XRD) pattern for different formamidinium iodide (FAI) to lead iodide (PbI_2) thickness ratios (increasing from left to right: -6%, standard and +6% - marked with triangles, circles and stars, respectively) with corresponding median power conversion efficiencies (PCEs). Standard refers to film thicknesses for FAI and PbI_2 of 280 nm and 300 nm respectively. **b** Guideline plot for maximum median PCE of formamidinium lead triiodide ($FAPbI_3$) perovskite solar cells (PSCs) on different hole transport layers (HTLs) depending on (001)-PbI_2-to-(100)-perovskite (PbI_2-to-PVK) peak ratio from XRD. **c** Current-voltage (*J-V*) characteristics and maximum power point (MPP) tracking of the champion PSC on MeO as HTL. Adapted with permission from American Chemical Society.[101]

By adjusting the deposited FAI layer thickness (standard = 280 nm (circles), -6% (triangles) and +6% (stars)) while keeping the deposited PbI_2 layer thickness constant at 300 nm, the composition of the final perovskite film was changed. Figure 5.9a shows the measured PbI_2-to-PVK peak ratio of the fabricated perovskite thin films, as well as the resulting median PCEs of the final PSCs on each of the five HTLs (see Figure A.10 and Figure A.11 for corresponding XRD pattern and full statistics). Decreasing the amount of deposited FAI (-6%) leads to an expected increase in the PbI_2-to-PVK peak ratio for all studied HTLs. However, when increasing the amount of deposited FAI (+6%), no consistent trend amongst all HTLs is observed. Perovskite thin films deposited on MeO and 2PACz show an increased PbI_2-to-PVK peak ratio, which stands in stark contrast to the expectation. Conversely, perovskite films on TaTm, NiO_x and PTAA show the expected further reduction in PbI_2-to-PVK peak ratio. Coupling the measured PbI_2-to-PVK peak ratios to the achieved median PCEs of the final PSCs reveals in a direct correlation of PCE to the previously observed differences in preferred orientations of the firstly deposited PbI_2 layer. PSCs on MeO and 2PACz, both HTLs with predominantly in-plane orientated PbI_2 crystals, achieve higher PCEs for lower PbI_2-to-PVK peak ratios, while in case for TaTm, NiO_x and PTAA, with a second preferred orientation of PbI_2, show an opposite trend. Plotting median PCEs over the corresponding PbI_2-to-PVK peak ratios a guideline plot with general trends for sequentially deposited PSCs on different HTLs with corresponding preferred regimes for optimum performance is obtained (Figure 5.9b). With the described vacuum-based two-step process, champion PCEs of 17.2% are achieved, the highest reported PCE for fully vacuum-processed pure FAPI PSCs in the *p-i-n* architecture so far (Figure 5.9c).

5.4 Variation of Lead Iodide Deposition Parameters

The previous results show that the growth and resulting quality of the perovskite layer is strongly influenced by the underlying PbI_2 layer, which also affects the performance of the solar cells.

This raises the question of whether it is possible to deliberately influence the morphological properties of the firstly deposited PbI_2 layer by adjusting the process parameters during its deposition. Deposition rate and substrate temperature during the process are two process parameters that are known to influence the perovskite layer quality in co-deposition processes.[59, 110] Corresponding studies for sequential layer deposition processes are not found yet. Hence, a variation of these two parameters is conducted in this chapter.

5.4.1 Impact on Growth of Lead Iodide Layer

Direct manipulation of the morphological and microstructural properties of the deposited PbI_2 layer by varying process parameters (deposition rate and substrate temperature) is studied next. For the variation in PbI_2 deposition rate (0.1 $Å s^{-1}$, 0.5 $Å s^{-1}$, 1.0 $Å s^{-1}$ and 2.0 $Å s^{-1}$) the substrate temperature was held constant at 20 °C, when varying the substrate temperature (05 °C, 20 °C, 45 °C and 70 °C) the PbI_2 deposition rate was held constant at 1.0 $Å s^{-1}$. Furthermore, PbI_2 layer thicknesses were kept at 300 nm and deposited on a vacuum-processed MeO-2PACz HTL, since it yielded best results.

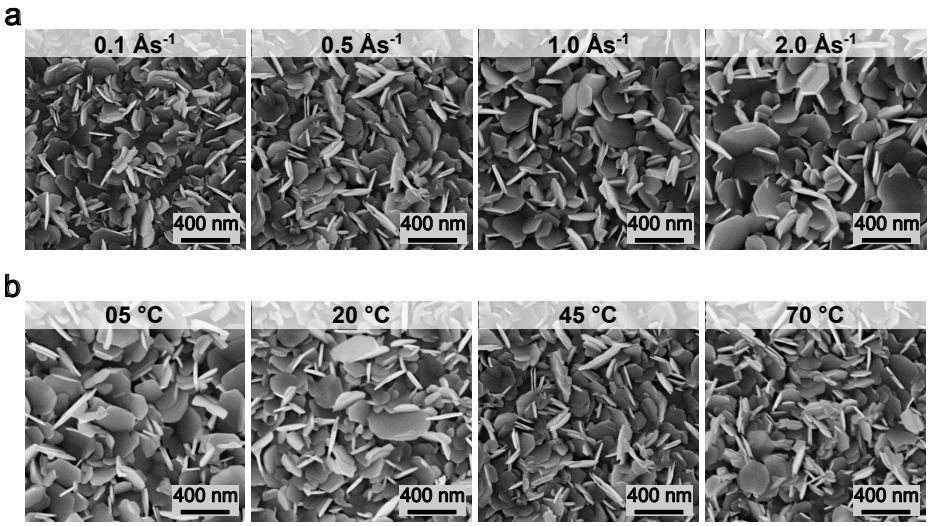

Figure 5.10: Top view scanning electron microscopy (SEM) images of deposited lead iodide (PbI_2) layers for varying process parameters. **a** Different PbI_2 deposition rates (0.1 $Å s^{-1}$, 0.5 $Å^{-1}$, 1.0 $Å s^{-1}$ and 2.0 $Å s^{-1}$) during process with constant substrate temperature of 20 °C. **b** Different substrate temperatures (05 °C, 20 °C, 45 °C and 70 °C) during process at constant deposition rate of 1.0 $Å s^{-1}$. Adapted with permission from American Chemical Society.[101]

Figure 5.10 shows the top view SEM images of both experimental series. Both parameters, deposition rate and substrate temperature show an effect on the PbI_2 platelet size. When depositing at higher deposition rates, a gradual increase in PbI_2 platelet size is visible (Figure 5.10a). Variation in substrate temperature shows an opposite effect. Higher substrate temperatures lead to smaller PbI_2 platelet sizes, while lower substrate temperatures show large PbI_2 platelets (Figure 5.10b). This proves the possibility to manipulate morphological properties of vacuum-deposited PbI_2 not only by the underlying substrate, but also through adjusting process parameters during the deposition (deposition rate and substrate temperature).

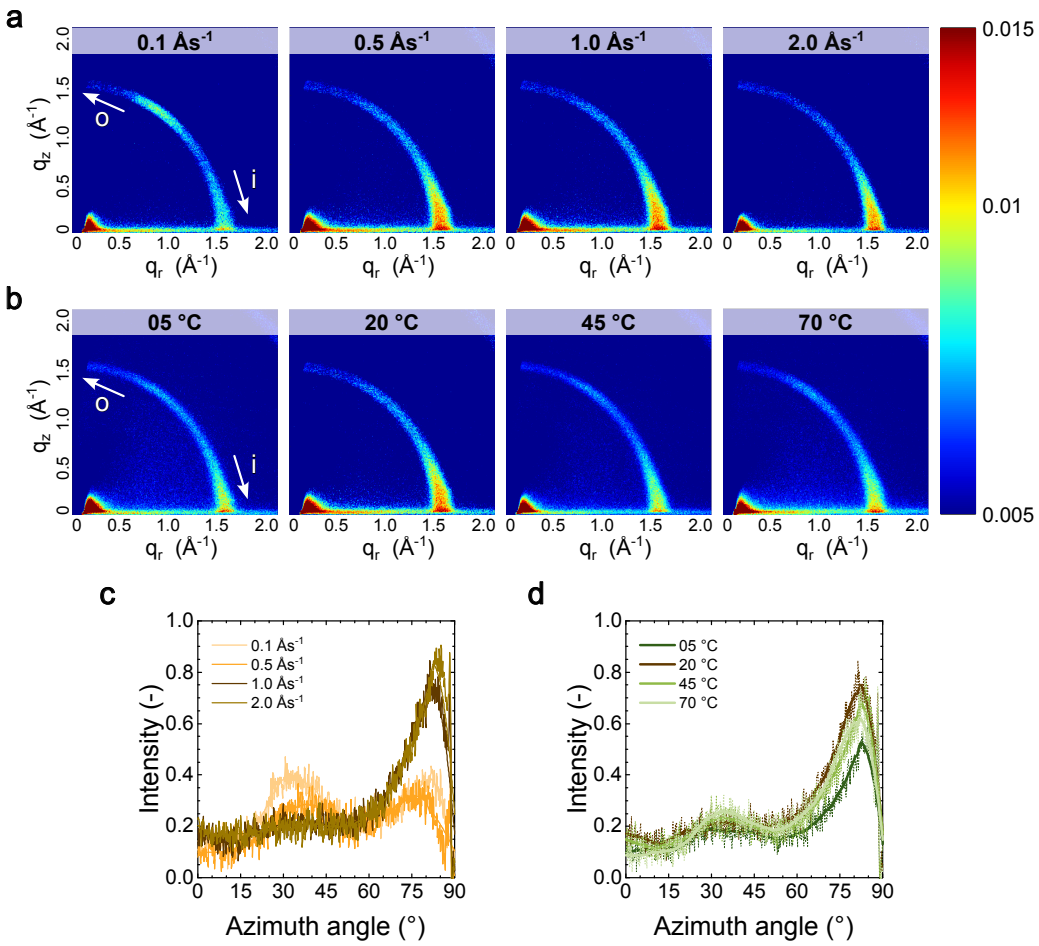

Figure 5.11: Grazing-incident X-ray scattering (GIWAXS) measurements of deposited lead iodide (PbI_2) layers processed with varying process parameters. **a** Different PbI_2 deposition rates (0.1 $Å s^{-1}$, 0.5 $Å s^{-1}$, 1.0 $Å s^{-1}$ and 2.0 $Å s^{-1}$) during process with constant substrate temperature of 20 °C. **b** Different substrate temperatures (05 °C, 20 °C, 45 °C and 70 °C) during process at constant deposition rate of 1.0 $Å s^{-1}$. **c/d** Pole figures from corresponding GIWAXS measurements of deposited PbI_2 layers at different deposition rates and substrate temperatures, respectively. Adapted with permission from American Chemical Society.[101]

Additional GIWAXS measurements of the deposited PbI_2 films further show how the orientation of the PbI_2 crystallites is impacted by changing deposition rates and substrate temperatures (Figure 5.11). All films show an orientation maximum in the in-plane orientation, as already previously observed. While a variation in substrate temperature doesn't show an effect on the preferred orientation of the PbI_2 crystal growth, (Figure 5.11b) slower deposition rates impact the crystal orientation. In case for deposition at 0.1 $Å s^{-1}$, a second orientation maximum in a more out-of-plane orientation, with similar angles of 60-70° to the substrate, is detected. Higher deposition rates on the other hand only show the previously observed orientation maximum perpendicular to the surface of the substrate (Figure 5.11a). A direct comparison of the crystal orientations depending on each of the varied process parameters, deposition rate and substrate temperature, is shown in the corresponding pole figures Figure 5.11c and Figure 5.11d, respectively.

These findings show the possibility to manipulate not only morphological, but also microstructural properties of vacuum-deposited PbI_2 layers through variation in process parameters, namely deposition rate and substrate temperature.

5.4.2 Effect on Conversion to Perovskite Phase

Next, to confirm the previously found impact of different morphological and microstructural properties of the PbI_2 layer on the perovskite formation, the differently processed PbI_2 layers are used to fabricate perovskite thin films. The resulting perovskite thin films are compared using surface and cross-sectional SEM images, as well as XRD, to analyze the conversion to perovskite phase.

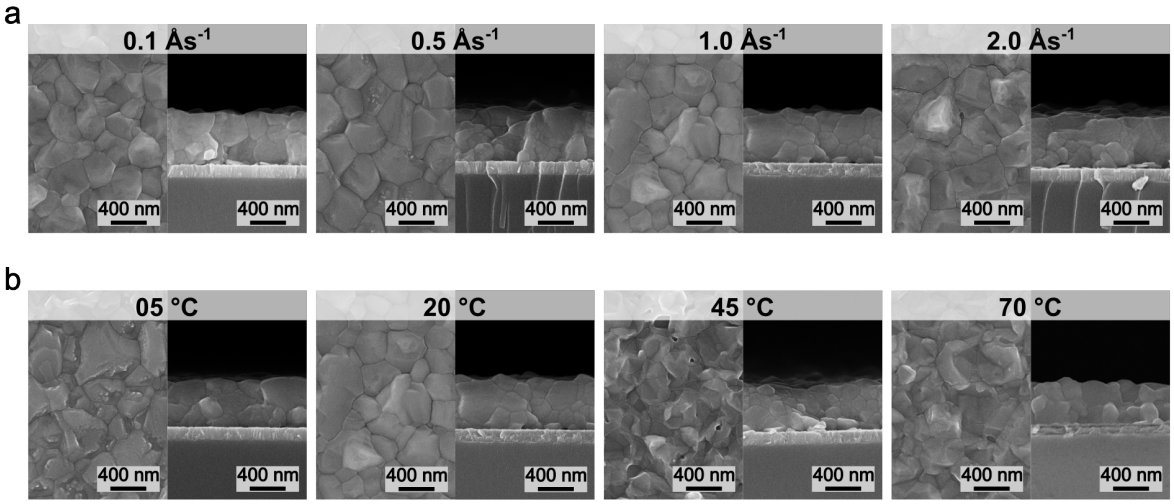

Figure 5.12: Top view and cross-sectional scanning electron microscopy images of deposited PbI_2 layers for varying process parameters. **a** Different PbI_2 deposition rates (0.1 $Å s^{-1}$, 0.5 $Å s^{-1}$, 1.0 $Å s^{-1}$ and 2.0 $Å s^{-1}$) during processes with constant substrate temperature of 20 °C. **b** Varying substrate temperatures (5 °C, 20 °C, 45 °C and 70 °C) with a constant deposition rate of 0.1 $Å s^{-1}$. All images have the same scale bar. Adapted with permission from American Chemical Society.[101]

SEM analysis of the fabricated FAPI thin films using PbI_2 layers deposited with varying process parameters is shown in Figure 5.12. While there are no detectable differences in the top-view SEM images when changing the PbI_2 deposition rate, slight changes in the cross-sectional images are visible (Figure 5.12a). It appears that PbI_2 layers deposited at lower deposition rates (0.1 $Å s^{-1}$ and 0.5 $Å s^{-1}$) lead to more less oriented, smaller vertical grains compared to the reference at 1.0 $Å s^{-1}$. A PbI_2 deposition rate of 2.0 $Å s^{-1}$ shows a very similar grain profile compared to the reference. Additionally, all layers show smaller grains close to the bottom (HTL/perovskite) interface, and larger grains towards the top interface (perovskite/ETL), which could be a result of the initial crystallization reaction starting at the PbI_2 and FAI interface. When comparing the perovskite layer with PbI_2 layers deposited at different substrate temperatures, distinct changes in morphology and grain profiles are detected (Figure 5.12b). Top-view SEM images reveal that higher substrate temperatures (45 °C and 70 °C) during the PbI_2 deposition step lead to smaller, more disoriented perovskite grains (Figure 5.12a), while a lower substrate temperature (5 °C) shows the largest perovskite grains. Cross-sectional SEM images show a similar trend. Largest grains are detected for the perovskite film grown on PbI_2 deposited on a cooled substrate, while higher substrate temperatures during the PbI_2 deposition lead to more smaller perovskite grains. Similar to the perovskite films displayed in Figure 5.12a, all perovskite films show larger perovskite grain structures closer to the top and smaller perovskite grain sizes at the bottom interface.

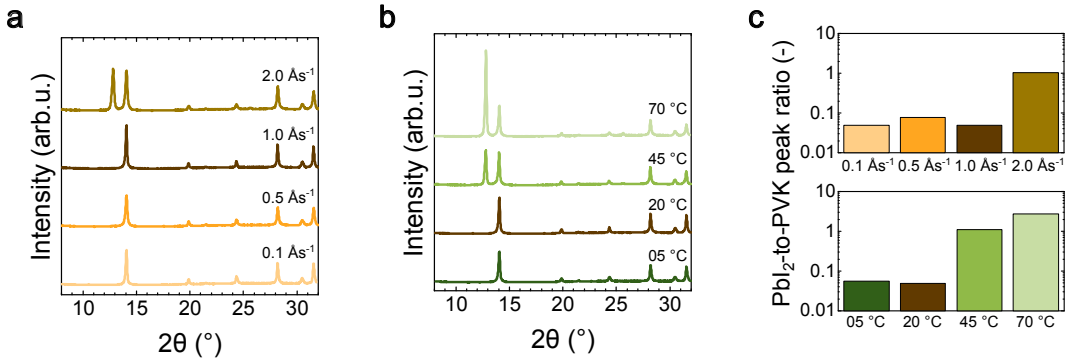

Figure 5.13: X-ray diffraction (XRD) pattern of fabricated perovskite thin films with varying PbI_2 deposition parameters (**a** = different deposition rates, **b** = different substrate temperatures). **c** Corresponding (001)-PbI_2-to-(100)-PVK peak ratios for all conditions. Adapted with permission from American Chemical Society.[101]

XRD analysis of the fabricated perovskite thin films show distinct differences in crystallinity (Figure 5.13a and Figure 5.13b). Especially, when calculating the corresponding PbI_2-to-PVK peak ratios, strong deviations in the grade of conversion are detected. Fast deposition rates and higher substrate temperatures during the PbI_2 deposition lead to more pronounced PbI_2-to-PVK peak ratios (Figure 5.13c). However, there is no clear correlation between morphological and microstructural properties of the PbI_2 layer to the conversion detectable. Subsequent, the fabricated perovskite films are built into PSCs to investigate their performance.

5.4.3 Analysis of Perovskite Solar Cell Performance

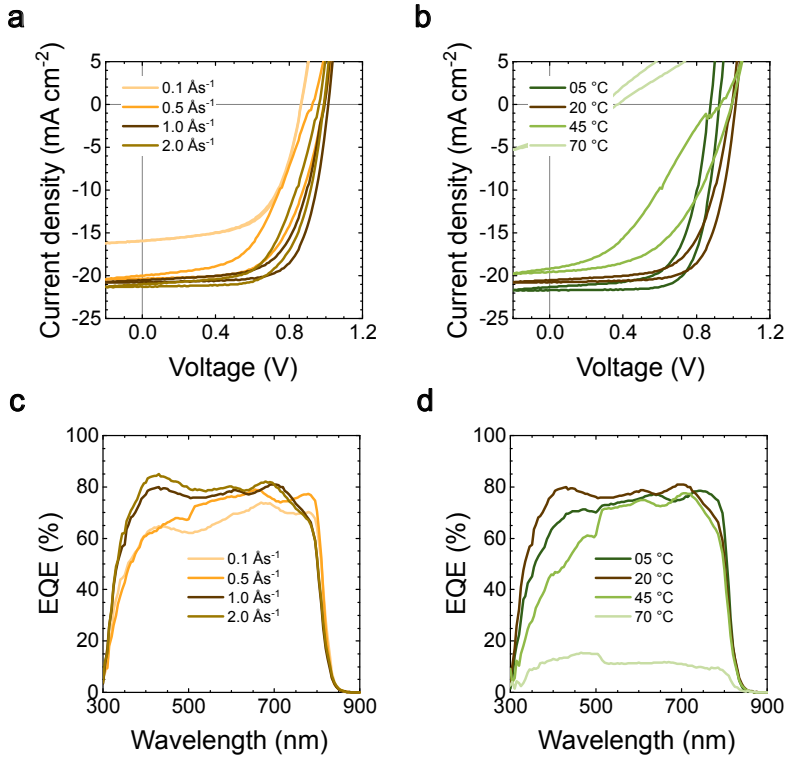

Figure 5.14: Current-voltage (*J*-*V*) characteristics of best-performing perovskite solar cells (PSCs) fabricated with lead iodide (PbI_2) layers deposited at varying deposition rates. (**a**) and at varying substrate temperatures (**b**). **c/d** Corresponding external quantum efficiency (EQE) analyses for best-performing PSCs fabricated with PbI_2 layers deposited at varying deposition rates (**c**) and at varying substrate temperatures (**d**). Adapted with permission from American Chemical Society.[101]

The *J-V* measurements of the best performing PSCs for each of the tested conditions are presented in Figure 5.14a/b. PSCs with slower deposited PbI_2 layers lead to a decrease in PCE, mainly due to lower J_{SC} and FF (Figure 5.14a). A similar trend is observed for increasing substrate temperatures (Figure 5.14b). PSCs with PbI_2 layers deposited onto substrates at 70 °C seem to be non-operational. A potential reason for this could be that the employed HTL (MeO) is damaged or ablated at this high temperature in the used high-vacuum process chamber before the PbI_2 deposition starts. Corresponding EQE measurements show an extremely poor EQE signal over the whole wavelength range (Figure 5.14d). However, this hypothesis could not be verified in this work. Additionally, results from EQE measurements are in line with the measured J_{SC}s from *J-V* analyses (Figure 5.14c/d). The observed general trends are furthermore in line with the corresponding boxplot statistics (Figure 5.15).

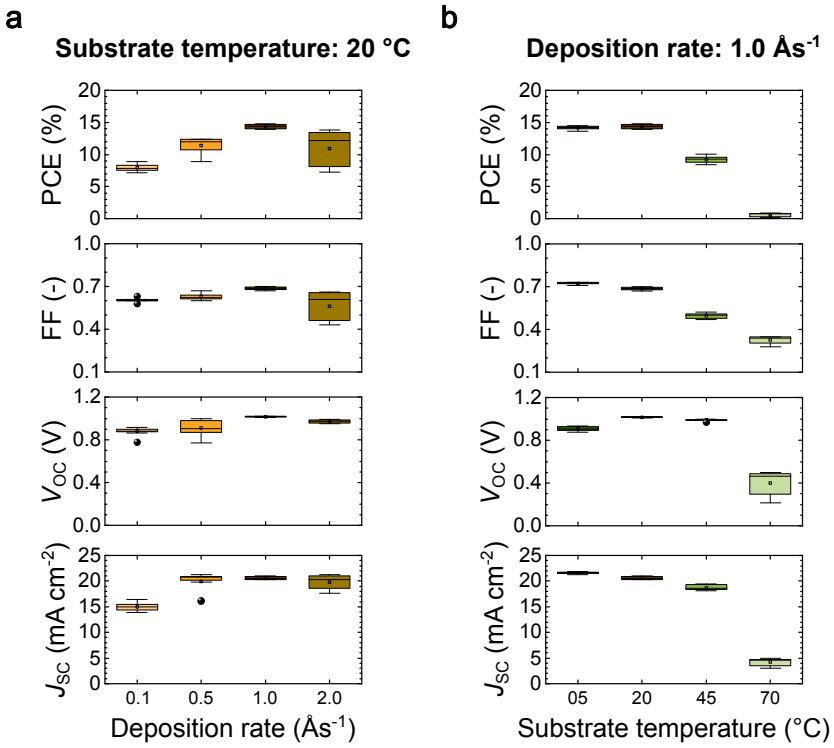

Figure 5.15: Boxplot statistics of perovskite solar cells (PSCs) fabricated with lead iodide (PbI_2) layers deposited at varying deposition rates (**a**) and at varying substrate temperatures (**b**). Adapted with permission from American Chemical Society.[101]

When correlating the PSC performance of all displayed conditions with the corresponding findings from XRD measurements, the earlier described findings for PSCs on a MeO HTL are confirmed. Lower PbI_2-to-PVK peak ratios result in higher PCEs of the corresponding PSCs, while higher PbI_2-to-PVK peak ratios lead to decreased solar cell performance.

5.5 Compositional Engineering in Sequential Layer Deposition Processes

Sequential layer deposition processes offer versatile pathways for compositional engineering. A straightforward approach involves the incorporation of additional precursors in one of the existing deposition steps, leading to a co-sublimation deposition in this process step. Alternatively, additional precursor materials can be introduced in additional deposition steps. In the literature, highest efficiencies for sequentially vacuum-deposited PSCs

have been reported for NBG perovskite compositions, such as $FA_xCs_{1-x}Pb(I:Cl)_3$. However, WBG perovskites are of critical importance for tandem solar cell architectures, where they serve as the top cell to complement lower bandgap absorbers such as Si or CIGS. In 2025, Soufiani *et al.* reported the first WBG PSCs employing a four-step deposition approach (FAI-$PbBr_2$-CsI-PbI_2), reaching PCEs of up to 16% with a perovskite bandgap of 1.7 eV.[102] Even though this result still lacks behind the highest PCEs achieved with co-deposited WBG PSCs, it proves the potential and competitiveness of sequential layer deposition processes for the fabrication of WBG PSCs.

5.5.1 Formamidinium-Cesium-based Double-Cation Perovskite Solar Cells

In this section, different approaches for the fabrication of FA-Cs based PSCs are presented. By introducing different Cs halide salts (CsX) as well as $PbBr_2$ to the inorganic scaffold *via* either co- or additional deposition steps, both NBG and WBG perovskite compositions are fabricated.

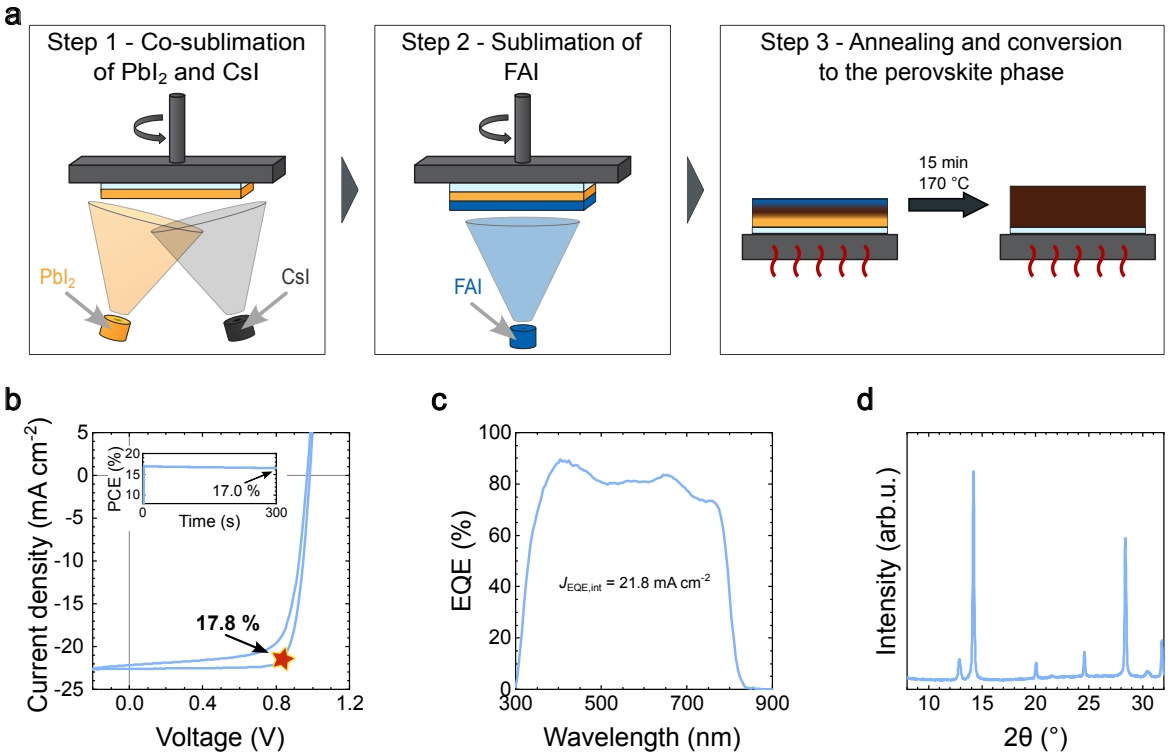

Figure 5.16: a Schematic of the employed sequential layer deposition process for the fabrication of $FACsPbI_3$ perovskite thin films with an additional annealing step, with Step 1 = co-sublimation of PbI_2 and CsI, Step 2 = sublimation of formamidinium iodide (FAI) and Step 3 = annealing and conversion to the perovskite phase. **b** Current-voltage (*J-V*) characteristics of best-performing $FACsPbI_3$ perovskite solar cell (PSC) with maximum power point (MPP)-tracking for 300 seconds. **c** Corresponding external quantum efficiency (EQE) measurement with integrated current density. **d** X-ray diffraction (XRD) pattern of corresponding $FACsPbI_3$ perovskite thin film.

Figure 5.16a shows the process schematic for the fabrication of $FACsPbI_3$ perovskite thin films using a two-step deposition process. CsI is deposited simultaneously to PbI_2 in the first deposition step, followed by the sublimation of FAI and the subsequent annealing step. By adjusting the PbI_2 to CsI deposition rates and final layer thicknesses during their co-sublimation, the final film stoichiometry can be controlled (in this case $FA_{0.83}Cs_{0.17}PbI_3$). The fabricated PSCs with the layer stack of [glass/ITO/MeO/$FA_{0.83}Cs_{0.17}PbI_3$/C_{60}-BCP/Ag] show improved performance compared to the original $FAPbI_3$ PSCs, with champion PCEs of 17.8%. MPP-tracking of the best-performing solar cells show a stabilized PCE of 17.0% (Figure 5.16b). Main improvements are a higher

J_{SC}, also confirmed by corresponding EQE measurements (Figure 5.16c) and an increased FF of up to 80% (see Figure A.12 for statistics). Interestingly, XRD analysis reveals a strongly pronounced (100)-perovskite signal and only a small residual PbI_2 peak, indicating a good grade of conversion (Figure 5.16d).

5.5.2 Cesium-Based Seed Layers for Narrow and Wide Bandgap Perovskite Solar Cells

A promising alternative to conventional compositional engineering involves the introduction of a CsX seed layer prior to the deposition of the $Pb(I:Br)_2$ scaffold. Škorjanc *et al.* have demonstrated that CsX seed layers positively influence both the crystallization dynamics and the photovoltaic performance of co-deposited PSCs.[159] However, comparable investigations focusing on fully sequentially processed PSCs remain limited in the current literature.

In this section, various CsX salts, namely CsI, CsBr, and CsCl, are used as seed layers underneath the lead-containing layer in the fabrication of NBG and WBG PSCs, in order to compare the impact of these CsX salts on film formation and overall device performance of the final PSCs.

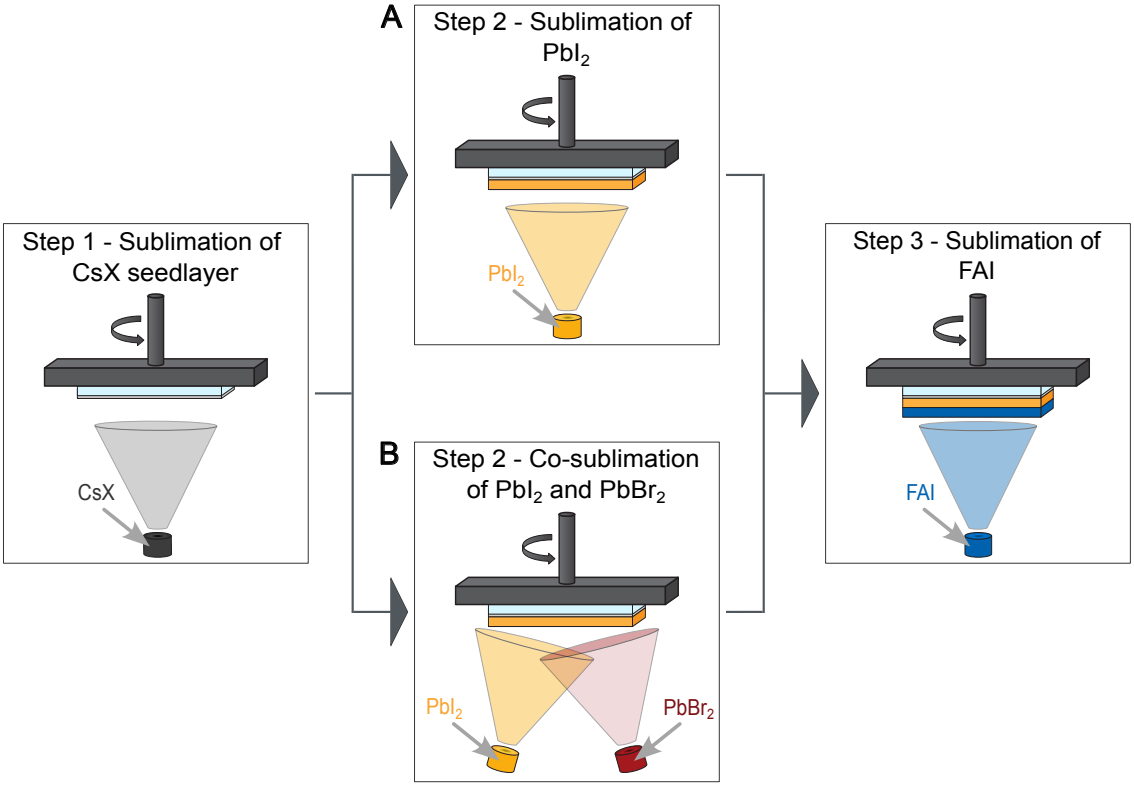

Figure 5.17: Schematic of the employed sequential layer deposition processes for the fabrication of narrow-bandgap (NBG) and wide-bandgap (WBG) perovskite thin films, with Step 1 = sublimation of cesium halide (CsX) seed layers, Step 2 = sublimation of lead iodide (PbI_2) for NBG perovskite compositions (**A**) or co-sublimation of PbI_2 and lead bromide ($PbBr_2$) for WBG perovskite compositions (**B**) and CsI, and Step 3 = sublimation of formamidinium iodide (FAI).

The employed fabrication processes for both NBG and WBG perovskites are shown in Figure 5.17. In a first deposition step, the different CsX (CsI, CsBr and CsCl) seed layers are deposited, followed by the lead halide ($Pb(I:Br)_2$) layer (**A** = NBG with the sublimation of PbI_2; **B** = WBG with a co-sublimation step of PbI_2 and $PbBr_2$). The last deposition step comprises the sublimation of FAI. Subsequently, the layer stack is annealed

for 10 minutes at 170 °C in ambient conditions (r.H. ~30%), like the previously presented deposition processes for pure $FAPbI_3$ and $FA_{0.83}Cs_{0.17}PbI_3$.

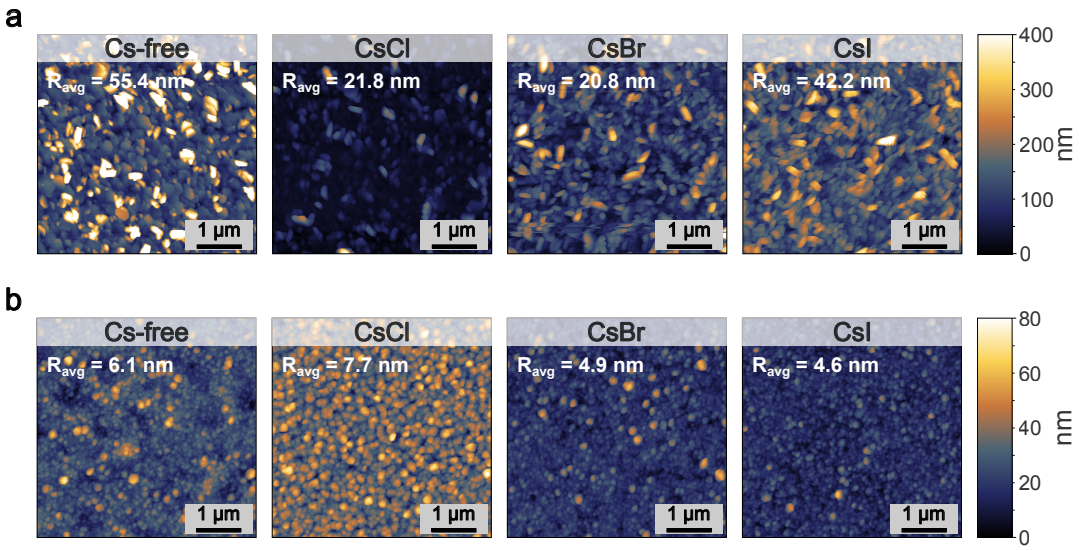

Figure 5.18: Atomic force microscopy (AFM) analysis of inorganic scaffold for **a** = lead iodide (PbI_2) and **b** = lead iodide-bromide ($Pb(I:Br)_2$) layers on different cesium halide (CsX) seed layers with average surface roughness (R_{avg}) values.

Different CsX seed layers have a direct influence on the morphology of the complete inorganic scaffold (Figure 5.18). As previously shown, different underlying HTLs lead to changes in the average surface roughness of the deposited PbI_2 layer, which can directly influence the following interdiffusion of the organic FAI into the inorganic scaffold, affecting the crystallization and film formation reaction. Figure 5.18a shows the differences in R_{avg} of the inorganic scaffolds (CsX/PbI_2) for the used NBG deposition process. Lowest R_{avg} (21.8 nm) are obtained when using a CsCl seed layer, while highest R_{avg} (55.42 nm) are measured when PbI_2 is deposited without any seed layer underneath. Similar trends are observed for inorganic scaffolds for the WBG process (Figure 5.18b). However, overall R_{avg} values for $CsX/Pb(I:Br)_2$ scaffolds are much lower compared (~one order of magnitude) to bromide-free scaffolds. Furthermore, while pure PbI_2 layers show the typical PbI_2-platelets, as also seen for PbI_2 on different HTLs, $Pb(I:Br)_2$ layers show much smaller and round grains, demonstrating a completely different surface morphology.

The different NBG and WBG inorganic scaffolds are used to fabricate PSCs with the device architecture [glass/ITO/MeO/perovskite/C_{60}/BCP/Ag] (Figure 5.19). In both cases, varying CsX seed layers impact the device performance, visible in both *J-V* and EQE analyses. In case of NBG PSCs all configurations yield similar PCEs of up to ~16 %, with small differences in V_{OC} and J_{SC} (Figure 5.19a and Figure A.13) which could be attributed to the slightly different bandgaps (Figure 5.19b) reaching from 1.53 eV for Cs-free up to 1.57 eV with a CsCl seed layer. WBG PSCs do show a strong influence of the underlying CsX seed layer on the photovoltaic performance of the fabricated PSCs. PSCs with a CsCl seed layer yield highest PCEs of 15.3%, achieving the highest V_{OC} (1.08 V) and FF (75.3 %) amongst all WBG configurations (Figure 5.19d). Similar to the NBG PSCs, different CsX seed layers lead to a change in bandgap for WBG configurations, reaching from 1.63 eV for Cs-free PSCs to 1.69 eV for PSCs with a CsCl seed layer (Figure 5.19e and Figure A.14).

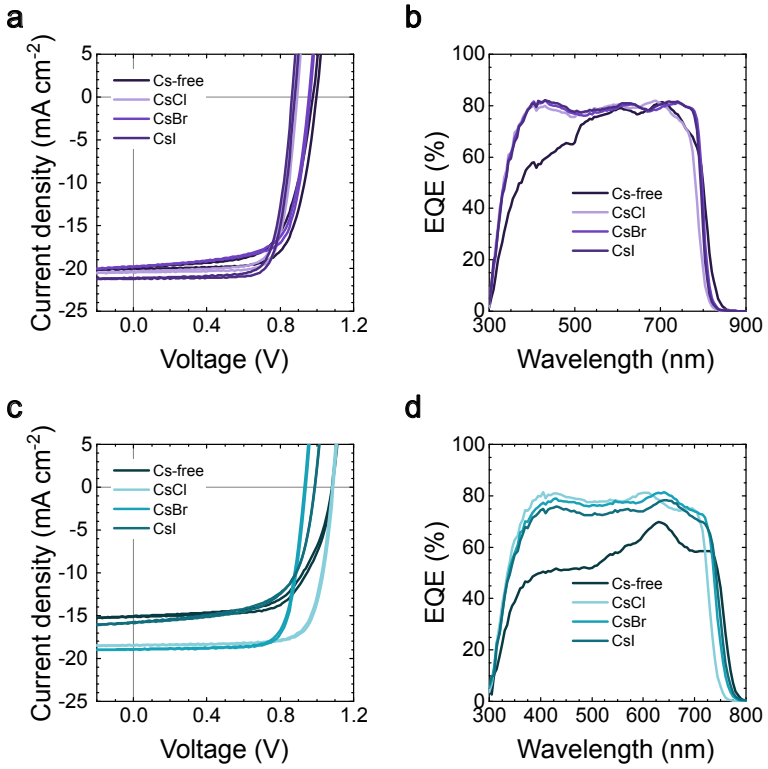

Figure 5.19: a/d Current-voltage (*J-V*) characteristics of best-performing narrow-bandgap (NBG) and wide-bandgap (WBG) perovskite solar cells (PSCs) with different cesium halide (CsX) seed layers. **b/e** Corresponding external quantum efficiency (EQE) measurements for NBG and WBG PSCs with extracted bandgaps for each configuration. **c/f** X-ray diffraction (XRD) pattern of corresponding perovskite thin films for NBG and WBG compositions.

Table 5.1: Overview of photovoltaic performance of champion perovskite solar cells (PSCs) with different bandgaps fabricated in this work using sequential layer deposition processes. Corresponding current-voltage (*J-V*) characteristics are displayed in Figure A.16.

Perovskite composition	Bandgap (eV)	PCE (%)	FF (%)	J_{SC} (mA cm^{-2})	V_{OC} (V)
$FAPbI_3$	1.52	17.2	79.9	22.5	1.01
$FA_{0.83}Cs_{0.17}PbI_3$	1.54	17.8	80.4	22.6	0.98
$FA_{0.85}Cs_{0.15}Pb(I_{0.95}Br_{0.05})_3$	1.58	15.8	72.0	20.9	1.05
$FA_{0.85}Cs_{0.15}Pb(I_{0.78}Br_{0.22})_3$	1.64	14.2	71.5	19.5	1.05
$FA_{0.85}Cs_{0.15}Pb(I_{0.71}Br_{0.24}Cl_{0.05})_3$	1.69	15.3	75.6	18.8	1.08

In this chapter, two alternative approaches for compositional engineering of sequentially deposited perovskites to fabricate FA-Cs-based wider bandgap PSCs are presented. Table 5.1 shows a summary of the highest achieved PCEs of sequentially deposited PSCs of this PhD thesis. Further optimization of the employed deposition processes and device architectures to further improve device performance shows great potential for perovskite-based single-junction and tandem photovoltaics.

5.6 Sequentially Deposited Perovskite/Silicon Tandem Solar Cells

2T perovskite/silicon TSCs have already surpassed the theoretical efficiency limit for single-junction solar cells, reaching record PCEs of 34.6%.[7] Most high-efficiency 2T perovskite/silicon TSCs are fabricated using

solution-based deposition methods. PCEs of 2T perovskite/silicon TSCs with fully vacuum-deposited perovskite top cells are lacking behind, with highest reported PCEs of around 25%, mainly limited by difficult process control, slower optimization cycling and difficulties to incorporate layer quality-improving additives into the perovskite composition.[50, 51, 102] The majority of reports on 2T perovskite/silicon TSCs employing vapor-phase-deposited perovskite top cells use co-deposition processes.

In this section a 2T perovskite/silicon TSC is presented, employing a sequentially deposited perovskite top cell on a mechanically polished silicon bottom cell, serving as a proof-of-concept for this fabrication approach.

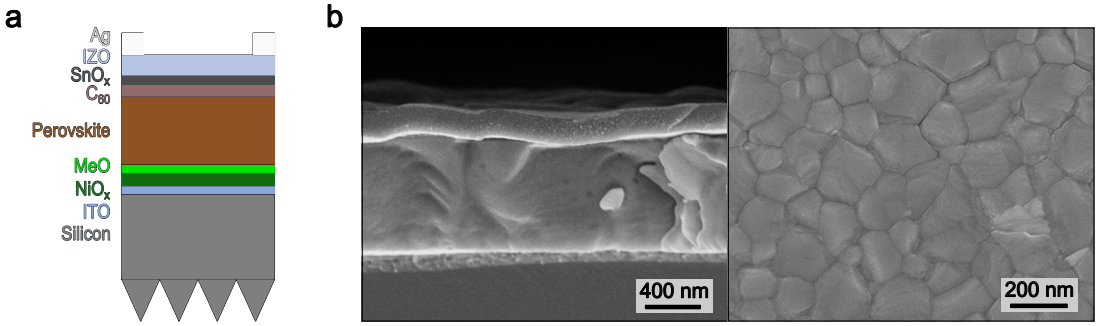

Figure 5.20: a Illustration of the employed layer stack of the fabricated two-terminal (2T) perovskite/silicon tandem solar cell (TSC). **b** Cross-sectional and top view scanning electron microscopy (SEM) images of the fabricated 2T TSC and corresponding surface of the deposited perovskite top cell.

The employed device architecture [silicon/ITO/NiO_x/MeO/perovskite/C_{60}/SnO_x/IZO/Ag] used for the 2T TSC is displayed in Figure 5.20a. For the top cell, a 1.69 eV WBG perovskite ($FA_{0.85}Cs_{0.15}Pb(I_{0.71}Br_{0.24}Cl_{0.05})_3$) was deposited using the previously described deposition process (Figure 5.17, process **B** with a CsCl seed layer). SEM analysis of the perovskite top cell shows a similar morphology to the single-junction reference devices, with columnar grain growth and average grain sizes of ~160 nm (Figure 5.20b).

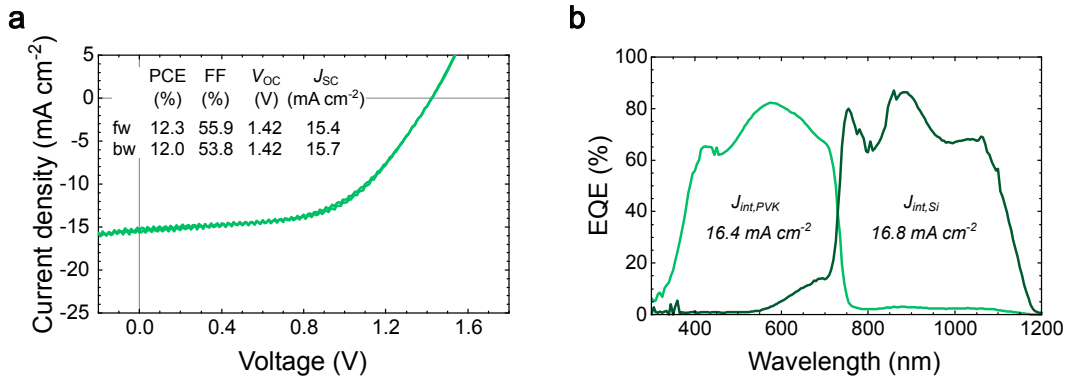

Figure 5.21: a Current-voltage (*J-V*) characteristics of fabricated two-terminal (2T) perovskite/silicon tandem solar cell (TSC). **b** Corresponding external quantum efficiency (EQE) analysis with integrated current densities (J_{int}) of both sub-cells.

The achieved PCE of the fabricated 2T perovskite/silicon TSC reaches ~12%, and is therefore much lower compared to reported PCEs of competitive fabrication methods. However, measured V_{OC}s of 1.42 V prove a voltage contribution of both sub-cells (Figure 5.21). It should be noted that during the time of fabrication, the NiO_x sputtering process suffered some problems regarding final layer quality, which might have contributed to the overall low performance of the tandem device. However, the presented architecture does still serve as a proof-of concept prototype for 2T perovskite/silicon TSCs with a perovskite top cell deposited *via* the earlier

presented sequential layer deposition process. Further optimization of the device architecture and incorporation of the perovskite top cell into the tandem device layer stack was not possible during this work but can improve the tandem device performance in the future.

Recently, Soufiani *et al*., for the first time, reported a 2T perovskite/silicon TSC on textured silicon bottom cells with a sequentially deposited perovskite top cell, using a three-step deposition sequence.[102] The fabricated TSC reaches PCEs of 24%, mainly suffering from a low V_{OC} of 1.61 V, while the corresponding WBG SJ devices reach PCEs of ~16%, comparable to the achieved PCEs in this thesis. However, their work shows the potential of sequential layer deposition to fabricate homogeneous large-area films, as well as fully-textured perovskite/silicon TSCs.

5.7 Summary

Sequential layer deposition has emerged as a promising approach to close the efficiency gap between vapor-based and solution-based fabrication methods, while retaining the inherent advantages of vapor phase deposition for industrial-scale production of PSCs. In this chapter, an in-depth investigation into the influence of various HTLs on perovskite crystallization and film formation within the sequential layer deposition process was conducted (research question **II**). Furthermore, different strategies for compositional engineering aimed at tuning the perovskite bandgap using sequential layer deposition are explored (research question **III**).

First, a baseline two-step vapor phase deposition process for the fabrication of pure FAPI perovskite thin films in the *p-i-n* architecture is established, involving the sequential deposition of PbI_2 and FAI, followed by a thermal annealing step to induce conversion to the perovskite phase. Using this process, PCEs of up to 17.2%, with stabilized MPP-tracking at 17.0%, are achieved, representing the highest reported values for pure FAPI PSCs in the *p-i-n* architecture, fabricated *via* sequential layer deposition. The established deposition process is applied across different HTLs, specifically vacuum-processed 2PACz and TaTm, sputtered NiO_x, as well as solution-processed PTAA, without further modification. SEM analysis revealed significant variations in the morphology of the firstly deposited PbI_2 layer across the different HTLs, with distinct R_{avg} on all configurations measured by AFM. Further characterization of the microstructural properties of the deposited PbI_2 layers using GIWAXS showed a change in the crystal orientation of the deposited PbI_2 crystallites. While PbI_2 crystallites on MeO and 2PACz exhibited a more in-plane orientation, PbI_2 deposition on TaTm, NiO_x and PTAA lead to a second orientation maximum in a more out-of-plane orientation. These changes in morphological and microstructural properties of the PbI_2 layer further showed a significant impact on the subsequent conversion to the final perovskite phase after the deposition of FAI. Especially striking were the strongly pronounced differences in PbI_2-to-PVK peak ratios from XRD measurements of the final perovskite thin films. By varying the layer thickness of FAI in relation to the layer thickness of PbI_2, a correlation of these PbI_2-to-PVK peak ratios and the PSC performance was found. PSCs on MeO and 2PACz, with more in-plane oriented PbI_2, performed best with lower PbI_2-to-PVK peak ratios from XRD. Conversely, devices TaTm, NiO_x and PTAA, which exhibited a second out-of-plane PbI_2 orientation, yielded highest PCEs for higher PbI_2-to-PVK peak ratios. From these results, a guideline plot for the investigated HTLs was derived to highlight the difficulty of comparing and correlating XRD pattern to final PSC performance across different HTLs. Given the importance of the morphological and microstructural properties of the firstly deposited PbI_2 layer on the subsequent conversion to the perovskite phase, the possibility of manipulating these properties by adjusting PbI_2 deposition parameters was investigated. While a variation of the PbI_2 deposition rate showed an influence on the PbI_2 crystal orientation as well as the morphology of the deposited PbI_2 layer, changes of the substrate temperature only affected the PbI_2 layer morphology. These results proved the possibility to alter with the morphological and microstructural properties of the vacuum-deposited PbI_2 layer.

Furthermore, various approaches for the incorporation of additional precursor materials, including different cesium halides and $PbBr_2$, into the established baseline process were studied, in order to adjust the final material composition and bandgap of the perovskite layer. By either introducing additional deposition steps or co-depositing inorganic precursors during the first deposition step, perovskite films with different bandgaps were fabricated. Incorporation of CsI *via* a co-deposited PbI_2-CsI inorganic scaffold achieved highest PCEs of up to 17.8% for a $FA_{0.85}Cs_{0.15}PbI_3$ perovskite composition. Further addition of $PbBr_2$ to the co-deposited $Pb(I:Br)_2$ layer in addition to varying CsX seed layers allowed for the fabrication of wider-bandgap PSCs, with bandgaps of up to 1.69 eV. Although the achieved PCEs of these WBG PSCs remain modest compared to other vapor-phase-deposited PSCs in the literature, these results confirmed the feasibility of bandgap tuning using inorganic precursors alone.

Finally, the integration of sequentially deposited WBG perovskite absorbers into monolithic perovskite/silicon tandem solar cells is demonstrated. While the achieved PCE is very low, the device serves as a proof-of-concept for the application of sequential layer deposition-based absorbers in tandem photovoltaic architectures.

6 Close-Space Sublimation Process for Wide-Bandgap Perovskite Solar Cells and Two-Terminal Perovskite/Silicon Tandem Solar Cells

Abstract

Bridging the gap between laboratory- to industrial-scale fabrication remains a key challenge for advancing industrialization of perovskite PV. Developing suitable and industrially relevant deposition methods for rapid processing and efficient upscaling is still undergoing research. Vapor phase deposition holds key features for continuous large-scale processing. However, conventional vapor phase deposition methods, co-deposition and sequential layer deposition, suffer from slow deposition rates compared to solution processed fabrication processes, stating a major hurdle for high-throughput fabrication. Close-space sublimation (CSS) is an alternative vapor phase deposition method that bears the potential to overcome the low deposition rates, while maintaining the key advantages of vapor phase deposition. Unfortunately, there are no reports on industrially suitable CSS process approaches for WBG perovskite compositions, yet. In this chapter, an innovative CSS process is presented for the fabrication of WBG perovskite-based solar cells with record PCEs up to 18.5%. Furthermore, the successful integration of these perovskite layers into monolithic perovskite/silicon TSCs on different silicon bottom cell morphologies is shown. Remarkably, on planar and textured silicon bottom cells, the morphological and microstructural perovskite layer qualities remain consistent without the need to adjust perovskite process parameters. Additionally, achieved PCEs are similar across all configurations, reaching maximum PCEs of up to 24% on industrially relevant micrometer-size textured silicon bottom cells. These results highlight the potential of CSS as an industrially relevant vapor-based fabrication method for rapid fabrication of efficient perovskite-based solar cells.

Acknowledgements and Contributions

Parts of this chapter review the accepted research article "*Close Space Sublimation as a Versatile Process for Efficient Perovskite/Silicon Tandem Solar Cells*" in *Nature Energy*, 2026 (10.1038/s41560-026-02068-9) by Alexander Diercks, Sofía Chozas-Barrientos, Lidón Gil-Escrig, Federico Ventosinos, Inma Gomar-Fernández, Cristina Roldán-Carmona, Nathan Rodkey, Tonghan Zhao, Julian Petermann, Maximiliano Senno, Vladimir Held, Perrine Carroy, Delfina Muñoz, Paul Fassl, Michele Sessolo, Ulrich W. Paetzold, and Henk J. Bolink.

This work is the result of a collaborative work with the University of Valencia (UV). It involved a 6-month research stay of Alexander Diercks in the research group "Molecular Opto-Electronic Devices (MOED)" at the "Instituto de Ciencias Moleculares (ICMol)", funded through a scholarship (Research Travel Grant) from the Karlsruhe House of Young Scientists (KHYS) and the European project NEXUS. The contributions of all authors according to the CRediT system are listed in Table A.4.

6.1 Introduction

Identifying suitable fabrication methods for a seamless transition from laboratory to industrial production is essential for successful commercialization of perovskite PV.[11, 40, 46, 47, 160] Especially, reported efficiencies above 34% for 2T perovskite/silicon TSCs, already surpassing the theoretical efficiency limits of single-junction solar cells, have demonstrated great potential for future photovoltaics. Without exception, high-efficiency perovskite/silicon TSCs are fabricated using solution-based (or hybrid) deposition methods for the perovskite absorber layer. [147, 161–165] However, these deposition methods are incompatible with industrial manufacturing, driving the need to establish rapid and scalable deposition methods for continuous fabrication.

Vapor phase deposition techniques present a compelling pathway for the scalable fabrication of PSCs. Their key advantages include the ability to achieve homogeneous film formation over large areas, compatibility with continuous in-line processing, and conformal coverage of textured bottom cell architectures, which is critical for tandem device integration.[40, 47, 48, 166, 167] Despite these benefits, vapor phase deposition methods are challenged by inherently low deposition rates, mainly due to the difficult sublimation behavior of the commonly employed organic precursor materials MAI and FAI, inhibiting high-throughput processing.[52, 55, 105, 168] Additionally, conventional vapor phase deposition processes require high-vacuum environments to reduce the mean free path in the gas phase. Most reported vapor phase deposition processes for the fabrication of PSCs employ either co-deposition or sequential layer deposition, with reported record PCEs of 23.1% and 26.4%, respectively.[42, 43] Reports on TSCs with vapor-phase-deposited perovskite top cells are scarce.[50, 51, 102] The highest reported PCE was achieved by Roß *et al.* in 2021, reaching 24.5% with a co-deposited FAMAPbI$_3$ perovskite absorber on top of a planar silicon bottom cell.[50]

An alternative sequential vapor phase deposition is close-space sublimation (CSS). In CSS, the gap between the substrate with the inorganic scaffold and the organic precursor source, which contains the precursor material, is decreased significantly to a few millimeters or less.[63, 64] The reduced gap allows for much higher deposition rates and elevated working pressures, typically in the range of 1-100 mbar. In 2024, Ihrenberger *et al.* reported high deposition rates of CSS-deposited CsPbBr$_3$ at 10μm/min.[62] Furthermore, due to the close proximity between substrate and source, CSS enables a higher material usage compared to sublimation from point sources.[62] Additionally, CSS processes typically employ elevated temperatures for the substrate during the deposition.[63, 64] When employed in two-step processes for the organic precursor deposition, the elevated substrate temperature leads to an *in-situ* conversion of the inorganic scaffold on the substrate to the perovskite phase during CSS-deposition. This lies in contrast to the previously described sequential layer deposition processes from point sources, in which an additional post-annealing step is required to promote interdiffusion of the precursor materials and conversion reaction to the final perovskite phase. Combining these aspects with the general advantages of vacuum-processes, CSS shows great potential for high-throughput and cost-effective industrial-scale fabrication.

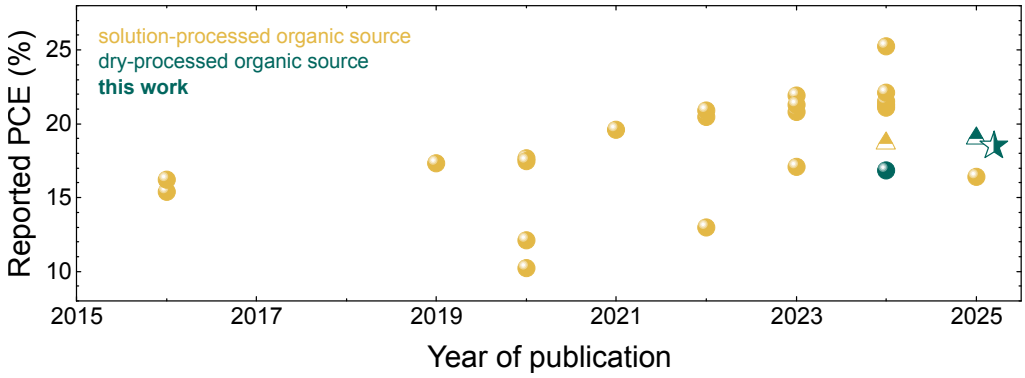

Figure 6.1: Reported power conversion efficiencies (PCEs) of close-space sublimation (CSS) processes or CSS process adaptations throughout the years (*updated until 17.10.2025*).

First reports on CSS for PSCs were published in 2016 by Guo *et al.*, describing a CSS fabrication process of methylammonium lead triiodide ($MAPbI_3$) PSCs reaching PCEs of up to 16.2%.[169] In the following years, reported PCEs further increased to 21.27% for formamidinium (FA)-based perovskite compositions. Zhang *et al.* reported on a $Cs_{0.14}FA_{0.86}Pb(Br_xI_{1-x})_3$ perovskite composition, reaching a PCE of 20.45%.[170] However, reports on the inverted *p-i-n* architecture are highly underrepresented in literature (Figure 6.1 and Table A.9).[64, 137, 171] Additionally, most studies focused on narrow bandgap perovskite compositions (E_g < 1.6 eV) (Table A.9).[63, 64, 137, 169–189] In 2024, Guesnay *et al.* showed the first WBG PSC in the *p-i-n* architecture fabricated by a CSS process with a maximum PCE of 16.82% for a bandgap of 1.63 eV, proving the potential of CSS processes for tandem applications.[171] However, nearly all studies that report on CSS use solvent-based organic source preparation resulting in single-use sources.[171, 177, 182, 188, 190, 191] The desired organic cation ratio is dissolved in IPA and then deposited on small glass substrates *via* spray-coating or spin-coating prior to processing. While reported PCEs employing such processes are great, these single-use sources are only applicable in laboratory-scale research and hinder scalability to large-area fabrication. To tackle this problem, Rodkey *et al.* described a CSS setup using a dry and reusable organic source design by using powders or pressed pellets of the employed organic precursor material.[63] This approach allowed for the fabrication of $FA_xCs_{1-x}Pb(I:Cl)_3$ PSCs in the *n-i-p* architecture with PCEs of up to 18.7% and a reusability of their source for more than 28 depositions. Gomar-Fernández *et al.* followed up on that approach, introducing a large-area dry organic source design (96 cm^2) to fabricate pure $MAPbI_3$ PSCs in the *p-i-n* architecture.[64] PCEs of the fabricated PSCs reached up to 18.8%, with a homogeneous deposition over 6 large-area substrates. This underscores the great potential of CSS as a scalable, and industry-suitable fabrication method for highly efficient PSCs. To date, there are no reports yet on WBG perovskite absorbers in the *p-i-n* architecture using a solvent-free CSS process.

In this chapter, a suitable CSS process for the fabrication of WBG perovskite absorbers is presented. Common approaches of compositional engineering, as employed in other vapor phase deposition methods, *via* the deposited inorganic precursor materials prove inefficient in CSS. An alternative strategy is developed to introduce bromine through the organic source. This reversed strategy allows for the fabrication of high-quality WBG perovskites. The fabricated MA-based WBG *p-i-n* PSCs reach PCEs of ~16% both in opaque single-junction and semitransparent device architectures. By introducing a vacuum-processed surface passivation layer between the perovskite and ETL interface, as well as an anti-reflective coating (ARC), an increase in PCE up to 18.5% is achieved. This represents the highest reported PCE for fully vapor-phase-deposited MA-based PSCs with a bandgap larger than 1.6 eV. Furthermore, the CSS-deposited perovskite layers are integrated into 2T perovskite/silicon TSCs using different silicon bottom cell morphologies (planar, nano-textured and micro-textured). Similar morphological and microstructural properties of the perovskite layer are revealed, without the need of adjusting perovskite process parameters. The fabricated 2T perovskite/silicon TSCs show comparable

PCEs of up to 24.3% on micro-textured silicon bottom cells, on par with reported champion PCEs of 2T perovskite/silicon TSCs with vapor-phase-deposited perovskite top cells.

6.2 Process Development for Wide-Bandgap Perovskites *via* Close-Space Sublimation

A sequential vapor deposition process is employed to fabricate WBG perovskite absorber layers using CSS for the deposition of the organic precursor materials. A schematic overview of the applied deposition process is presented in Figure 6.2. In the initial deposition step, an inorganic scaffold is deposited *via* thermal sublimation from a crucible under high vacuum conditions (~10^{-6} mbar). The subsequent deposition step involves the CSS of the organic cations from a large-area powder source. During this step, the organic source and the substrate are heated to the desired temperatures. To initiate the deposition, the CSS chamber is evacuated to 1 mbar. The elevated substrate temperature leads to an *in-situ* conversion of the sublimed organics with the inorganic scaffold, resulting in the formation of the perovskite phase. Upon completion of the process, the chamber is flushed with N_2, and the samples are subsequently removed from the setup.

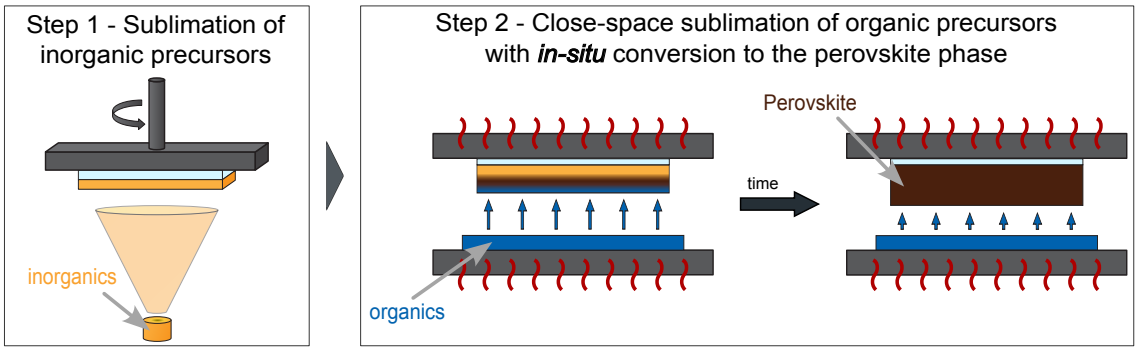

Figure 6.2: Schematic of employed close-space sublimation (CSS) process for the fabrication of perovskite thin films. Step 1 shows the sublimation of the inorganic precursor materials from an effusion source. Step 2 displays the CSS of the organic precursor materials from a large-area powder source with *in-situ* conversion to the perovskite phase.

As previously mentioned in Chapter 4, studies on vapor phase deposition processes usually employ iodide-based organic precursor materials. Reports on the successful sublimation and use of alternative halide-organic compounds are either nonexistent or rare. Consequently, for the fabrication of WBG perovskites *via* vapor phase deposition the mixed-halide ratio to tune the bandgap is typically adjusted through the inorganic precursors.[98, 102]

In a first attempt to fabricate FA-based PSCs *via* CSS, two distinct inorganic scaffolds (pure PbI_2 and pure $PbBr_2$) are prepared and converted using a pure FAI organic source. The expected nominal compositions of the resulting perovskite phases are $FAPbI_3$ (in case of PbI_2) and $FAPb(I_{0.33}Br_{0.67})_3$ (in case of $PbBr_3$). Two CSS deposition times (10 minutes and 35 minutes) are selected to ensure complete conversion of the deposited inorganic scaffolds. Photoluminescence (PL) measurements reveal that the bandgap of the resulting perovskite thin films, independent of the inorganic scaffold, shifted towards similar bandgaps, even prior to full conversion (Figure 6.3). This implies that a halide-exchange reaction occurs during the CSS process, in which bromine from the $PbBr_2$ scaffold is replaced by iodine from the FAI source.

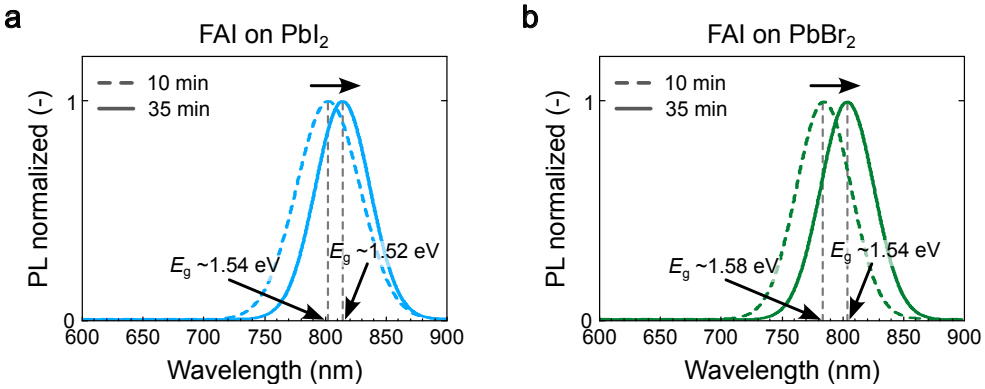

Figure 6.3: Photoluminescence (PL) analysis of CSS-processed FAI-based perovskite absorbers. **a** PL shift after conversion of pure PbI_2 inorganic scaffold after two different CSS deposition times (10 min and 35 min). **b** PL shift after conversion of pure $PbBr_2$ inorganic scaffold after two different CSS deposition times (10 min and 35 min)

To determine whether this effect is specific to FA-based systems, a similar experiment is performed using MAI as the organic source instead of FAI. However, similar results were observed. In both cases, the final perovskite films exhibit a nearly bromine-free composition, with PL peaks corresponding to bandgaps close to that of $MAPbI_3$, even before reaching full conversion (Figure 6.4). These findings reaffirm the previous findings from a pure FAI organic source and suggest that controlling the mixed-halide ratio *via* the inorganic scaffold is not a viable strategy for CSS-processed perovskites.

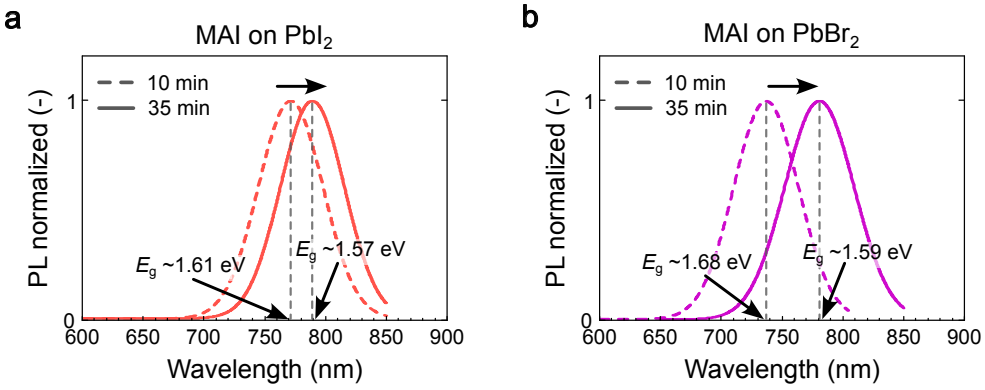

Figure 6.4: Photoluminescence (PL) analysis of CSS-processed MAI-based perovskite absorbers. **a** PL shift after conversion of pure PbI_2 inorganic scaffold after two different CSS deposition times (10 min and 35 min). **b** PL shift after conversion of pure $PbBr_2$ inorganic scaffold after two different CSS deposition times (10 min and 35 min)

To address the issue of halide incorporation from the inorganic scaffold, a reversed strategy is explored next. In this approach, a pure PbI_2 inorganic scaffold is converted using mixed-halide organic precursor sources. Specifically, MAI and MABr are mixed in four different relative weight ratios (1:0, 3:1, 1:1, and 0:1) to see the effect of a mixed-halide organic source on the final perovskite composition. Figure 6.5a-d presents the PL spectra of the resulting perovskite thin films after a CSS deposition time of 10 minutes. The PL peak of the perovskite film converted with pure MAI corresponds to the same bandgap observed in Figure 6.5a. However, with increasing bromide content in the organic source, the PL peak shifts toward shorter wavelengths. Notably, the film converted with pure MABr exhibits a PL emission corresponding to a bandgap of 1.88 eV, significantly higher than expected for the nominal $MAPb(I_{0.33}Br_{0.67})_3$ composition (Figure 6.5d). This suggests the occurrence of a reversed halide-exchange reaction, in which iodine from the inorganic PbI_2 scaffold is replaced by bromine from the MABr source. The bandgaps of the perovskite films fabricated using MAI:MABr

ratios of 3:1 and 1:1 were measured at 1.63 eV and 1.77 eV, respectively (Figure 6.5b/c). These results indicate that the halide ratio of the organic precursor source predominantly determines the final perovskite composition.

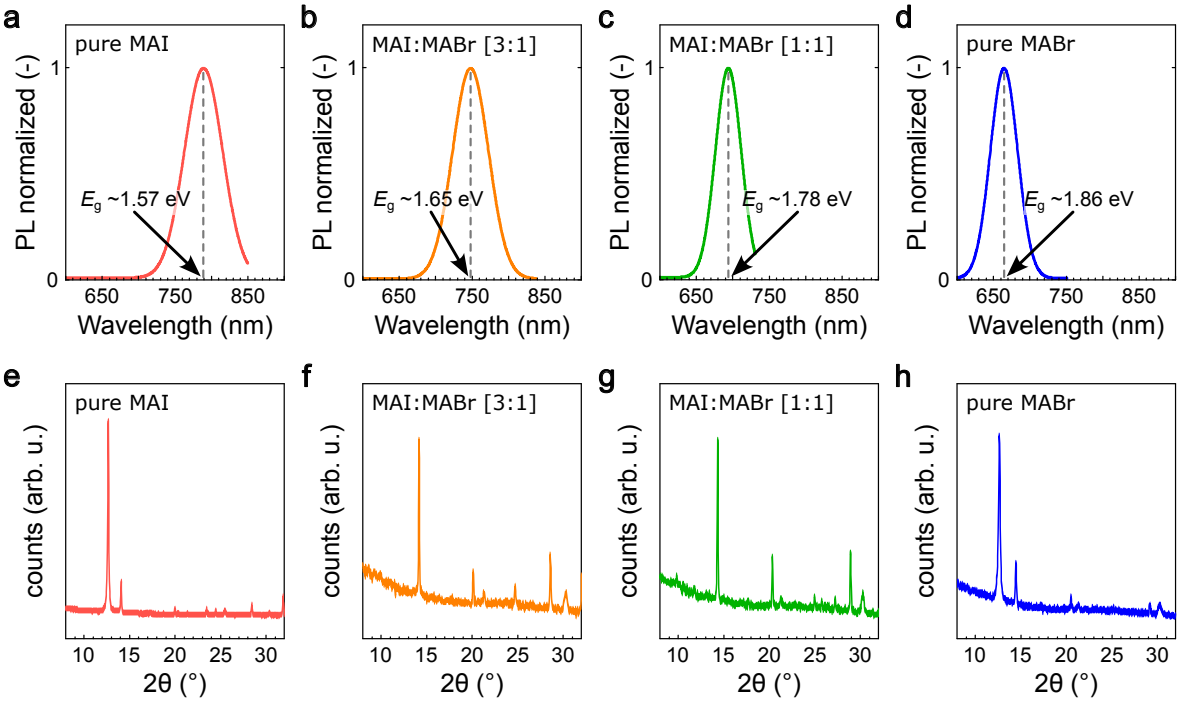

Figure 6.5: Photoluminescence (PL) analysis of CSS-processed perovskite absorbers with mixed MAI:MABr organic sources. **a-d** PL shift after conversion of pure PbI_2 inorganic scaffold with varying MAI:MABr organic source compositions (1:0, 3:1, 1:1, 0:1). **e-h** Corresponding X-ray diffraction (XRD) pattern of the resulting perovskite thin films.

Interestingly, corresponding XRD measurements of the perovskite thin films reveal that mixed organic sources facilitate faster conversion of the inorganic scaffold (Figure 6.5e-h). In cases where pure MAI or pure MABr were used, the XRD patterns show prominent PbI_2 peaks, indicating incomplete conversion (Figure 6.5e/h). In contrast, for films processed with mixed organic sources, no PbI_2 signal is detectable after just 10 minutes of CSS, suggesting complete conversion of the inorganic scaffold (Figure 6.5f/g).

6.3 Fabrication of Methylammonium-based Wide-Bandgap Perovskite Solar Cells

The halide ratio in mixed-halide organic sources governs the bandgap of the final perovskite composition. As shown in the previous section, conversion of a pure PbI_2 inorganic scaffold with a mixed MAI:MABr organic source with a relative weight ratio of 3 mg:1 mg results in perovskite thin films with a bandgap of ~1.63 eV.

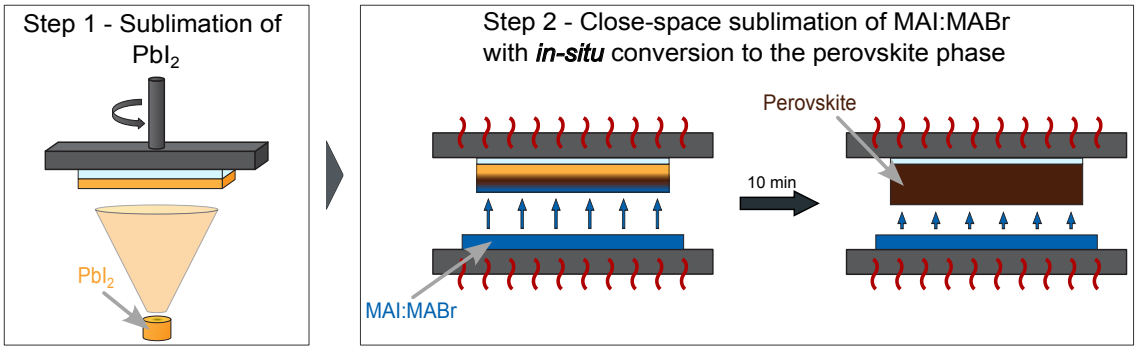

Figure 6.6: Schematic of employed close-space sublimation (CSS) process for the fabrication of wide-bandgap perovskite thin films. Step 1 shows the sublimation of lead iodide (PbI_2) from an effusion source. Step 2 displays the CSS of a MAI:MABr mixture with *in-situ* conversion to the $MAPb(I:Br)_3$ perovskite phase.

The developed fabrication process for WBG perovskites is used to fabricated PSCs to explore the full potential of CSS-processed PSCs, employing a fully vacuum-processed layer stack consisting of [ITO/p-doped:TaTm-TaTm/ MAPIBr/C_{60}/BCP/Ag] (Figure 6.7a). As deposited PSCs, without any post-treatment of the perovskite layer, exhibited functional *J-V* characteristics, achieving PCEs of up to 14.6%, with a V_{OC} of 1.06 V, a FF of 70.2%, and a J_{SC} of 19.6 mA cm^{-2} (Figure 6.7b). However, relatively low V_{OC} and FF values were observed, which limited overall device performance.

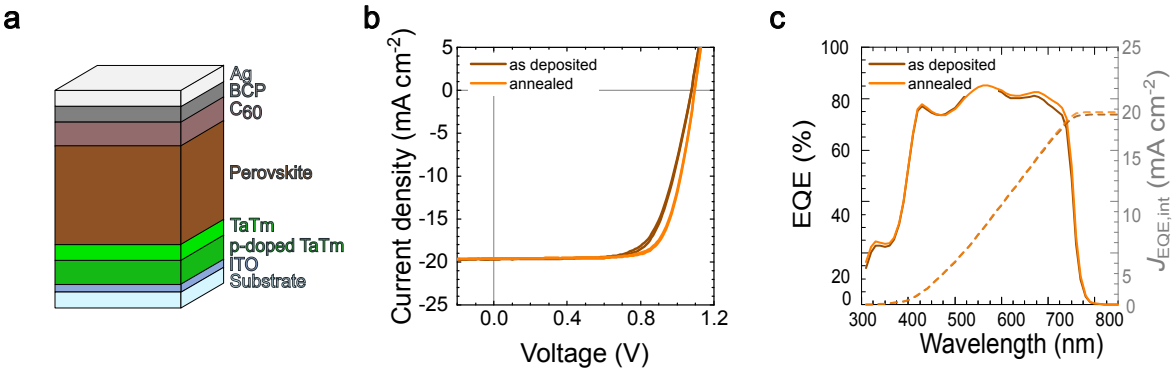

Figure 6.7: a Illustration of employed layer stack for opaque single-junction perovskite solar cells (PSCs) in the *p-i-n* architecture. **b** Comparison of current-voltage (*J-V*) characteristics of as deposited and annealed PSCs. **c** Corresponding external quantum efficiency (EQE) measurements with integrated current densities ($J_{EQE,int}$).

To enhance PSC performance, a post-annealing step was introduced following CSS deposition of the perovskite thin films. This step consisted of annealing for 10 minutes at 100 °C in a humidity-controlled environment with a relative humidity of approximately 35%. The additional annealing resulted in a significant improvement in PCE to values exceeding 16%, primarily attributed to a reduction in series resistance, which led to notable gains in V_{OC} and FF (Figure 6.7b and Figure A.17). Interestingly, J_{SC} values remained nearly unchanged under both conditions (~19 mA cm^{-2}), as confirmed by EQE measurements (Figure 6.7c). The low EQE intensity in the short-wavelength range (300 nm to ~380 nm) was attributed to strong light absorption by the thick HTL used in the device architecture (Figure A.18).

Table 6.1: Photovoltaic parameters of CSS-processed champion perovskite solar cells (PSCs) with as deposited and annealed perovskite thin films (Figure A.17 for full statistics).

	PCE (%)	FF (%)	V_{OC} (V)	J_{SC} (mA cm^{-2})	$J_{EQE,int}$ (mA cm^{-2})
as deposited	14.6	70.2	1.06	19.6	18.7
annealed	16.2	74.5	1.10	19.7	18.9

6.3.1 Effect of Post-Annealing Step on Morphology and Microstructure

Further analysis of the thin film properties of the two perovskite layers was conducted using PL measurements (Figure 6.8a). No difference in bandgap was detected, indicating that the post-annealing step does not result in a noticeable change in perovskite composition. This observation is consistent with XRD analysis, which revealed very similar diffraction patterns, suggesting no significant variation in crystallinity (Figure 6.8b).

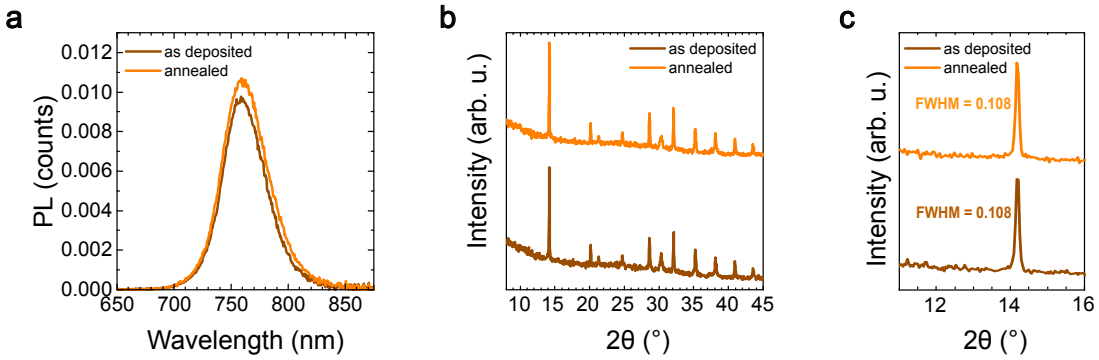

Figure 6.8: a Photoluminescence (PL) measurements of as deposited and annealed perovskite thin films. **b** Comparison of X-ray diffraction (XRD) pattern of as deposited and annealed perovskite thin films. **c** Full-width at half-maximum (FWHM) analysis of the (100)-perovskite peak from corresponding XRD measurements of as deposited and annealed perovskite thin films.

It is noted that the full width at half maximum (FWHM) of the (001)-perovskite peak increases slightly for post-annealed layers. The relative (001)-perovskite to (100)-PbI_2 peak ratio remains comparable in both cases (Figure 6.8c), indicating similar grade of crystallinity for both perovskite layers.

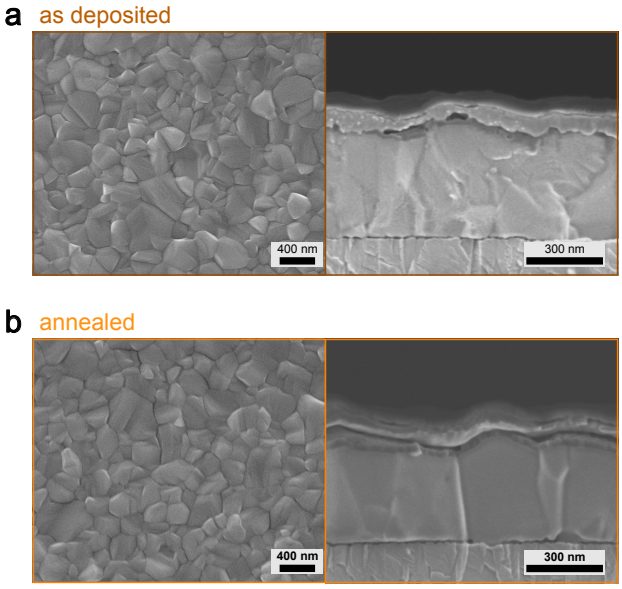

Figure 6.9: a/b Scanning electron microscopy (SEM) analysis of the surface of the perovskite thin film and cross-section of the corresponding perovskite solar cells (PSCs) for as deposited and annealed perovskite thin films, respectively.

Cross-sectional SEM images of both perovskite layers reveal differences in intra-grain morphology (Figure 6.9a/b). The as deposited perovskite layer exhibits a more disoriented growth pattern, characterized by visible horizontal grain boundaries throughout the layer. In contrast, post-annealed layers display a more columnar growth with significantly fewer horizontal grain boundaries. Corresponding top-view SEM images show similar grain sizes for both conditions (Figure 6.9a/b).

In summary, a post-annealing step of the CSS-processed WBG perovskite thin films leads to an increase in device performance of the final solar cells. The post-annealing step however does not alter with the crystallinity or composition of the perovskite film but leads to a smoother vertical perovskite grain morphology.

6.4 Layer Stack Optimization and Semitransparent Device Architectures

Passivation of bulk or surface defects of the perovskite absorber layer can lead to an increase in device performance. The majority of reported passivation strategies uses solution-based deposition methods for the employed materials.[192–194] In vapor phase deposition processes, bulk defect passivation is quite challenging, since any passivation material must be integrated in the perovskite absorber layer by co-deposition along the perovskite precursors. $EDAI_2$ has been reported as an effective surface passivant of the perovskite/C_{60} interface, which can be deposited *via* solution-processing or vapor phase deposition.[195, 196]

Furthermore, to enhance the performance of the solar cell, anti-reflective coatings (ARCs) are applied. These ARCs (usually vacuum-processed LiF or MgF_2) reduce surface reflection of the incoming light at the TCO, therefore enhancing light harvesting of the perovskite absorber, leading to an increased current density.[197, 198]

6.4.1 Optimized Fully Vacuum-Processed Perovskite Solar Cells

The employed optimized fully vacuum-processed layer stack of the fabricated WBG PSCs is displayed in Figure 6.10a. Deposition of a thin $EDAI_2$ (1 nm) layer between the perovskite absorber and C_{60}, acting as a surface passivation layer, and an additional LiF (85 nm) ARC lead to an increase in both V_{OC} and J_{SC}, respectively, as shown in the corresponding *J-V* curves (Figure 6.10b). The corresponding champion device with an optimized layerstack employing both $EDAI_2$ and LiF achieves PCEs of up to 18.5% with negligible hysteresis and a stabilized PCE of 18.2% after 300 seconds of MPP-tracking (Figure A.19). This result represents the highest reported PCE for fully vacuum-processed WBG (E_g > 1.6 eV) PSCs in the *p-i-n* architecture using a CSS deposition process.

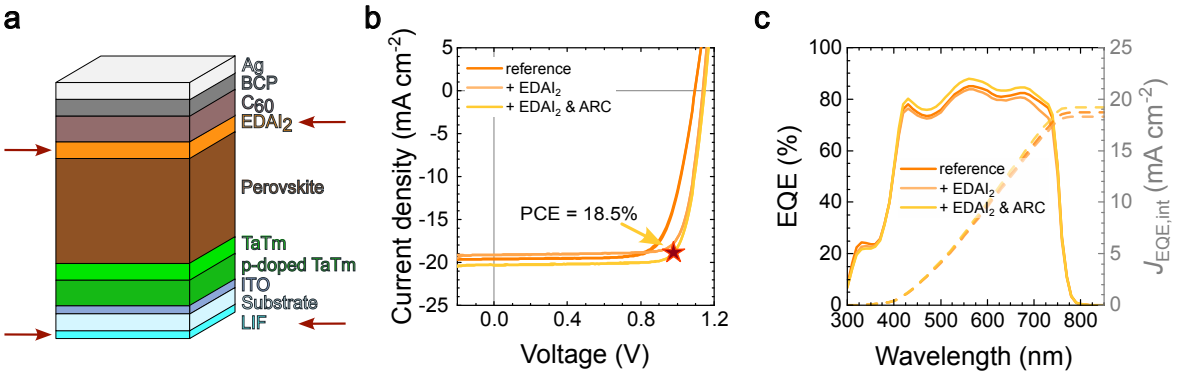

Figure 6.10: a Illustration of optimized layer stack for opaque single-junction perovskite solar cells (PSCs) in the *p-i-n* architecture with vacuum-processed $EDAI_2$ and LiF as surface passivation and anti-reflective coating (ARC). **b** Effect of $EDAI_2$ and $EDAI_2$+LiF on the current-voltage (*J-V*) characteristics opaque single-junction PSCs. **c** Corresponding external quantum efficiency (EQE) measurements with integrated current densities ($J_{EQE,int}$).

Compared to the best-performing opaque reference PSC, the main improvement is a 50 mV increase in V_{OC}. The application of LiF as ARC results in a slight increase in J_{SC} to 20.3 mA cm^{-2}, as confirmed by EQE measurements (Figure 6.10c). A comparison of the photovoltaic performance parameters of all configurations is presented in Table 6.2.

Table 6.2: Photovoltaic parameters of CSS-processed champion perovskite solar cells (PSCs) with surface passivation ($EDAI_2$) as well as with surface passivation and anti-reflective coating (LiF).

	PCE (%)	FF (%)	V_{OC} (V)	J_{SC} (mA cm^{-2})	$J_{EQE,int}$ (mA cm^{-2})
reference	16.2	74.5	1.10	19.7	18.9
+ $EDAI_2$	17.4	79.9	1.14	19.1	18.4
+ $EDAI_2$ & LiF	18.5	79.2	1.15	19.5	19.2

6.4.2 Semitransparent Perovskite Solar Cells for Tandem Photovoltaics

Integration of PSCs into tandem photovoltaics requires efficient semitransparent (ST) architectures for the perovskite top cell. Changing the non-transparent metal rear electrode with a TCO layer allows the non-absorbed light to pass through and be absorbed by the underlying bottom cell of the tandem device.

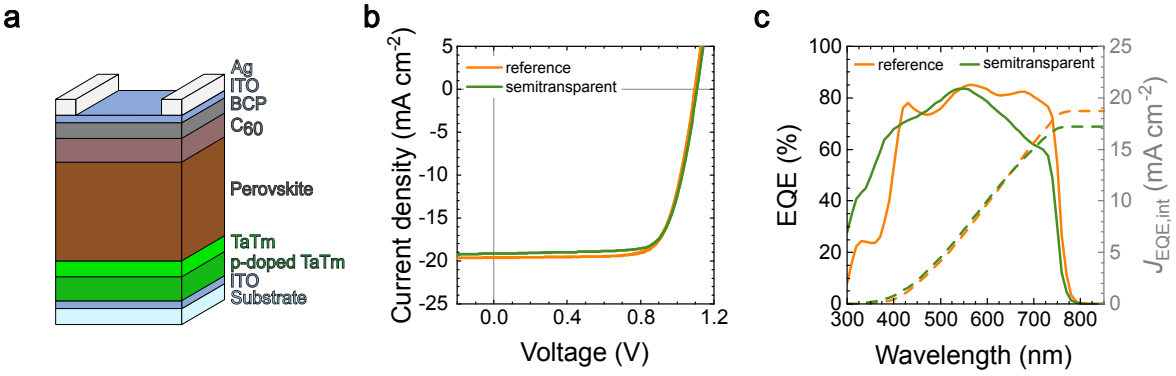

Figure 6.11: **a** Illustration of employed layer stack for semitransparent single-junction perovskite solar cells (PSCs) in the *p-i-n* architecture with a transparent ITO electrode. **b** Comparison of current-voltage (*J-V*) characteristics of opaque reference PSCs and top-illuminated semitransparent PSCs. **c** Corresponding external quantum efficiency (EQE) measurements with integrated current densities ($J_{EQE,int}$).

To assess the suitability of CSS-processed WBG PSCs for monolithic TSC applications, ST PSCs are fabricated. For the fabrication of ST PSCs, a 75 nm thin ITO layer is deposited *via* sputtering, while the rest of the layer stack is kept identical to that of the opaque reference PSCs (Figure 6.11a). In a monolithic integration with a suitable bottom cell, such as silicon, the semitransparent devices are illuminated from the top through the ST top electrode. Figure 6.11b presents the *J-V* measurements of ST PSCs under top illumination, alongside the *J-V* curve of the opaque reference device. Top-illuminated ST devices reache PCEs of up to 16.2%, similar to the ones of their opaque reference counterparts (Figure 6.7b, and Figure A.20). Corresponding EQE measurements are shown in Figure 6.11c, with integrated J_{SC} values closely matching those obtained from *J-V* measurements. A summary of the photovoltaic parameters of the best-performing opaque and semitransparent PSCs is provided in Table 6.3.

For the ST architecture, a drop in EQE is observed at wavelengths >600 nm compared to opaque PSCs, attributed to the reduced optical path length in the active layer. This effect could be mitigated by employing thicker perovskite films. Top illumination results in increased EQE at shorter wavelengths, which is attributed to absorption by the thick organic HTL deposited on the glass side of the substrate Figure A.18.

In summary, these findings demonstrate strong potential for the integration of CSS-processed ST WBG PSCs into tandem photovoltaic architectures.

Table 6.3: Photovoltaic parameters of CSS-processed champion perovskite solar cells (PSCs) in opaque and semitransparent architecture (Figure A.20 for full statistics).

	PCE (%)	FF (%)	V_{OC} (V)	J_{SC} (mA cm^{-2})	$J_{EQE,int}$ (mA cm^{-2})
opaque reference	16.2	74.5	1.10	19.6	18.9
semitransparent	16.2	75.3	1.10	19.5	17.3

6.5 Integration into Two-Terminal Perovskite/Silicon Tandem Architectures

Reported PCEs of 2T perovskite/silicon TSCs have already exceeded 34%, surpassing the theoretical efficiency limit of single-junction solar cells.[7, 24] However, most high-efficiency 2T perovskite/silicon TSCs are fabricated using solution-based methods for the deposition of the perovskite top cell. In contrast, studies employing vapor phase deposition techniques for the perovskite layer remain scarce.[50, 51, 102]

In 2021, Roß *et al.* successfully integrated a co-deposited $FAMAPbI_3$ perovskite top cell into a 2T perovskite/silicon TSC on textured silicon. The device achieved a PCE of 24.5%, which remains the highest reported efficiency for a fully-textured vapor-phase-deposited perovskite/silicon TSC to date.[50] More recently, in 2024, Chozas-Barrientos *et al.* demonstrated a fully vacuum-processed 2T perovskite/silicon TSC on industrially relevant, micrometer-textured silicon bottom cells, achieving PCEs of up to 22%.[51]

In this section, the previously developed ST PSCs are integrated into both planar and nano-textured silicon bottom cells to evaluate the potential of the CSS method for fabricating 2T perovskite/silicon TSCs (Figure 6.12a/b). To accommodate the changes in surface morphology, the thicknesses of the charge transport layers and electrodes were adjusted. Specifically, for textured substrates, layer thicknesses were increased by a factor of 1.5 to account for the enlarged surface area and to ensure comparable coverage relative to planar surfaces. The perovskite deposition process itself was kept identical across all bottom cell configurations. Without further modification of the ST layer stack, the resulting tandem devices achieved PCEs of approximately 18% in both configurations (Figure 6.12c/d).

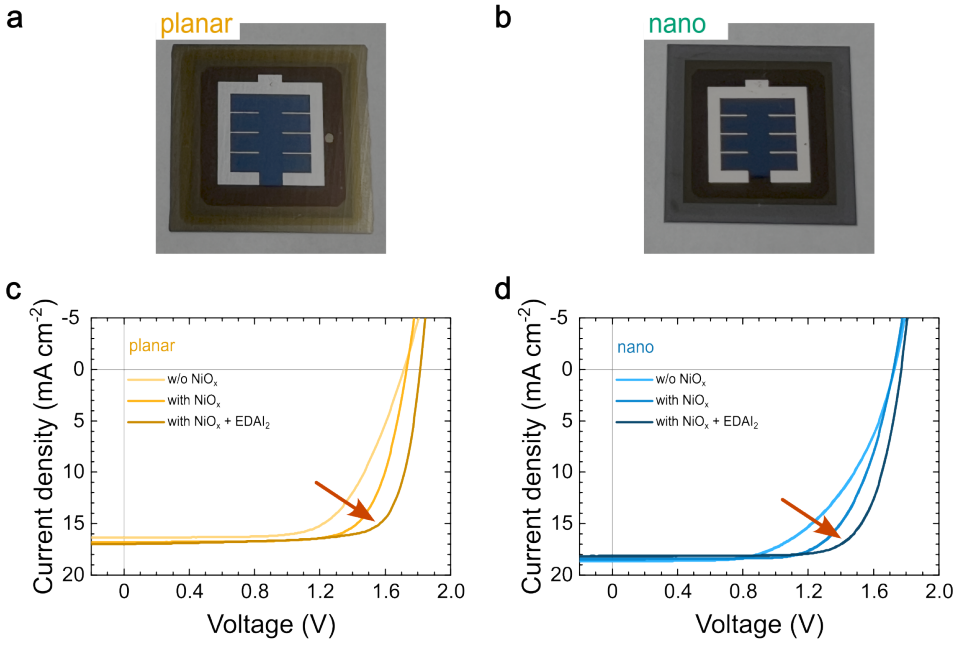

Figure 6.12: a Images of fabricated two-terminal (2T) perovskite/silicon tandem solar cells (TSCs) with planar and nano-textured silicon bottom cells. **b/c** Current-voltage (*J-V*) characteristics with integrated NiO_x hole transport layer and $EDAI_2$ surface passivation of planar and nano-textured 2T TSCs, respectively.

Device performance was significantly improved by introducing an additional NiO_x HTL between the recombination junction and the p-doped TaTm HTL. This modification led to an enhanced FF in both planar and textured configurations. Furthermore, the integration of a vacuum-processed $EDAI_2$ interlayer resulted in additional performance gains, with final PCEs reaching 23.6% and 23.9%, respectively (Figure 6.12c/d and Table 6.4).

Table 6.4: Photovoltaic parameters of Layer stack optimization for CSS-processed two-terminal (2T) perovskite/silicon tandem solar cells (TSCs) on planar and nanometer-size textured silicon bottom cells.

	PCE (%)	FF (%)	V_{OC} (V)	J_{SC} (mA cm^{-2})
planar	18.4	65.6	1.71	16.3
planar with NiO_x	21.5	73.8	1.73	16.8
planar with $EDAI_2$	23.6	76.5	1.81	17.0
nano-textured	18.4	57.1	1.73	18.7
nano-textured with NiO_x	21.6	68.1	1.72	18.5
nano-textured with $EDAI_2$	23.9	74.3	1.77	18.2

6.5.1 Planar, Nano- and Micro-Textured Perovskite/Silicon Tandem Solar Cells

Surface texturing of the silicon bottom cell leads to improved light-incoupling and less reflection losses, leading to higher J_{SC}s of the solar cell. To explore the full potential of CSS for the fabrication of efficient 2T perovskite/silicon TSCs, the optimized layer stack was applied to micrometer size textures, as commonly used in industry (Figure 6.13a).

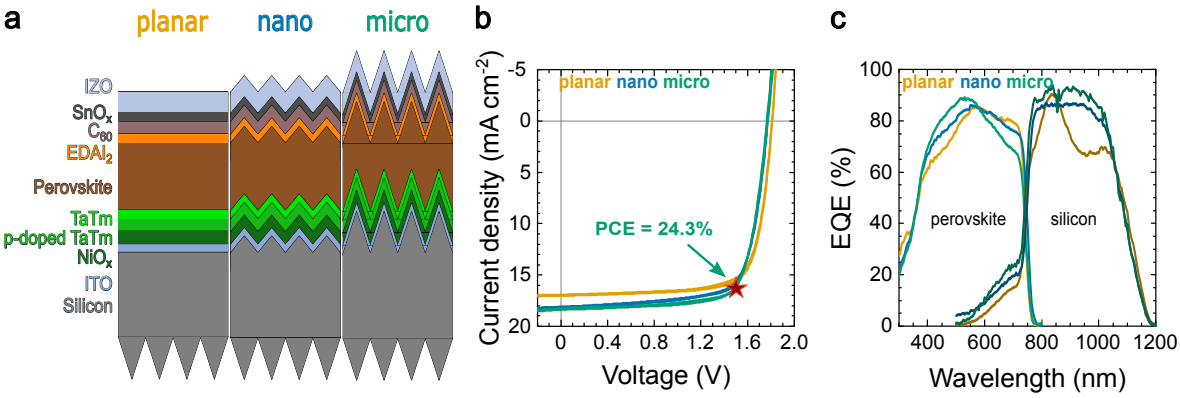

Figure 6.13: **a** Optimized layer stack for two-terminal (2T) perovskite/silicon tandem solar cells (TSCs) on planar, nano-textured and micro-textured silicon bottom cells. **b** Comparison of current-voltage (*J-V*) characteristics of fabricated 2T perovskite/silicon TSCs. **c** Corresponding external quantum efficiency (EQE) measurements.

Figure 6.13b shows the *J-V* characteristics of the champion tandem devices fabricated on each bottom cell morphology. All devices achieve similar PCEs of 23.6%, 23.9% and 24.5% for planar, nano- and micro-textured configuration. These results are comparable to those reported for fully vacuum-processed 2T perovskite/silicon TSCs on textured bottom cells in the literature.[50, 51] With V_{OC}s in the range of 1.77-1.81 V, a successful integration of the perovskite top cell without significant voltage losses is indicated. Interestingly, the planar device yields the highest V_{OC} of 1.81 V, whereas the nano- and micro-textured devices achieve higher J_{SC}s of 18.2 and 18.3 mA cm^{-2}, respectively. A summary of the photovoltaic parameters of all configurations is given in Table 6.5.

Table 6.5: Photovoltaic parameters of two-terminal (2T) perovskite/silicon tandem solar cells (TSCs) on planar, nano-textured and micro-textured silicon bottom cells.

	PCE (%)	FF (%)	V_{OC} (V)	J_{SC} (mA cm^{-2})	$J_{EQE,PVK}$ (mA cm^{-2})	$J_{EQE,Si}$ (mA cm^{-2})
planar	23.6	76.4	1.81	17.0	18.0	16.4
nano-textured	23.9	74.3	1.77	18.2	18.7	18.0
micro-textured	24.3	75.1	1.77	18.3	18.2	19.3

Corresponding EQE measurements are displayed in Figure 6.13c. The integrated current densities of the three perovskite top cells reach values around ~18 mA cm^{-2} on all three bottom cell morphologies with similar bandgaps (Figure A.21). It can be observed that surface texturing leads to an increase in the integrated current generated by the silicon bottom cell, with integrated current densities of 16.4 mA/cm^{-2} for the planar, 18.0 mA/cm^{-2} for the nano- and 19.3 mA cm^{-2} for the micro-textured configurations. This leads to different current-limiting regimes for the resulting tandem devices, resulting in bottom cell limitation in the planar configuration and top cell-limitation in the micro-textured configuration. The device performance could be enhanced further by compositional engineering of the perovskite absorber to tailor its photocurrent and achieve optimal current matching for each bottom cell morphology.

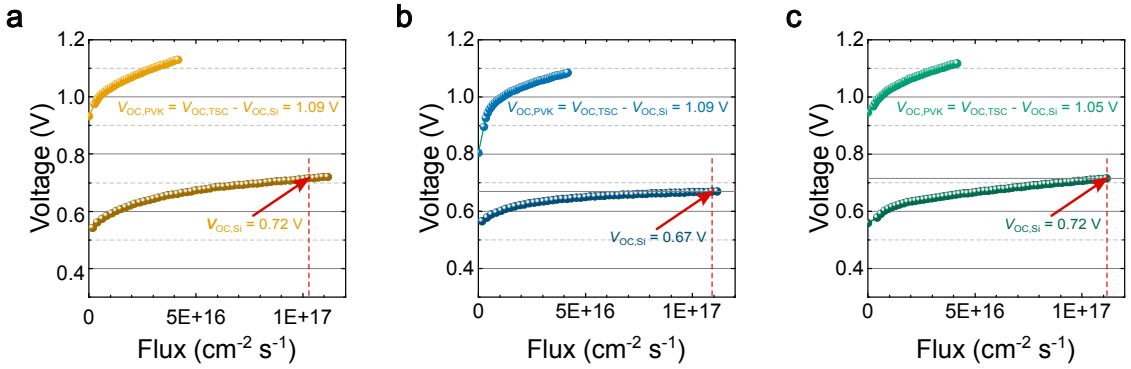

Figure 6.14: Suns-V_{OC} with selective illumination measurements of both sub-cells of corresponding tandem solar cells (TSCs) (**a** = planar, **b** = nano-textured and **c** = micro-textured). The V_{OC} contribution of the perovskite top cell ($V_{OC,PVK}$) is estimated by deducting the extracted V_{OC} of the silicon bottom cell ($V_{OC,Si}$) from the V_{OC} of the full TSC ($V_{OC,TSC}$) from current-voltage (J-V) characteristics (Table 6.4).

Figure 6.14 shows the corresponding Suns-V_{OC} with selective illumination measurements of the three tandem devices. Suns-V_{OC} with selective illumination is used to analyze the quality and contribution of both sub-cells in a tandem device independently.[51] Therefore, collimated LEDs with wavelengths of 450 nm and 920 nm are employed to selectively illuminate the perovskite top cell and the silicon bottom cell, respectively. Since the V_{OC} is proportional to the natural logarithm of the J_{SC}, which itself scales linearly with illumination intensity, a logarithmic dependence of voltage on light flux is expected for a well-functioning device. In contrast, shunted devices typically exhibit linear or sub-logarithmic behavior.[51] As shown in Figure 6.14a/b/c, a clear logarithmic voltage-flux relationship was observed for the perovskite top cells fabricated on all three bottom cell morphologies, indicating robust performance and minimal shunt leakage. When combined with EQE analysis, the illumination flux corresponding to 1 sun at the selected wavelengths (450 nm for the perovskite top cell and 940 nm for the silicon bottom cell) can be accurately determined. Consequently, the voltage measured at this flux corresponds to the V_{OC} of the respective sub-cell. The measured TSCs reveal a V_{OC} of the perovskite top cell of 1.09 V, 1.09 V and 1.05 V of the planar, nano-textured and micro-textured configuration.

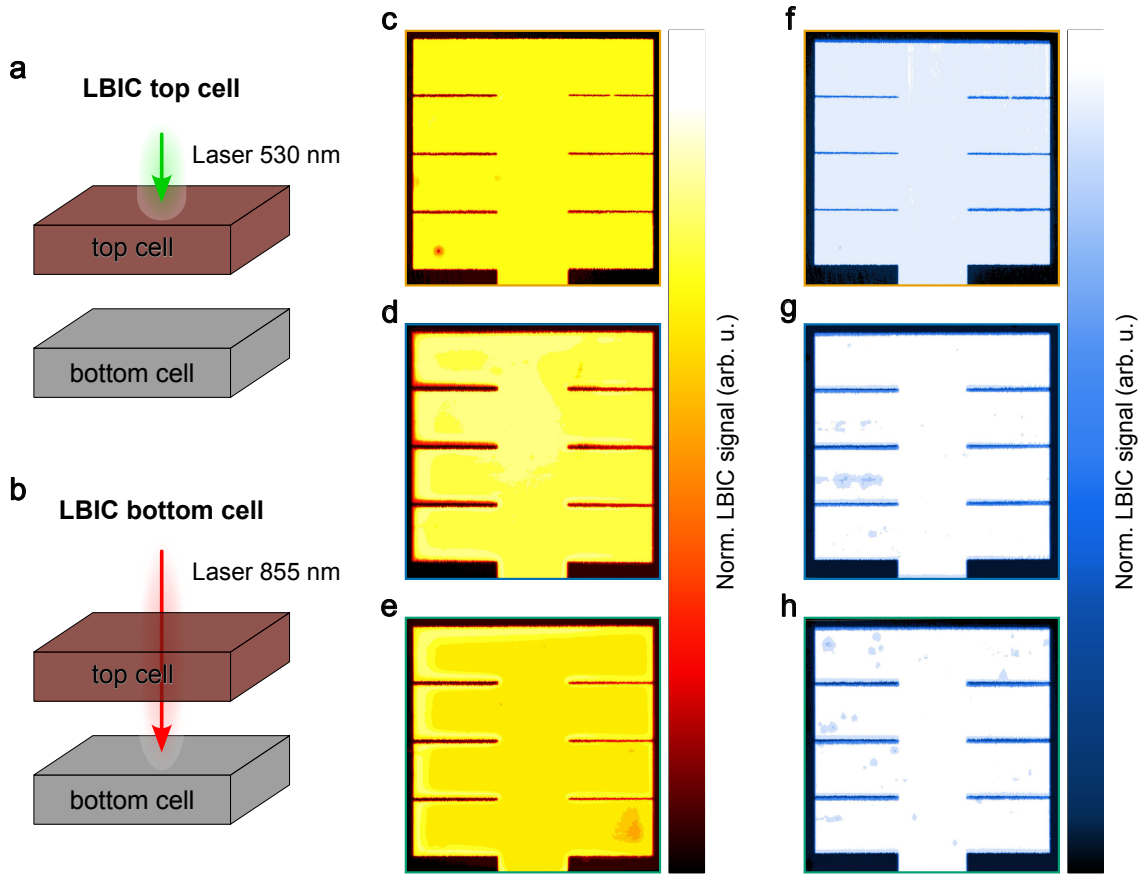

Figure 6.15: a/b Illustration of laser beam-induced current (LBIC)-mapping measurement setup with individual excitation of both sub-cells using lasers with different wavelengths of 530 nm and 855 nm for the perovskite top cell and silicon bottom cells, respectively. **c/d/e** LBIC-maps of the perovskite top cells for the three different tandem configurations planar, nano-textured and micro-textured, respectively. **f/g/h** Corresponding LBIC-maps of the silicon bottom cells for the three different tandem configurations planar, nano-textured and micro-textured, respectively.

The feasibility of fabricating homogeneous single-junction devices over a large area using CSS has already been demonstrated by Gomar-Fernández *et al.*[64] To assess the uniformity of CSS-processed perovskite absorbers on the differently textured silicon bottom cells, laser-beam induced current (LBIC)-mapping measurements of the fabricated tandem solar cells were conducted. By selectively exciting each sub-cell with lasers of different wavelengths (530 nm for the perovskite top cells and 855 nm for the silicon bottom cells) and scanning across the entire active area, the spatial homogeneity of charge carrier extraction can be evaluated (Figure 6.15a/b). The resulting LBIC-maps show homogeneous signals for all perovskite top cells in all configurations (planar, nano-textured, and micro-textured), indicating good coverage and comparable layer quality across all areas (Figure 6.15c-h). Visual dark spots on the silicon bottom cells imply the presence of particles that might have accumulated during processing or due to insufficient cleaning of the bottom cells (Figure 6.15f/h).

6.5.2 Analysis of Perovskite Growth on Different Silicon Bottom Cell Morphologies

Since the fabricated 2T perovskite/silicon TSCs show comparable device performances across different bottom cell morphologies, the growth and microstructural properties of the CSS-deposited perovskite absorber layers on the three different silicon bottom cells is investigated next using SEM, GIWAXS and k-imaging.

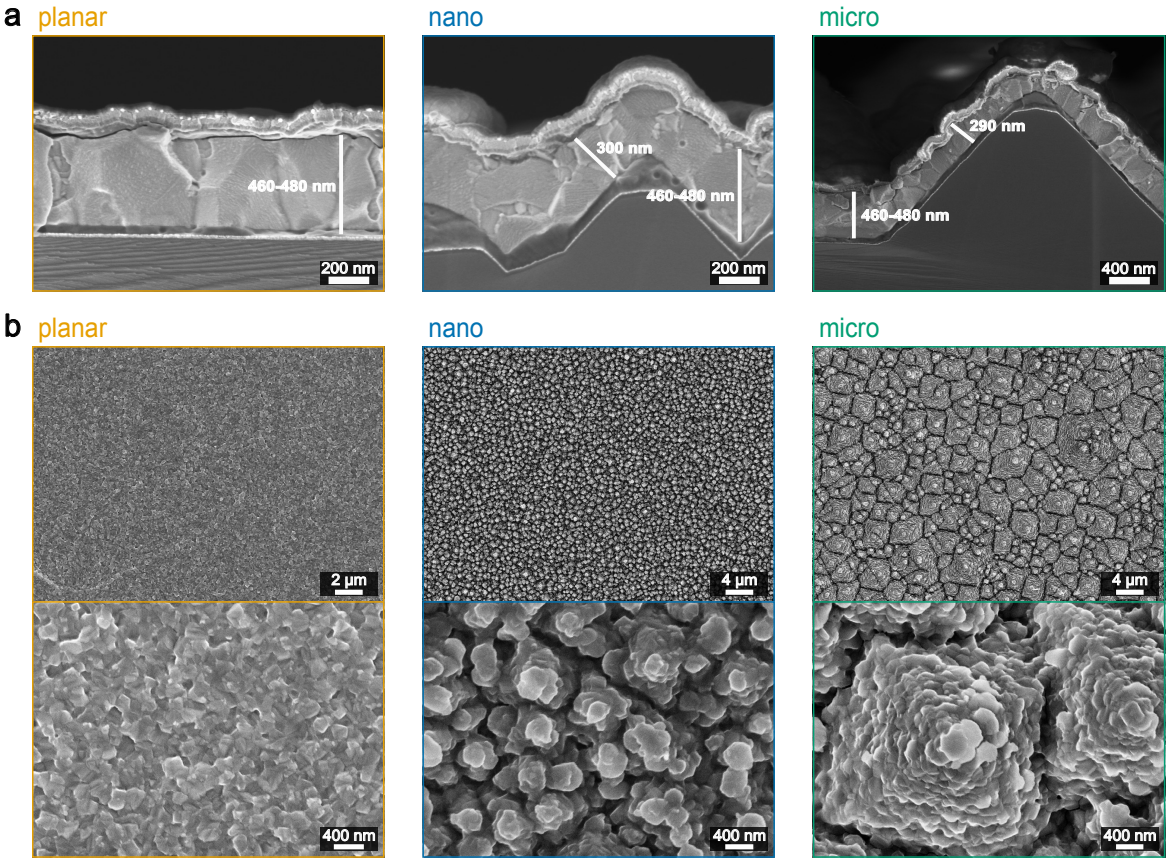

Figure 6.16: a Cross sectional scanning electron microscopy (SEM) images of different two-terminal (2T) perovskite/silicon tandem solar cells (TSCs) on planar, nano-textured and micro-textured silicon bottom cells, showing similar perovskite morphologies and layer thicknesses, as well as conformal coverage of the pyramids. **b** SEM surface images of the perovskite top cell deposited on the three different silicon bottom cells (planar, nano-textured and micro-textured), showing complete and homogeneous coverage over the whole area.

SEM analysis of the perovskite absorber layers allows for a comparison of their morphological properties across the different silicon bottom cells (Figure 6.16). Cross-sectional SEM images reveal similar perovskite layer morphologies across all configurations. Comparable horizontal grain sizes and columnar grain growth, comparable to the opaque reference (Figure 6.9) is detected in all three cases. Thickness measurements along the light incident direction reveal similar perovskite film thicknesses in the range of 460-480 nm across all configurations. However, when measuring perpendicular to the pyramid facets, a reduction in effective perovskite film thickness to approximately 300 nm is noted for the nano- and micro-textured substrates, as expected. Furthermore, the perovskite layer shows a conformal coverage of the textured silicon substrates (Figure 6.16a). Complete coverage is further confirmed by surface SEM imaging (Figure 6.16b). Due to the differently textured surfaces, a comparison of grain sizes from top-view images is difficult. However, none of the configurations show pinholes, larger defects of uncovered pyramids, indicating similar layer qualities independent of the underlying substrate.

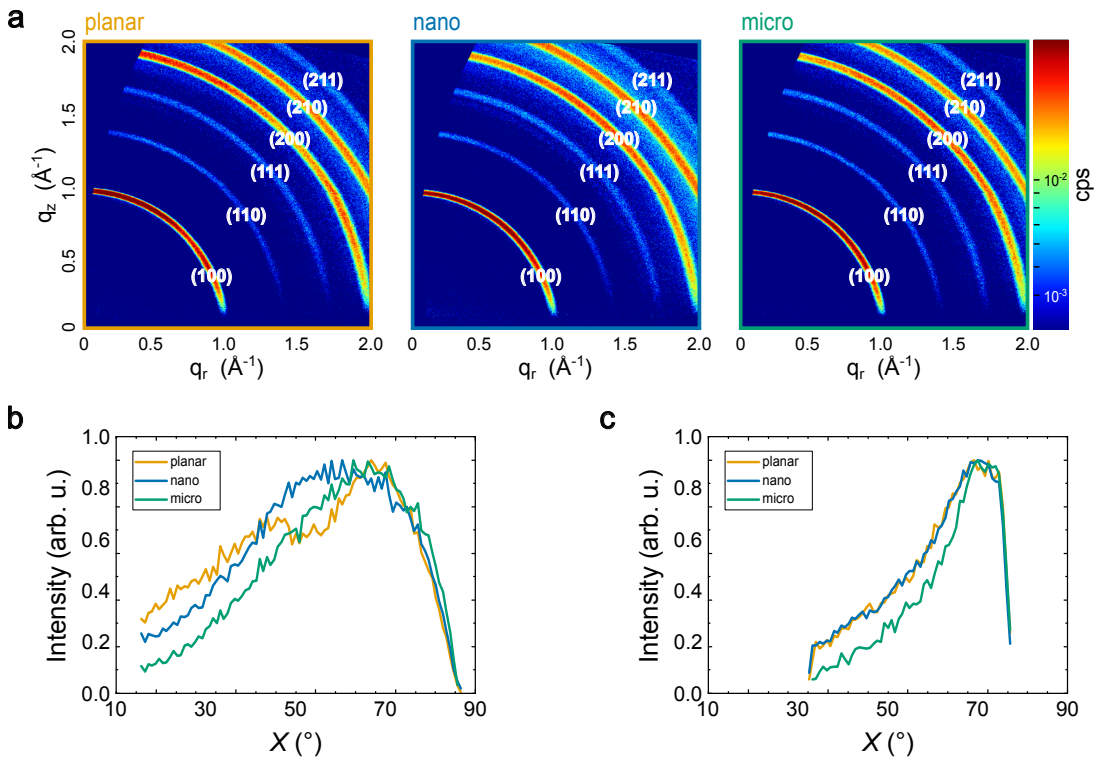

Figure 6.17: a Grazing-incident wide-angle X-ray scattering (GIWAXS) measurements of the deposited perovskite top cell on the three different silicon bottom cell morphologies (planar, nano-textured and micro-textured), with annotated crystal planes for the perovskite phase. **b/c** GIWAXS pole figure of the (100)- and (210)-perovskite plane, respectively, for all three configurations, indicating similar crystal orientations independent of the texture of the underlying silicon bottom cell.

GIWAXS measurements of the perovskite absorber layers deposited on the three different silicon bottom cells (planar, nano- and micro-textured) further show that not only morphological, but also microstructural properties of the perovskite layer are comparable across all configurations (Figure 6.17). The GIWAXS patterns presented in Figure 6.17a reveal similar crystallographic orientation for any of the configurations, independent of the silicon bottom cell morphology. This observation is further corroborated by the corresponding pole figures (Figure 6.17b/c), of the (100)- and (210)-perovskite planes, which confirm texture-independent growth across all samples. Moreover, the perovskite layers exhibit comparable degrees of crystallinity, as indicated by similar FWHM values of the (100)-perovskite diffraction peak (Figure A.22).

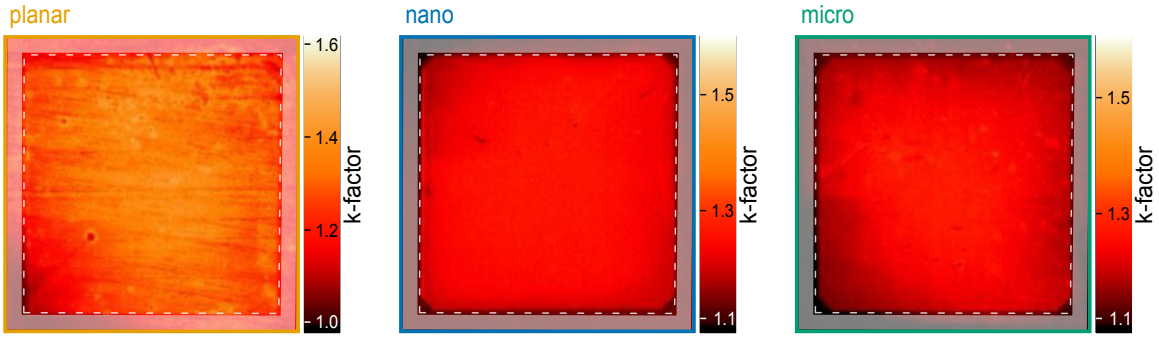

Figure 6.18: a Spatially resolved k-factor images derived from intensity-dependent photoluminescence (PL)-mapping of the active area (1 cm^2) of the deposited perovskite thin films on planar, nano-textured and micro-textured silicon bottom cell morphologies.

Previous LBIC-measurements of the fabricated perovskite/silicon tandem solar cells already proved homogeneous deposition of the CSS-processed perovskite layers over the whole active areas, independent of the silicon bottom cell morphology. Further analysis *via* spatially resolved k-imaging of the CSS-processed perovskite absorbers on the differently textured silicon bottom cells allow for an approximation of the k-factor of the perovskite thin films.[199, 200] The k-maps are obtained from intensity-dependent PL-mapping measurements. Interestingly, perovskite absorbers deposited on textured silicon bottom cells (nano-textured and micro-textured) exhibit slightly lower k-factors (~1.2-1.3) than perovskite absorbers deposited on planar silicon bottom cells (~1.3-1.4). This indicates, that perovskite absorbers on planar silicon might suffer from slightly higher non-radiative recombination losses than those deposited on textured silicon bottom cells. Nonetheless, the measured k-maps again prove a homogeneous deposition of the CSS-processed perovskite absorbers on all three silicon bottom cells.

These results demonstrate the potential of CSS to produce highly uniform perovskite films over large areas, independent of the underlying substrate texture. Combined with its ability to achieve comparable optoelectronic film properties and PSC performance across different silicon bottom cells without the need of adjusting deposition parameters, as well as the capability of fast processing, CSS emerges as a highly promising deposition technique for industry-compatible, scalable, and high-throughput manufacturing.

6.6 Summary

Close-space sublimation (CSS) is an alternative vapor-phase deposition method that holds promise for bridging the gap between laboratory-scale and industrial-scale fabrication of perovskite materials, particularly due to its scalable and fast processing capabilities. This chapter explores the potential of CSS to overcome the inherently low deposition rates of organic precursor materials, with the goal of fabricating WBG single-junction PSCs (research question **IV**). These perovskite absorbers are then integrated into monolithic perovskite/silicon TSCs to study the influence of differently textured silicon bottom cells on the growth of CSS-processed WBG perovskite absorbers, along with their impact on the overall performance of the final TSCs (research question **V**).

A two-step vapor phase deposition process comprising of the subsequent deposition of the inorganic scaffold from an effusion source and the CSS deposition of the organic precursor materials is employed in this chapter. One of the main differences of CSS to other two-step vapor phase deposition processes, the substrate is kept at elevated temperatures close to the temperature of the source, resulting in an *in-situ* conversion of the deposited inorganic scaffold to the perovskite phase during CSS deposition.

In the course of developing a suitable process sequence for the fabrication of WBG perovskite absorbers, it became evident that the preparation of mixed-halide perovskites *via* CSS is not straightforward. In vapor-phase deposition, the mixed-halide composition is typically controlled by adjusting the ratio of inorganic precursor salts (e.g.: PbI_2-to-$PbBr_2$ ratio) in combination with an iodine-containing organic salt, such as MAI or FAI. This approach however proved ineffective when using CSS for the organic deposition. During the conversion of pure PbI_2 and pure $PbBr_2$ ratios using a pure inorganic scaffolds with iodine organic sources (FAI and MAI), all resulting perovskite films exhibited a similar iodine-rich composition. Conversely, when pure PbI_2 scaffolds were converted using a pure bromine organic source, the resulting films consistently showed a bromine-rich composition, with only trace amounts of iodine remaining in the perovskite structure. These findings suggest that, in CSS, the halide composition of the organic source predominantly determines the final perovskite composition. This occurs independently of the halide ratio in the inorganic scaffold, likely due to a halide-exchange reaction during the CSS process.

In order to fabricate WBG perovskites, a reversed strategy was applied. Using a mixed halide organic source, in this case MAI:MABr, lead to the formation of a perovskite absorber with a bandgap of ~1.63 eV. This

approach was then used to fabricate PSCs in the *p-i-n* architecture. Remarkably, CSS deposition times of only 10 minutes are sufficient for full conversion of a 250 nm thick inorganic scaffold, showing the great potential for fast processing *via* CSS. It was found, that even though the perovskite is formed *in-situ* during the CSS deposition step, a post-annealing step of the CSS-processed perovskite layers leads to a strong improvement of the final PSC performance. PCEs of up to 18.5% were achieved with an optimized, fully vacuum-processed layer stack. These results are the highest reported PCE for fully vapor-phase-deposited $MAPbIBr_3$ PSCs in the *p-i-n* architecture with a bandgap > 1.6 eV.

These perovskite absorbers were then integrated into monolithic perovskite/silicon tandem solar cells. Using three different silicon bottom cell morphologies (planar, nanometer-sized and micrometer-sized pyramides), the growth behavior of CSS-processed perovskites was investigated. Noteworthy, independent of the underlying bottom cell, the perovskite absorber layer revealed comparable layer properties without the need to adjust perovskite process parameters to accomodate for the different bottom cell morphologies. This ability sets CSS apart from other vapor phase deposition methods that need adjustment of process parameters for different substrate morphologies. SEM and GIWAXS revealed similar grain sizes, crystallinity and crystal orientation across all bottom cell morphologies. Intensity-dependent PL-mapping further proved the capability of CSS to fabricate homogeneous perovskite films with comparable optoelectronic qualities across differently textured substrates. The fabricated 2T perovskite/silicon TSCs reached similar PCEs of 23.6%, 23.9% and 24.3% on planar, nano-textured and micro-textured silicon bottom cells, respectively. These values are comparable to the highest reported PCEs (24.5%) of 2T perovskite/silicon TSCs using vapor-phase-deposited perovskite top cells.

7 Conclusion and Outlook

7.1 Conclusion

The envisioned breakthrough of perovskite photovoltaics demands rapid progress in scalable fabrication methods. A major challenge remains in bridging the gap between laboratory-scale research and industrial-scale production, which is essential for commercialization. In this context, the development of industrially relevant deposition techniques for fast, repeatable and reproducible processing is critical. Sequential vapor phase deposition is a promising candidate for industrial manufacturing, considering reported PCEs of more than 26% and its ability to homogeneously deposit over large areas and textured substrates, which is especially important for 2T perovskite/silicon TSCs. However, vapor phase deposition processes suffer from challenging process control, reproducibility and repeatability issues on a laboratory scale as well as slow deposition rates of the organic precursor materials. In response, this work aims to improve the understanding of these challenges and to develop strategies to overcome them in order to fabricate highly efficient perovskite-based solar cells *via* sequential layer deposition processes. In the following, the results and findings addressing the five research questions formulated in Section 1.2 are discussed:

I. Analysis of sublimation behavior of FAI for improved reproducibility and repeatability of FAI-based vapor phase deposition processes

One of the major challenges in vapor phase deposition processes is the poor reproducibility and repeatability of experimental results. This significantly impedes rapid scientific progress and impedes commercialization. While numerous studies have investigated the sublimation behavior of MAI, corresponding studies on FAI are scarce. In Chapter 4, a comprehensive technological analysis of the sublimation behavior of FAI is conducted, focusing on two often overlooked parameters: (i) precursor particle size and (ii) sublimation crucible geometry. It is demonstrated that the particle size distribution of commercially available FAI powders substantially varies across different fabrication batches and even across bottles from the same fabrication batch. This leads to inconsistent experimental conditions in laboratory-scale processes, in which usually only a few grams of material are extracted from the precursor bottles for each deposition. Sublimation experiments show that variations in the particle size distribution strongly affect the directionality of the emitted FAI vapor flux when depositing from conical crucibles. This highlights the importance to homogenize the precursor particle size prior to deposition. This limitation can be overcome when using cylindrical crucibles, which show an overall more homogeneous emission profile. These features clearly position cylindrical crucibles as the preferred choice for achieving higher reproducible deposition even without prior homogenization of the precursor powder. However, exact specification of the used sublimation crucible geometry is not always provided in literature, even though it plays a crucial role. Further sublimation experiments with commonly employed inorganic precursor materials show that the effusion characteristics are material dependent. Furthermore, it is found that the deposition homogeneity over a substrate strongly depends on the exact layout of the vacuum chamber. Especially in multi-material sublimation processes (co-deposition or sequential layer deposition) the precise dimensions of the vacuum chamber play a critical role in ensuring homogeneous film formation. Variations in the emission profiles therefore lead to changes in the deposition homogeneity on the substrate for each material, resulting in non-homogeneous material ratios across larger areas. Commercial laboratory systems are usually designed with constant and fixed

lateral source-to-substrate distances for each sublimation source but vary depending on the supplier and chosen size of the vacuum chamber. An alternative setup with optimized source positions for each precursor material is proposed to overcome this intrinsic limitation. In summary, the results indicate that homogenization of the precursor powder in combination with cylindrical crucibles are advantageous for improving reproducibility of vapor phase deposition processes in laboratory-scale setups. Additionally, the material-specific behavior implies that vacuum chamber dimensions are of utmost importance since they significantly influence the deposition homogeneity.

II. Understanding substrate-dependent growth of sequentially deposited perovskite thin films

In sequential layer deposition processes perovskite phase formation is initiated during a thermal annealing step following the successive depositions. Here, the conversion reaction occurs at the interfaces of the subsequently deposited layers. This represents a fundamental distinction from co-deposition, where the initial crystallization occurs directly on the underlying surface. The perovskite formation in co-deposition processes was found to be strongly influenced by the underlying substrate, leading to the necessity of re-optimizing process parameters for different substrates to achieve comparable perovskite layer qualities. In Chapter 5, the influence of various HTLs on the formation of sequentially deposited pure $FAPbI_3$ perovskites in the *p-i-n* architecture is systematically investigated. Significant differences in the final perovskite quality are observed across different substrates. It is shown that the type of substrate not only impacts the perovskite formation but already affect the growth of the initially deposited PbI_2 layer. Changes in the morphological properties, such as the average surface roughness and size of the PbI_2 platelets, as well as in the microstructural properties, namely the orientation of the PbI_2 crystallites, are detected. It is found that the growth and layer properties of the initially deposited PbI_2 layer can be deliberately manipulated by adjusting process parameters, such as deposition rate and substrate temperature, during its deposition. A clear correlation between the obtained XRD pattern and the PCE of the fabricated PSCs on the different HTLs could be established. It is based on the microstructural properties of the inorganic layer on different HTLs, mainly the orientation of the deposited PbI_2 crystallites. This leads to a guideline plot for process optimization on different HTLs. These results prove, for the first time, a substrate-dependent perovskite formation for sequentially deposited perovskite thin films, providing in-depth understanding for sequential layer deposition processes. Using the developed two-step process, fully vacuum-processed $FAPbI_3$ PSCs with PCEs of up to 17.2% in the *p-i-n* architecture are achieved.

III. Compositional engineering for sequentially deposited wide-bandgap perovskite absorber layers

Efficient perovskite/silicon TSCs require WBG perovskite absorbers. Building upon the two-step deposition process developed for fabricating NBG $FAPbI_3$ PSCs in the *p-i-n* architecture, the next step involves bandgap tuning through compositional engineering. In contrast to co-deposition processes, sequential layer deposition offers several possibilities for the incorporation of additional precursor materials. Either by introducing additional deposition steps, leading to multi-step (> two) processes, or by incorporating additional precursor materials into one of the two existing steps, resulting in a co-deposition step. In Chapter 5, both approaches are explored to fabricate WBG perovskite thin films for TSCs. By incorporating different cesium-halide salts, either *via* co-deposition with PbI_2 or as a pre-deposited seed layer prior to the deposition of PbI_2, the PCE could be increased to 17.8% for a $FACsPbI_3$ perovskite composition. However, efficient perovskite/silicon TSCs require perovskite top cells with bandgaps in the range of 1.68 eV. To address this, a three-step deposition sequence is developed, consisting of the deposition of a cesium-halide seed layer, followed by a co-deposition step of PbI_2 and $PbBr_2$, and finally the deposition of FAI. This process enables the fabrication of PSCs with bandgaps up to 1.69 eV in the *p-i-n* architecture, achieving PCEs of ~16%. While the PCEs lack behind reported PCEs of vapor-phase-deposited WBG PSCs, the presented approach highlights the ease and applicability of compositional engineering in sequential layer deposition processes. The fabricated WBG perovskite absorbers are

integrated into planar 2T perovskite/silicon TSCs. Although the final tandem device exhibits a poor PCE of only 14%, the voltage-addition of the independent sub-cells confirmed successful technological integration. This device therefore serves as a proof-of-concept, highlighting the feasibility of the approach while underscoring the need for further optimization. Optimization of the WBG perovskite top cell performance and overall device architecture will further boost the performance of the 2T perovskite/silicon TSCs.

IV. Increasing deposition rates of organic precursor materials

To address the challenge of slow deposition rates of the organic precursors and limited potential to accelerate the deposition process, an alternative two-step vapor phase deposition approach, close-space sublimation (CSS) is explored in Chapter 6. This approach combines the deposition of the inorganic layer using conventional effusion sources, followed by a CSS-step of the organic precursors from a large area powder source. Here, the gap between the substrate and the source is reduced to a few millimeters. During CSS, the elevated substrate temperature during the deposition enables the *in-situ* conversion of the inorganic scaffold into the perovskite phase. In conventional vapor phase deposition, such as co-deposition or sequential layer deposition, bandgap tuning for the fabrication of WBG perovskites is usually achieved *via* the deposited inorganic precursors. Attempts to adjust the halide ratio in the CSS process solely through the inorganic scaffold proved ineffective due to halide-exchange reactions occurring during CSS deposition of the organic precursors. Using a reversed strategy by employing a mixed-halide organic source, it is found that the halide composition of the organic source predominantly dictates the final perovskite composition in CSS processes. Even though the exact mechanism behind this observed halide-exchange reaction is elusive, it reveals fundamental differences between conventional sequential vapor phase deposition and CSS-based processes. To fabricate WBG perovskite thin films using CSS, a mixed MAI:MABr organic source is used. The fabricated *p-i-n* PSCs employing these CSS-processed WBG absorbers yield PCEs around 14.5%. It is found, that an additional post-annealing step in ambient atmosphere with a controlled humidity (r.H. = 30%) after the perovskite deposition improves the performance of the PSCs to 16%. Optimization of the layer stack with a vacuum-processed $EDAI_2$ passivation layer and LiF as an anti-reflective coating further lead to a champion PCE of 18.5%. These values prove the great potential of CSS for the fabrication of efficient WBG PSCs. Additionally, CSS facilitates rapid deposition of the organic precursors. With deposition times of only 10 minutes being sufficient for complete conversion of a 250 nm thick inorganic scaffold, CSS outperforms any of the conventional vapor phase deposition methods in regard of organic deposition rate. Deposition rates could even be accelerated by further reducing the gap between the substrate and the organic precursor source. This fast-processing capability is critical for scalable manufacturing and positions CSS as a highly promising technique for industrial perovskite solar cell production.

V. Integration of fully vacuum-processed perovskite top cells into two-terminal perovskite/silicon tandem architectures

In order to investigate the potential of the CSS-processed perovskite absorbers as a top cell for perovskite/silicon TSCs, ST PSCs are fabricated, reaching similar PCEs compared to the opaque devices. These ST PSCs are integrated as top cells into 2T perovskite/silicon tandem architectures. Three different silicon bottom cells with varying surface morphologies, namely planar, nano-textured and micro-textured, are used to investigate the influence of differently textured substrates on the growth of the CSS-processed perovskite absorbers. The resulting PCEs of the fabricated 2T perovskite/silicon TSCs are comparable across all configurations, with record efficiencies of 23.6%, 23.9% and 24.3% achieved on planar, nano- and micro-textured silicon bottom cells, respectively. These values are comparable to the highest reported PCEs for TSCs utilizing vapor-phase-deposited perovskite top cells. While conventional vapor phase deposition methods typically require re-optimizaton of the process paramters when transitioning from planar to textured substrates, the CSS-processed perovskite top cells exhibit comparable optoelectronic properties independent of the employed silicon bottom cell morphology.

Characterization of the deposited perovskite thin films on the differently textured silicon bottom cells reveal that all perovskite films exhibit similar morphological and microstructural properties. This distinction from conventional vapor phase deposition methods highlights the great process robustness of CSS. Homogeneous and conformal perovskite coverage in all configurations further highlight the potential of CSS for scalable processing over larger areas. This robustness underscores the versatility of CSS as a promising approach for scalable and fast TSC fabrication.

7.2 Outlook

The overarching goal of this thesis is to advance the fundamental understanding of sequential vapor phase deposition processes for perovskite PV and to help address the key challenges that constrain reproducibility and scalability of this promising fabrication approach.

In Chapter 4 of this thesis, a technological analysis of the sublimation behavior of FAI reveals the influence of crucible geometry and precursor particle size on the emission profile, as well as the crucial role of vacuum chamber design on the deposition homogeneity. Consequently, transferring an established process from one setup to another is not straightforward and represents a major challenge for reproducibility and repeatability. Moreover, successful process optimization requires not only an understanding of precursor material properties, but also careful consideration of technological and mechanical aspects of the used vacuum deposition system. One of the persistent challenges of laboratory scale vapor phase deposition processes is the poor reproducibility and repeatability, a problem that is rarely discussed in the literature. As negative or non-reproducible results are seldom published, the field lacks systematic insights into the causes of process variability and transfer difficulties. The findings presented here suggest that more detailed reporting of experimental parameters including used sublimation crucible geometry and precise vacuum chamber dimensions would significantly improve the ability of other researchers to reproduce published results. Enhancing reproducibility and repeatability on a laboratory scale, by establishing clearer reporting standards and emphasizing transparent process documentation, could greatly accelerate progress in the rapidly evolving and highly promising field of vapor phase deposition of PSCs.

Chapter 5 discusses the first investigation of substrate-dependent perovskite growth of sequentially deposited perovskites, revealing strong differences in the final perovskite film properties. Future research should focus on a more detailed analysis of different substrate materials to gain a fundamental understanding of the chemical processes driving the conversion reaction in sequential layer deposition processes. By studying substrate-dependent reactions and interface interactions, valuable insights into the mechanisms governing the perovskite formation can be obtained. A further step will be the definition of substrate classes that exhibit comparable behavior to facilitate process optimization and enhance overall understanding of sequential layer deposition processes. This classification should not be limited to HTL materials only, but also include ETL materials, relevant for PSCs in the *n-i-p* architecture. Establishing such substrate classes could significantly simplify optimization cycles and enable more targeted process tuning across device architectures. While XRD has proven insufficient for a precise comparison of material compositions on different substrates, it nevertheless provides a useful guideline for process optimization. Combining XRD with complementary techniques such as X-ray photon spectroscopy (XPS) or Time-of-Flight Secondary Ion Mass Spectrometry (ToF-SIMs) will allow a more comprehensive understanding of film formation and interfacial reactions. *In-situ* analysis of the perovskite formation reaction during annealing can provide further insights into the exact reaction mechanisms occurring during the conversion. Another promising direction involves the optimization of deposition sequences for WBG perovskite absorbers, enabling the fabrication of tandem-relevant PSCs. Optimization of the employed tandem architecture offers substantial potential to further enhance PCE of sequentially deposited 2T perovskite/silicon TSC. A particular advantage of vapor phase deposition is its ability to conformally coat textured substrates,

which is especially relevant for integrating perovskite top cells on textured silicon bottom cells. Transition to textured silicon bottom cells for 2T perovskite/silicon TSCs should be the focus in the future. A recent report by Soufiani *et al.* shows the successful integration of a sequentially deposited WBG PSCs into a fully textured 2T perovskite/silicon tandem architecture, reaching PCEs around 24%.[102] While the fabricated TSC suffers from rather low V_{OC} and FF, it shows the potential of sequential layer deposition to fabricate efficient monolithic perovskite/silicon TSCs on non-planar surfaces. In addition, the demonstrated bandgap tunability of vapor-phase-deposited perovskites provides opportunities to adapt top cell properties for tandem configurations with various bottom cell materials, such as copper indium gallium selenide or low-bandgap perovskites. Finally, scalability remains an essential prerequisite for the industrial implementation of vapor phase deposition processes. The findings presented in this thesis, particularly regarding crucible effects and improved process control in sequential layer deposition, lay the groundwork for more homogeneous large-area deposition. Achieving this will be a decisive step toward reproducible, scalable, and high-performance perovskite solar modules.

In Chapter 6, an alternative sequential layer deposition method, CSS, was explored. CSS represents a highly promising alternative to overcome one of the main limitations of vapor-based perovskite fabrication methods, the slow deposition rates of organic precursor materials. By enabling approximately one order of magnitude higher deposition rates as compared to sublimation from effusion crucibles, CSS combines the inherent advantages of vapor phase deposition such as excellent film uniformity and conformal coverage over textured substrates with high-throughput processing. The results presented in this thesis for both single-junction PSCs and perovskite/silicon TSCs demonstrate that CSS is a versatile and robust technique for the fabrication of high-efficiency perovskite-based solar cells. Its compatibility with different absorber compositions and device architectures underlines its potential as a key process for scalable, high-throughput manufacturing. A crucial aspect that requires further investigation is the halide exchange reaction occurring during the sublimation and conversion of the organic precursors. A detailed understanding of this reaction is essential to enable precise process control and reproducibility. To this end, *in-situ* characterization methods, such as gas chromatography, mass spectrometry and photoluminescence, could provide valuable insights into the chemical dynamics within the CSS chamber. Future research should also focus on exploring alternative material compositions. This can be explored by integrating additional organic A-site cations, such as methylammonium chloride or different formamidinium halide salts, into the organic source during CSS. Additionally, introducing molecules for bulk-passivation, such as butylammonium iodide or propane-1,3-diammonium iodide, could improve the intrinsic film properties and quality. To further increase the overall deposition speed of CSS-based sequential vapor phase deposition processes, the CSS-deposition of inorganic precursors should be explored. In literature, deposition speeds of 10 μm/min for $CsPbBr_3$ have already been reported, showcasing the potential of CSS for the deposition of purely inorganic precursor materials. In general, CSS shows great potential as a cost-efficient and industrially scalable deposition technique. Therefore, future work should thus aim to transfer the process to large-area perovskite solar modules and perovskite/silicon tandem devices, paving the way for highly efficient and commercially viable PSC manufacturing.

A key challenge for perovskite PV remains long-term stability. Although stability was not the focus of this work, it represents a critical factor for future device performance and commercialization. Perovskite formation mechanisms from vapor phase deposition, both co-deposition and sequential layer deposition, differ significantly from those of solution-based fabrication processes. In combination with the absence of residual solvents in vapor-phase-deposited perovskites, these differences could lead to changes of the intrinsic material properties which can influence long-term stability of the PSCs. Consequently, long-term stability studies of sequentially deposited PSCs are of utmost importance for advancing these fabrication methods towards reliable and commercially viable applications and assess their suitability for real-world applications.

A Appendix

A.1 Author Contributions according to CRediT System

When publishing within collaborative research projects, CRediT (Contributor Roles Taxonomy) is a standardized framework to clearly define and acknowledge the specific contributions of each author to a research work and reduces disagreements between collaboration partners.[201] It defines 14 roles related to the process of a scientific work (Table A.1):

Table A.1: Overview of the categories used in this work to identify the contributions of different authors according to the contributor role taxonomy (CRediT) by Brand *et al.*[201]

Category	Definition
Conceptualization	Ideas; formulation or evolution of overarching research goals and aims
Methodology	Development or design of methodology; creation of models
Investigation	Conducting a research and investigation process, specifically performing the experiments, or data/evidence collection
Data Curation	Management activities to annotate (produce metadata), scrub data and maintain research data (including software code, where it is necessary for interpreting the data itself) for initial use and later reuse
Software	Programming, software development; designing computer programs; implementation of the computer code and supporting algorithms; testing of existing code components
Formal Analysis	Application of statistical, mathematical, computational, or other formal techniques to analyze or synthesize study data
Validation	Verification, whether as a part of the activity or separate, of the overall replication/reproducibility of results/experiments and other research outputs
Writing – Original Draft	Preparation, creation and/or presentation of the published work, specifically writing the initial draft (including substantive translation)
Writing – Review & Editing	Preparation, creation and/or presentation of the published work by those from the original research group, specifically critical review, commentary or revision – including pre- or post-publication stages
Visualization	Preparation, creation and/or presentation of the published work, specifically visualization/data presentation
Project Administration	Management and coordination responsibility for the research activity planning and execution
Funding Acquisition	Acquisition of the financial support for the project leading to this publication
Resources	Provision of study materials, reagents, materials, patients, laboratory samples, animals, instrumentation, computing resources, or other analysis tools
Supervision	Oversight and leadership responsibility for the research activity planning and execution, including mentorship external to the core team

Particle Size Matters – Impact of Particle Size and Crucible Geometry on Sublimation Behavior of Formamidinium Iodide

The research article "*Particle Size Matters – Impact of Particle Size and Crucible Geometry on Sublimation Behavior of Formamidinium Iodide*" was published in **Advanced Materials Technologies** (*doi.: 10.1021/acsenergylett.4c03315*) by Alexander Diercks (A.D.), Julian Petry (J.P.), Thomas Feeney (T.F.), Richard Thelen (R.T.), Paul Fassl (P.F.) and Ulrich W. Paetzold (U.W.P.). (cite) A.D. and J.P. contributed equally to this work.

Alexander Diercks and Julian Petry conceived the idea and developed research plans. Alexander Diercks and Julian Petry designed experiments and conducted their execution. Alexander Diercks conducted sublimation processes, characterizations and simulations. Julian Petry performed the analysis of FAI particle size distribution. Thomas Feeney helped with the sublimation processes. Richard Thelen provided the facilities and technical assistance for film thickness measurements. Julian Petry assisted in structuring the corresponding manuscript. Julian Petry, Paul Fassl and Thomas Feeney assisted in writing and editing the corresponding manuscript. Paul Fassl and Ulrich W. Paetzold supervised the project.

Table A.2: Author contributions according to the CRediT system – "*Particle Size Matters – Impact of Particle Size and Crucible Geometry on Sublimation Behavior of Formamidinium Iodide*"

Category	**Authors**	**Details**
Conceptualization	**A.D.** & J.P.	Original idea
Methodology	**A.D.** & J.P. & R.T.	R.T. assisted with white-light interferometry measurements
Investigation	**A.D.** & J.P.	–
Data Curation	**A.D.** & J.P.	–
Software		–
Formal Analysis	**A.D.** & J.P.	–
Validation	**A.D.** & J.P.	–
Writing – Original Draft	**A.D.** & J.P.	–
Writing – Review & Editing	**A.D.** & J.P. & P.F. % T.F.	–
Visualization	**A.D.** & J.P.	–
Project Administration	U.W.P. & P.F.	–
Funding Acquisition	U.W.P. & P.F.	–
Resources	U.W.P. & P.F. & R.T.	–
Supervision	U.W.P. & P.F.	–

Sequential Evaporation of Inverted $FAPbI_3$ Perovskite Solar Cells – Impact of Substrate on Crystallization and Film Formation

The research article "*Sequential Evaporation of Inverted $FAPbI_3$ Perovskite Solar Cells – Impact of Substrate on Crystallization and Film Formation*" was published in **ACS Energy Letters** (*doi.: 10.1021/acsenergylett.4c03315*) by Alexander Diercks (A.D.), Julian Petry (J.P.), Thomas Feeney (T.F.), Roja Singh (R.S.), Tonghan Zhao (T.Z.), Hang Hu (H.H.), Yang Li (Y.L.), Ulrich W. Paetzold (U.W.P.) and Paul Fassl (P.F.).[101]

Alexander Diercks conceived the idea and developed the research plans. Alexander Diercks designed the experiments and conducted their execution. Alexander Diercks conducted most sublimation processes, characterizations and data analysis. Julian Petry performed some sublimation processes of inorganics and assisted in data analysis. Thomas Feeney performed some FAI sublimation processes and X-ray diffraction measurements. Roja Singh performed X-ray diffraction measurements. Tonghan Zhao performed grazing-incident X-ray scattering measurements and assisted in data analysis. Hang Hu and Yang Li assisted in data analysis and structuring the manuscript. Julian Petry, Thomas Feeney and Paul Faßl assisted in writing and editing the corresponding manuscript. Paul Faßl and Ulrich W. Paetzold supervised the project.

Table A.3: Author contributions according to the CRediT system – "*Sequential Evaporation of Inverted $FAPbI_3$ Perovskite Solar Cells – Impact of Substrate on Crystallization and Film Formation*"

Category	Authors	Details
Conceptualization	**A.D.**	Original idea
Methodology	**A.D.**	–
Investigation	**A.D.** & J.P. & T.F. & R.S. & T.Z. & H.H. & Y.L.	T.F., R.S., T.Z., H.H. and Y.L assisted with characterization
Data Curation	**A.D.**	–
Software		–
Formal Analysis		–
Validation		–
Writing – Original Draft	**A.D.**	–
Writing – Review & Editing	**A.D.** & J.P. & T.F. & P.F. & U.W.P.	–
Visualization	**A.D.**	–
Project Administration	U.W.P. & P.F.	–
Funding Acquisition	U.W.P. & P.F.	–
Resources	U.W.P. & P.F.	–
Supervision	U.W.P. & P.F.	–

Close-Space Sublimation as a Versatile Deposition Process for Efficient Perovskite/Silicon Tandem Solar Cells

The research article "*Close-Space Sublimation as a Versatile Deposition Process for Efficient Perovskite/Silicon Tandem Solar Cells*" by Alexander Diercks (A.D.), Sofía Chozas-Barrientos (S.C.-B.), Lidón Gil-Escrig (L.G.-E.), Federico Ventosinos (F.V.), Inma Gomar-Fernández (I.G.-F.), Cristina Roldán-Carmona (C.R.-C.), Nathan Rodkey (N.R.), Tonghan Zhao (T.Z.), Julian Petermann (J.P.), Maximiliano Senno (M.Sen.) Perrine Carroy (P.C.), Delfina Muñoz (D.M.), Paul Fassl (P.F.), Michele Sessolo (M.Ses.), Ulrich W. Paetzold (U.W.P.) and Henk J. Bolink (H.J.B.) was accepted for publication in **Nature Energy** (*doi.: 10.1038/s41560-026-02068-9)*). A.D. and S.C.-B. contributed equally to this work.

Table A.4: Author contributions according to the CRediT system – "*Close-Space Sublimation - Versatile Deposition Process for Efficient Perovskite/Silicon Tandem Solar Cells*"

Category	**Authors**	**Details**
Conceptualization	**A.D.** & S.C.-B. & U.W.P. & H.J.B.	Original idea
Methodology	**A.D.** & S.C.B	–
Investigation	**A.D.** & S.C.B. & L.G.-E. & F.V. & I.G.-F. & C.R.-C. & T.Z. & J.P.	L.G.-E. & F.V. & I.G.-F. & C.R.-C. & T.Z. & J.P. & N.R. & M.Sen. & V.H. assisted with characterizations
Data Curation	**A.D.** & S.C.-B.	–
Software		–
Formal Analysis		–
Validation	**A.D.** & S.C.-B.	–
Writing – Original Draft	**A.D.** & S.C.-B.	–
Writing – Review & Editing	**A.D.** & S.C.-B. & U.W.P. & H.J.B.	–
Visualization	**A.D.**	–
Project Administration	U.W.P. & H.J.B.	–
Funding Acquisition	U.W.P. & H.J.B. & P.F.	–
Resources	U.W.P. & H.J.B. & M.Ses. & P.C. & D.M.	P.C. & D.M. provided the silicon bottom cells
Supervision	U.W.P. & H.J.B.	–

A.2 Supporting Information

Table A.5: Summary of all publications reporting on vapor phase deposition processes using FAI with respective material suppliers as stated in the corresponding publication (updated until 17.10.2025).[43, 52, 59, 98–102, 104, 106, 113–129]

Author	DOI	Year	PCE (%)	Eg (eV)	Process	FAI supplier
Tavakoli *et al.*	10.1088/1361-6463/aaebf1	2018	17.7	1.56	sequential dep.	not mentioned
Ji *et al.*	10.1039/d0tc01550d	2020	16.6	1.58	co-dep.	Sigma-Aldrich
Gil-Escrig *et al.*	10.1021/acsenergylett.0c01473	2020	18.8	1.53	co-dep.	Greatcell Solar Materials
Gil-Escrig *et al.*	10.1021/acsenergylett.0c02445	2021	16.2	1.71	co-dep.	Greatcell Solar Materials
Roß *et al.*	10.1002/aenm.202101460	2021	20.4	1.53	co-dep.	Greatcell Solar Materials
Feng *et al.*	10.1039/d1ee00634g	2021	21.31	1.57	sequential dep.	synthesized
Kroll *et al.*	10.1039/d2se00373b	2022	15.6	1.63	co-dep.	Sigma-Aldrich
Lin *et al.*	10.1002/adfm.202208392	2022	20.19	1.52	sequential dep.	Greatcell Solar Materials
Li *et al.*	10.1126/sciadv.abo7422	2022	24.42	1.55	sequential dep.	Greatcell Solar Materials
Lohmann *et al.*	10.1021/acsenergylett.2c00865	2022	19.3	1.55	co-dep.	Greatcell Solar Materials
Susic *et al.*	10.1021/acsenergylett.2c00304	2022	16.4	1.72	co-dep.	Greatcell Solar Materials
Chiang *et al.*	10.1021/acsenergylett.3c00564	2023	17.8	1.77	co-dep.	Greatcell Solar Materials
Susic *et al.*	10.1020/admi.202202271	2023	19.0	1.64	co-dep.	Greatcell Solar Materials
Yan *et al.*	10.1021/acsenergylett.3c01368	2023	19.8	1.58	co-dep.	Greatcell Solar Materials
Yuan *et al.*	10.1021/acsami.2c14658	2023	19.3	1.56	co-dep.	Dynamo
Lin *et al.*	10.1002/smll.202307960	2023	22.0	1.55	sequential dep.	Greatcell Solar Materials
Li *et al.*	10.1002/adfm.202211232	2023	24.36	1.53	sequential dep.	Greatcell Solar Materials
Leyden *et al.*	10.1002/solr.202400575	2024	19.8	1.61	co-dep.	Greatcell Solar Materials
Shih *et al.*	10.1016/j.solener.2024.112872	2024	15.7	1.61	co-dep.	Greatcell Solar Materials
Xu *et al.*	10.1002/adfm.202312037	2024	17.8	1.67	co-dep.	Greatcell Solar Materials
Feeney *et al.*	10.1016/j.matt.2024.02.004	2024	17.0	1.55	co-dep.	Greatcell Solar Materials
Zou *et al.*	10.1016/j.mtener.2024.101506	2024	15.01	1.54	sequential dep.	Greatcell Solar Materials
Zhou *et al.*	10.1016/j.joule.2024.02.019	2024	26.4	1.52	sequential dep.	Greatcell Solar Materials
Diercks *et al.*	10.1021/acsenergylett.4c03315	2025	17.8	1.56	sequential dep.	Greatcell Solar Materials
Nambiar *et al.*	10.1039/D5EL00017C	2025	21.0	1.55	sequential dep.	Dynamo
Siliavka *et al.*	10.1002/aenm.202500963	2025	18.34	1.5	sequential dep.	Sigma-Aldrich
Soufiani *et al.*	10.1002/solr.202500412	2025	16.0	1.7	sequential dep.	Dynamo
Feeney *et al.*	10.1002/adfm.202517873	2025	23	1.68	co-dep.	Dynamo

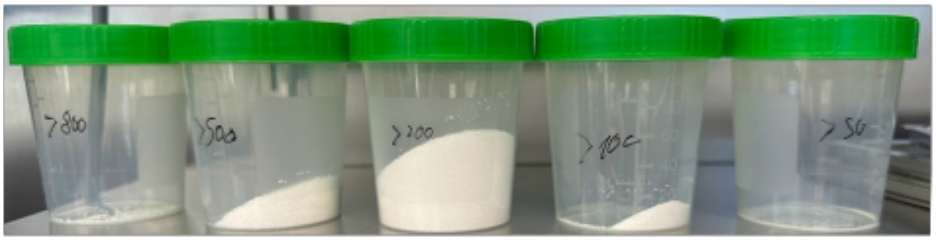

Figure A.1: Particle size distribution analysis of formamidinium iodide (FAI) precursor powder from Greatcell Solar Materials. The indicated fractions are obtained by using analytical sieves of different mesh sizes.

Table A.6: Measured layer thicknesses of the three defined particle size fractions of formamidinium iodide after deposition from conical and cylindrical crucibles, as well as of lead iodide and cesium iodide.

Position	**FAI small** conical	**FAI mid** conical	**FAI big** conical	**FAI small** cylind.	**FAI mid** cylind.	**FAI big** cylind.	**PbI_2** cylind.	**CsI** cylind.
75.6	–	–	–	400	375	300	639	475
103.9	570	510	490	400	380	310	456	436
132.2	320	340	380	250	250	330	387	358
160.5	164	175	190	230	210	200	361	301
188.8	140	170	190	220	190	150	240	243
217.1	120	150	140	125	115	100	187	197
245.4	40	60	130	100	90	80	143	162

Table A.7: A- and n-values for the used fit function of all used materials depending on the used crucible geometry for material deposition.

Material	**Crucible geometry**	**A-value**	**n-value**
FAI small	conical	1.10 E8	12.15
FAI mid	conical	7.96 E7	8.46
FAI big	conical	6.92 E7	6.45
FAI small	cylindrical	4.51 E7	4.05
FAI mid	cylindrical	4.34 E7	4.34
FAI big	cylindrical	3.69 E7	3.52
PbI_2	cylindrical	6.84 E7	4.59
CsI	cylindrical	5.04 E7	2.93

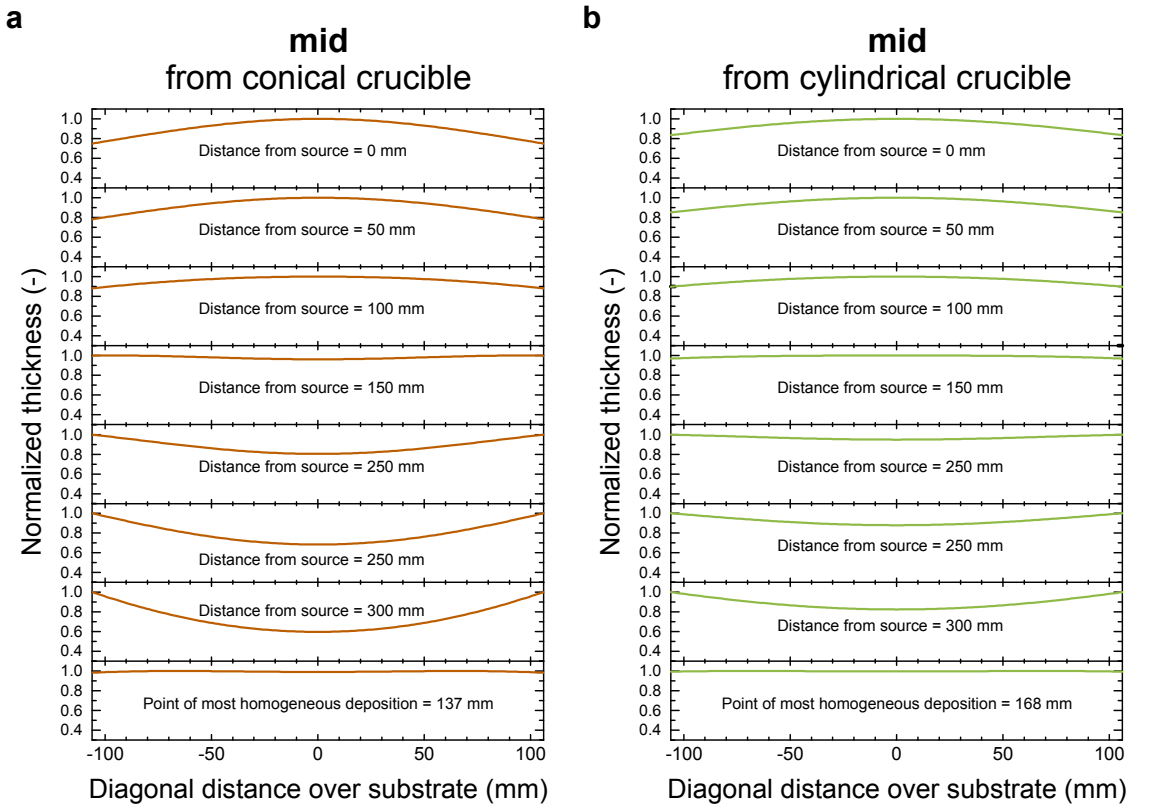

Figure A.2: Diagonal thickness profiles over substrate at different lateral source-to-substrate distances (0 mm, 50 mm, 100 mm, 150 mm, 200 mm, 250 mm, 300 mm, and point of most homogeneous deposition) for the FAI mid particle size fraction (**a** = from conical crucible, **b** = from cylindrical crucible).

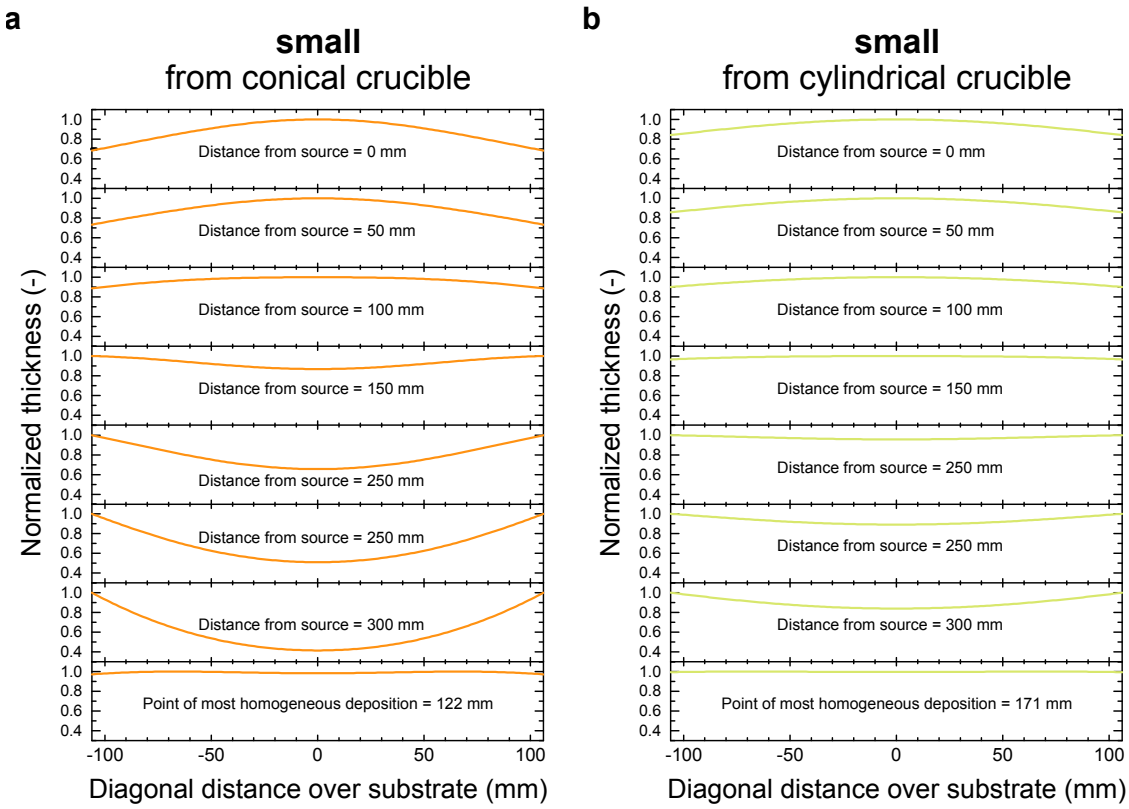

Figure A.3: Diagonal thickness profiles over substrate at different lateral source-to-substrate distances (0 mm, 50 mm, 100 mm, 150 mm, 200 mm, 250 mm, 300 mm, and point of most homogeneous deposition) for the small particle size fraction (**a** = from conical crucible, **b** = from cylindrical crucible).

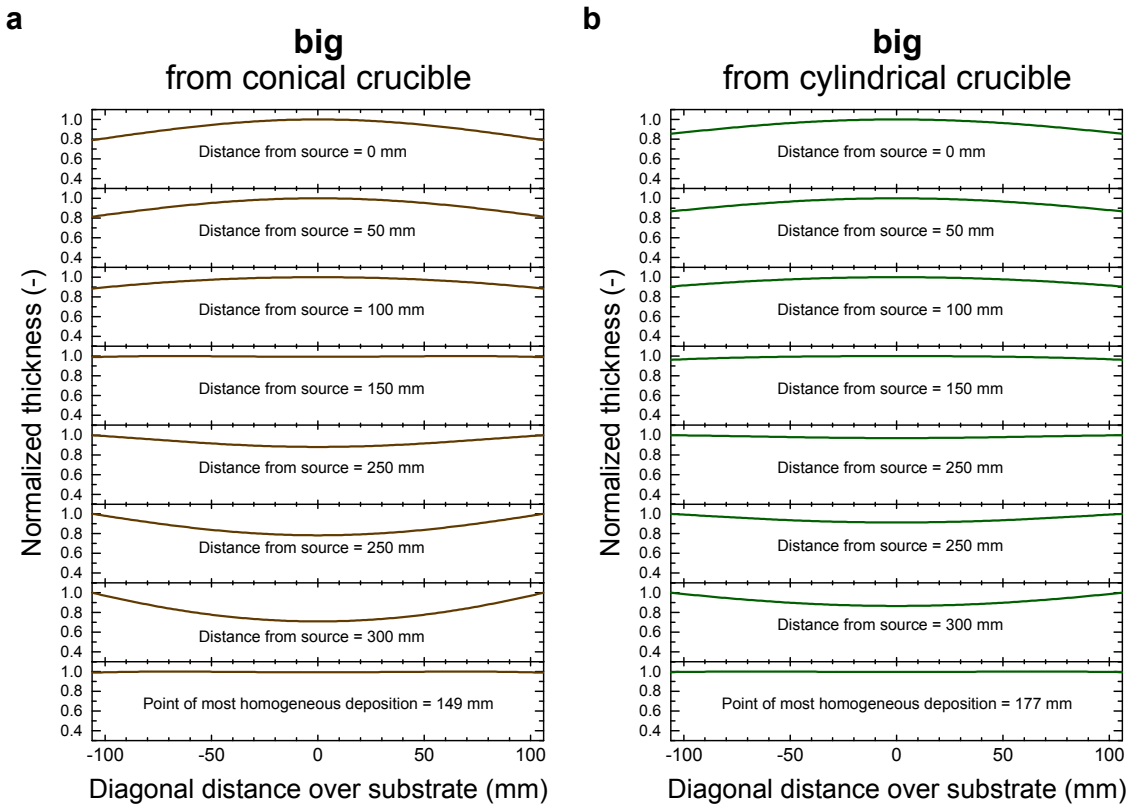

Figure A.4: Diagonal thickness profiles over substrate at different lateral source-to-substrate distances (0 mm, 50 mm, 100 mm, 150 mm, 200 mm, 250 mm, 300 mm, and point of most homogeneous deposition) for the big particle size fraction (**a** = from conical crucible, **b** = from cylindrical crucible).

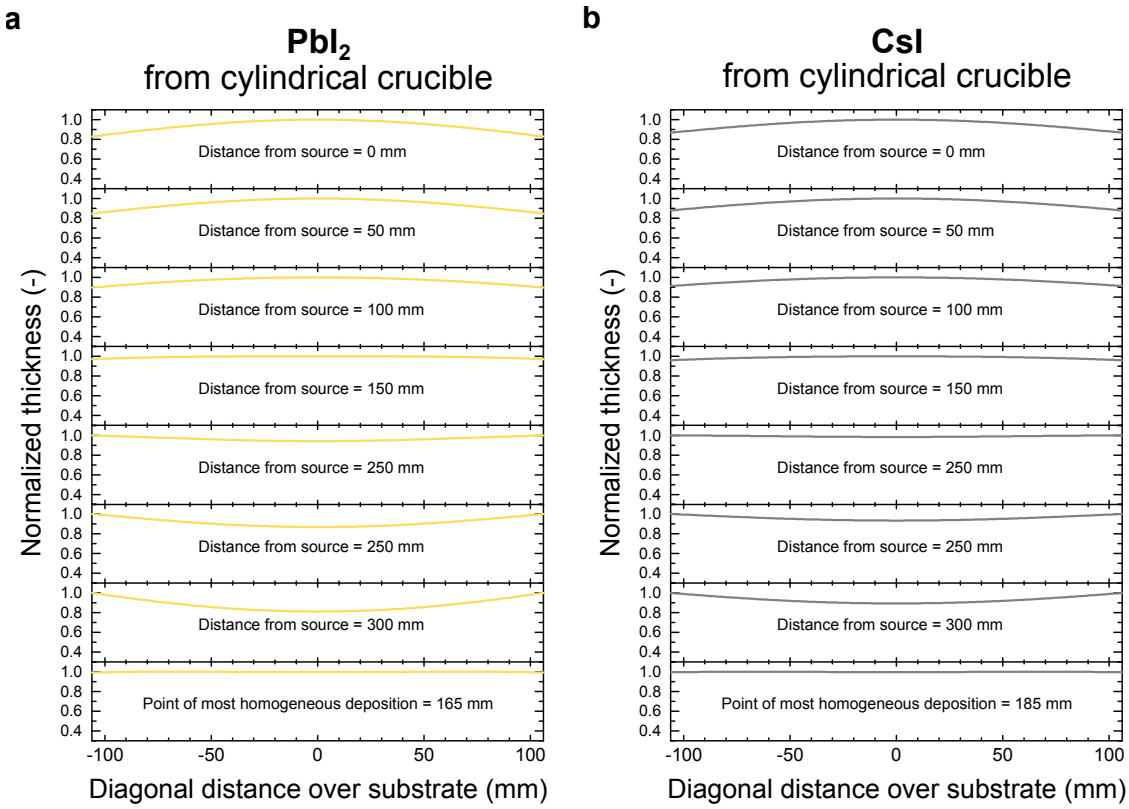

Figure A.5: Diagonal thickness profiles over substrate at different lateral source-to-substrate distances (0 mm, 50 mm, 100 mm, 150 mm, 200 mm, 250 mm, 300 mm, and point of most homogeneous deposition) for the inorganic precursors PbI_2 and CsI deposited from cylindrical crucibles (**a** = PbI_2, **b** = CsI).

Table A.8: Summary of all publications on sequential layer deposition processes with corresponding photovoltaic parameters (updated until 17.10.2025).[43, 100–103, 111, 113, 115, 116, 122, 126–128, 130–137]

Author	DOI	Year	Cell arch.	Perovskite composition	PCE [%]
Chen *et al.*	10.1002/adma.201402461	2014	*p-i-n*	$MAPbI_{3-x}Cl_x$	15.4
Yang *et al.*	10.1039/c5ta01824b	2015	*n-i-p*	$MAPbI_{3-x}Cl_x$	16.03
Ng *et al.*	10.1039/c4ta05070c	2015	*n-i-p*	$MAPbI_3$	12.5
Hsiao *et al.*	10.1002/adma.201601505	2016	*n-i-p*	$MAPbI_3$	17.6
Tavakoli *et al.*	10.1039/c6qm00379f	2017	*n-i-p*	$MAPbI_3$	15.9
Tavakoli *et al.*	10.1088/1361-6463/aaebf1	2018	*n-i-p*	$MAFAPbI_{3-x}Cl_x$	17.7
Tavakoli *et al.*	10.1002/pssr.202000449	2020	*p-i-n*	$MAPbI_3$	19.4
Tavakoli *et al.*	10.1002/solr.202000552	2020	*n-i-p*	$MAPbI_3$	20.3
Choi *et al.*	10.1002/solr.202100415	2021	*n-i-p*	$MAPbI_3$	18.5
Feng *et al.*	10.1039/D1EE00634G	2021	*n-i-p*	$FACsPbI_3$	21.31
Smecca *et al.*	10.1039/d1ta02535j	2021	*p-i-n*	$MAPbI_3$	17.48
Lin *et al.*	10.1002/adfm.202208392	2022	*n-i-p*	$FAPbI_3$	20.19
Li *et al.*	10.1126/sciadv.abo7422	2022	*n-i-p*	$FACsPbI_{3-x}Cl_x$	24.42
Lin *et al.*	10.1002/smll.202307960	2023	*n-i-p*	$FACsPbI_{3-x}Cl_x$	22.0
Li *et al.*	10.1002/adfm.202211232	2023	*n-i-p*	$FACsPbI_{3-x}Cl_x$	24.36
Zou *et al.*	10.1016/j.mtener.2024.101506	2024	*p-i-n*	$FAPbI_{3-x}Cl_x$	15.01
Zhou *et al.*	10.1016/j.joule.2024.02.019	2024	*n-i-p*	$MAFACsPbI_{3-x}Cl_x$	26.41
Diercks *et al.*	10.1021/acsenergylett.4c03315	2025	*p-i-n*	$FAPbI_3$	17.2
Diercks *et al.*	10.1021/acsenergylett.4c03315	2025	*p-i-n*	$FACsPbI_3$	17.8
Nambiar *et al.*	10.1039/D5EL00017C	2025	*p-i-n*	$FACsPbI_3$	21.0
Siliavka *et al.*	10.1002/aenm.202500963	2025	*p-i-n*	$FAPbI_3$	18.34
Soufiani *et al.*	10.1002/solr.202500412	2025	*p-i-n*	$FACsPbI_{3-x}Br_x$	16.0

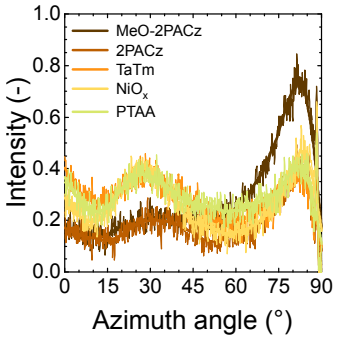

Figure A.6: Grazing-incident wide-angle X-ray scattering (GIWAXS) pole figures of vacuum-deposited PbI_2 layers on different hole transport layers (HTLs).

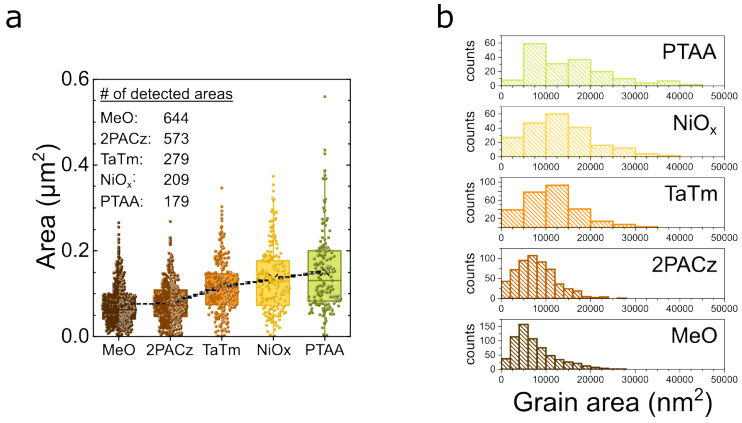

Figure A.7: Grain size analysis of fabricated $FAPbI_3$ perovskite thin films on different hole transport layers (HTLs). The individual grain areas were determined using the software ImageJ.

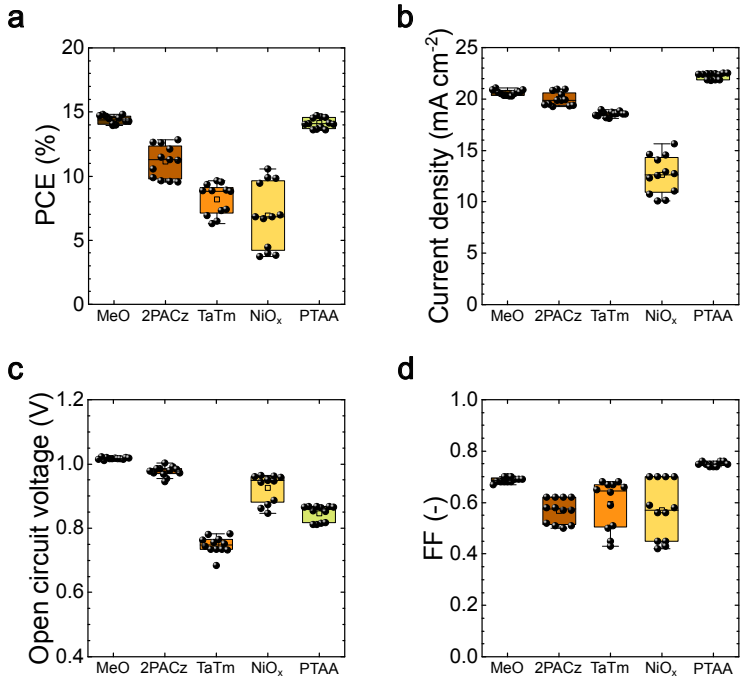

Figure A.8: Boxplot statistics of $FAPbI_3$ perovskite solar cells (PSCs) fabricated on different hole-transport layers (HTLs).

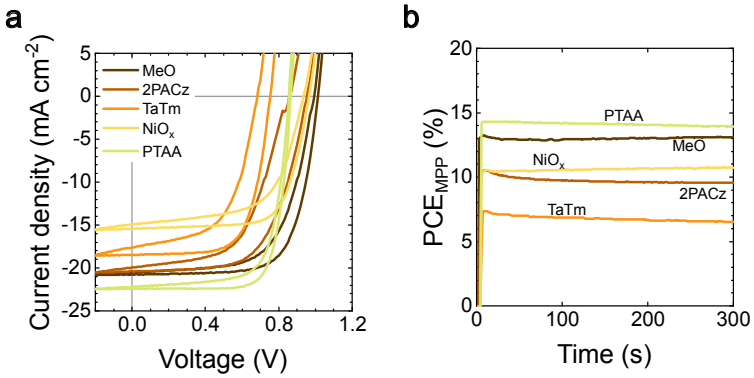

Figure A.9: Current-voltage (*J-V*)characteristics (**a**) of perovskite solar cells (PSCs) fabricated on different hole-transport layers (HTLs) and (**b**) corresponding maximum power point (MPP)-tracking for 300 seconds.

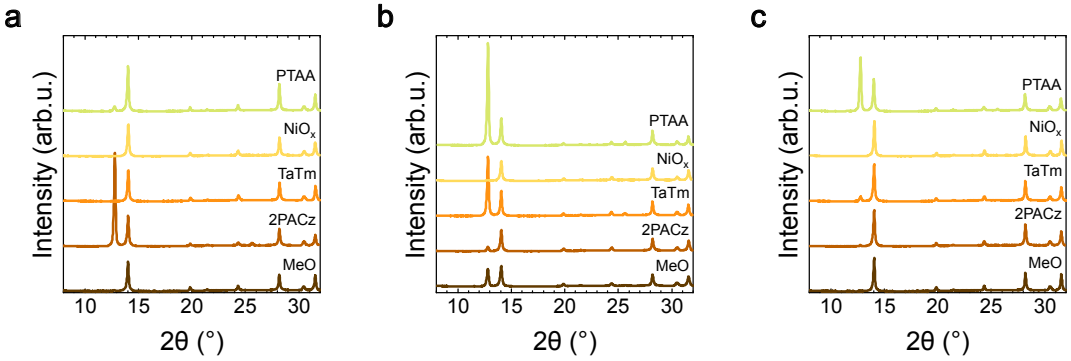

Figure A.10: X-ray diffraction (XRD) pattern for different formamidinium iodide (FAI) to lead iodide (PbI_2) thickness ratios, increasing from **a** = -6%, to **b** = standard and **c** = +6%.

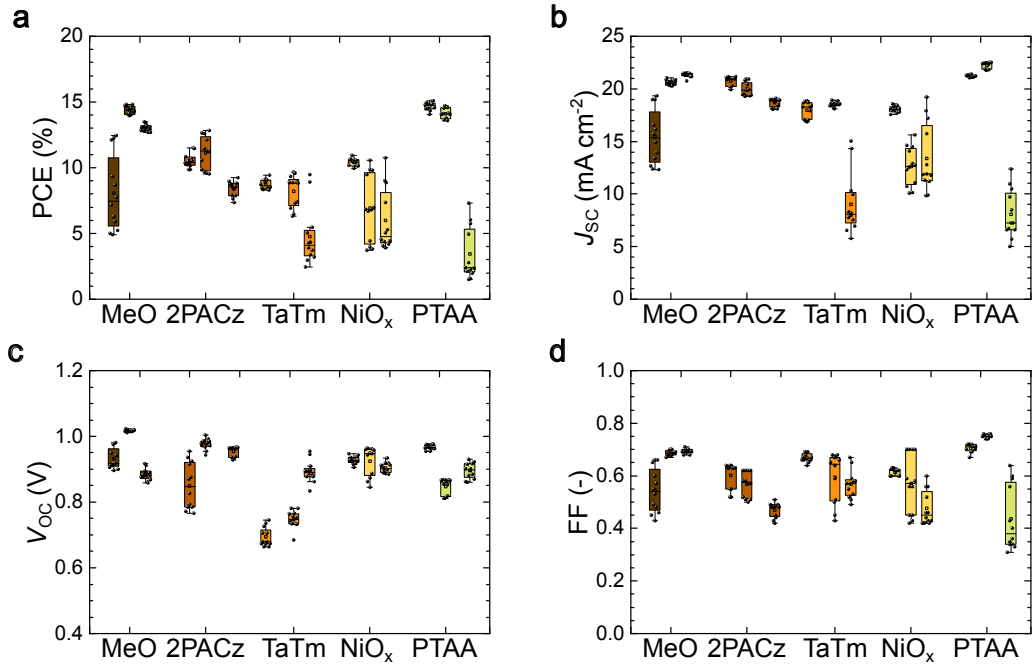

Figure A.11: Boxplot statistics for PSCs on different HTLs fabricated with different formamidinium iodide (FAI) to lead iodide (PbI_2) thickness ratios increasing from left to right (-6%, standard, +6%).

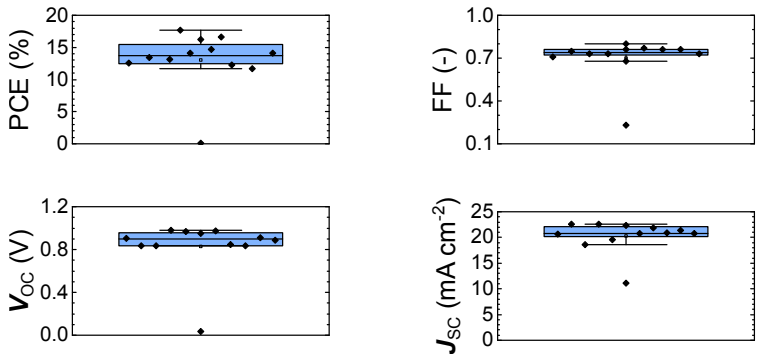

Figure A.12: Boxplot statistics for fabricated $FA_{0.85}Cs_{0.15}PbI_3$ PSCs on MeO-2PACz.

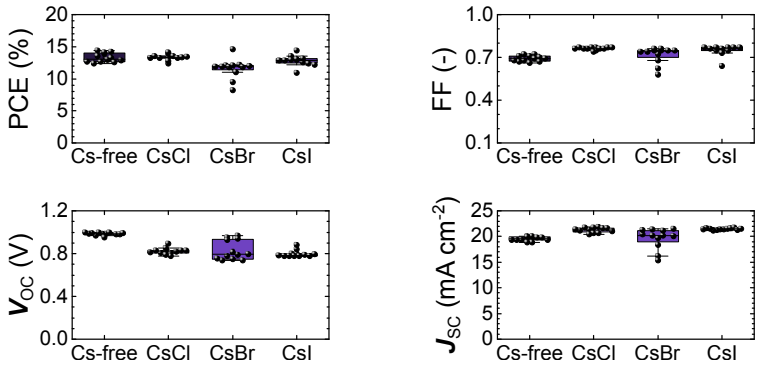

Figure A.13: Boxplot statistics for fabricated narrow-bandgap (NBG) PSCs on different cesium halide (CsX) seedlayers on MeO-2PACz.

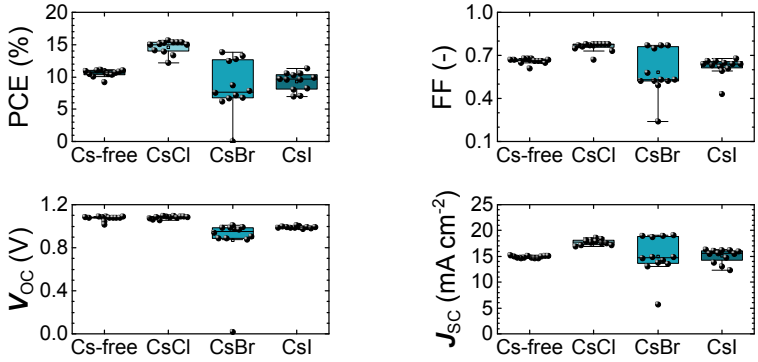

Figure A.14: Boxplot statistics for fabricated wide-bandgap (WBG) PSCs on different cesium halide (CsX) seedlayers on MeO-2PACz.

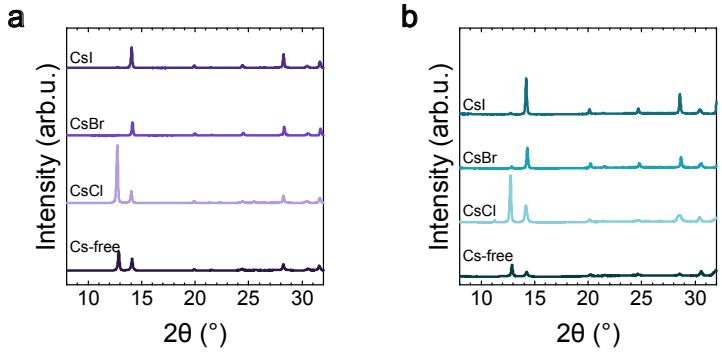

Figure A.15: X-ray diffraction (XRD) pattern for (**a**) narrow-bandgap (NBG) and (**b**) wide-bandgap (WBG) perovskite thin films fabricated on different cesium halide (CsX) seedlayers.

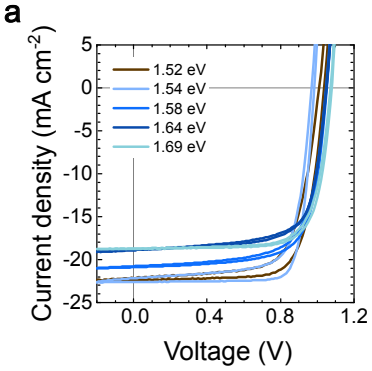

b

Perovskite composition	Bandgap (eV)	PCE (%)	FF (%)	J_{SC} (mA cm^{-2})	V_{OC} (V)
$FAPI_3$	1.52 eV	17.2	79.9	22.5	1.01
$FA_{0.85}Cs_{0.15}PbI_3$	1.54 eV	17.8	80.4	22.6	0.98
$FA_{0.85}Cs_{0.15}Pb(I_{0.95}Br_{0.5})_3$	1.58 eV	15.8	72.0	20.9	1.05
$FA_{0.85}Cs_{0.25}Pb(I_{0.78}Br_{0.22})_3$	1.64 eV	14.2	71.5	19.5	1.05
$FA_{0.85}Cs_{0.15}Pb(I_{0.71}Br_{0.24}Cl_{0.05})_3$	1.69 eV	15.3	75.6	18.8	1.08

Figure A.16: Current-voltage (*J-V*) characteristics of best-performing perovskite solar cells (PSCs) with different bandgaps (E_g = 1.52, 1.54, 1.58, 1.64 and 1.69 eV) fabricated during the span of this thesis.

Table A.9: Summary of publications on close-space sublimation processes employing solution-processed or solvent-free organic sources with corresponding photovoltaic parameters (updated until 17.10.2025).[63, 64, 137, 169–183, 185–189]

Author	**DOI**	**Year**	**Cell arch.**	**Organic source [wet/dry]**	**Perovskite**	**PCE [%]**
Li *et al.*	10.1002/pssr.201510386	2016	*n-i-p*	wet	$MAPbI_3$	15.4
Guo *et al.*	10.1039/c5ee03620h	2016	*n-i-p*	wet	$MAPbI_3$	16.03
Lin *et al.*	10.1016/j.nanoen.2019.03.014	2019	*n-i-p*	wet	$MAPbI_3$	17.3
Deng *et al.*	10.1039/d0se00088d	2020	*n-i-p*	wet	$FA_{0.76}Cs_{0.24}PbI_zBr_z$	17.66
Harding *et al.*	10.1039/d0ra01640c	2020	*n-i-p*	wet	$MAPbI_3$	12.1
Pérez-Gutierrez *et al.*	10.1039/c5ee03620h	2020	*n-i-p*	wet	$MAPbI_zCl_{3-z}$	10.06
Smecca *et al.*	10.1039/d1ta02535j	2020	*p-i-n*	wet	$MAPbI_3$	17.48
Luo *et al.*	10.1016/j.scib.2021.01.031	2021	*n-i-p*	wet	Rb-$Cs_{0.14}FA_{0.86}PbI_zBr_{3-z}$	19.6
Niu *et al.*	10.1002/solr.202100102	2021	*n-i-p*	wet	Rb-$Cs_{0.14}FA_{0.86}PbI_zBr_{3-z}$	19.6
Kuba *et al.*	10.1021/acsaem.2c01468	2022	*n-i-p*	wet	$MAPbI_3$	14.1
Zhang *et al.*	10.1021/acsaem.2c00132	2022	*n-i-p*	wet	$FA_{0.86}Cs_{0.14}PbI_zBr_{3-z}$	20.45
Luo *et al.*	10.1016/j.mssp.2023.107603	2022	*n-i-p*	wet	$FAPbI_3$	20.91
Zou *et al.*	10.1021/acsomega.3c00318	2023	*p-i-n*	wet	$FA_xCs_yPbI_zBr_{3-z}$	17.1
Wang *et al.*	10.1002/adma.202304625	2023	*p-i-n*	wet	$FA_xCs_yPbI_zBr_{3-z}$	21.9
Zhao *et al.*	10.1002/solr.202300062	2023	*n-i-p*	wet	$FA_xCs_yPbI_zBr_{3-z}$	20.8
Tie *et al.*	10.1021/acsaem.3c00676	2023	*n-i-p*	wet	$FA_xCs_yPbI_3$	21.27
Zhang *et al.*	10.1039/d4se00320a	2024	*n-i-p*	wet	$FA_xCs_yPbI_zBr_{3-z}$	21.09
Fan *et al.*	10.1021/acsaem.4c00080	2024	*n-i-p*	wet	$FA_xCs_yPbI_zBr_{3-z}$	21.29
Wang *et al.*	10.1002/adma.202401416	2024	*n-i-p*	wet	3D/2D $FA_xCs_yPbI_zBr_{3-z}$	25.25
Hu *et al.*	10.1016/j.cej.2024.156259	2024	*n-i-p*	wet	$FA_xCs_yPbI_zBr_{3-z}$	21.54
Guesnay *et al.*	10.1002/aenm.202303423	2024	*p-i-n*	wet	$FA_xCs_yPbI_zBr_{3-z}$	16.82
Rodkey *et al.*	10.1021/acsenergylett.3c02792	2024	*n-i-p*	dry	$FA_xCs_yPbI_zCl_{3-z}$	18.7
Duan *et al.*	10.1002/adfm.202313435	2024	*n-i-p*	wet	$FA_xCs_yPbI_3$	22.11
Kim *et al.*	10.1002/solr.202400859	2025	*n-i-p*	wet	$MAPbI_{3-x}Cl_x$	16.41
Gomar-Fernández *et al.*	10.1002/adma.201402461	2025	*p-i-n*	dry	$MAPbI_{3-x}Cl_x$	18.8

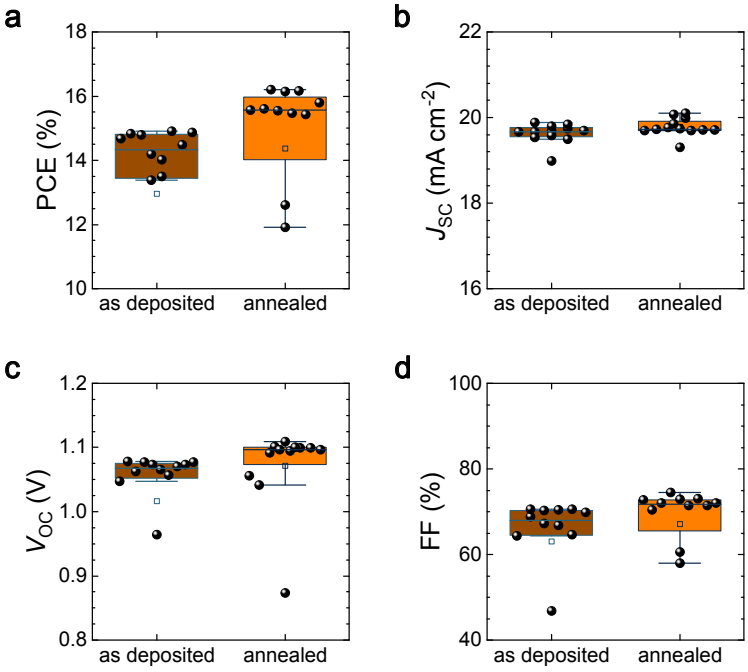

Figure A.17: Boxplot statistics for CSS-processed wide-bandgap (WBG) perovskite solar cells (PSCs) fabricated with as deposited and annealed perovskite absorber layers.

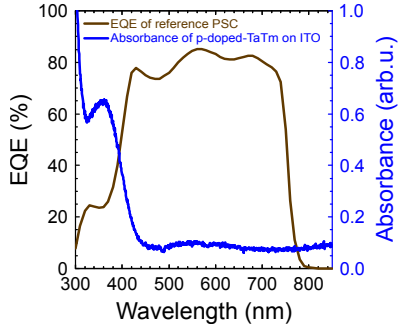

Figure A.18: Absorbance measurement of thick p-doped TaTm hole-transport layer (HTL) over an exemplary external quantum efficiency (EQE) measurement of a CSS-processed wide-bandgap (WBG) perovskite solar cell (PSC) to explain the poor EQE response at lower wavelengths.

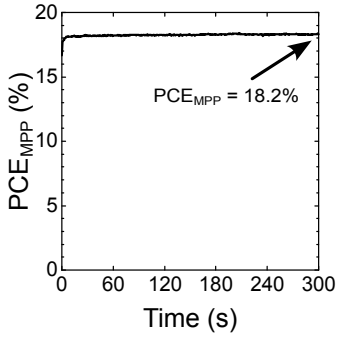

Figure A.19: Maximum power point (MPP)-tracking of CSS-processed champion perovskite solar cell with an optimized layer stack, showing a stable performance of 18.2%.

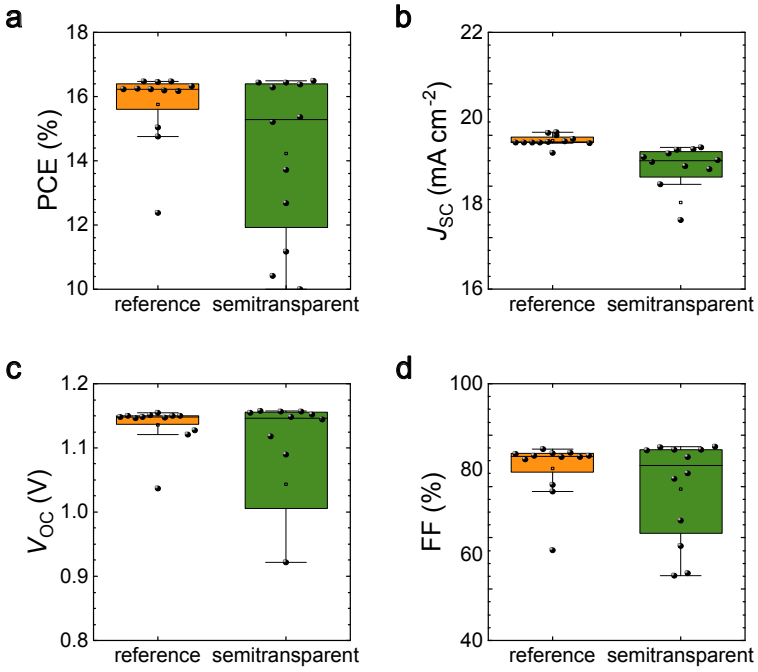

Figure A.20: Boxplot statistics for CSS-processed wide-bandgap (WBG) perovskite solar cells (PSCs) fabricated in the opaque and semitransparent (ST) device architecture.

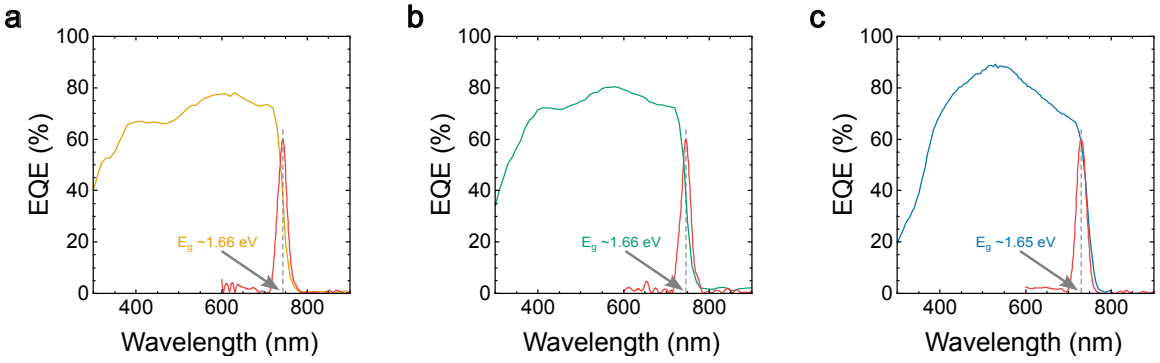

Figure A.21: Bandgap determination from external quantum efficiency (EQE) measurements of the perovskite top cell fabricated on the three differently textured silicon bottom cells (**a** = planar, **b** = nano-textured and **c** = micro-textured).

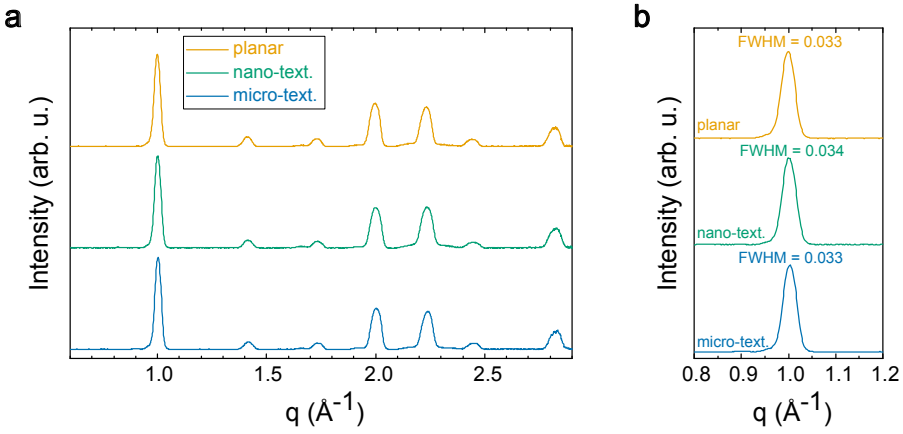

Figure A.22: **a** 2D Grazing-incident wide-angle X ray scattering (GIWAXS) patterns of two-terminal perovskite/silicon tandem solar cells (TSCs) on different silicon bottom cells. **b** (100) perovskite peak on different silicon bottom cell morphologies with corresponding full width at half maximum (FWHM).

List of Figures

List of Tables

Bibliography

[1] Anand S. Subbiah et al. “High-Performance Perovskite Single-Junction and Textured Perovskite/Silicon Tandem Solar Cells via Slot-Die-Coating”. In: *ACS Energy Letters* 5 (2020), pp. 3034–3040. DOI: 10.1021/acsenergylett.0c01297.

[2] R. Saidur et al. “A review on global wind energy policy”. In: *Renewable and Sustainable Energy Reviews* 14 (2010), pp. 1744–1762. ISSN: 1364-0321. DOI: https://doi.org/10.1016/j.rser.2010.03.007.

[3] Fiseha Mekonnen Guangul et al. “Solar Energy as Renewable Energy Source: SWOT Analysis”. In: *2019 4th MEC International Conference on Big Data and Smart City (ICBDSC)* (2019), p. 2934. DOI: 10.1109/ICBDSC.2019.8645580.

[4] S. Philipps et al. *Photovoltaics Report at Fraunhofer ISE*. https://www.ise.fraunhofer.de/de/veroeffentlichungen/studien/photovoltaics-report.html [Zugriff am: 2025-10-10]. 2025.

[5] LONGi Green Energy Technology Co. *LONGi Sets New World-Record for Silicon Solar Cell Efficiency*. https://www.longi.com/en/news/longi-hi-mo9-bc-world-record. (accessed 2025-10-10). 2024.

[6] Hua Wu et al. “Silicon heterojunction back-contact solar cells by laser patterning”. In: *Nature* 635 (Nov. 2024), pp. 604–609. ISSN: 0028-0836. DOI: 10.1038/s41586-024-08110-8.

[7] National Renewable Energy Laboratory (NREL). *Best Research-Cell Efficiency Chart*. https://www.nrel.gov/pv/cell-efficiency [Zugriff am: 2025-10-10]. 2025.

[8] Martin A. Green et al. “Solar Cell Efficiency Tables (Version 66)”. In: *Progress in Photovoltaics: Research and Applications* 33 (7 2025), pp. 795–810. DOI: 10.1002/pip.3919.

[9] Armin Richter et al. “Reassessment of the Limiting Efficiency for Crystalline Silicon Solar Cells”. In: *IEEE Journal of Photovoltaics* 3 (4 2013), pp. 1184–1191. ISSN: 2156-3381. DOI: 10.1109/JPHOTOV.2013.2270351.

[10] Zhengjie Chen et al. “A Study of the Performance of Submerged Arc Furnace Smelting of Industrial Silicon”. In: *Silicon* 10 (2018), pp. 1121–1127. ISSN: 1876-9918. DOI: 10.1007/s12633-017-9584-3.

[11] Tobias Abzieher et al. “Vapor phase deposition of perovskite photovoltaics: short track to commercialization?” In: *Energy & Environmental Science* 17 (5 2024), pp. 1645–1663. ISSN: 1754-5692. DOI: 10.1039/D3EE03273F.

[12] T. Jesper Jacobsson et al. “An open-access database and analysis tool for perovskite solar cells based on the FAIR data principles”. In: *Nature Energy* 7 (1 Dec. 2021), pp. 107–115. ISSN: 2058-7546. DOI: 10.1038/s41560-021-00941-3.

[13] Jian Gong et al. “Perovskite photovoltaics: life-cycle assessment of energy and environmental impacts”. In: *Energy and Environmental Science* 8 (7 2015), pp. 1953–1968. DOI: 10.1039/C5EE00615E.

[14] Prashat V. Kamat. “Evolution of Perovskite Photovoltaics and Decrease in Energy Payback Time”. In: *The Journal of Physical Chemistry Letters* 4 (21 2013), pp. 3733–3734. DOI: 10.1021/jz402141s.

[15] Samuel D. Stranks et al. “Electron-Hole Diffusion Lengths Exceeding 1 Micrometer in an Organometal Trihalide Perovskite Absorber”. In: *Science* 342 (6156 Oct. 2013), pp. 341–344. ISSN: 0036-8075. DOI: 10.1126/science.1243982.

[16] Stefaan De Wolf et al. “Organometallic Halide Perovskites: Sharp Optical Absorption Edge and Its Relation to Photovoltaic Performance”. In: *The Journal of Physical Chemistry Letters* 5 (6 Mar. 2014), pp. 1035–1039. ISSN: 1948-7185. DOI: 10.1021/jz500279b.

[17] Marina R. Filip et al. “Steric engineering of metal-halide perovskites with tunable optical band gaps”. In: *Nature Communications* 5 (1 Dec. 2014), p. 5757. ISSN: 2041-1723. DOI: 10.1038/ncomms6757.

[18] E. L. Unger et al. “Roadmap and roadblocks for the band gap tunability of metal halide perovskites”. In: *Journal of Materials Chemistry A* 5 (23 2017), pp. 11401–11409. ISSN: 2050-7488. DOI: 10.1039/C7TA00404D.

[19] Xueyu Tian et al. “Life cycle energy use and environmental implications of high-performance perovskite tandem solar cells”. In: *Science Advances* 6 (31 2020), eabb0055. DOI: 10.1126/sciadv.abb0055.

[20] Moritz H. Futscher et al. “Efficiency Limit of Perovskite/Si Tandem Solar Cells”. In: *ACS Energy Letters* 1 (4 2016), pp. 863–868. ISSN: 2380-8195. DOI: 10.1021/acsenergylett.6b00405.

[21] Felix Lang et al. “Revealing Fundamental Efficiency Limits of Monolithic Perovskite/Silicon Tandem Photovoltaics through Subcell Characterization”. In: *ACS Energy Letters* 6 (11 2021), pp. 3982–3991. ISSN: 2380-8195. DOI: 10.1021/acsenergylett.1c01783.

[22] Bruno Ehrler et al. “Photovoltaics Reaching for the Shockley–Queisser Limit”. In: *ACS Energy Letters* 5 (9 2020), pp. 3029–3033. ISSN: 2380-8195. DOI: 10.1021/acsenergylett.0c01790.

[23] Fabrizio Gota et al. “Energy Yield Modelling of Textured Perovskite/Silicon Tandem Photovoltaics with Thick Perovskite Top Cells”. In: *Optics Express* 30 (9 Apr. 2022), pp. 14172–14188. ISSN: 1094-4087. DOI: 10.1364/OE.447069.

[24] LONGi Green Energy Technology Co. *34.85% LONGi Breaks World Record for Crystalline Silicon-Perovskite Tandem Solar Cell Efficiency Again*. https://www.longi.com/en/news/silicon-perovskite-tandem-solar-cells-new-world-efficiency. (accessed 2025-10-10). 2025.

[25] Akihiro Kojima et al. “Organometal Halide Perovskites as Visible-Light Sensitizers for Photovoltaic Cells”. In: *Journal of the American Chemical Society* 131 (17 2009), pp. 6050–6051. ISSN: 0002-7863. DOI: 10.1021/ja809598r.

[26] Qi Jiang et al. “Surface Reaction for Efficient and Stable Inverted Perovskite Solar Cells”. In: *Nature* 611 (7936 2022), pp. 278–283. ISSN: 0028-0836. DOI: 10.1038/s41586-022-05268-x.

[27] Do-Kyoung Lee et al. “Materials and Methods for High-Efficiency Perovskite Solar Modules”. In: *Solar RRL* 6 (3 2022), p. 2100455. ISSN: 2367-198X. DOI: 10.1002/solr.202100455.

[28] Florian Mathies et al. “Multipass Inkjet Printed Planar Methylammonium Lead Iodide Perovskite Solar Cells”. In: *Journal of Materials Chemistry A* 4 (48 2016), pp. 19207–19213. ISSN: 2050-7496. DOI: 10.1039/C6TA07972E.

[29] Florian Mathies et al. “Advances in Inkjet-Printed Metal Halide Perovskite Photovoltaic and Optoelectronic Devices”. In: *Energy Technology* 8 (4 2020), p. 1900991. ISSN: 2194-4296. DOI: 10.1002/ente.201900991.

[30] Helge Eggers et al. “Inkjet-Printed Micrometer-Thick Perovskite Solar Cells with Large Columnar Grains”. In: *Advanced Energy Materials* 10 (6 2020), p. 1903184. ISSN: 1614-6832. DOI: 10.1002/aenm.201903184.

[31] Yehao Deng et al. “Scalable Fabrication of Efficient Organolead Trihalide Perovskite Solar Cells with Doctor-Bladed Active Layers”. In: *Energy & Environmental Science* 8 (5 2015), pp. 1544–1550. ISSN: 1754-5692. DOI: 10.1039/C4EE03907F.

[32] Hanlin Hu et al. “Room-Temperature Meniscus Coating of >20% Perovskite Solar Cells: A Film Formation Mechanism Investigation”. In: *Advanced Functional Materials* 29 (25 2019), p. 1900092. ISSN: 1616-3028. DOI: 10.1002/adfm.201900092.

[33] Jinxin Yang et al. “Ink Engineering in Blade-Coating Large-Area Perovskite Solar Cells”. In: *Advanced Energy Materials* 12 (28 2022), p. 2200975. ISSN: 1614-6832. DOI: 10.1002/aenm.202200975.

[34] James E. Bishop et al. “Fully Spray-Coated Triple-Cation Perovskite Solar Cells”. In: *Scientific Reports* 10 (2020), p. 6610. ISSN: 2045-2322. DOI: 10.1038/s41598-020-63674-5.

[35] Hongkun Cai et al. “High Efficiency over 20% of Perovskite Solar Cells by Spray Coating via a Simple Process”. In: *ACS Applied Energy Materials* 3 (10 2020), pp. 9696–9702. ISSN: 2574-0962. DOI: 10.1021/acsaem.0c01129.

[36] Li-Hui Chou et al. “Progress in Spray Coated Perovskite Films for Solar Cell Applications”. In: *Solar RRL* 6 (4 2022), p. 2101035. ISSN: 2367-198X. DOI: 10.1002/solr.202101035.

[37] Rahul Patidar et al. “Slot-Die Coating of Perovskite Solar Cells: An Overview”. In: *Materials Today Communications* 22 (2020), p. 100808. ISSN: 2352-4928. DOI: 10.1016/j.mtcomm.2019.100808.

[38] Ke Xu et al. “Slot-Die Coated Triple-Halide Perovskites for Efficient and Scalable Perovskite/Silicon Tandem Solar Cells”. In: *ACS Energy Letters* 7 (10 2022), pp. 3600–3611. ISSN: 2380-8195. DOI: 10.1021/acsenergylett.2c01506.

[39] Jinzhao Li et al. “Ink Design Enabling Slot-Die Coated Perovskite Solar Cells with >22% Power Conversion Efficiency, Micro-Modules, and 1 Year of Outdoor Performance Evaluation”. In: *Advanced Energy Materials* 13 (33 2023), p. 2203898. ISSN: 1614-6832. DOI: 10.1002/aenm.202203898.

[40] Julian Petry et al. “Industrialization of Perovskite Solar Cell Fabrication: Strategies to Achieve High-Throughput Vapor Deposition Processes”. In: *EES Solar* 1 (1 July 2025), pp. 404–418. ISSN: 3033-4063. DOI: 10.1039/D5EL00069F.

[41] Mingzhen Liu et al. “Efficient planar heterojunction perovskite solar cells by vapour deposition”. In: *Nature* 501 (7467 Sept. 2013), pp. 395–398. ISSN: 0028-0836. DOI: 10.1038/nature12509.

[42] Ezra Alvianto et al. “Industry-Compatible Fully Laminated Perovskite-CIGS Tandem Solar Cells with Co-Evaporated Perovskite”. In: *Advanced Materials* (Sept. 2025). ISSN: 15214095. DOI: 10.1002/adma.202505571.

[43] Junjie Zhou et al. “Highly efficient and stable perovskite solar cells via a multifunctional hole transporting material”. In: *Joule* 8 (6 June 2024), pp. 1691–1706. ISSN: 25424351. DOI: 10.1016/j.joule.2024.02.019.

[44] Luisa Quintino. “Overview of coating technologies”. In: *Surface Modification by Solid State Processing* (2014), pp. 1–24. DOI: 10.1533/9780857094698.1.

[45] Andresa Baptista et al. “Sputtering Physical Vapour Deposition (PVD) Coatings: A Critical Review on Process Improvement and Market Trend Demands”. In: *Coatings* 8 (11 2018), p. 402. ISSN: 2079-6412. DOI: 10.3390/coatings8110402.

[46] Yana Vaynzof. “The Future of Perovskite Photovoltaics—Thermal Evaporation or Solution Processing?” In: *Advanced Energy Materials* 10 (48 Dec. 2020), p. 2003073. ISSN: 1614-6832. DOI: 10.1002/aenm.202003073.

[47] Felix Utama Kosasih et al. “Thermal evaporation and hybrid deposition of perovskite solar cells and mini-modules”. In: *Joule* 6 (12 Dec. 2022), pp. 2692–2734. ISSN: 25424351. DOI: 10.1016/j.joule.2022.11.004.

[48] David B. Ritzer et al. “Upscaling of perovskite solar modules: The synergy of fully evaporated layer fabrication and all-laser-scribed interconnections”. In: *Progress in Photovoltaics: Research and Applications* 30 (4 Apr. 2022), pp. 360–373. ISSN: 1062-7995. DOI: 10.1002/pip.3489.

[49] Lidón Gil-Escrig et al. “Fully Vacuum-Processed Perovskite Solar Cells on Pyramidal Microtextures”. In: *Solar RRL* 5 (1 Jan. 2021). ISSN: 2367-198X. DOI: 10.1002/solr.202000553.

[50] Marcel Roß et al. “Co-Evaporated Formamidinium Lead Iodide Based Perovskites with 1000 h Constant Stability for Fully Textured Monolithic Perovskite/Silicon Tandem Solar Cells”. In: *Advanced Energy Materials* 11 (35 Sept. 2021), p. 2101460. ISSN: 1614-6832. DOI: 10.1002/aenm.202101460.

[51] Sofía Chozas-Barrientos et al. “Molecular Recombination Junction for Vacuum-Deposited Perovskite/Silicon Two-Terminal Tandem Solar Cells”. In: *ACS Energy Letters* 10 (Apr. 2025), pp. 1733–1740. ISSN: 23808195. DOI: 10.1021/acsenergylett.5c00155.

[52] Martin Kroll et al. “Insights into the evaporation behaviour of FAI: material degradation and consequences for perovskite solar cells”. In: *Sustainable Energy & Fuels* 6 (13 June 2022), pp. 3230–3239. ISSN: 2398-4902. DOI: 10.1039/D2SE00373B.

[53] Robert Heidrich et al. “Impact of dynamic co-evaporation schemes on the growth of methylammonium lead iodide absorbers for inverted solar cells”. In: *Scientific Reports* 12 (1 Dec. 2022). ISSN: 20452322. DOI: 10.1038/s41598-022-23132-w.

[54] Jennifer Emara et al. “Impact of Film Stoichiometry on the Ionization Energy and Electronic Structure of CH3NH3PbI3 Perovskites”. In: *Advanced Materials* 28 (3 Jan. 2016), pp. 553–559. ISSN: 15214095. DOI: 10.1002/adma.201503406.

[55] Kassio P.S. Zanoni et al. “Photovoltaic Devices Using Sublimed Methylammonium Lead Iodide Perovskites: Long-Term Reproducible Processing”. In: *Solar RRL* 7 (7 Apr. 2023). ISSN: 2367198X. DOI: 10.1002/solr.202201073.

[56] Marcel Roß et al. “Revealing the Role of Methylammonium Iodide Purity on the Vapor-Phase Deposition Process of Perovskites”. In: *Solar RRL* 6 (10 2022), p. 2200500. ISSN: 2367-198X. DOI: 10.1002/solr.202200500.

[57] Juliane Borchert et al. “Impurity Tracking Enables Enhanced Control and Reproducibility of Hybrid Perovskite Vapor Deposition”. In: *ACS Applied Materials and Interfaces* 11 (32 Aug. 2019), pp. 28851–28857. ISSN: 19448252. DOI: 10.1021/acsami.9b07619.

[58] Selina Olthof et al. “Substrate-dependent electronic structure and film formation of MAPbI3 perovskites”. In: *Scientific Reports* 7 (1 Jan. 2017), p. 40267. ISSN: 2045-2322. DOI: 10.1038/srep40267.

[59] Marcel Roß et al. “Co-Evaporated p-i-n Perovskite Solar Cells beyond 20% Efficiency: Impact of Substrate Temperature and Hole-Transport Layer”. In: *ACS Applied Materials & Interfaces* 12 (35 Sept. 2020), pp. 39261–39272. ISSN: 1944-8244. DOI: 10.1021/acsami.0c10898.

[60] Tobias Abzieher et al. “From Groundwork to Efficient Solar Cells: On the Importance of the Substrate Material in Co-Evaporated Perovskite Solar Cells”. In: *Advanced Functional Materials* 31 (42 Oct. 2021), p. 2104482. ISSN: 1616-301X. DOI: 10.1002/adfm.202104482.

[61] Seren Dilara Öz et al. “Effect of Hole Extraction Layer on the Composition of Thermally Evaporated Formamidinium-Based Mixed Halide Perovskites”. In: *ACS Applied Materials & Interfaces* 17 (16 2025), pp. 24535–24546. ISSN: 1944-8244. DOI: 10.1021/acsami.4c21701.

[62] Jakob Ihrenberger et al. “Solution-Free Growth of CsPbBr3 Perovskite Films Using a Fast and Scalable Close Space Sublimation Method”. In: *Crystal Growth and Design* 24 (13 July 2024), pp. 5542–5548. ISSN: 15287505. DOI: 10.1021/acs.cgd.4c00249.

[63] Nathan Rodkey et al. “Close-Space Sublimation as a Scalable Method for Perovskite Solar Cells”. In: *ACS Energy Letters* 9 (3 Mar. 2024), pp. 927–933. ISSN: 23808195. DOI: 10.1021/acsenergylett.3c02794.

[64] Inma Gomar-Fernandez et al. “Large Area Close-Space Sublimation Enables Efficient and Stable Perovskite Solar Cells”. In: *EES Solar* (2025). ISSN: 3033-4063. DOI: 10.1039/D5EL00145E.

[65] Victor Moritz Goldschmidt. “Die Gesetze der Krystallochemie”. In: *Die Naturwissenschaften* 14 (21 May 1926), pp. 477–485.

[66] Jin-Wook Lee et al. “Rethinking the A cation in halide perovskites”. In: *Science* 375 (Feb. 2022), eabj1186. ISSN: 0036-8075. DOI: 10.1126/science.abj1186.

[67] Zhen Li et al. “Stabilizing Perovskite Structures by Tuning Tolerance Factor: Formation of Formamidinium and Cesium Lead Iodide Solid-State Alloys”. In: *Chemistry of Materials* 28 (2016), pp. 284–292. ISSN: 0897-4756. DOI: 10.1021/acs.chemmater.5b04107.

[68] T. Jesper Jacobsson et al. “Goldschmidt’s Rules and Strontium Replacement in Lead Halogen Perovskite Solar Cells: Theory and Preliminary Experiments on CH3NH3SrI3”. In: *The Journal of Physical Chemistry C* 119.45 (2015), pp. 25673–25683. DOI: 10.1021/acs.jpcc.5b06436.

[69] Qiaojiao Gao et al. “Halide Perovskite Crystallization Processes and Methods in Nanocrystals, Single Crystals, and Thin Films”. In: *Advanced Materials* 34 (2022), p. 2200720. ISSN: 0935-9648. DOI: 10.1002/adma.202200720.

[70] Nam-Gyu Park. “Perovskite solar cells: an emerging photovoltaic technology”. In: *Materials Today* 18 (2 Mar. 2015), pp. 65–72. ISSN: 1369-7021. DOI: 10.1016/j.mattod.2014.07.007.

[71] K. Xerxes Steirer et al. “Defect Tolerance in Methylammonium Lead Triiodide Perovskite”. In: *ACS Energy Letters* 1 (July 2016), pp. 360–366. ISSN: 2380-8195. DOI: 10.1021/acsenergylett.6b00196.

[72] Jun Kang et al. “High Defect Tolerance in Lead Halide Perovskite CsPbBr3”. In: *The Journal of Physical Chemistry Letters* 8 (Jan. 2017), pp. 489–493. ISSN: 1948-7185. DOI: 10.1021/acs.jpclett.6b02800.

[73] Christian Wehrenfennig et al. “High Charge Carrier Mobilities and Lifetimes in Organolead Trihalide Perovskites”. In: *Advanced Materials* 26 (Mar. 2014), pp. 1584–1589. ISSN: 0935-9648. DOI: 10.1002/adma.201305172.

[74] Y. Chen et al. “Extended carrier lifetimes and diffusion in hybrid perovskites revealed by Hall effect and photoconductivity measurements”. In: *Nature Communications* 7 (Aug. 2016), p. 12253. ISSN: 2041-1723. DOI: 10.1038/ncomms12253.

[75] Chelsea Q. Xia et al. “Limits to Electrical Mobility in Lead-Halide Perovskite Semiconductors”. In: *The Journal of Physical Chemistry Letters* 12 (14 2021), pp. 3607–3617. ISSN: 1948-7185. DOI: 10.1021/acs.jpclett.1c00619.

[76] Jun Hong Noh et al. “Chemical Management for Colorful, Efficient, and Stable Inorganic–Organic Hybrid Nanostructured Solar Cells”. In: *Nano Letters* 13 (Mar. 2013), pp. 1764–1769. ISSN: 1530-6984. DOI: 10.1021/nl400349b.

[77] Shuxia Tao et al. “Absolute energy level positions in tin- and lead-based halide perovskites”. In: *Nature Communications* 10 (2019), p. 2560. ISSN: 2041-1723. DOI: 10.1038/s41467-019-10468-7.

[78] Peter Würfel et al. *Physics of Solar Cells: From Basic Principles to Advanced Concepts*. Wiley-VCH Verlag GmbH & Co. KGaA, Weinheim, Germany, 2016.

[79] Uli Würfel et al. “Charge Carrier Separation in Solar Cells”. In: *IEEE Journal of Photovoltaics* 5.1 (2015), pp. 461–469. DOI: 10.1109/JPHOTOV.2014.2363550.

[80] Pietro Caprioglio et al. “On the Relation between the Open-Circuit Voltage and Quasi-Fermi Level Splitting in Efficient Perovskite Solar Cells”. In: *Advanced Energy Materials* 9 (33 2019), p. 1901631. ISSN: 1614-6832. DOI: 10.1002/aenm.201901631.

[81] Tim Hellmann et al. “The Electronic Structure of MAPI-Based Perovskite Solar Cells: Detailed Band Diagram Determination by Photoemission Spectroscopy Comparing Classical and Inverted Device Stacks”. In: *Advanced Energy Materials* 10 (42 2020), p. 2002129. ISSN: 1614-6832. DOI: 10.1002/aenm.202002129.

[82] William Shockley et al. “Detailed Balance Limit of Efficiency of p-n Junction Solar Cells”. In: *Journal of Applied Physics* 32 (3 Mar. 1961), pp. 510–519. ISSN: 0021-8979. DOI: 10.1063/1.1736034.

[83] T. Tiedje et al. “Limiting Efficiency of Silicon Solar Cells”. In: *IEEE Transactions on Electron Devices* 31 (5 1984), pp. 711–716. DOI: 10.1109/T-ED.1984.21594.

[84] Sven Rühle. “Tabulated Values of the Shockley–Queisser Limit for Single Junction Solar Cells”. In: *Solar Energy* 130 (2016), pp. 139–147. ISSN: 0038-092X. DOI: 10.1016/j.solener.2016.02.015.

[85] A. De Vos. “Detailed Balance Limit of the Efficiency of Tandem Solar Cells”. In: *Journal of Physics D: Applied Physics* 13 (5 May 1980), p. 839. DOI: 10.1088/0022-3727/13/5/018.

[86] Giles E. Eperon et al. “Metal Halide Perovskite Tandem and Multiple-Junction Photovoltaics”. In: *Nature Reviews Chemistry* 1 (2017), p. 0095. ISSN: 2397-3358. DOI: 10.1038/s41570-017-0095.

[87] Hui Li et al. “Perovskite Tandem Solar Cells: From Fundamentals to Commercial Deployment”. In: *Chemical Reviews* 120 (18 2020), pp. 9835–9950. DOI: 10.1021/acs.chemrev.9b00780.

[88] Michele De Bastiani et al. “Recombination Junctions for Efficient Monolithic Perovskite-Based Tandem Solar Cells: Physical Principles, Properties, Processing and Prospects”. In: *Materials Horizons* 7 (11 2020), pp. 2791–2809. DOI: 10.1039/D0MH00990C.

[89] Niraj N. Lal et al. “Perovskite Tandem Solar Cells”. In: *Advanced Energy Materials* 7 (18 2017), p. 1602761. ISSN: 1614-6840. DOI: 10.1002/aenm.201602761.

[90] Yuxin Yao et al. “Phase-Stable Wide-Bandgap Perovskites for Four-Terminal Perovskite/Silicon Tandem Solar Cells with Over 30% Efficiency”. In: *Small* 18 (38 2022), p. 2203319. ISSN: 1613-6829. DOI: 10.1002/smll.202203319.

[91] K. S. Sree Harsha. *Principles of Vapor Deposition of Thin Films*. Elsevier Ltd., 2006.

[92] F. C. Frank et al. “One-Dimensional Dislocations. I. Static Theory”. In: *Proceedings of the Royal Society A: Mathematical, Physical and Engineering Sciences* 198 (1949), pp. 205–216. ISSN: 1364-5021.

[93] Frederick Charles Frank et al. “One-Dimensional Dislocations. II. Misfitting Monolayers and Oriented Overgrowth”. In: *Proceedings of the Royal Society A: Mathematical, Physical and Engineering Sciences* 198 (1949), pp. 216–225. ISSN: 1364-5021.

[94] F. C. Frank et al. “One-Dimensional Dislocations. III. Influence of the Second Harmonic Term in the Potential Representation on the Properties of the Model”. In: *Proceedings of the Royal Society A: Mathematical, Physical and Engineering Sciences* 200 (1060 Dec. 1949), pp. 125–134. ISSN: 1364-5021. DOI: 10.1098/rspa.1949.0163.

[95] F. C. Frank et al. “One-Dimensional Dislocations. IV. Dynamics”. In: *Proceedings of the Royal Society A: Mathematical and Physical Sciences* 201 (1065 1950), pp. 261–268. ISSN: 0080-4630.

[96] M. Volmer et al. “Keimbildung in übersättigten Gebilden”. In: *Zeitschrift für Physikalische Chemie* 119U (1 1926), pp. 277–301. DOI: 10.1515/zpch-1926-11927.

[97] I. N. Stranski et al. “Zur Theorie der Orientierten Ausscheidung von Ionenkristallen Aufeinander”. In: *Monatshefte für Chemie* 71 (1937), pp. 351–364. ISSN: 0026-9247. DOI: 10.1007/BF01798103.

[98] Lidón Gil-Escrig et al. “Efficient Wide-Bandgap Mixed-Cation and Mixed-Halide Perovskite Solar Cells by Vacuum Deposition”. In: *ACS Energy Letters* 6 (2 Feb. 2021), pp. 827–836. ISSN: 2380-8195. DOI: 10.1021/acsenergylett.0c02445.

[99] Isidora Susic et al. “Quadruple-Cation Wide-Bandgap Perovskite Solar Cells with Enhanced Thermal Stability Enabled by Vacuum Deposition”. In: *ACS Energy Letters* 7 (4 Apr. 2022), pp. 1355–1363. ISSN: 2380-8195. DOI: 10.1021/acsenergylett.2c00304.

[100] Jiangshan Feng et al. “High-throughput large-area vacuum deposition for high-performance formamidine-based perovskite solar cells”. In: *Energy & Environmental Science* 14 (5 2021), pp. 3035–3043. ISSN: 1754-5692. DOI: 10.1039/D1EE00634G.

[101] Alexander Diercks et al. “Sequential Evaporation of Inverted FAPbI3 Perovskite Solar Cells - Impact of Substrate on Crystallization and Film Formation”. In: *ACS Energy Letters* (2025), pp. 1165–1173. ISSN: 23808195. DOI: 10.1021/acsenergylett.4c03315.

[102] A. Mahboubi Soufiani et al. “Sequentially Evaporated Wide Bandgap Perovskite Absorber for Large-Area and Reproducible Fabrication of Solar Cells”. In: *Solar RRL* (2025). ISSN: 2367198X. DOI: 10.1002/solr.202500412.

[103] Mohammad Mahdi Tavakoli et al. “Multilayer evaporation of MAFAPbI3-xClx for the fabrication of efficient and large-scale device perovskite solar cells”. In: *Journal of Physics D: Applied Physics* 52 (3 Jan. 2019), p. 034005. ISSN: 0022-3727. DOI: 10.1088/1361-6463/aaebf1.

[104] Lidón Gil-Escrig et al. “Efficient Vacuum-Deposited Perovskite Solar Cells with Stable Cubic FA _{1– x} MA _x PbI ₃”. In: *ACS Energy Letters* 5 (9 Sept. 2020), pp. 3053–3061. ISSN: 2380-8195. DOI: 10.1021/acsenergylett.0c01473.

[105] Nathan Rodkey et al. “Incremental Feeding of Perovskite Powders: Angstrom-Precision Growth for Single-Source Solar Cell Fabrication”. In: *Advanced Engineering Materials* 26 (10 May 2024). ISSN: 15272648. DOI: 10.1002/adem.202400636.

[106] Thomas Feeney et al. “Understanding and exploiting interfacial interactions between phosphonic acid functional groups and co-evaporated perovskites”. In: *Matter* 7 (6 June 2024), pp. 2066–2090. ISSN: 25902385. DOI: 10.1016/j.matt.2024.02.004.

[107] Beom Soo Kim et al. “Deposition Kinetics and Compositional Control of Vacuum-Processed CH3NH3PbI3Perovskite”. In: *Journal of Physical Chemistry Letters* 11 (16 Aug. 2020), pp. 6852–6859. ISSN: 19487185. DOI: 10.1021/acs.jpclett.0c01995.

[108] Karl L. Heinze et al. “Importance of methylammonium iodide partial pressure and evaporation onset for the growth of co-evaporated methylammonium lead iodide absorbers”. In: *Scientific Reports* 11 (1 Dec. 2021). ISSN: 20452322. DOI: 10.1038/s41598-021-94689-1.

[109] Andrés-Felipe Castro-Méndez et al. “Tailoring Interface Energies via Phosphonic Acids to Grow and Stabilize Cubic FAPbI ₃ Deposited by Thermal Evaporation”. In: *Journal of the American Chemical Society* 146 (27 July 2024), pp. 18459–18469. ISSN: 0002-7863. DOI: 10.1021/jacs.4c03911.

[110] Lidón Gil-Escrig et al. “Tuning Substrate Temperature for Enhanced Vacuum-Deposited Wide-Bandgap Perovskite Solar Cells: Insights from Morphology, Charge Transport, and Drift-Diffusion Simulations”. In: *EES Solar* 1 (3 2025), pp. 391–403. DOI: 10.1039/D5EL00021A.

[111] Sheng-Yi Hsiao et al. “Efficient All-Vacuum Deposited Perovskite Solar Cells by Controlling Reagent Partial Pressure in High Vacuum”. In: *Advanced Materials* 28 (32 Aug. 2016), pp. 7013–7019. ISSN: 0935-9648. DOI: 10.1002/adma.201601505.

[112] Vladimir Held et al. “Evolution of Structure and Optoelectronic Properties during Halide Perovskite Vapor Deposition”. In: *Journal of Physical Chemistry Letters* 13 (51 Dec. 2022), pp. 11905–11912. ISSN: 19487185. DOI: 10.1021/acs.jpclett.2c03422.

[113] Mohammad Mahdi Tavakoli et al. “High-quality organohalide lead perovskite films fabricated by layer-by-layer alternating vacuum deposition for high efficiency photovoltaics”. In: *Materials Chemistry Frontiers* 1 (8 2017), pp. 1520–1525. ISSN: 2052-1537. DOI: 10.1039/C6QM00379F.

[114] Ran Ji et al. “Thermally evaporated methylammonium-free perovskite solar cells”. In: *Journal of Materials Chemistry C* 8 (23 June 2020), pp. 7725–7733. ISSN: 20507526. DOI: 10.1039/d0tc01550d.

[115] Dongxu Lin et al. “Vapor Deposited Pure alpha-FAPbI3 Perovskite Solar Cell via Moisture-Induced Phase Transition Strategy”. In: *Advanced Functional Materials* 32 (48 Nov. 2022), p. 2208392. ISSN: 1616-301X. DOI: 10.1002/adfm.202208392.

[116] Hang Li et al. “Sequential vacuum-evaporated perovskite solar cells with more than 24% efficiency”. In: *Science Advances* 8 (28 July 2022), eabo7422. ISSN: 2375-2548. DOI: 10.1126/sciadv.abo7422.

[117] Kilian B. Lohmann et al. “Solvent-Free Method for Defect Reduction and Improved Performance of p-i-n Vapor-Deposited Perovskite Solar Cells”. In: *ACS Energy Letters* 7 (6 June 2022), pp. 1903–1911. ISSN: 23808195. DOI: 10.1021/acsenergylett.2c00865.

[118] Yu Hsien Chiang et al. “Vacuum-Deposited Wide-Bandgap Perovskite for All-Perovskite Tandem Solar Cells”. In: *ACS Energy Letters* 8 (6 June 2023), pp. 2728–2737. ISSN: 23808195. DOI: 10.1021/acsenergylett.3c00564.

[119] Isidora Susic et al. “Combinatorial Vacuum-Deposition of Wide Bandgap Perovskite Films and Solar Cells”. In: *Advanced Materials Interfaces* 10 (4 Feb. 2023). ISSN: 21967350. DOI: 10.1002/admi.202202271.

[120] Siyu Yan et al. “A Templating Approach to Controlling the Growth of Coevaporated Halide Perovskites”. In: *ACS Energy Letters* 8 (10 Oct. 2023), pp. 4008–4015. ISSN: 23808195. DOI: 10.1021/acsenergylett.3c01368.

[121] Qimu Yuan et al. “Thermally Stable Perovskite Solar Cells by All-Vacuum Deposition”. In: *ACS Applied Materials and Interfaces* 15 (1 2023), pp. 772–781. ISSN: 19448252. DOI: 10.1021/acsami.2c14658.

[122] Dongxu Lin et al. “Modulating the Distribution of Formamidinium Iodide by Ultrahigh Humidity Treatment Strategy for High-Quality Sequential Vapor Deposited Perovskite”. In: *Small* 20 (12 Mar. 2024), p. 2307960. ISSN: 1613-6810. DOI: 10.1002/smll.202307960.

[123] Matthew R. Leyden et al. “Loading Precursors into Self-Assembling Contacts for Improved Performance and Process Control in Evaporated Perovskite Solar Cells”. In: *Solar RRL* 8 (21 Nov. 2024), p. 2400575. ISSN: 2367-198X. DOI: 10.1002/solr.202400575.

[124] Chun Jen Shih et al. “Exploring buried interface in all-vapor-deposited perovskite photovoltaics”. In: *Solar Energy* 280 (Sept. 2024). ISSN: 0038092X. DOI: 10.1016/j.solener.2024.112872.

[125] Yue Yu Xu et al. “Octahedral Tilt Enables Efficient and Stable Fully Vapor-Deposited Perovskite/Silicon Tandem Cells”. In: *Advanced Functional Materials* 34 (11 Mar. 2024). ISSN: 16163028. DOI: 10.1002/adfm.202312037.

[126] Sheng Zou et al. “Scalable large area perovskite solar cell modules fabricated with high humidity tolerance by vacuum deposition”. In: *Materials Today Energy* 40 (Mar. 2024), p. 101506. ISSN: 24686069. DOI: 10.1016/j.mtener.2024.101506.

[127] Rahul A. Nambiar et al. “Interdiffusion control in sequentially evaporated organic–inorganic perovskite solar cells”. In: *EES Solar* 1 (2 2025), pp. 129–138. ISSN: 3033-4063. DOI: 10.1039/D5EL00017C.

[128] Elena Siliavka et al. “Additive Engineering of Sequentially Evaporated FAPbI3 Solar Cells”. In: *Advanced Energy Materials* 15 (30 2025), p. 2500963. ISSN: 1614-6832. DOI: 10.1002/aenm.202500963.

[129] Thomas Feeney et al. “High-Rate FA-Based Co-Evaporated Perovskites: Understanding Rate Limitations and Practical Considerations to Overcome Their Impact”. In: *Advanced Functional Materials* (2025), e17873. ISSN: 1616-3028. DOI: 10.1002/adfm.202517873.

[130] Chang-Wen Chen et al. “Efficient and Uniform Planar-Type Perovskite Solar Cells by Simple Sequential Vacuum Deposition”. In: *Advanced Materials* 26 (38 Oct. 2014), pp. 6647–6652. ISSN: 0935-9648. DOI: 10.1002/adma.201402461.

[131] Hang Li et al. “Molten Salt Strategy for Reproducible Evaporation of Efficient Perovskite Solar Cells”. In: *Advanced Functional Materials* 33 (10 Mar. 2023), p. 2211232. ISSN: 1616-301X. DOI: 10.1002/adfm.202211232.

[132] Dong Yang et al. “Alternating precursor layer deposition for highly stable perovskite films towards efficient solar cells using vacuum deposition”. In: *Journal of Materials Chemistry A* 3 (18 2015), pp. 9401–9405. ISSN: 2050-7488. DOI: 10.1039/C5TA01824B.

[133] Annie Ng et al. “Efficiency enhancement by defect engineering in perovskite photovoltaic cells prepared using evaporated PbI ₂ /CH ₃ NH ₃ I multilayers”. In: *Journal of Materials Chemistry A* 3 (17 May 2015), pp. 9223–9231. ISSN: 2050-7488. DOI: 10.1039/C4TA05070C.

[134] Mohammad Mahdi Tavakoli et al. “All-Vacuum-Processing for Fabrication of Efficient, Large-Scale, and Flexible Inverted Perovskite Solar Cells”. In: *physica status solidi (RRL) – Rapid Research Letters* 15 (1 Jan. 2021), p. 2000449. ISSN: 1862-6254. DOI: 10.1002/pssr.202000449.

[135] Mohammad Mahdi Tavakoli et al. “Efficient, Hysteresis-Free, and Flexible Inverted Perovskite Solar Cells Using All-Vacuum Processing”. In: *Solar RRL* 5 (1 Jan. 2021), p. 2000552. ISSN: 2367-198X. DOI: 10.1002/solr.202000552.

[136] Yunseong Choi et al. “Toward All-Vacuum-Processable Perovskite Solar Cells with High Efficiency, Stability, and Scalability Enabled by Fluorinated Spiro-OMeTAD through Thermal Evaporation”. In: *Solar RRL* 5 (9 Sept. 2021), p. 2100415. ISSN: 2367-198X. DOI: 10.1002/solr.202100415.

[137] Emanuele Smecca et al. “Two-step MAPbI3deposition by low-vacuum proximity-space-effusion for high-efficiency inverted semitransparent perovskite solar cells”. In: *Journal of Materials Chemistry A* 9 (30 Aug. 2021), pp. 16456–16469. ISSN: 20507496. DOI: 10.1039/d1ta02535j.

[138] Karl L. Heinze et al. “Structural Evolution of Sequentially Evaporated (Cs,FA)Pb(I,Br)3 Perovskite Thin Films via In-Situ X-Ray Diffraction”. In: *physica status solidi (a)* 221 (3 Feb. 2024), p. 2300690. ISSN: 1862-6300. DOI: 10.1002/pssa.202300690.

[139] Siyang Wang et al. “Over 24% efficient MA-free CsxFA1-xPbX3 perovskite solar cells”. In: *Joule* 6 (6 June 2022), pp. 1344–1356. ISSN: 25424351. DOI: 10.1016/j.joule.2022.05.002.

[140] Anyi Mei et al. “Stabilizing Perovskite Solar Cells to IEC61215:2016 Standards with over 9,000-h Operational Tracking”. In: *Joule* 4 (12 Dec. 2020), pp. 2646–2660. ISSN: 25424351. DOI: 10.1016/j.joule.2020.09.010.

[141] Yifei Kang et al. “Thermal Shock Fabrication of Ion-Stabilized Perovskite and Solar Cells”. In: *Advanced Materials* 34 (32 Aug. 2022), p. 2203166. ISSN: 0935-9648. DOI: 10.1002/adma.202203166.

[142] Amran Al-Ashouri et al. “Conformal monolayer contacts with lossless interfaces for perovskite single junction and monolithic tandem solar cells”. In: *Energy & Environmental Science* 12 (11 Nov. 2019), pp. 3356–3369. ISSN: 1754-5692. DOI: 10.1039/C9EE02268F.

[143] Zhen Li et al. “Organometallic-functionalized interfaces for highly efficient inverted perovskite solar cells”. In: *Science* 376 (6591 Apr. 2022), pp. 416–420. ISSN: 0036-8075. DOI: 10.1126/science.abm8566.

[144] Elizabeth S. Parrott et al. “Growth modes and quantum confinement in ultrathin vapour-deposited MAPbI ₃ films”. In: *Nanoscale* 11 (30 2019), pp. 14276–14284. ISSN: 2040-3364. DOI: 10.1039/C9NR04104D.

[145] Jingbi You et al. “Moisture Assisted Perovskite Film Growth for High Performance Solar Cells”. In: *Applied Physics Letters* 105 (18 Nov. 2014), p. 183902. ISSN: 0003-6951. DOI: 10.1063/1.4901510.

[146] Giles E. Eperon et al. “The Importance of Moisture in Hybrid Lead Halide Perovskite Thin Film Fabrication”. In: *ACS Nano* 9 (9 2015), pp. 9380–9393. ISSN: 1936-0851. DOI: 10.1021/acsnano.5b03626.

[147] Florent Sahli et al. “Fully Textured Monolithic Perovskite/Silicon Tandem Solar Cells with 25.2% Power Conversion Efficiency”. In: *Nature Materials* 17 (9 2018), pp. 820–826. ISSN: 1476-1122. DOI: 10.1038/s41563-018-0115-4.

[148] Raphael Pesch et al. “Hybrid Two-Step Inkjet-Printed Perovskite Solar Cells”. In: *Solar RRL* 8 (13 July 2024), p. 2100882. ISSN: 2367-198X. DOI: 10.1002/solr.202400165.

[149] Ronja Pappenberger et al. “Bandgap Engineering of Two-Step Processed Perovskite Top Cells for Perovskite-Based Tandem Photovoltaics”. In: *Advanced Functional Materials* (2023). ISSN: 16163028. DOI: 10.1002/adfm.202311424.

[150] Van Son Nguyen et al. “Solvent-vapor assisted conversion process for hybrid perovskites coupling thermal evaporation and slot-die coating”. In: *Materials Science in Semiconductor Processing* 158 (May 2023), p. 107358. ISSN: 13698001. DOI: 10.1016/j.mssp.2023.107358.

[151] Julian A. Steele et al. “How to GIWAXS: Grazing Incidence Wide Angle X-Ray Scattering Applied to Metal Halide Perovskite Thin Films”. In: *Advanced Energy Materials* 13 (27 July 2023). ISSN: 1614-6832. DOI: 10.1002/aenm.202300760.

[152] Dongrui Jiang et al. “Non-laser and all-vapor-phase processed perovskite solar modules stabilized by naturally formed barrier layers”. In: *Joule* 8 (4 Apr. 2024), pp. 1161–1175. ISSN: 25424351. DOI: 10.1016/j.joule.2024.02.007.

[153] Juan Zhang et al. “Efficient and Stable Inverted Perovskite Solar Modules Enabled by Solid–Liquid Two-Step Film Formation”. In: *Nano-Micro Letters* 16 (1 Dec. 2024), p. 190. ISSN: 2311-6706. DOI: 10.1007/s40820-024-01408-2.

[154] Ziyi Li et al. “Surface-Orientation Elimination of Vapor-Deposited PbI ₂ Flakes for Efficient Perovskite Synthesis on Curved Solar Cells”. In: *ACS Applied Materials & Interfaces* 13 (38 Sept. 2021), pp. 45496–45504. ISSN: 1944-8244. DOI: 10.1021/acsami.1c12283.

[155] Aqiang Liu et al. “Solution evaporation processed high quality perovskite films”. In: *Science Bulletin* 63 (23 Dec. 2018), pp. 1591–1596. ISSN: 20959273. DOI: 10.1016/j.scib.2018.11.004.

[156] Liguo Tan et al. “Combined Vacuum Evaporation and Solution Process for High-Efficiency Large-Area Perovskite Solar Cells with Exceptional Reproducibility”. In: *Advanced Materials* 35 (13 Mar. 2023), p. 2205027. ISSN: 0935-9648. DOI: 10.1002/adma.202205027.

[157] You Gao et al. “Rethinking the Role of Excess/Residual Lead Iodide in Perovskite Solar Cells”. In: *Advanced Functional Materials* 33 (26 June 2023), p. 2215171. ISSN: 1616-301X. DOI: 10.1002/adfm.202215171.

[158] Nikhil Kalasariya et al. “Controlling Lead Halide Residue in Perovskite Solar Cells: A Method to Improve the Photostability and Hysteresis”. In: *Solar RRL* 8 (1 Jan. 2024), p. 2300788. ISSN: 2367-198X. DOI: 10.1002/solr.202300788.

[159] Viktor Škorjanc et al. “Seed Layers for Wide-Band Gap Coevaporated Perovskite Solar Cells: CsCl Regulates Band Gap and Reduces Process Variability”. In: *ACS Energy Letters* 9 (11 2024), pp. 5639–5646. ISSN: 2380-8195. DOI: 10.1021/acsenergylett.4c02173.

[160] Erkan Aydin et al. “Pathways toward commercial perovskite/silicon tandem photovoltaics”. In: *Science* 383 (6679 Jan. 2024), pp. 1–13. ISSN: 10959203. DOI: 10.1126/science.adh3849.

[161] Oussama Er-raji et al. “Electron Accumulation Across the Perovskite Layer Enhances Tandem Solar Cells with Textured Silicon”. In: *Science* 0 (0 2025), eadx1745. ISSN: 0036-8075. DOI: 10.1126/science.adx1745.

[162] Zhiliang Liu et al. “Strained heterojunction enables high-performance, fully textured perovskite/silicon tandem solar cells”. In: *Joule* (Oct. 2024). ISSN: 25424351. DOI: 10.1016/j.joule.2024.06.015.

[163] Oussama Er-raji et al. “Tailoring Perovskite Crystallization and Interfacial Passivation in Efficient, Fully Textured Perovskite Silicon Tandem Solar Cells”. In: *Joule* 8 (10 2024), pp. 2811–2833. ISSN: 2542-4351. DOI: 10.1016/j.joule.2024.06.018.

[164] Xuntian Zheng et al. “Solvent engineering for scalable fabrication of perovskite/silicon tandem solar cells in air”. In: *Nature Communications* 15 (1 Dec. 2024). ISSN: 20411723. DOI: 10.1038/s41467-024-49351-5.

[165] Xin Yu Chin et al. “Interface Passivation for 31.25%-Efficient Perovskite/Silicon Tandem Solar Cells”. In: *Science* 381 (6653 July 2023), pp. 59–63. ISSN: 0036-8075. DOI: 10.1126/science.adg0091.

[166] Abhyuday Paliwal et al. “Fully vacuum-deposited perovskite solar cells in substrate configuration”. In: *Matter* 6 (10 Oct. 2023), pp. 3499–3508. ISSN: 25902385. DOI: 10.1016/j.matt.2023.07.011.

[167] Jorge Ávila et al. “Vapor-Deposited Perovskites: The Route to High-Performance Solar Cell Production?” In: *Joule* 1 (3 Nov. 2017), pp. 431–442. ISSN: 25424351. DOI: 10.1016/j.joule.2017.07.014.

[168] Manuel Piot et al. “Fast Coevaporation of 1 micrometer Thick Perovskite Solar Cells”. In: *ACS Energy Letters* 8 (11 Nov. 2023), pp. 4711–4713. ISSN: 2380-8195. DOI: 10.1021/acsenergylett.3c01724.

[169] Qiang Guo et al. “The growth of a CH3NH3PbI3 thin film using simplified close space sublimation for efficient and large dimensional perovskite solar cells”. In: *Energy and Environmental Science* 9 (4 Apr. 2016), pp. 1486–1494. ISSN: 17545706. DOI: 10.1039/c5ee03620h.

[170] Gaojie Zhang et al. “Ultrafast Growth of High-Quality Cs0.14FA0.86Pb(BrxI1-x)3 Thin Films Achieved Using Super-Close-Space Sublimation”. In: *ACS Applied Energy Materials* 5 (5 May 2022), pp. 5797–5803. ISSN: 25740962. DOI: 10.1021/acsaem.2c00132.

[171] Quentin Guesnay et al. “Pizza Oven Processing of Organohalide Perovskites (POPOP): A Simple, Versatile and Efficient Vapor Deposition Method”. In: *Advanced Energy Materials* 14 (10 Mar. 2024). ISSN: 16146840. DOI: 10.1002/aenm.202303423.

[172] Guijun Li et al. “Low cost, high throughput and centimeter-scale fabrication of efficient hybrid perovskite solar cells by closed space vapor transport”. In: *Physica Status Solidi - Rapid Research Letters* 10 (2 Feb. 2016), pp. 153–157. ISSN: 18626270. DOI: 10.1002/pssr.201510386.

[173] Dongxu Lin et al. “Stable and scalable 3D-2D planar heterojunction perovskite solar cells via vapor deposition”. In: *Nano Energy* 59 (May 2019), pp. 619–625. ISSN: 22112855. DOI: 10.1016/j.nanoen.2019.03.014.

[174] Xi Deng et al. “Improving the crystal growth of a Cs0.24FA0.76PbI3-xBrxperovskite in a vapor-solid reaction process using strontium iodide”. In: *Sustainable Energy and Fuels* 4 (5 May 2020), pp. 2491–2496. ISSN: 23984902. DOI: 10.1039/d0se00088d.

[175] Alexander J. Harding et al. “The growth of methylammonium lead iodide perovskites by close space vapor transport”. In: *RSC Advances* 10 (27 Apr. 2020), pp. 16125–16131. ISSN: 20462069. DOI: 10.1039/d0ra01640c.

[176] Enrique Pérez-Gutiérrez et al. “Compositional study of mixed halide perovskite films CH3NH3Pb(I1-xBrx)3 and CH3NH3Pb(I1-xClx)3 prepared by close space sublimation”. In: *Materials Today Communications* 25 (Dec. 2020). ISSN: 23524928. DOI: 10.1016/j.mtcomm.2020.101384.

[177] Long Luo et al. “19.59% Efficiency from Rb0.04-Cs0.14FA0.86Pb(BryI1-y)3 perovskite solar cells made by vapor–solid reaction technique”. In: *Science Bulletin* 66 (10 May 2021), pp. 962–964. ISSN: 20959281. DOI: 10.1016/j.scib.2021.01.031.

[178] Cheng Niu et al. “High-Performance Rb–Cs0.14FA0.86Pb(BrxI1-x)3 Perovskite Solar Cells Achieved by Regulating the Halogen Exchange in Vapor–Solid Reaction Process”. In: *Solar RRL* 5 (5 May 2021). ISSN: 2367198X. DOI: 10.1002/solr.202100102.

[179] Austin G. Kuba et al. “Two-Step Close-Space Vapor Transport of MAPbI3Solar Cells: Effects of Electron Transport Layers and Residual PbI2”. In: *ACS Applied Energy Materials* 5 (9 Sept. 2022), pp. 10731–10741. ISSN: 25740962. DOI: 10.1021/acsaem.2c01468.

[180] Wentao Luo et al. “Growing phase-stable alpha-FAPbI3 thin films through a mixing-vapor-solid reaction”. In: *Materials Science in Semiconductor Processing* 164 (Sept. 2023). ISSN: 13698001. DOI: 10.1016/j.mssp.2023.107603.

[181] Qin Zou et al. “Effects of Lead Iodide Crystallization on Photovoltaic Performance of Perovskite Solar Cells by the Vapor-Solid Reaction Method”. In: *ACS Omega* 8 (13 Apr. 2023), pp. 12430–12438. ISSN: 24701343. DOI: 10.1021/acsomega.3c00318.

[182] Yulong Wang et al. “Grain Boundary Elimination via Recrystallization-Assisted Vapor Deposition for Efficient and Stable Perovskite Solar Cells and Modules”. In: *Advanced Materials* 35 (44 Nov. 2023). ISSN: 15214095. DOI: 10.1002/adma.202304625.

[183] Fuping Zhao et al. “Two-Step Vapor-Solid Reaction for the Growth of High-Quality CsFA-Based Lead Halide Perovskite Thin Films”. In: *Solar RRL* 7 (11 June 2023). ISSN: 2367198X. DOI: 10.1002/solr.202300062.

[184] Fengguo Tie et al. “Valine-Modified PbI2 for the Growth of Pinhole-Free Lead Halide Perovskite Thin Films by Vapor-Solid Reaction”. In: *ACS Applied Energy Materials* 6 (12 June 2023), pp. 6681–6688. ISSN: 25740962. DOI: 10.1021/acsaem.3c00676.

[185] Junshuai Fan et al. “Fabrication of Large-Grained Perovskite Films Utilizing a Recrystallization Approach Involving Multiple Vapor Annealing Steps”. In: *ACS Applied Energy Materials* 7 (9 May 2024), pp. 3740–3749. ISSN: 25740962. DOI: 10.1021/acsaem.4c00080.

[186] Yulong Wang et al. “Ordered Perovskite Structure with Functional Units for High Performance and Stable Solar Cells”. In: *Advanced Materials* 36 (25 June 2024). ISSN: 15214095. DOI: 10.1002/adma.202401416.

[187] Shenghan Hu et al. “Unveiling the role of Cs ion in perovskite phase formation during solid–vapor reactions”. In: *Chemical Engineering Journal* 499 (Nov. 2024). ISSN: 13858947. DOI: 10.1016/j.cej.2024.156259.

[188] Changyu Duan et al. “Oriented Growth for Efficient and Scalable Perovskite Solar Cells by Vapor–Solid Reaction”. In: *Advanced Functional Materials* 34 (21 May 2024), p. 2313435. ISSN: 16163028. DOI: 10.1002/adfm.202313435.

[189] Youngmin Kim et al. “Solvent-Free MACl Post-Treatment Using Close-Spaced Sublimation Method for Dry-Processed Perovskite Solar Cells”. In: *Solar RRL* (2025). ISSN: 2367198X. DOI: 10.1002/solr.202400859.

[190] Changyu Duan et al. “Stoichiometric Gradient Rebalancing Achieves Surface Reconstruction and Bulk Homogenization in High-Performance Vapor-deposited Perovskite Solar Cells†”. In: *Journal of Materials Chemistry A* 13 (13 July 2025), pp. 24675–24684. ISSN: 2050-7488. DOI: 10.1039/d5ta03102h.

[191] Yichen Dou et al. “Enhanced Buried Interface Engineering for Efficient Inverted Perovskite Solar Cells Fabricated via Vapor–Solid Reaction”. In: *Small Methods* 9 (4 Apr. 2025). ISSN: 23669608. DOI: 10.1002/smtd.202401339.

[192] Ronja Pappenberger et al. “Versatile Two-Step Process for Perovskite-Based Tandem Photovoltaics”. In: *Solar RRL* 9 (13 Apr. 2025), p. 2500193. ISSN: 2367198X. DOI: 10.1002/solr.202500193.

[193] Saba Gharibzadeh et al. “Record Open-Circuit Voltage Wide-Bandgap Perovskite Solar Cells Utilizing 2D/3D Perovskite Heterostructure”. In: *Advanced Energy Materials* 9 (21 2019), p. 1803699. ISSN: 1614-6840. DOI: 10.1002/aenm.201803699.

[194] Saba Gharibzadeh et al. “Two Birds with One Stone: Dual Grain-Boundary and Interface Passivation Enables >22% Efficient Inverted Methylammonium-Free Perovskite Solar Cells”. In: *Energy & Environmental Science* 14 (11 2021), pp. 5875–5893. ISSN: 1754-5692. DOI: 10.1039/D1EE01508G.

[195] Shuaifeng Hu et al. “A Universal Surface Treatment for p-i-n Perovskite Solar Cells”. In: *ACS Applied Materials and Interfaces* 14 (50 Dec. 2022), pp. 56290–56297. ISSN: 19448252. DOI: 10.1021/acsami.2c15989.

[196] Shuaifeng Hu et al. “Optimized Carrier Extraction at Interfaces for 23.6% Efficient Tin–Lead Perovskite Solar Cells”. In: *Energy & Environmental Science* 15 (5 May 2022), pp. 2096–2107. ISSN: 1754-5706. DOI: 10.1039/D2EE00288D.

[197] Michael Spence et al. “A Comparison of Different Textured and Non-Textured Anti-Reflective Coatings for Planar Monolithic Silicon–Perovskite Tandem Solar Cells”. In: *ACS Applied Energy Materials* 5 (5 2022), pp. 5974–5982. ISSN: 2574-0962. DOI: 10.1021/acsaem.2c00361.

[198] Wenhui Li et al. “An Amorphous MgF2 Anti-Reflective Thin Film for Enhanced Performance of Inverted Organic–Inorganic Perovskite Solar Cells”. In: *RSC Advances* 14 (4 2024), pp. 2757–2762. ISSN: 2046-2069. DOI: 10.1039/D3RA08456F.

[199] Benjamin Hacene et al. “Imaging of Recombination Rates and Lifetime in Perovskite Thin Film Processing”. In: *Small Methods* 9 (7 Feb. 2025), p. 2402119. ISSN: 23669608. DOI: 10.1002/smtd.202402119.

[200] Julian Petermann et al. “Advanced Photoluminescence Imaging Method for Robust and Scalable Perovskite Quality Monitoring in Monolithic Tandem Solar Cells”. In: *Solar RRL* 9 (13 July 2025), p. 2500074. ISSN: 2367198X. DOI: 10.1002/solr.202500074.

[201] Amy Brand et al. “Beyond Authorship: Attribution, Contribution, Collaboration, and Credit”. In: *Learned Publishing* 28 (2 2015), pp. 151–155. ISSN: 0953-1513. DOI: 10.1087/20150211.

List of Publications, Conference Contributions and Awards

Journal Articles

Peer-Reviewed Publications (First Author)

- **Alexander Diercks**, Julian Petry, Thomas Feeney, Roja Singh, Tonghan Zhao, Hang Hu, Yang Li, Ulrich W. Paetzold and Paul Fassl. "Sequential Evaporation of Inverted $FAPbI_3$ Perovskite Solar Cells - Impact of Substrate on Crystallization and Film Formation". In: *ACS Energy Letters* 10.3 (2025), pp. 1165–1173. DOI: 10.1021/acsenergylett.4c03315.

- **Alexander Diercks**[*], Julian Petry[*], Thomas Feeney, Richard Thelen, Paul Fassl, and Ulrich W. Paetzold. "Particle Size Matters - Impact of Particle Size and Crucible Geometry on Sublimation Behavior of FAI". In: *Advanced Materials Technologies* (2025), e01549. DOI: 10.1002/admt.202501549.

- **Alexander Diercks**[*], Sofía Chozas-Barrientos[*], Lidón Gil-Escrig, Federico Ventosinos, Inma Gomar-Fernández, Cristina Roldán-Carmona, Nathan Rodkey, Tonghan Zhao, Julian Petermann, Maximiliano Senno, Vladimir Held, Perrine Carroy, Delfina Muñoz, Paul Fassl, Michele Sessolo, Ulrich W. Paetzold[*], and Henk J. Bolink[*]. "Close-space sublimation as a versatile deposition process for efficient perovskite silicon tandem solar cells". In: *Nature Energy* (2025). DOI: 10.1038/s41560-026-02068-9.

Peer-Reviewed Publications (Co-Author)

- David B. Ritzer, Bahram A. Nejand, Marco A. Ruiz-Preciado, Saba Gharibzadeh, Hang Hu, **Alexander Diercks**, Thomas Feeney, Bryce S. Richards, Tobias Abzieher, and Ulrich W. Paetzold. "Translucent perovskite photovoltaics for building integration". In: *Energy & Environmental Sciences* 16 (2023), pp. 2212–2225. DOI: 10.1039/D2EE04137E.

- Ahmed Farag, Thomas Feeney, Ihteaz M. Hossain, Fabian Schackmar, Paul Fassl, Kathrin Küster, Rainer Bäuerle, Marco A. Ruiz-Preciado, Mario Hentschel, David B. Ritzer, **Alexander Diercks**, Yang Li, Bahram A. Nejand, Felix Laufer, Roja Singh, Ulrich Starke, and Ulrich W. Paetzold. "Evaporated Self-Assembled Monolayer Hole Transport Layers: Lossless Interfaces in p-i-n Perovskite Solar Cells". In: *Advanced Energy Materials* 13.8 (2023), p. 2203982. DOI: 10.1002/aenm.202203982.

- Hang Hu, David B. Ritzer, **Alexander Diercks**, Yang Li, Roja Singh, Paul Fassl, Qihao Jin, Fabian Schackmar, Ulrich W. Paetzold, and Bahram A. Nejand. "Void-free buried interface for scalable processing of *p-i-n*-based $FAPbI_3$ perovskite solar modules". In: *Joule* 7.7 (2023), pp. 1574-1592. DOI: 10.1016/j.joule.2023.05.017.

- Hang Hu, Sophie X. An, Yang Li, Seyedamir Orooji, Roja Singh, Fabian Schackmar, Felix Laufer, Qihao Jin, Thomas Feeney, **Alexander Diercks**, Fabrizio Gota, Somayeh Moghadamzadeh, Ting Pan,

Michael Rienäcker, Robby Peibst, Bahram A. Nejand, and Ulrich W. Paetzold. "Triple-junction perovskite–perovskite–silicon solar cells with power conversion efficiency of 24.4%". In: *Energy & Environmental Science* 17.8 (2024), pp. 2800-2814. DOI: 10.1039/D3EE03687A.

- Ronja Pappenberger, **Alexander Diercks**, Julian Petry, Somayeh Moghadamzadeh, Paul Fassl and Ulrich W. Paetzold. "Bandgap Engineering of Two-Step Processed Perovskite Top Cells for Perovskite-Based Tandem Photovoltaics". In: *Advanced Functional Materials* 34.9 (2024), pp. 2311424. DOI: 10.1002/adfm.202311424.

- Roja Singh, Hang Hu, Thomas Feeney, **Alexander Diercks**, Felix Laufer, Yang Li, The Duong, Fabian Schackmar, Bahram A. Nejand, and Ulrich W. Paetzold. "Danger in the Dark: Stability of Perovskite Solar Cells with Varied Stoichiometries and Morphologies Stressed at Various Conditions". In: *ACS Applied Materials & Interfaces* 16.21 (2024), pp. 27450-27462. DOI: 10.1021/acsami.4c04350.

- Thomas Feeney*, Julian Petry*, Abderrezak Torche, Dirk Hauschild, Benjamin Hacene, Constantin Wansorra, **Alexander Diercks**, Michelle Ernst, Lothar Weinhardt, Clemens Heske, Ganna Gryn'ova, Ulrich W. Paetzold, and Paul Fassl. "Understanding and exploiting interfacial interactions between phosphonic acid functional groups and co-evaporated perovskites". In: *Joule* 7.6 (2024), pp. 2066-2090. DOI: 10.1016/j.matt.2024.02.004.

- Raphael Pesch, **Alexander Diercks**, Julian Petry, Alexander Welle, Ronja Pappenberger, Fabian Schackmar, Helge Eggers, Johannes Sutter, Ulrich Lemmer, Ulrich W. Paetzold. "Hybrid Two-Step Inkjet-Printed Perovskite Solar Cells". In: *Solar RRL* 8.13 (2024), pp. 2400165. DOI: 10.1002/solr.202400165.

- Julian Petry, Viktor Škorjanc, **Alexander Diercks**, Thomas Feeney, Amedeo Morsa, Sara R Kimmig, Jens Baumann, Frank Löffler, Stefan Auschill, Joshua Damm, Daniel Baumann, Felix Laufer, Jona Kurpiers, Michael Müller, Lars Korte, Steve Albrecht, Marcel Roß, Ulrich W. Paetzold, and Paul Fassl. "Industrialization of perovskite solar cell fabrication: strategies to achieve high-throughput vapor deposition processes". In: *EES Solar* 1 (2025), pp. 404-418. DOI: 10.1039/D5EL00069F.

- Ronja Pappenberger, Roja Singh, **Alexander Diercks**, Tonghan Zhao, Raphael Pesch, Julian Petry, Daniel Baumann, Xuzheng Liu, and Ulrich W. Paetzold. "Versatile Two-Step Process for Perovskite-Based Tandem Photovoltaics". In: *Solar RRL* 9.13 (2025), pp. 2500193. DOI: 10.1002/solr.202500193.

- Thomas Feeney, Aleksandra Miaskiewicz, Julian Petry, Felix Laufer, Roja Singh, Stefanie Severin, Viktor Škorjanc, **Alexander Diercks**, Suresh Maniyarasu, Lars Korte, Steve Albrecht, Ulrich W. Paetzold, Marcel Roß and Paul Fassl. "High-rate FA-based co-evaporated perovskites: Understanding rate limitations and practical considerations to overcome their impact". In: *Advanced Functional Materials* (2025), e17873. DOI: 10.1002/adfm.202517873.

- Ting Pan, Tonghan Zhao, Roja Singh, Felix Laufer, Weimu Xu, Julian Petermann, Benjamin Hacene, **Alexander Diercks**, Thomas Feeney, Sachin Kinge, Lingyi Fang, Hang Hu, Ulrich W. Paetzold. "Controlling Crystallization Dynamics of Sn-Pb Mixed Perovskite Films for Efficient Scalable Photovoltaics". In: *EES Solar* 2 (2026), pp. 425-435. DOI: 10.1039/D6EL00012F.

- Julian Petry, Ronja Pappenberger, Alexander Welle, Tonghan Zhao, **Alexander Diercks**, Raphael Pesch, Moritz Krause, Paul Fassl, Ulrich W. Paetzold. "Benchmarking Inorganic Deposition Routes for Hybrid Two-Step Processed Perovskite Solar Cells: A Materials Perspective". In: *Solar RRL* (2026) 2. DOI: 10.1002/solr.202500698.

Conference Contributions

Conference Proceedings

- Thomas Feeney, Aleksandra Miaskiewicz, Julian Petry, Felix Laufer, Roja Singh, Stefanie Severin, Viktor Škorjanc, **Alexander Diercks**, Suresh Maniyarasu, Lars Korte, Steve Albrecht, Ulrich W. Paetzold, Marcel Roß, and Paul Fassl. "Deposition rate limitations for FA-based co-evaporated perovskites and how to overcome them". In: *Proceedings of International Conference on Perovskite Thin Film Photovoltaics and Perovskite Photonics and Optoelectronics (NIPHO25)*, 2025. URL: Proceedings of International Conference on Perovskite Thin Film Photovoltaics and Perovskite Photonics and Optoelectronics.
- Ronja Pappenberger, Roja Singh, **Alexander Diercks**, Tonghan Zhao, and Ulrich W. Paetzold. "Dual Bimolecular Passivation Strategy for Enhanced Efficiency and Stability in Perovskite Solar Cells *via* a Solution-Based Two-Step Process". In: *2025 IEEE 53rd Photovoltaic Specialists Conference (PVSC)*, 2025. URL: 10.1109/PVSC59419.2025.11132818.
- Julian Petry, Viktor Škorjanc, **Alexander Diercks**, Thomas Feeney, Amedeo Morsa, Sara Rose Kimmig, Jens Baumann, Stefan Auschill, Josua Damm, Jona Kurpiers, Michael Müller, Lars Korte, Steve Albrecht, Marcel Roß, Ulrich W. Paetzold, and Paul Fassl. "Industrialization of Perovskite Solar Cell Fabrication: Strategies towards High-Throughput PVD Processes". In: *2025 IEEE 53rd Photovoltaic Specialists Conference (PVSC)*, 2025. URL: 10.1109/PVSC59419.2025.11132872.
- **Alexander Diercks**, Julian Petry, Thomas Feeney, Ulrich W. Paetzold, and Paul Fassl. "Particle Size Matters-Impact of Particle Size and Crucible Geometry on Sublimation Behavior of Formamidinium Iodide". In: *Proceedings of MATSUS Fall 2025 Conference (MATSUSFall25)*, 2025. URL: Proceedings of MATSUS Fall 2025 Conference.

Oral and Poster Contributions (First Author)

- **Poster – MATSUS23 Conference**
  Alexander Diercks, Thomas Feeney, Julian Petry, Ahmed Farag, Roja Singh, Paul Fassl, and Ulrich W. Paetzold. "All-Vacuum Processed Methylammonium-free Perovskite Solar Cells in *p-i-n* Architecture *via* a Sequential Layer Deposition Process". *Materials for Sustainable Development Conference 2023*. Valencia, Spain. March 06-10, 2023.
- **Poster – tandemPV Workshop 2023**
  Alexander Diercks, Paul Fassl, and Ulrich W. Paetzold. "All-Vacuum Processed Methylammonium-free Perovskite Solar Cells in *p-i-n* Architecture *via* a Sequential Layer Deposition Process". *tandemPV Workshop 2023*. Chambéry, France. June 06-08, 2023.
- **Talk – EUPVSEC 2023**
  Alexander Diercks, Thomas Feeney, Julian Petry, Ahmed Farag, Roja Singh, Paul Fassl, and Ulrich W. Paetzold. "All-Vacuum Processed Methylammonium-free Perovskite Solar Cells in *p-i-n* Architecture *via* a Sequential Layer Deposition Process". *40th European Photovoltaic Solar Energy Conference and Exhibition 2023*. Lisbon, Portugal. September 18-22, 2023.
- **Talk – HOPV 2024**
  Alexander Diercks, Julian Petry, Thomas Feeney, Roja Singh, Paul Fassl, and Ulrich W. Paetzold. "Understanding Substrate-Dependent Growth of Sequentially Evaporated Perovskite Thin Films". *16th International Conference on Hybrid and Organic Photovoltaics 2024*. Valencia, Spain. May 13-15, 2024.

- **Talk – PVSEC-35 2024**
  Alexander Diercks, Julian Petry, Thomas Feeney, Roja Singh, Hang Hu, Paul Fassl, and Ulrich W. Paetzold. "Sequential Evaporation Process for Fabrication of Fully Vacuum-Processed Perovskite Solar Cells: Effect of HTL on Morphology and Crystallization". *35th International Photovoltaic Science and Engineering Conference*. Numazu, Japan. November 10-15, 2024.

- **Invited Talk – MATSUS25 Conference**
  Alexander Diercks and Ulrich W. Paetzold. "Vapor Phase Deposition for Perovskite-Based Tandem Photovoltaics". *Materials for Sustainable Development Conference 2025*. Valencia, Spain. October 20-24, 2025.

- **Talk – MATSUS25 Conference**
  Alexander Diercks, Julian Petry, Thomas Feeney, Paul Fassl, and Ulrich W. Paetzold. "Particle Size Matters - Impact of Particle Size and Crucible Geometry on Sublimation Behavior of Formamidinium Iodide". *Materials for Sustainable Development Conference 2025*. Valencia, Spain. October 20-24, 2025.

Awards

- **Student Award (Oral Talk) – PVSEC-35 2024**
  Alexander Diercks, Julian Petry, Thomas Feeney, Roja Singh, Hang Hu, Paul Fassl, and Ulrich W. Paetzold. "Sequential Evaporation Process for Fabrication of Fully Vacuum-Processed Perovskite Solar Cells: Effect of HTL on Morphology and Crystallization". *35th International Photovoltaic Science and Engineering Conference*. Numazu, Japan. November 10-15, 2024.

Supervised Student Projects

- **Waseem Akram**. "*Combined Evaporation and Inkjet Printing*". Master's thesis. 2022.

- **Moritz Krause**. "*Trategies to Increase Production Throughput for Perovskite Absorbers using Hybrid Deposition Methods*". Master's thesis. 2025.

Acknowledgements

I would like to take this opportunity to thank everyone who has supported me throughout the journey of my PhD. This work would not have been possible without the support of my supervisor, colleagues, collaborators, friends and family.

First, I want to thank my PhD supervisor Prof. Dr. Ulrich W. Paetzold for giving me the opportunity to pursue my PhD in his research group "Next Generation Photovoltaics" at KIT. I am truly thankful for his continuous support and guidance, patience and persistence, and all discussions along the way. I feel very fortunate to have been part of his group. I would also like to take the opportunity to thank Prof. Dr. Henk J. Bolink for taking on the role of second reviewer.

Additionally, I want to thank Dr. Paul Fassl for his supervision and guidance during my PhD. I am very grateful to both Prof. Dr. Ulrich W. Paetzold and Dr. Paul Fassl for allowing me to go to various conferences and project-meetings around the world – it has always been a lot of fun!

To all my colleagues and members of the "Perovskite Taskforce": Thank you for all the valuable input, help, ideas and support during the years. At this point, I particularly would like to thank my fellow sublimation-subgroup colleagues Julian Petry, Thomas Feeney and Joshua Damm who made all this time much more enjoyable and fun. Special thanks to all collaborators and co-authors of publications involved in this work: Julian Petry, Thomas Feeney, Roja Singh, Hang Hu, Yang Li, Tonghan Zhao, Julian Petermann and Richard Thelen. A special thanks to Julian Petry, Joshua Damm, Thomas Feeney, Ronja Pappenberger, Felix Laufer and Paul Fassl for their valuable input and proofreading of this thesis.

During my PhD I had the wonderful opportunity to spend six months as a visiting student in the research group of Prof. Henk J. Bolink at the University of Valencia. I would like to sincerely thank Prof. Dr. Henk J. Bolink, Prof. Dr. Ulrich W. Paetzold and Dr. Paul Fassl for this great opportunity! Also, I want to thank all members of the MOED group for the great time and their constant support throughout my stay. A very special thanks goes to Sofía, Javi, Inma, Federico, Cristina, Michele and Lidón for making my time in Valencia so enjoyable. Thanks for all the help, discussions and especially all the fun activities outside lab. I also want to thank the *Karlsruhe House of Young Scientists (KHYS)* for funding my research stay with a scholarship (Research Travel Grant).

I would like to sincerely thank Nicole Klöfer, Dr. Jurana Hetterich, Astrid Henne, Reza Akbarzadeh Naseri, Christian Kayser, Julian Schickle, Felix Geislhöringer, Hans Vögele and Mario Sütsch for all their administrative and technical support at LTI over the past few years.

Finally, I would like to thank my family and friends who have supported me throughout these years of my PhD. Most importantly, I want to thank my parents for their endless support and encouragement at every point in my life. The same goes for my two amazing brothers, to whom I can always turn for help or advice and who are always there for me. Vielen Dank!